

THE UNIVERSITY OF HULL

Understanding the Mechanism & Effects of Stent Fracture: A Combined  
Experimental & Finite Element Analysis

being a Thesis submitted for the Degree of Doctor of Philosophy  
in the University of Hull

by

Mohammad Hossein Izadian, MEng (Hons)

May 2018

# Abstract

Atherosclerosis is a common heart disease, categorised by a build-up of fatty substances (plaque) in the inner surface of the coronary arteries and causing obstruction to the blood flow to vital organs and other parts of body. Over time, the arteries become narrowed which can lead to serious complications such as angina, heart attack, and stroke. There are several treatments to slow down the progress and reduce the risk, including medication and medical procedures. Percutaneous coronary intervention (PCI) is a non-surgical procedure which reopens blocked arteries and restores the blood flow. In some cases the PCI involves a tiny mesh tube known as a stent, which is placed in the narrowed artery to widen the lumen, support the vessel wall and prevent restenosis. Whilst this is generally successful procedure, stents might cause further problems such as stent fracture, in-stent restenosis, and stent thrombosis. Stent fracture is known to be associated with a number of factors; stent length, stent overlap, vessel tortuosity, degree of calcification of lesions, stent design, and the conditions under which the stent operates.

The first part of this thesis presents a design-independent finite element analysis evaluation of the relative stresses induced in a coronary stent when placed in an angulated vessel geometry. This was achieved by idealising the stent to a thin tube, with the structural modulus of the tube representing that of a stent-like structure (this could be adapted for different types of stent structure). The artery and stent were then subjected to a displacement representing a bending movement of  $20^\circ$ . Furthermore, various artery angles were modelled from  $30^\circ$  to  $90^\circ$  and each time the angle was transformed in  $10^\circ$ . This series of finite element analyses computed the stress distribution associated with the displacement, hence quantifying the relationship between the vessel angle and the stress when considering the “hinge-type” movement that the vessel will undergo with each heartbeat. This constant repetitive loading constitutes the most severe mechanical loading that the stent will undergo, which far exceeds the radial expansion/contraction

systolic/diastolic of the vessel or any torsional effects. It was observed that changes in stresses within the stent model are directly proportional to the vessel angulation, which stresses increased when the vessel angles became more severe. Furthermore, the bending region where was associated with the hinge-type movement experienced higher amounts of stress in the idealised stent model, and severe vessel angle caused a larger area undergo higher stress. The values increase at a greater rate once an angle of 75 degree has been exceeded, which agrees with clinical observation. Also areas of high stress corresponded to areas where fractures are seen clinically.

The second part involved the mechanical testing of 9 samples of four different stent designs; Multi-Link Vision<sup>®</sup>, PRO-Kinetic Energy, BioMatrix NeoFlex<sup>™</sup> and Promus PREMIER. Stents deployed at nominal pressure into physiological mock artery at initial angle of 90°, were then subjected to a 20° continuous repetitive hinge-type movement, at a rate of approximately 1100rpm (cycles per minute). By 300 million cycles fractures were identified in 7 stents, and are limited to only the Biomatrix design (34.67±28.78 million cycles), exhibiting between one and four strut fractures. Fractures were first seen to occur at 13.5 million cycles, where fractures were observed in 2 stents. All fractures were seen to occur at the ring linker parts of the stent and in the areas which would undergo the most severe tensile and compressive loading.

This study shows that artery angulation has a significant impact on the stent stress, and more tortuous vessel increases the risk of stent fracture. Also *in vitro* experimental work illustrates that stent material and structure play an important role in stent flexibility.

# Acknowledgement

I would like to thank a list of people for their kindly help, who without them it was impossible to overcome the difficulties during this period.

I would like to express my gratitude to my supervisor Dr Catherine Dobson for her continuous advice, support and sincere encouragement throughout this study. I would like to thank Dr John Caplin and Dr. Angela Hoye for their continual help in the clinical background of this study. I would like to express my appreciation to Professor Michael Fagan, Sue Taft and all those who I have worked with in the Medical Engineering Research Group, University of Hull, for their kindly help and support. I would also like to thank Peter Kazinczi, Stuart Butterick and people in the Mechanical Workshop at University of Hull for their help and contribute to design and build the test rig. I would like to thank Boston Scientific Corporation for providing Promus PREMIER Stents for our experiment. I would like to thank the Hull and East Riding Cardiac Trust and University of Hull for their financial support.

Finally, I would like to give my deepest, warm and sincere thanks to my family, parents and brothers. I send my endless love to you for your continuous generous support and encouragement throughout everything I have done.

Thank you all

# Table of Contents

Abstract	
Acknowledgement	
Table of Contents .....	i
List of Figures .....	iii
List of Tables.....	xiv
Glossary .....	xv
1. Introduction.....	- 1 -
2. Background.....	- 6 -
2.1. Introduction .....	- 6 -
2.2. The Heart .....	- 6 -
2.3. Coronary Arteries .....	- 9 -
2.4. Coronary Heart Disease.....	- 11 -
2.5. Treatment Techniques .....	- 13 -
2.5.1. Angioplasty .....	- 14 -
2.5.2. Coronary Stent Placement.....	- 16 -
2.5.3. Stents.....	- 18 -
2.5.4. Drug Eluting Stent (DES).....	- 21 -
2.6. Summary .....	- 23 -
3. Literature Review .....	- 24 -
3.1. Incidence, Predictors & Clinical Relevance of Stent fracture (SF).....	- 24 -
3.2. Finite Element & Fatigue Life Analysis of Stent .....	- 38 -
3.3. Bench Testing of Stents.....	- 56 -
3.4. Summary .....	- 68 -
4. Idealised Modelling of a Stent in an Angulated Coronary Artery .....	- 70 -
4.1. Introduction .....	- 70 -
4.2. Methodology .....	- 71 -
4.2.1. Effective Modulus for Idealised Stent.....	- 72 -
4.2.2. Validation & Convergence Study .....	- 74 -
4.2.3. Stenting in Angulated Artery .....	- 75 -
4.2.4. Stent in Linear Artery.....	- 78 -
4.2.5. Stent in Non-Linear Artery .....	- 84 -
4.3. Results .....	- 85 -
4.3.1. Stent Results in Linear Artery.....	- 86 -

4.3.2.	Stent Results in Non-Linear Artery.....	- 93 -
4.4.	Discussion .....	- 99 -
4.4.1.	Stent in Linear Artery Model .....	- 100 -
4.4.2.	Stent in Non-Linear Artery Model.....	- 104 -
5.	In vitro Experimental Fatigue Test .....	- 109 -
5.1.	Introduction .....	- 109 -
5.2.	Methodology .....	- 110 -
5.2.1.	Experimental Procedure .....	- 111 -
5.2.2.	Testing Protocol 1 .....	- 114 -
5.2.3.	Testing Protocol 2 .....	- 115 -
5.2.4.	Stent Durability Experiment .....	- 115 -
5.3.	Results .....	- 118 -
5.3.1.	Testing Protocol 1 Result .....	- 118 -
5.3.2.	Testing Protocol 2 Result .....	- 121 -
5.3.3.	Stent Durability Result .....	- 122 -
5.4.	Discussion .....	131
6.	Discussion.....	136
7.	Conclusion & Future Work.....	143
8.	References.....	146
	Appendix I.....	157
	Appendix II .....	164

# List of Figures

Figure 2.1: Heart valves and chambers (Healthwise 2007). .....	- 7 -
Figure 2.2: Blood circulation in the heart (Healthwise 2007).....	- 8 -
Figure 2.3: Coronary arteries. The right coronary artery (RCA), and the left coronary artery (LCA) (Texas heart institute 2016).....	- 9 -
Figure 2.4: Coronary arteries. The two main arteries, right coronary artery and left coronary artery has been divided into many SB (Gray’s Anatomy 2005).....	- 10 -
Figure 2.5: The heart with coronary artery circled. Coronary artery disease (Atherosclerosis) demonstrated in B and C. A) Healthy artery, B) Narrowed artery due to build-up of plaque, C) Narrowed artery due to build-up plaque of with superimposed blood clot (thrombus) (MelbourneHeartcare 2015). .....	- 12 -
Figure 2.6: The Medina coronary bifurcation lesions classification. It uses binary number (0,1) to indicate presence of a lesion in MA (the proximal segment), MA the distal segment and SB, respectively, in a bifurcation artery (Medina et al. 2006).....	- 13 -
Figure 2.7: Angioplasty result, A) Blockage prior to angioplasty, B) After balloon angioplasty, C) After stent is placed (Heartsite 2013). .....	- 16 -
Figure 2.8: Stenting procedure. A) The catheter is inserted to the site of coronary obstruction, B) The balloon is inflated, thus the stent is expanded and compresses the plaque against the artery wall, C) The balloon is deflated and removed from the artery while the stent remains in place (Park 2013). .....	- 18 -
Figure 2.9: Expanded Cypher stent (Cordis Corporation, California, USA).....	- 19 -
Figure 2.10: The two main stent structure, A) Opened cell, and B) Closed cell. ....	- 20 -
Figure 3.1: Representation of (A) opened cell stent (Multi-Link 8, Abbott Vascular) and (B) closed cell stent (Cypher, Cordis Corporation). .....	- 26 -

Figure 3.2: Quantifying the hinge motion of the coronary arteries. The difference between angle  $\alpha$  ( $^{\circ}$ ) end of diastole (left) and angle  $\beta$  ( $^{\circ}$ ) end of systole is the degree of hinge motion. Also the maximal angle in target lesion is represented as  $\beta$  ( $^{\circ}$ ) (Ino et al. 2009)..... - 32 -

Figure 3.3: (A) Fracture grade and the white arrows indicate fractured struts. (B) Calcification degree mild= barely seen or focally localized (Almost 25% of stent), moderate= multiple sites, and severe = highly visible diffuse calcification (more than 75% of stent length is associated with calcification). White arrows indicate calcified area (Nakazawa et al. 2009)..... - 33 -

Figure 3.4: Structure of stents as well as common location of fracture in A) Taxus stent at straight longitudinal segment, and B) Cypher stent at N-shaped linker segment. . - 34 -

Figure 3.5: Sketch of A) a bending load  $M$  for the unit stent and B) Multiple bending load  $M1$  and  $M2$  for the whole stent (Wu et al. 2007)..... - 41 -

Figure 3.6: Deformation of stent under bending load A) the unit stent and B) the whole stent (Wu et al. 2007)..... - 41 -

Figure 3.7: Max inverse FSF location or the zone with lowest FSF on FE stent (Marrey et al. 2006)..... - 43 -

Figure 3.8: Geometry of (A) semi-elliptical (centre) flaw, and (B) corner flaw at stent wall (Marrey et al. 2006)..... - 44 -

Figure 3.9: Distribution of von-Mises stress within the stent model due to A) effect of diastolic pressure, and B) effect of systolic pressure (Barrera et al. 2012)..... - 46 -

Figure 3.10: Location of minimum and maximum stress (Li et al. 2010). ..... - 47 -

Figure 3.11: SEM at curvature of ring (A) before simulation (B) after simulation (Li et al. 2010). ..... - 48 -

Figure 3.12: Geometrical reconstruction of LAD: A) Medical image from CTA and CCA, and B) 3D model (Morlacchi et al. 2013). ..... - 49 -

Figure 3.13: Maximum von Mises stress at the overlapping segment after the stenting procedure (Morlacchi et al. 2013)..... - 49 -

Figure 3.14: (A) Straight vessel model, and (B) curved vessel model (Wei Wu et al. 2007). .....	- 50 -
Figure 3.15: Change in outer diameter of stent during expansion (Eshghi et al. 2011).....	- 53 -
Figure 3.16: Stress distribution in the stent after balloon deflation A) idealise non-folded angioplasty balloon, B) an idealised folded angioplasty balloon, and C) folded model of a semi-compliant angioplasty balloon. The left side models representing the free deployment stress distribution, and the right models representing the artery deployment stress distribution (Martin & Boyle 2013). .....	- 54 -
Figure 3.17: (A) Coronary artery model, (B) Cardiac wall surrounded half of the artery model, and (C) Cross section of vessel lumen without and with (gray area) calcified lesion (Morlacchi et al. 2014).....	- 55 -
Figure 3.18: Loading and displacement conditions during the cardiac cycle (Morlacchi et al. 2014).....	- 55 -
Figure 3.19: distribution of von-Mises stress after stent deployment A) non-calcified, and B) calcified artery (Morlacchi et al. 2014).....	- 56 -
Figure 3.20: Stent experiment model (Mori & Saito 2005).....	- 59 -
Figure 3.21: stent configuration after the bending test (Mori & Saito 2005). .....	- 60 -
Figure 3.22: Coronary artery route model to measure the track-ability force. (Szabadits et al. 2009).....	- 61 -
Figure 3.23: The test apparatus set up to determine the longitudinal strength of a stent. A) A polytetrafluoroethylene (PTFE) tube with 2.75mm inner diameter placed inside a silicone tube with 3.5mm inner diameter. B) The stent is deployed and the distal portion secured the distal portion within the PTFE tube with 5mm of the proximal portion exposed in the silicone tube. Subsequently, a rod (R) connected to an Instron testing machine compress the sample. C) The rod (R) is removed after compressing the stent. (Ormiston et al. 2014). .....	- 62 -

Figure 3.24: Proximal deformation after 0.5N compression force on six different coronary stent design. Microcomputed tomography images were taken to illustrate the inflow hoop angle (red line). The bottom is the proximal view of stent lumen (red area), beneath it the mean and standard deviation (SD) compressed distance of each design (Ormiston et al. 2014) .....	- 63 -
Figure 3.25: The testing instrument Bose ELF 3220 (Bose Corporation, Eden Prairie, ...-	64 -
Figure 3.26: Over expansion of a stent. A) Side view of distal segment of stent at nominal pressure, and oversized at the proximal segment. B) Large cell enlargement, and C) struts straightened at crown connector by an average of $77 \pm 8^\circ$ at NP placement to $146 \pm 15^\circ$ after over expansion (Ng et al. 2016).....	- 66 -
Figure 3.27: Specimen dimensions where w is the strut size. All samples have 4mm gauge length and three struts which two of them were to support the specimen and avoid any damage prior to the test. Once the example was placed in the testing rig, the supporting struts were snipped. (Murphy et al. 2003).....	- 67 -
Figure 3.28: The lower part of test rig without a specimen. The sample tube is located over the pin bar, and then upper grip part is lowered on top of the sample. (Murphy et al. 2003). .....	- 67 -
Figure 4.1: 3D digitised Cypher stent in AVIZO.....	- 72 -
Figure 4.2: The FE model of the Cypher (Cordis Corporation, USA) stent, 3mm ID and 28mm length. ....	- 73 -
Figure 4.3: Deformation of A) artery and B) stent models when both ends of the models were constrained in all DOF, and a force was applied in y-direction (negative) to a node in the middle of each model.....	- 74 -
Figure 4.4: Mesh model of A) artery, B) stent.....	- 75 -
Figure 4.5: Artery model at initial angle ( $30^\circ$ ) at its mid-length. The angle can be adjusted up to $90^\circ$ , and undergo a displacement loading to represent cardiac loading. ....	- 76 -

Figure 4.6: A completed idealised FE model at initial angle of 30°. A) Idealised meshed stent comprising shell elements, and B) full model of idealised stent (purple area) within the artery model (blue area). ..... - 77 -

Figure 4.7: Model I; artery modelled with linear isotropic material properties. Displacement load between 5° and 20° was applied in the x-direction to nodes at the top end of the artery for 9.5mm (blue part), and the lower end of the artery was constrained in all DOF for 13mm (yellow part). ..... - 79 -

Figure 4.8: Model II; artery modelled with linear isotropic material properties. Displacement load and constrained area were limited to the segment of artery which housed the stent. Displacement between 5° and 20° was applied in the x-direction to the artery nodes for 10.5mm (blue part), and the lower end of the artery was constrained in all DOF for 10.5mm (yellow part). ..... - 79 -

Figure 4.9: Model III; artery modelled with linear isotropic material properties. Displacement load between 5° and 20° was applied in the x-direction to nodes at the top end of the artery for 9.5mm (blue part), and the lower end of the artery which housed the stent was constrained in all DOF for 10.5mm (yellow part). ..... - 80 -

Figure 4.10: Model IV; artery modelled with linear isotropic material properties. Displacement load between 5° and 20° was applied in the x-direction to nodes at the top end of the artery for 9.5mm (blue part), and the lower end of the artery which housed the stent was constrained in all DOF for 7mm (yellow part). ..... - 81 -

Figure 4.11: Model V; artery modelled with linear isotropic material properties. Two identical displacement load were applied to both ends of the artery on all nodes on the half outer surface of the artery for 9.5mm (blue part), where in the top section it is in the x-direction and in the bottom section it is in both y and x direction. All exterior nodes in the middle segment of the artery were constrained in all DOF (yellow part). ..... - 82 -

Figure 4.12: Model VI; artery modelled with linear isotropic material properties. Two identical displacement load were applied to both ends of the artery on all nodes on the

half outer surface of the artery for 9.5mm (blue part), where in the top section it is in the x-direction and in the bottom section it is in both y and x direction. One exterior node in the outer surface of artery at the back of bending region was constrained in all DOF.- 82

-  
Figure 4.13: Model VII; artery modelled with linear isotropic material properties. Two identical displacement load were applied to both ends of the artery on all nodes on the half outer surface of the artery for 9.5mm (blue part), where in the top section it is in the x-direction and in the bottom section it is in both y and x direction. One node in the inner surface of artery at the bending region was constrained in all DOF..... - 83 -

Figure 4.14: Model VIII; artery modelled with linear isotropic material properties. Two identical displacement load were applied to both ends of the artery on all nodes on the half outer surface of the artery for 9.5mm (blue part), where in the top section it is in the x-direction and in the bottom section it is in both y and x direction. Two nodes in the inner and outer surface of artery at the bending region were constrained in all DOF.- 83

-  
Figure 4.15: Model IX; artery modelled with linear isotropic material properties. Two identical displacement load were applied to both ends of the artery on all nodes on the half outer surface of the artery for 9.5mm (blue part), where in the top section it is in the x-direction and in the bottom section it is in both y and x direction. Three nodes in the inner and both sides of artery surface at the bending region were constrained in all DOF.

..... - 84 -

Figure 4.16: Models VI to IX simulated angulate artery with non-linear material property for the artery..... - 85 -

Figure 4.17: Stress distribution within idealised stent model at an initial angulation of 70°. A total of 20° displacement load was exerted to the linear models artery I to IX. A) 1<sup>st</sup> principal (tensile) stress, B) 3<sup>rd</sup> principal (compressive) stress..... - 87 -

Figure 4.18: Stress distribution and displacement within idealised stent model at an initial angulation of 70°. A total of 20° displacement load was applied to the linear models artery I to IX. A) Von-Mises stress distribution, and B) displacement of the stent model. . - 88 -

Figure 4.19: The tensile stress distribution within the stent model in the linear artery with 70° initial angle in the IX design under 20° displacement load. The same node was chosen throughout the models to compare the stresses..... - 89 -

Figure 4.20: Variation of displacement in the stent with respect to initial vessel angulation, when a total 20° displacement load applied. The vessel has linear material properties..... - 90 -

Figure 4.21: Variation of tensile stress at the specified node in the stent with respect to initial vessel angulation, when a total 20° displacement load applied. The vessel has linear material properties..... - 90 -

Figure 4.22: Variation of compressive stress at the specified node in the stent with respect to initial vessel angulation, when a total 20° displacement load applied. The vessel has linear material properties..... - 91 -

Figure 4.23: Variation of von-Mises stress at the specified node in the stent with respect to initial vessel angulation, when a total 20° displacement load applied. The vessel has linear material properties..... - 91 -

Figure 4.24: Variation of maximum tensile stress in the stent with respect to initial vessel angulation, when a total 20° displacement load applied. The vessel has linear material properties..... - 92 -

Figure 4.25: Variation of maximum compressive stress in the stent with respect to initial vessel angulation, when a total 20° displacement load applied. The vessel has linear material properties..... - 92 -

Figure 4.26: Variation of maximum von-Mises stress in the stent with respect to initial vessel angulation, when a total 20° displacement load applied. The vessel has linear material properties..... - 93 -

Figure 4.27: Stress distribution within idealised stent model at an initial angulation of 70°. A total of 20° displacement load was applied to the non-linear models artery VI to IX. 1 <sup>st</sup> principal stress (top row), 3 <sup>rd</sup> principal stress (middle row), and von-Mises stress (bottom row). .....	- 94 -
Figure 4.28: Variation of tensile stress at the specified node in the stent with respect to initial vessel angulation, when a total 20° displacement load applied. The vessel has non-linear material properties.....	- 95 -
Figure 4.29: Variation of compressive stress at the specified node in the stent with respect to initial vessel angulation, when a total 20° displacement load applied. The vessel has non-linear material properties. ....	- 95 -
Figure 4.30: Variation of von-Mises stress at the specified node in the stent with to initial vessel angulation, when a total 20° displacement load applied. The vessel has non-linear material properties.....	- 96 -
Figure 4.31: Variation of displacement in the stent with respect to initial vessel angulation, when a total 20° displacement load applied. The vessel has non-linear material properties. ....	- 96 -
Figure 4.32: Variation of maximum tensile stress in the stent with respect to initial vessel angulation, when a total 20° displacement load applied. The vessel has non-linear material properties.....	- 97 -
Figure 4.33 Variation of maximum compressive stress in the stent with respect to initial vessel angulation, when a total 20° displacement load applied. The vessel has non-linear material properties.....	- 97 -
Figure 4.34: Variation of maximum von-Mises stress e in the stent with to initial vessel angulation, when a total 20° displacement load applied. The vessel has non-linear material properties.....	- 98 -

Figure 4.35: Variations of the tensile stress distribution within the stent model in the non-linear artery with initial angle from 30° to 90° in the IX design under 20° applied displacement..... - 99 -

Figure 4.36: Variation of tensile stress in the stent with respect to initial vessel angulation, when a total 20° displacement load applied. A comparison of the non-linear and linear artery material properties. .... - 106 -

Figure 4.37: Variation of compressive stress in the stent with respect to initial vessel angulation, when a total 20° displacement load applied. A comparison of the non-linear and linear artery material properties. .... - 106 -

Figure 4.38: Variation of von-Mises stress in the stent with respect to initial vessel angulation, when a total 20° displacement load applied. A comparison of the non-linear and linear artery material properties. .... - 107 -

Figure 5.1: Procedure of stent placement in angulated mock artery. A) Loading arm is set at initial angle of 90°, B) the mock artery is placed into the loading arm at the pre-determined initial angle, C & D) Catheter inserts via prepared pathway to deploy stent at the initial angle..... - 112 -

Figure 5.2: Stent deployment in silastic tubing at predetermined angle in loading arm (90°) ..... - 113 -

Figure 5.3: Stent testing rig – capable of testing 28 angulated samples simultaneously, subjecting each stent to an identical repetitive hinge motion loading of 20° ..... - 113 -

Figure 5.4: Two identical (ID= 3mm, 28mm length) Cypher (Cordis Corporation, USA) stents deployed in two types of silastic tubing; A) BDC labs tube (thin tube), and B) Bose corporation tube (thick tube) at initial 90° . .... - 115 -

Figure 5.5: A) Upgraded test rig, optimised the capacity and speed of test. B) Inset of stent deployed in testing arm at initial 90° showing direction of hinge-movement totalling 20° . .... - 116 -

Figure 5.6: Sample of micro-CT images of stents: A) Multi-Link Vision, B) PRO-Kinetic Energy, C) BioMatrix, and D) Promus PREMIER when deployed at initial 90° into the mock artery tube.....	- 117 -
Figure 5.7: Fractures observed in Cypher stent deployed in silastic tubing of wall thickness 0.75 mm, after 552,257 cycles. ....	- 119 -
Figure 5.8: Single fracture observed in Cypher stent deployed in silastic tubing of wall thickness 0.45 mm, after 552,257 cycles. ....	- 119 -
Figure 5.9: 16 fractures observed in Cypher stent deployed in silastic tubing of wall thickness 0.45 mm, after approx. 4.2 million cycles.....	- 120 -
Figure 5.10: 6 fractures observed in Cypher stent deployed in silastic tubing of wall thickness 0.75 mm, after approx. 4.2 million cycles.....	- 120 -
Figure 5.11: Fracture frequency of deployed stent in silicon mock artery with two different wall thicknesses. Blue line indicates the progress of fracture in thicker tube versus orange line for the thinner tube. ....	- 121 -
Figure 5.12: Micro-CT images of deployed Multi Link 8 stent at 90° initial angle in thin tube (BDS labs tube). A) Deployed stent before starting the test, B) Red circles define the strut fracture after 225 million cycles where the stent was subjected to 25° (between 95° and 70°) repetitive hinge-type movement. ....	- 122 -
Figure 5.13: Micro-CT images of three samples of Multi-Link Vision stent design: A) Deployed stent in to the mock artery at initial angle of 90° before starting the test, B) After 300 million cycles no fracture was identified.....	- 123 -
Figure 5.14: Micro-CT images of three samples of PRO-Kinetic Energy stent design: A) Deployed stent in to the mock artery at initial angle of 90° before starting the test, B) After 300 million cycles no fracture was identified.....	- 123 -
Figure 5.15: Micro-CT images of three samples of Promus PREMIER stent design: A) Deployed stent in to the mock artery at initial angle of 90° before starting the test, B) After 300 million cycles no fracture was identified.....	- 124 -

Figure 5.16: Micro-CT images of sample A to C of BioMatrix stent design. The progress of strut fracture from beginning to end of the experiment at 300 million cycles.....	- 125 -
Figure 5.17: Micro-CT images of sample D to F of BioMatrix stent design. The progress of strut fracture from beginning to end of the experiment at 300 million cycles.....	- 126 -
Figure 5.18: Micro-CT images of sample G to I of BioMatrix stent design. The progress of strut fracture from beginning to end of the experiment at 300 million cycle .....	- 127 -
Figure 5.19: Representative $\mu$ -CT images of the strut fracture in 7 samples of BioMatrix stent design. With total A) one B) four, C) four, D) two, E) one, F) two, and G) two struts fractures.....	129
Figure 5.20: Number of stent strut fractures observed for BioMatrix stents, vs. number of cycles of 20°hinge loading, on a vessel of initial angulation of 90° .	130
Figure 5.21: Mean and standard deviation (SD) of number of strut fracture to number of cycles for the BioMatrix stent design.....	130
Figure 6.1: A) Distribution of tensile stress within the stent model at initial angle 90°, when it was housed by non-linear artery model IX subjected to 20° displacement. B) Site of strut fracture in a BioMatrix sample, when it was deployed at initial 90°and then subjected to 20° repetitive hinge-type movement. Stent fracture occurs at sites of increased stress on the stent due to hinge movement.....	141

# List of Tables

Table 3.1: Classification of stent fracture (Nakazawa et al. 2009). .....	- 27 -
Table 3.2: Odds ratio of risk factor for stent fracture (Kuramitsu et al. 2012). .....	- 36 -
Table 3.3: Mechanical properties of L-605 Co-Cr alloy (Marrey et al. 2006). .....	- 42 -
Table 3.4: Stress and fatigue safety factor (FSF) at the worst case fatigue location (Marrey et al. 2006). .....	- 43 -
Table 3.5: Important standard and regulations for medical device manufactures (The British Standards Institution 2018). .....	- 57 -
Table 4.1: Stent properties base on the Cypher stent (Mortier et al. 2009), and the effective modulus of idealised stent model .....	- 74 -
Table 4.2: Material property for the artery model, linear and non-linear model .....	- 76 -
Table 5.1: Material properties of different alloys used for coronary stent (O'Brien et al. 2010, Huibregtse & Juan F. Granada 2011). .....	- 109 -
Table 5.2: Specification of the four stent designs tested. (NP= Nominal pressure for 3mm ID) .....	- 118 -
Table 5.3: Site and total number of strut fracture within the four stent designs, 9 of each after 300 million cycles bend test.....	128

# Glossary

<b>AMI</b>	Acute myocardial infarction.
<b>Angina</b>	The most common symptom of coronary heart disease and reduction in blood flow. It is characterised by shortness of breath or/and chest pain, or sometimes pain in the arm, neck, stomach and jaw.
<b>Angioplasty</b>	A technique to reopen blocked or obstructed arteries utilising a balloon inserted at the site via a catheter.
<b>Atherectomy</b>	A procedure where a sharp blade is mounted at the end of a catheter to cut and remove plaque from an artery.
<b>Atherosclerosis</b>	A disease causing hardening and narrowing of the arteries by deposition of plaque on the inner walls of the blood vessel.
<b>atm</b>	Atmospheric pressure.
<b>BA</b>	Bifurcation angle.
<b>Bifurcation</b>	A division into two branches.
<b>BMS</b>	Bare metal stent.
<b>BPM</b>	Beats per minute.
<b>CABG</b>	Coronary artery bypass graft
<b>CHD</b>	Coronary heart disease
<b>DES</b>	Drug eluting stent.
<b>Distal</b>	Situated away from the centre of the body or from the point of attachment.
<b>DOF</b>	Degree of freedom.
<b>EES</b>	Everolimus eluting stent.
<b>FE</b>	Finite element.

<b>FSF</b>	Fatigue safety factor
<b>Ischemia</b>	Decrease of blood flow and oxygen to body organ especially the heart due to narrowed blood vessel.
<b>ISR</b>	In-stent restenosis.
<b>IVUS</b>	Intravascular ultrasound.
<b>LAD</b>	Left anterior descending artery.
<b>LCR</b>	Left coronary artery.
<b>LCX</b>	Left circumflex artery.
<b>LM</b>	Left main artery.
<b>MA</b>	Main artery.
<b>MACE</b>	Major adverse cardiac event.
<b>MI</b>	Myocardial infarction also known as heart attack.
<b>OR</b>	Odds ratio.
<b>PCI</b>	Percutaneous coronary intervention.
<b>PES</b>	Paclitaxel eluting stent.
<b>Proximal</b>	Situated nearer to the centre of the body or the point of attachment.
<b>RCA</b>	Right coronary artery.
<b>RPM</b>	Revolution per minute
<b>SB</b>	Side branch.
<b>SES</b>	Sirolimus eluting stent.
<b>SF</b>	Stent fracture.
<b>ST</b>	Stent thrombosis.
<b>Stent</b>	A tiny mesh tube which is inserted in a narrow artery as the part of PCI.

<b>SVG</b>	Saphenous vein graft.
<b>Thrombosis</b>	Local coagulation or clotting of the blood in a part of the circulatory system.
<b>TLR</b>	Target lesion revascularization.
<b>μCT</b>	Micro computed tomography.
<b>3D</b>	Three dimensional.

# 1. Introduction

The human heart is a muscular organ which supplies the required oxygen and nutrition to the body through the blood circulation system. There are two main arteries in the heart, the right coronary artery (RCA) and the left coronary artery (LCA), which are divided into several branches and supplies the entire heart muscle and substituent cardiac cells. Therefore, it is essential that these arteries and branches fully function without any disruption. However, in some cases the arteries become clogged by an accumulation of fatty deposits (atheroma), known as atherosclerosis. Atherosclerosis is the most common heart disease that causes restriction in the blood flow which supplies oxygen to vital organs. It is a life threatening disease and can lead to major problems such as heart attacks and strokes, although it may initially be asymptomatic. Hence, it is suggested to have health check every five years for anyone over 40 years old (British Heart Foundation 2014).

There are various treatments for the condition, however none can reverse atherosclerosis. Percutaneous coronary intervention (PCI) is a non-invasive procedure which restores the blood flow, sometimes involving stenting to prevent restenosis in the blocked artery. Although, stenting in the coronary arteries revolutionised PCI, it can also cause complications such as stent fracture (SF) which is associated with in-stent restenosis (ISR) and conceivably stent thrombosis (ST), aneurysm formation, and myocardial infarction (MI) (Lee et al. 2007, Kuramitsu et al. 2012, Chakravarty et al. 2010).

Incidence of SF has been reported very broadly 0.8% to 29% (Nakazawa et al. 2009, Wiktor et al. 2016) between numerous studies. This is due to varying definition and classification of fracture, the method of diagnosis, and the population considered within the studies (Alexopoulos 2011, Kim et al. 2010). The diagnosis of SF is quite difficult especially when only a single strut is fractured (type 1), so the exact incidence of it is

largely unknown. For instance, angiography is the most common way to follow up the procedure which has low sensitivity particularly for type 1 of SF when compared with intravascular ultrasound (IVUS), but it is not always performed routinely. Therefore, SF may not be recognised immediately, while the clinical manifestation of SF might occur only after 2 days of implantation, or up to 2 years after the implantation which it can lead to late adverse cardiac events such as myocardial infarction (MI), and even sudden death (Lee et al. 2007).

Several factors are known to impact and increase the SF rate such as stent design and composition, stent size and the thickness of its struts, site of implantation (mostly at a region of high tortuosity), as well as the application of high pressure during stent dilation. In addition, in a number of studies some other factors have been identified as independent predictors of SF associating it with increased lesion complexity, including extensive calcification, the change in angulation of the lesion after stenting, stent length, overlapping stents, proximal vessel tortuosity, total occlusions, ostial location and treatment of the right coronary artery (RCA) (Carter 2008, Adlakha et al. 2010). Hence, the chance of SF at bifurcation and in highly angulated vessels is higher, as the stress on the stent increases due to it undergoing a type of hinge-type movement as a result of heart contraction.

The aim of the present study was to assess the influence of vessel angulation on stresses within the stent, and hence likelihood of stent fracture. To understand the mechanism of stent fracture in tortuous vessels, a combination of computer modelling and mechanical testing was conducted. Firstly, a series of design independent idealised finite element (FE) models were constructed to represent stents positioned in arteries with varying degrees of angulation ranging between 30° and 90°. An applied displacement (values ranging from 5 degrees to 20 degrees) was applied to represent the hinge movement experienced by the stent during the cardiac cycle. Moreover, the artery was as attributed first linear and then

non-linear material properties to determine the impact of this variable on the predicted stresses in the stent. The magnitude of tensile, compressive and von Mises stress in the stent model as well as the stress distribution within the stent model were considered. This aimed to increase understanding of the relationship between angle of tortuosity and stent stress, along with the relationship between angle of displacement during the cardiac cycle and stent stress. To our knowledge, this is the first attempt to develop FE models which are able to investigate the relation between stent stress and artery angulation. Although it is an idealised model, the work has potential to provide a clear overview of stent mechanical loading in angulated vessels. Secondly, long-term mechanical bench testing was performed to examine the fatigue life of four types of commercial stents designs: MULTI-LINK VISION<sup>®</sup> (Abbott Vascular), PRO-Kinetic Energy (BIOTRONIK), BioMatrix NeoFlex<sup>™</sup> (Biosensors International), and Promus PREMIER<sup>™</sup> (Boston Scientific). A sample size of 9 stents in each group underwent a deflection of 20° in the test rig at high speed (approximately 1100 cycles per minute). The *in vitro* experiment involved testing stents in angulated silicon synthetic vessels at a predetermined initial angle, and then subjected to a repetitive loading to represent the cardiac cycle movement (hinge movement). The experiment was running continuously and only interrupted for regular checking of fracture using a  $\mu$ CT scanner to inspect the structure. Once a fracture was detected within a stent, a full  $\mu$ CT scan was undertaken to create a FE model of the actual stent for future work (not within the scope of this thesis), and then the testing continued with the procedure repeated when further fractures occurred until total separation occurred. Furthermore, the predicted stress distribution from computer modelling were compared to stent fractures observed through the *in vitro* experiment analyses. Comparisons between these two studies, were used as a measure to evaluate the influence of mechanical loading on the SF.

This thesis consists of seven chapters, plus a glossary to define technical terms and appendix. The appendixes contain fundamental study and the model parameters, as well as full sets of the FE results. The content of chapters is briefly described below:

Some basic background knowledge of heart anatomy, including the coronary arteries, coronary heart disease (atherosclerotic), treatments of the disease, a brief history of percutaneous coronary intervention and its procedure, as well as introduction to coronary stents and the different types is discussed in Chapter 2.

Chapter 3 is a literature review including clinical studies of stent fracture incidence, influence factors, and its complications. Also included were previous FE modelling studies of stenting procedures under various boundary conditions. Furthermore, mechanical experiment were discussed individually in the final section of Chapter 3.

Chapter 4 describes the development of idealised finite element models of stents in angulated arteries. Properties of the idealised stent model were obtained through software based on data from micro-CT of a Cypher stent (Cordis, corporation, USA. ID=3mm, 28mm in length). The idealised stent model was housed by the artery model with various initial angles, with several different boundary conditions applied, and subjected to an angular displacement. The development of the models is described and the results obtained and discussed.

The *in vitro* experimental testing of different types of stent designs is described in Chapter 5. Firstly, a pilot study was conducted, using two Cypher stents (Cordis, corporation, USA. ID=3mm, 28mm in length) to identify the suitable physiological mock artery for use in the study, as well as capability testing of the test rig. Consequently, the adapted test rig was used for a full study which was performed by deploying 9 samples each of four stent designs into the mock artery at initial angle  $90^\circ$ , and then subjected to a repetitive  $20^\circ$

displacement. Each sample was examined in turn by  $\mu$ CT at specified intervals to identify evidence of strut fracture.

Chapter 6 gives a summary of key results from FE modelling and *in vitro* experiment, and the whole project is discussed including the relevance to the current literature.

Chapter 7 outlines the conclusion of the thesis follow by suggestions for future work.

To summarise, the main objectives of the work were as follows:

1. To develop a series of idealised finite element models of stents in angulated artery models.
2. To understand the impact of artery angulation on the stent stress.
3. To identify high risk location of stent fracture under such boundary conditions.
4. To develop and carry out *in vitro* experimental test procedure to evaluate failure time of different stent designs, when they are deployed at an initial angle and subjected to a repetitive displacement, as well as investigate the location and progression of strut fracture in each case

## **2. Background**

### **2.1. Introduction**

The essential background of heart's structure and blood circulation is presented in this chapter, with the focus being on coronary arteries. The geometry and type of coronary arteries are discussed, as well as coronary heart disease (CHD), and factors that can increase the risk of atherosclerosis. In the following, the pathology and available treatments are discussed.

### **2.2. The Heart**

The heart is a muscular organ located in the middle of the thoracic cavity between the lungs. It contracts regularly and continuously to supply oxygen and nutrients to the body by pumping blood through two circuits, the pulmonary and the systemic (or general) circulation (Lakatta 2011).

The anatomy of the heart is shown in Figure 2.1. It consists four chambers; the right and left atria are known as the two upper chambers, and the right and left ventricles are known as the two lower chambers. However, these chambers are functioning as 2-sided pump, where in the right side low pressure venous blood pumps into the lungs, and the arterial blood pumps to the systemic circulation via the left side high pressure system.

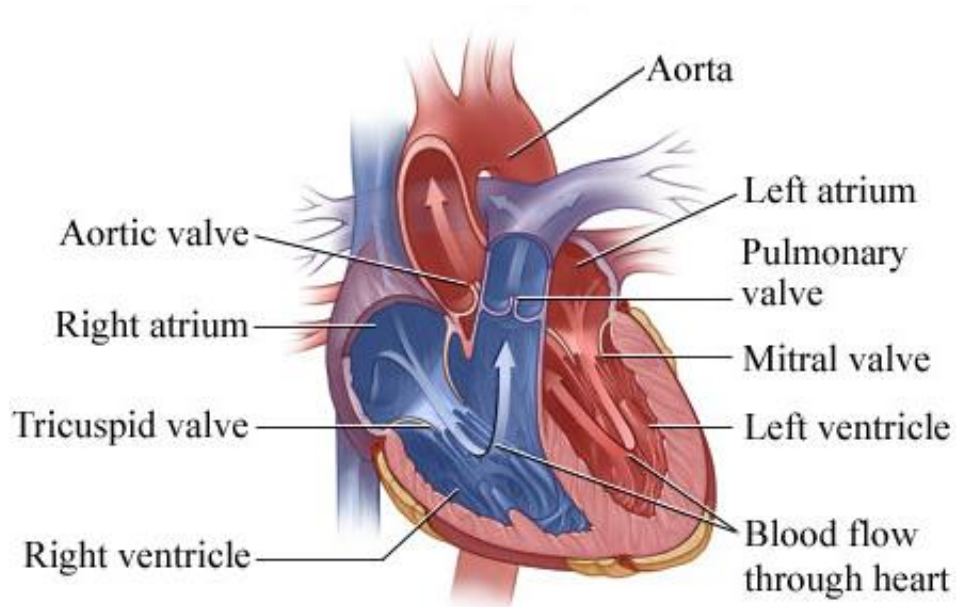


**Figure 2.1: Heart valves and chambers (Healthwise 2007).**

The heart has two sets of atrioventricular valves tricuspid and mitral (bicuspid), and two sets of semilunar valves pulmonic and aortic to avoid blood backflow in the heart chambers (Marieb 2010, Lilly 2014).

Blood in low oxygen and high carbon dioxide passes from the superior and inferior vena cava and the coronary sinus to the right atrium, and then through tricuspid valve flows to the right ventricle. Contraction of the right ventricle leads to closure in the tricuspid valve, hence the blood in the right ventricle ejects to the pulmonary trunk through the pulmonic valve. The pulmonary circuit delivers the blood to the lungs and pulmonary veins from the pulmonary trunk via the right and the left pulmonary arteries. The lungs exhales carbon dioxide and receives oxygen, and then oxygenated blood delivers to the left atrium through the pulmonary veins. Blood leaves the left atrium and flows to the left ventricle via the mitral valve. Contraction of the left ventricle leads to closure in the mitral valve, hence the blood in the left ventricle ejects to the aorta through the aortic valve. The systemic circuit circulates blood throughout the body from the aorta. The superior vena cava receives blood from the tissues of the head, neck and upper extremities, and the inferior vena cava receives the blood from lower part of the body. Finally, those blood

delivers to the right atrium from both the superior and inferior vena cava. (Elaine N 2010, Lakatta 2011, Lilly 2014). Figure 2.2 illustrates the circulation of blood through the heart.

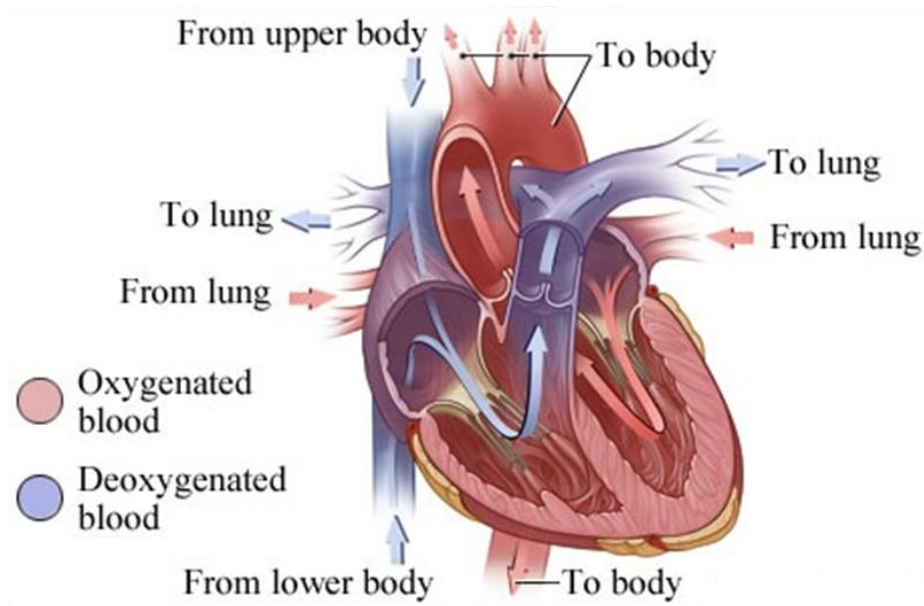


**Figure 2.2: Blood circulation in the heart (Healthwise 2007).**

The blood circulation through the heart is associated with several events, which is known as the cardiac cycle. The cardiac cycle, systole and diastole cause pumping blood repetitively through the heart chambers. During systole phase, both the atrial and the ventricular muscle contract in order to eject the blood from the chambers. This contraction leads to increased pressure within the chambers and is necessary to decrease. Whereas, during the diastole phase the chambers are more relax and hence, the pressure falls in both the atrial and ventricular chambers. (Julian 2004). This phenomenon causes the heartbeat and it is very dependent on when it is measured, whilst resting or after exercise, because fast heartbeats are as a direct result of fast blood flow. In additional, the heart rate may increase by others factors such as fever, stress, and an overactive thyroid (Deckelbaum 1992). However the standard healthy heart rate might be varied between 60 and 100 beats per minute (bpm) for adults at rest (British Heart Foundation 2014b).

## 2.3. Coronary Arteries

The normal human heart has two main coronary arteries, known as the epicardial coronary artery system, however, in some rare cases people might have only one or even three coronary arteries (Jr et al. 1992) The right coronary artery (RCA) and the left coronary artery (LCA), both originate from the aorta as shown in Figure 2.3. These two major arteries and their branches separate the ventricles and the atrium as well as separate the left and right side of the ventricle chamber (Waller et al. 1992, Deckelbaum 1992, Katz & Ness 2015).

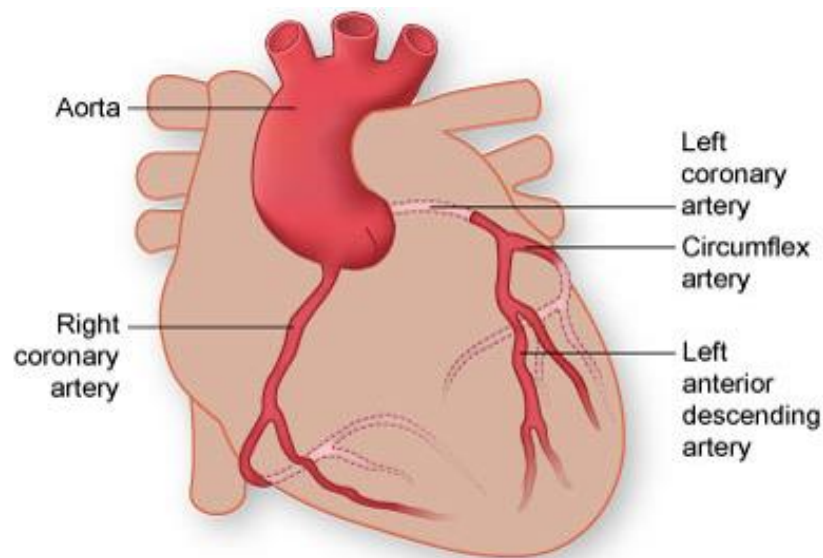


**Figure 2.3: Coronary arteries. The right coronary artery (RCA), and the left coronary artery (LCA) (Texas heart institute 2016).**

The left main artery (LM) which is the first branch of LCA, divides into the left anterior descending (LAD) and the left circumflex artery (LCX) (Smuclovisky 2011). The LAD commonly supplies blood to the anterior left ventricular and 2/3 of the interventricular septum. The LCX runs to the left, between the left ventricle and the left atrium to supply blood to most of the left atrium and lateral part of the left ventricle (Lakatta 2011). 40% to 50% of myocardial infarction are due to an occlusion in the LAD, while it is between 15% and 20% for the LCX (Katz & Ness 2015).

The RCA runs on the posterior side of the heart, parallels to the LAD and supplies blood to the bottom and backside of the heart including the entire right atria and a part of the left atria, the right ventricle and some parts of the left ventricle, the interatrial septum, and one-third of the interventricular septum (Deckelbaum 1992, Lakatta 2011). The chance of heart attack in the RCA due to an occlusion has been reported to be between 30% and 40% (Katz & Ness 2015). In addition, the inner diameter of the LM, LAD, LCX, and RCA has been reported as  $4.4\pm 0.4$ ,  $3.6\pm 0.4$ ,  $3.4\pm 0.5$ , and  $3\pm 0.5$  mm, respectively (Jr et al. 1992).

The main coronary arteries (MA) are divided into many branches (through artery bifurcation) in order to supply oxygen and nutrition to all the muscles of the heart (see Figure 2.4). The bifurcation of an artery (BA) generates an angle between the MA and the side branches (SB) which has angulation varying from  $15^\circ$  to  $120^\circ$  (Chaichana et al. 2011). Additionally, the MA may also have some degree of angulation (curve geometry) which can vary between  $30^\circ$  and  $150^\circ$  (Liu et al. 2015), hence the deployment of stents in these regions may be inherently challenging.

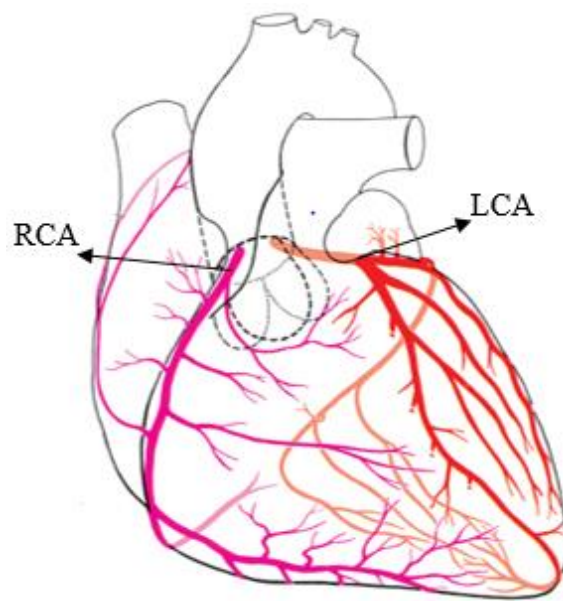


**Figure 2.4: Coronary arteries. The two main arteries, right coronary artery and left coronary artery has been divided into many SB (Gray's Anatomy 2005).**

Furthermore, the systole and diastole cycle (heartbeats) causes the arteries to undergo a significant amount of repetitive hinge-type movement. The degree of movement varies depending on the intensity of blood flow and location of the vessels. For example by obtaining angiographic images (x-ray image), the angle of this hinge-type motion has been measured as  $22.8\pm 4.9^\circ$  in the left anterior descending (LAD) while in the right coronary artery (RCA) it increases to  $31.0\pm 13.1^\circ$ , which might be due to its location and geometry (Ino et al. 2009).

## **2.4. Coronary Heart Disease**

At the present time, the major cause of death as a result of cardiovascular disease is genetic predisposition and unhealthy lifestyle which can affect mostly the elderly but also in some cases young people (Katona et al. 2013). Accumulations of plaque inside the arteries is known as atherosclerosis which may affect any artery in the body. Atherosclerosis in the heart arteries causes local blockages or narrowing and hardening of the coronary arteries over time, and it is one of the most common coronary heart disease (CHD). It causes the blood flow to be restricted and the symptoms of reduction in blood flow might result in some pain or discomfort which it is known as angina. Angina is a primary sign of CHD, and the patient feels pain in the chest, neck, jaw, shoulder, or in the left arm as well as shortness of breath and a feeling of pressure or heaviness on the chest. However, angina may not happen for many patients and myocardial ischemia occurs for majority of the patients without any symptoms as a result of silent ischemia (Katz & Ness 2015, Deckelbaum 1992).

Atherosclerosis in coronary arteries (see Figure 2.5) is mainly due to accumulated bad cholesterol (low density lipoproteins), calcium, and other substances (fatty deposits) inside the coronary artery (Combined 2007). Plaque or atheroma is made of lipids, smooth muscle cells, and white cells that might appear at an age as early as 40 (Tran 2004, Lam

2012). However, atheroma build-up is incrementally developed and it may take up to 20 years or more to completely block the arteries. Generally, the symptoms of atherosclerosis occur when 50% to 70% of the coronary artery is obstructed (Deckelbaum 1992). If a blood clot forms and blocks the blood flow to the heart, heart attack, or even death can occur.

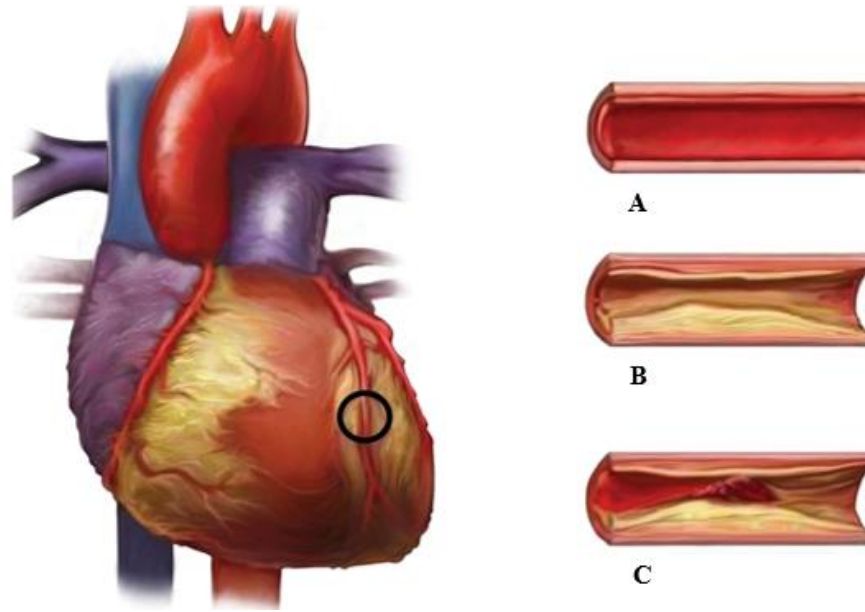


**Figure 2.5: The heart with coronary artery circled. Coronary artery disease (Atherosclerosis) demonstrated in B and C. A) Healthy artery, B) Narrowed artery due to build-up of plaque, C) Narrowed artery due to build-up plaque of with superimposed blood clot (thrombus) (MelbourneHeartcare 2015).**

It has been determined that plaque accumulation would mostly take place at the curvature of arteries or in the both MA and SB of bifurcation arteries (BA), where the wall shear stress is low (Asakura & Karino 1990). Also BA has several type of lesions, thus it has been classified in terms of location of the lesions, in order to identify proper treatment techniques. There are a number of classifications, but the most recent one has been described by Medina et al. (2006) the provides the information in a simple way (see Figure 2.6).

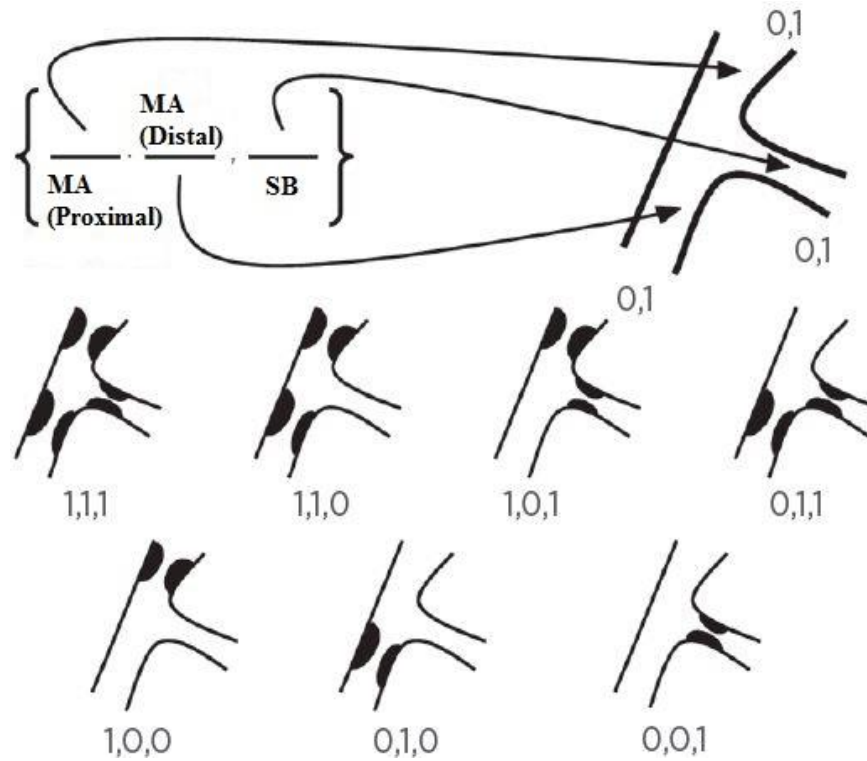


**Figure 2.6: The Medina coronary bifurcation lesions classification. It uses binary number (0,1) to indicate presence of a lesion in MA (the proximal segment), MA the distal segment and SB, respectively, in a bifurcation artery (Medina et al. 2006).**

There are numerous risk factors for the disease, some of which are non-preventable, although there are also some which are preventable (i.e. lifestyle related). Increasing age, gender (males have greater risk), and heredity including race are the factors that can't be controlled or changed. On the other hand, there are some other major factors which can be treated or controlled such as smoking, high level of cholesterol in blood, high blood pressure, physical inactivity, diabetes, and obesity (overweight) as well as high stress in life which can all damage the arteries. (Tran 2004, American Heart Association 2015, Katz & Ness 2015).

## 2.5. Treatment Techniques

Even though CHD cannot be cured completely, suitable treatment can help to reduce the symptoms and the possibility of further issues. Sometimes changing life style or pharmaceutical intervention can help to control the disease, as well as slow or stop the plaque build-up inside the arteries, hence improving heart function (National Heart Lung

and Blood Institute 2009). The risk of CHD can be reduced significantly by simple changes in lifestyle such as stopping smoking, having a healthy diet, and doing regular exercise. Moreover, there are wide range of drugs available to control and reduce blood pressure or blood cholesterol as well as to widen vessels and to thin the blood (for example aspirin, nitrates, anti-coagulents, ACE inhibitors, and statins). These types of medication usually form part of a long term treatment strategy to reduce the risk of heart problems.

However, in some CHD cases, the patient may need to have a clinical procedure or surgery, due to the severity of the atherosclerosis. Depending on how advanced the disease is, there are three different options (NHS 2014):

- I. Coronary angioplasty
- II. Coronary artery bypass graft (CABG)
- III. Heart transplant

### **2.5.1. Angioplasty**

In 1960s, in order to treat and reopen a blocked artery, the patient had to have open surgery and stay in a hospital around a week or more. More recently, percutaneous coronary intervention (PCI) was introduced and mostly used to treat patients who suffer from heart disease. PCI is a largely successful procedure which it has completely changed the method of treatment with shorter recovery time, much less invasive when compared to open surgery, and improves heart function in cases that may have failed to respond to medication.

Also known as balloon angioplasty, the first PCI was introduced by Andreas Gruentzig in 1977. He used a plain balloon catheter to re-open obstructed coronary vessels. In the beginning, patients who were associated with low risk features such as short, separate, concentric, non-calcified lesions in proximal coronary arterial section, as well as non-

angulated segment underwent PCI (Ryan et al. 1993). Afterwards, in 1988 atherectomy (a sharp blade was mounted on end of a catheter to cut and remove plaque from an artery) and laser cut was introduced, and then since 1993, using coronary stent increased gradually till the present (Dawkins et al. 2005).

In angioplasty a catheter (thin flexible tube) is inserted into the blocked artery through an incision in the thigh or arm in order to deliver a balloon to the narrowed section of the artery, and then by inflating the balloon the fatty deposits are compressed against the artery wall re-establishing increased blood flow. However, the compressed objects and plaques tend to regain the original shape after balloon angioplasty which is called recoil. Furthermore, the compressed plaques start to multiply shortly after the artery is re-opened and build-up fatty deposits and block the artery again over 3 to 6 months (Lam 2012). This occurrence is also known as restenosis.

Currently, PCI is widely used as an alternative treatment to surgical or medical intervention, and this is as a result of improvements in equipment and skill which makes it safe to apply PCI to more complicated clinical scenarios (Hannan et al. 2000). However, in many cases balloon angioplasty did not produce satisfactory results, with a low initial success rate and a high occurrence of late restenosis. Therefore, other techniques and devices have been developed to overcome the PCI problems. One of the devices is endovascular scaffolding such as stents and the other one is the debulking technique (rotative or directional atherectomy) (Rogers et al. 1999).

There are a number of challenges to the angioplasty technique, including calcification of lesions, restenosis, malapposition of stents and stent fracture. First, the blockage area does not have even degrees of stiffness, because the blood clot has a soft and smooth surface while the plaque has different degrees of calcification (rough and stiff surface), and so the combination of them could create uneven hardness levels (see Figure 2.7A). Thus,

when the balloon inflates in such an area, it would not be able to expand equally at all parts. This phenomenon creates irregular shape with crack on the surface of the plaque (see Figure 2.7B), which increases the risk of restenosis or possibly resulting in complete blockage (Heartsite 2013).

Introducing a stent into the procedure can facilitate wider opening of the blocked arteries, increasing the length of the widened section and result in a more uniform, and smooth lumen post-procedure, as well as reducing the chance of restenosis almost by 10 times (see Figure 2.7C) (Heartsite 2013). Nevertheless, approximately 6% of cases need further treatment due to stent failure and adverse outcome following PCI (Hannan et al. 2000). For instance, it has been reported that there is up to 25% possibility of in-stent restenosis (ISR) (arteries become narrow or block again after stenting) occurring within one year after stent placement, due to scar tissue and sometimes blood clotting in the arteries as a result (Dangas et al. 2010, Farooq et al. 2011).



**Figure 2.7: Angioplasty result, A) Blockage prior to angioplasty, B) After balloon angioplasty, C) After stent is placed (Heartsite 2013).**

## **2.5.2. Coronary Stent Placement**

When a cardiologist suspects that a person has narrowing or blockage in his/her artery, angiography techniques will be used to find out the position of any narrowing or blockage in the arteries. Angiography is an x-ray imaging procedure which provides a clear image of all arteries. Also sometimes intravascular ultrasound (IVUS) might be used to distinguish the exact size and location of obstruction. Based on this diagnosis of the lesion,

the cardiologist selects the optimum type of guide wire (extremely thin wire with flexible tip), catheter, balloon and stent for the procedure (Phatak 2013).

During the PCI procedure, the patient is given an oral calcium antagonist to prevent high blood pressure and to slow the heartbeat. Also a temporary pacemaker might be installed to adjust the heartbeat. Furthermore, to avoid angina and arrhythmia some drugs such as verapamil or nitro-glycerine may be added to the saline solution. The patient is given local anaesthetic, hence the patient is conscious during the procedure. At top of the patient's groin or in the arm, a small incision is made and then a catheter along with a guide wire which it has a deflated balloon at its tip, is inserted into the femoral artery and guided along the tortuous route through all vessels to the occluded artery. This is monitored radiographically throughout the procedure, with iodinated solution (colourless dye) injected to make the vessel visible under angiogram, because normally the coronary arteries are not clear and visible on x-ray (Heartsite 2013). Once the catheter and tips reach the coronary artery and blockage area, the deflated balloon at the catheter tip, is usually inflated gently to nominal atmosphere pressure (atm) (various between 8atm to 12atm for different type of stents), although pressures of up to 20atm could be used, depending on the stent and artery diameter. This procedure compresses the plaque and fatty deposits against the inner artery wall, opening the blood vessel and restoring the blood flow. As the balloon is inflated, the stent is expanded to the size of wall artery and held at this diameter for 20 to 30 seconds. After this, the balloon is deflated and removed from the artery while the stent remains *in situ* at the location of the narrowing or occluded artery keeping open the lumen of the vessel open to enable blood flow (see Figure 2.8) (Heartsite 2013).

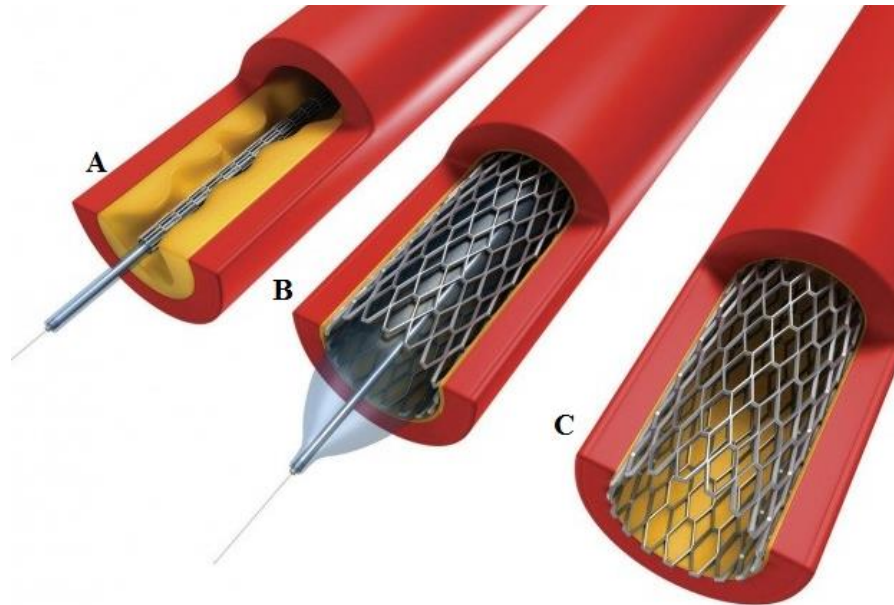


**Figure 2.8: Stenting procedure. A) The catheter is inserted to the site of coronary obstruction, B) The balloon is inflated, thus the stent is expanded and compresses the plaque against the artery wall, C) The balloon is deflated and removed from the artery while the stent remains in place (Park 2013).**

The duration of PCI surgery often takes between 40 minutes to one hour. However, this procedure could take much longer if the location of the lesion is difficult to access, hence the procedure would be more complicated and required more steps (Heartsite 2013).

Stenting in bifurcation arteries (BA) is more complicated and according to the type of lesion, different techniques such as skirt technique, provisional stenting, culotte stenting, the crush technique, and kissing balloon stenting may be used. Nevertheless, these techniques and complications are outside the scope of this project, and this study is aiming to analyse the mechanism of stent fracture (SF) in an angulated coronary artery.

### **2.5.3. Stents**

Cardiovascular stents are vascular support structures (tiny mesh tubes) which were originally made of 316L stainless steel. They are permanent implants and designed to keep coronary vessels open and prevent restenosis in the arteries after an angioplasty procedure. Moreover, stenting may be used in weak arteries to improve blood flow and prevent any arterial rupture (National Heart Lung and Blood Institute 2013). More

recently, stents have been developed made from more flexible and stable materials such as nickel chromium (Ni-Cr)- titanium alloy, cobalt chromium (Co-Cr) alloy, and platinum chromium (Pt-Cr) alloys (Menown et al. 2010). An example of 316L stainless steel Cypher™ stent (Cordis Corporation, California, USA) is shown in Figure 2.9, although many difference stent designs are available in order to treat different type of lesions and arteries (i.e. bifurcation arteries) , and can be categorised by design, method of expansion, material, and coating.

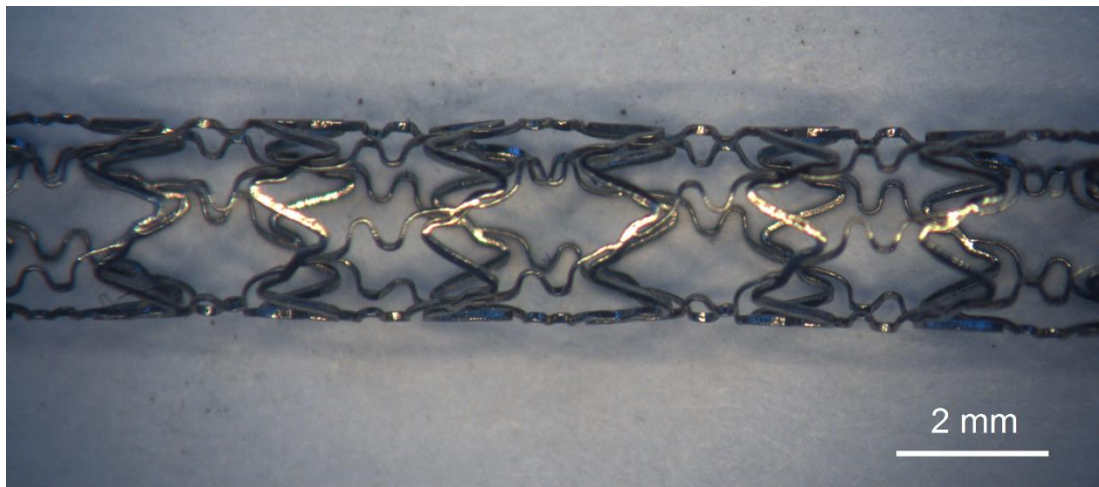


**Figure 2.9: Expanded Cypher stent (Cordis Corporation, California, USA)**

There are two types of stent expansion mechanisms: self-expansion and balloon-expansion. The self-expansion stents have a spring like structure, are delivered by a catheter and then removal of the catheter results in stent expansion to the diameter of artery. These stents are made of Ni-Cr and titanium alloy which have super-elastic properties and often are used in carotid and femoral arteries (Ther et al. 2002). The balloon expandable stents are mounted on an angioplasty balloon, and as the balloon inflates, the stent expands and implants in a narrowing area permanently. However, there are bio-absorbable stents in order to avoid restenosis and recoil for a few months after deployment, and then will be absorbed by the body. The idea of these kind of stents is to prevent any risks which are associated with metal and implanted device such as stent thrombosis (formation of blood clots) and stent fracture (Gonzalo & Macaya 2012).

However, there are some shortcomings with them such as fast and slow degradation rates. There have been several corrosion test and simulation studies to evaluate the procedure of degradation in *in vivo* (Zhen et al. 2013, Galvin et al. 2017) .

In terms of stent structures, there are open cell and closed cell designs (see Figure 2.10). Although the closed cell designs have more uniform structure and provide higher radial strength, the cells are connected sequentially peak-to-peak creating a more rigid body when compared to the open cell, where rings are linked by struts periodically providing more flexibility, conformability, better side branch access (Sangiorgi et al. 2007).

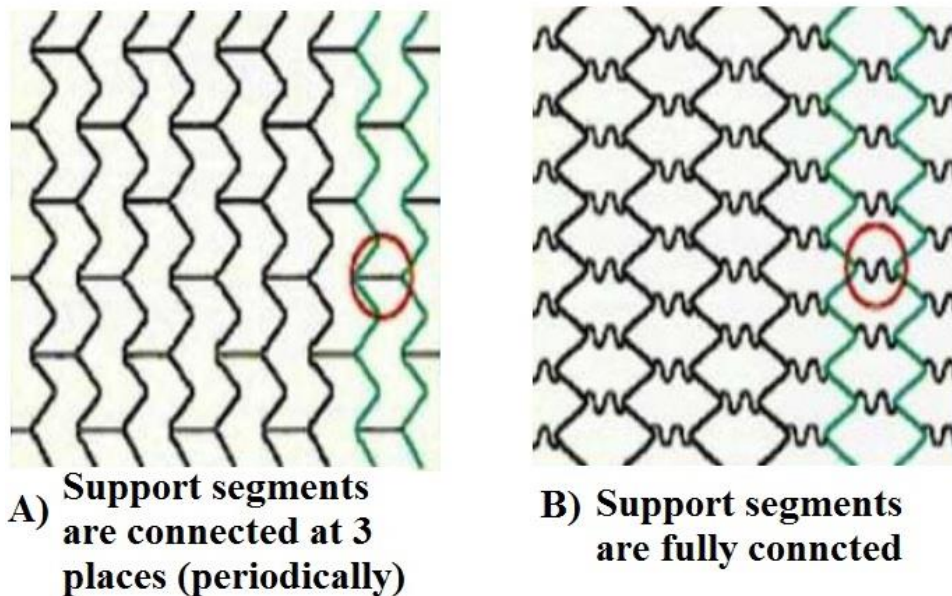


**Figure 2.10: The two main stent structure, A) Opened cell, and B) Closed cell.**

Additionally, stents can be grouped according to their coating. The first generation of stents were introduced with no coating and known as bare metal stents (BMS). Nevertheless, some complications such as thrombosis and target vessel revascularization (TVR) lead to develop the drug eluting stents (DES) to minimize the risk of blood clots and tissue growth after the PCI procedure (Burt & Hunter 2006).

## **2.5.4. Drug Eluting Stent (DES)**

In the early days of the balloon angioplasty era, the rate of restenosis was reported to be between 35% and 40% due to significant growth of neointimal tissue, whereas using BMS reduced the restenosis rate approximately to 25%. Later, the advent of drug eluting stents (DES) decreased the risk of restenosis further by 8.6% and they become the principal device for PCI, now used in almost 90% of cases (Nair & Quadros 2011, Simard et al. 2014).

DES are coated with a polymer which release anti-proliferative drugs slowly and continuously over the time once positioned in the artery, to reduce the risk of ISR. Anti-proliferative is the range of drugs such as sirolimus and paclitaxel used to prevent ISR after stent implantation by stopping or retarding the spread of cells, especially malignant cells in arteries (Oliva et al. 2004). The initial clinical results for the sirolimus-eluting stent (SES) and paclitaxel-eluting stent(PES) showed that blood vessels can still become obstructed again, but the rate of ISR is markedly reduced in DES when compared to the bare-metal incidence (Lee 2008). Although the DES have decreased the rate of ISR significantly in comparison with PCI and BMS, but the risk of sudden occlusion, known as stent thrombosis (ST) suggested to be increased in DES due to delay endothelial tissue formation (Egred et al. 2008).

The initial clinical trials results of SES proved that it is able to curb neointimal accumulation and its formation. The first test in a patient was performed in 2001 with promising outcomes, where no potential stenosis or thrombosis was observed after one year (Sousa et al. 2001). Furthermore, according to 2 systematic studies (Kastrati et al. 2005, Schömig et al. 2007) and reviews, the overall results illustrated that SESs have superiority over PESs due to their late ISR and target vessel revascularization (TVR) while the PESs increased rate of myocardial infarction (MI).

Numerous improvements were implemented to create the second generation of DES. Parclitaxel is one of the coronary stents which is developed from the early design of PES. The Taxus Element improved it by designing an exclusive polymer which ensures the release of the drug within 12 weeks. Another development was using platinum chromium, enabling a decrease in strut thickness and an improvement in radio-opacity over its precursors (Cannon et al. 2011). A randomised study showed that the result from both designs is comparable over 12 months. However, in comparison with BMS, late lumen loss (difference in stented diameter after implantation and later follow up) is improved but still not much difference in ST to previous PES and BMS (Min et al. 2006).

Second generation DESs everolimus-eluting stent (EES) and the zotarolimus-eluting stent (ZES) have better flexibility and thinner strut size than the BMS and the first DESs generation. The ZES is also a strong cobalt chromium scaffold with unique phosphorylcholine polymer coating increasing biocompatibility and decreasing inflammation (Mukherjee & Moliterno 2009).

The second generation stents were identified to be more safe and efficient in comparison with the first DESs generation and BMSs. Also in an observational study the results were illustrated that the new second generation of DESs are associated with lower chance of ST and ISR (Simard et al. 2014). Although, drug eluting stents provided major advancement, there are still some problems that have not been solved and are still reported in the drug eluting stent era, and likewise, these complications might cause a rise in the risk of ISR and probably ST (Aoki et al. 2007).

Some mechanisms of failure which are still evident are stent fracture (SF), longitudinal deformation, and recoil, which can lead to adverse clinical outcomes (Wiktor et al. 2016). Stent fracture, albeit an uncommon phenomenon, has been reported as one of the causes of stent thrombosis (ST), restenosis (SR), and target lesion revascularisation (TLR)

(Sianos et al. 2004, Chinikar & Sadeghipour 2014). In chapter 3.1, clinical impact and incidence of SF is reviewed and assessed in further details.

## **2.6. Summary**

This chapter has introduced some background knowledge of heart, its function, and the most common heart disease (atherosclerosis), which are necessary to understand the contents of this thesis. It has been shown that many factors cause an occlusion in the coronary arteries, some of which can be prevented or retarded by changes in life-style. Also a brief review of PCI and stenting treatment was covered, as well as their development through the time. However, other techniques to treat the disease have not been presented in this chapter to restrict coverage to that necessary for the present work.

### **3. Literature Review**

Medical engineering is a science that provides superior understanding of biological and medical problems by using various scientific theories. Over recent years, studying heart stent fracture, knowledge from mechanical engineering and also biological fields were integrated, and a number of clinical, *in-vitro* experiment, computer and finite element models have been developed. This literature review is categorised into coronary stent fracture, incidence, predictor factors, and clinical implication of stent fracture. A review of FE modelling as well as the knowledge and research performed as *in-vitro* experiment. All the presented information is considered relevant to this study.

#### **3.1. Incidence, Predictors & Clinical Relevance of Stent fracture (SF)**

Every year nearly 2.5 million DESs are used in order to treat coronary artery disease around the world. Although coronary stents are a successful treatment technique and have benefits, there are still some complications associated with them such as stent fracture (SF), stent thrombosis (ST), in-stent restenosis (ISR), and late target lesion revascularization (TLR). SF in coronary arteries is one of the most interesting issues. It is difficult to detect, and normally reported with clinical complications such as ISR, thrombosis, TLR, and myocardial infarction thereby intensifying major adverse cardiac events (MACE) and the risk of morbidity and mortality. Available literature has proposed that for DES, drug delivery at SF site will be disordered and hence increase the risk of ISR. Moreover, thrombosis is reported due to direct contact of metal at fracture strut with the luminal surface. Conversely, a theory by Park et al. (2011) indicated there is no significant difference in terms of clinical implication between SF group and non-SF group. Nevertheless, Aoki et al. (2007) and Shaikh et al. (2008) determined and suggested that SF can increase and encourage the rate of ISR. The time to fracture is variable and can be

just 2 days or 2 years after implantation (Min et al. 2006), however on a routine follow-up angiography the mean time of detecting SF was reported to be  $15.6 \pm 11.6$  months after DES implantation (Lee et al. 2009).

Aoki et al. (2007) along with several reports (Sianos et al. 2004, Halkin et al. 2004, Hamilos et al. 2005, Lee et al. 2007) believe that the risk of stent strut fracture may increase under particular conditions such as increasing stent length, overlapping of stents, tortuosity of vessels and vessel movement during the cardiac cycle (mainly in saphenous vein (SV) graft and RCA). Furthermore, over expansion or maximum inflation have been suggested as possible factor of SF by Aoki et al. (2007) and Shaikh et al. (2008), however, neither of them presented statistically. It should be noted that the cardiac cycle and heart contraction involves 5 types of movement; translocation, rotation, twisting, accordion-like motion, and movement towards the centre of the ventricular chamber (Reichek 1999). All of these loads apply external mechanical loads which leads to axial stress on the stent. These repetitive forces can cause metal fatigue and eventually stent fracture (Adlakha et al. 2010). The RCA has a higher risk of SF due to its anatomy and excessive tortuosity, which creates a twisting and also hinge-type motion during the cardiac cycle, and as a result increases metal fatigue. In a meta-analysis study by Chakravarty et al. (2010), it was reported that 56.4% of SF occurred in the RCA, then LAD, LCX, SVG and LM with 30.4%, 10.9%, 1.7%, and less than 0.01% respectively.

Other various factors are remarked as predisposing for SF, such as vessel geometry, stent design, a hinge motion, angulations, calcification and bifurcation angle, all of which can affect the likelihood of SF. In general, SF and its mechanism is a complex process, combining several factors that include anatomy, physiology and stent design, material and method of fabrication.

The design of the actual stent will also have an effect. Stent design configuration can be divided into two main categories, open cell versus closed cell (see Figure 3.1). SF has been detected in all types of BMSs and DESs, including Taxus™ Boston Scientific, Nobori® Terumo, and Endeavor® Medtronic ranging from 0.84% (Chung et al. 2008) to 8.4% (Umeda et al. 2009) but it has been seen to occur more often in closed cell design stents (e.g. Cypher™ Cordis Corporation), in comparison with other type of DES and BMS. The Cypher structure is a closed-cell design, where the cells are connected to each other by thin struts. In this type of stent, the scaffold is more rigid and it has greater stiffness than open cell designs, and as a result these stents are more prone to fracture especially at bifurcations or in highly angulated vessels. However, closed cell DES designs can distribute the drug more evenly than open cell, and they are also more visible radiographically and for IVUS, enabling improved detection of SF (Canan & Lee 2010, Alexopoulos 2011). Conversely, the open- cell stent type has more longitudinal flexibility due to the periodic nature of the linkage (Alexopoulos 2011, Adlakha et al. 2010). Lee et al. (2007) evaluated the clinical impact of SF in DES where two type of stents SES and PES were deployed in 530 patients, and it was determined that all fractures (in 10 patients) occurred in SES (Cypher). Similarly, the results of another study by Shaikh et al. (2008), correlated with occurrence of SF in SES and PES, where the incidence of SF in SES was reported significantly higher than PES, 29 (82.8%) versus 6 (17.2%) cases respectively.

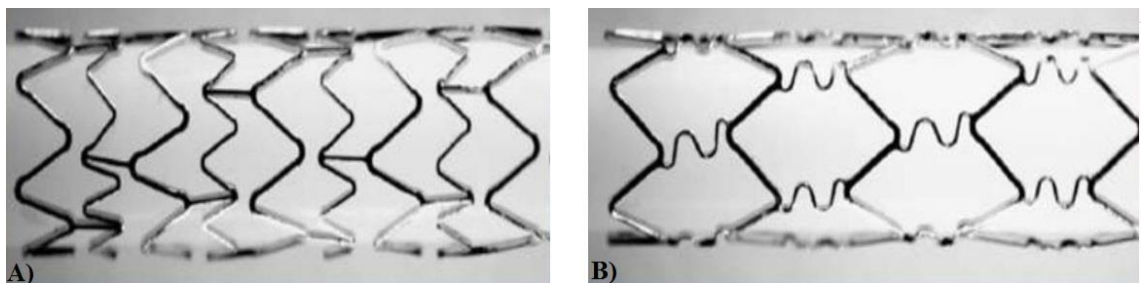


**Figure 3.1: Representation of (A) opened cell stent (Multi-Link 8, Abbott Vascular) and (B) closed cell stent (Cypher, Cordis Corporation).**

All stents are designed for approximately 10 years life time or  $4 \times 10^8$  cardiac cycles (systolic/ diastolic) where the heart rate is assumed to be 70 BPM (Marrey et al. 2006, Barrera et al. 2014). As a result of the repetitive loading on the stent induced by the heart movement, micro-cracks may initiate due to the continual heart pulsation, these cracks do not need to propagate very far to result in a fracture of the struts (Marrey et al. 2006). Furthermore, the stress within the stent will further increase when the continuous pulsatile loading is combined with factors such as excessive movement and curvature of the vessel, especially in RCA where the anatomy can be challenging for stent placement and durability (Nakazawa et al. 2009, Canan & Lee 2010, Adlakha et al. 2010) .

SF in the coronary arteries is classified according to the degree of disconnection of the struts, which could range from fracture within a single strut to total separation of sections of the stent and displacement. Table 3.1 outlines the classification based on the grade of coronary SF as detected by cine-angiography and IVUS. It is likely that the fracture starts with a single strut (type I) and then continues to the worsening classifications, or possibly in some cases simultaneous multi-strut fracture could occur, causing separation which then progresses into stent displacement (type V) (Nakazawa et al. 2009), although no study has been conducted until now to quantify this fracture mechanism.

<b>Classification</b>	<b>Morphology</b>
<b>I</b>	Single strut fracture
<b>II</b>	$2 \leq$ strut fractures
<b>III</b>	$2 \leq$ strut fractures with deformation
<b>IV</b>	Numerous struts fracture with transection but no gap
<b>V</b>	Numerous struts fracture with transection with gap

**Table 3.1: Classification of stent fracture (Nakazawa et al. 2009).**

Most stents are made out of 316L stainless steel which has good mechanical properties as well as providing corrosion resistance. Later, stents used other metals such as tantalum, titanium and nickel which give the benefits of biocompatibility, corrosion resistance and as well as improving the elasticity properties (Bertrand et al. 1998). Some clinical reports have indicated a relationship between increased strut thickness and restenosis rates (Kastrati et al. 2001, Pache et al. 2003), hence cobalt alloys have been used to design new stents with thinner struts without compromising the radial strength. The higher density of this alloy enables a stent design with thinner struts, but improved radiopacity (Medtronic 2002). However, Nakazawa et al. (2009) suggested that changing the material may not have an effect on mechanism of stent failure, although it is known that cobalt chromium and platinum have less susceptibility to corrosion than stainless steel. Incidence of SF in DES has been reported to be more frequent in comparison with BMS (Chung et al. 2008), where there is a speculation that the method and preparation the surface of stent for polymer coating, and drug elution may have a detrimental effect on their durability with respect to corrosion (Nakazawa et al. 2009, Adlakha et al. 2010). Correspondingly, a larger number of stent thromboses (ST) and acute myocardial infarctions (AMI) have been reported with DES when compared with BMS. In BMS, the neointimal layer grows around the stent which limits the contact of the stent with the artery wall, thus in case of any fracture, thrombus formation will be minimised. However, with DES there is no neointimal layer encompassing the stent and, therefore in the event of fracture, the stent is in direct contact with the arterial lumen, leading to thrombosis and then AMI (Lousinha et al. 2011).

Lee et al. (2007) conducted a systematic analysis of angiography of 530 patients who underwent a PCI with a DES, sirolimus eluting stent (SES) (Cypher™, Cordis Corp) and paclitaxel eluting stent (PES) (Taxus®, Boston Scientific Corp) with a follow up repeat angiography at 32 months. The first fracture was detected after 7 days implantation while

the latest one occurred at day 620 (mean time= 226 days). They observed 10 SFs (1.9%) where all of them occurred in SES Cypher stent, which might be due to their closed cell design compared with the PES Taxus stent open cell design. The stent lengths ranged from 13- 33 mm (mean=  $19.7 \pm 7.7$  mm) and inflation pressures between 8 and 20 atm to have diameter range 2- 3.5 mm (mean=  $2.9 \pm 0.5$  mm) (Lee et al. 2007).

Several factors were considered during the study and it was found that age and gender did not have an effect on SF. In addition, the incidence was reported in epicardial artery (3 cases), left main artery and SV graft (3 cases) as well as in arteries with excessive tortuosity (bends  $\geq 75^\circ$ ) (4 cases). 6 SFs were located in the middle portion of the stent with 4 other cases occurring in the proximal part of the stent where complete transverse disarticulation was observed. Likewise, 60% of SF cases had a moderate degree of calcification versus 40% with severe calcification, and 5 cases of fracture occurred at or near an overlapping stent sites since axial stiffness at this portion increases and acts as a fulcrum due to vessel movement. With longer stents, a larger area is covered and therefore the radial forces which affect the deformation of the stent will be greater, especially when positioned in a tortuous area or where calcified lesions are present (Sianos et al. 2004). Furthermore, 4 cases of SF had post-dilation with an oversized balloon reinforcing the results of another study by Sianos et al. (2004) which suggested that this post-dilation could predispose to fracture.

Although SF occurred in 1.9% of the cases there was still up to 70% incidence of an adverse event. Increased restenosis rate, distribution of drug elution, and distortion of the stent structure and polymer coating are other clinical consequences of SF.

In an observational study by Aoki et al. (2007), they investigated incidence of stent fracture in SES. 256 of 280 patients with 307 lesions underwent angiography follow-up at 8 months (mean=  $240 \pm 43$  days) which is almost the same as Lee et al. (2007) reports.

SF was defined as complete separation, and it was observed in 8 stents (2.6%) which were diagnosed by IVUS. All fractures occurred at the hinge point of the stent (end of systole and end of diastole), where 5 of them were located in RCA, 2 in the SV graft, and one in LAD. Also one of them was positioned at the overlapping site. Moreover, SF had an impact on the clinical adverse events, where the rate of restenosis and target lesion revascularization (TLR) was reported at 37.5% and 50% respectively in lesions with SF, and 12.4% and 11% in lesions without SF (Aoki et al. 2007); this was suggested to be due to decreased drug delivery at the fracture points (Morice 2002).

Shaikh et al. (2008) examined 188 of 3,920 lesions with ISR. 35 (18.6%) SFs were diagnosed, where only cases with total separation were considered. Once again it was observed that SF occurred more in SES type with 29 incidences out of the total 121 compared with 6 fractures in 67 PESs. Furthermore, a univariate analysis confirmed that SF arose in RCA more significantly (57.1%, odds ratio (OR) = 2.5) than LAD (34.2%), LCX (5.7%), SV graft (2.8%). Also they determined that stenting in a vessel with angulation  $\geq 75^\circ$  (OR= 13.8), and overlapping stent (OR= 3.9) had a higher risk of fracture, whereas the length of the stent was not identified as an independent predictor for SF. Clearly, odds ratio (OR) figures show that the odds of fracture is higher when stents given these particular exposure, compared to the odds of the outcome occurring in the absence of that exposure. Shaikh et al. (2008) in agreement with Sianos et al. (2004) and Lee et al. (2007) suggested that SF at overlapping site is as a result of developing a hinge point that deforms the metal structure which leads to strut fracture (Leong et al. 2008).

With regard to frequency, predictors, and clinical impact of SF after SES (Cypher<sup>TM</sup>), Umeda et al. (2009) conducted a study in which 382 patients with 430 lesions underwent angiography follow-up after 6 to 9 months (mean=  $6.9 \pm 2.5$  months) of initial procedure. 46 fractures (10.7%) were observed in 33 lesions, where 23 of those (50%) out of total 46 fractures were detected as partial fracture (single strut (69.7%) or multiple struts

(30.3%) fracture) and similarly 50% of occurrence was identified as complete SF. Analogous to previous reports, the incidence of SF in RCA (odd ratio= 3.26) and tortuous vessels (bend angle=  $58.7 \pm 24^\circ$ ) was significantly higher with 58% and 73%, respectively. Additionally, Umeda et al. (2009) suggested that a change in angulation of the artery after stent implantation plays an important role in SF (OR= 1.55), as it was observed that change in angle after stent implantation was more prevalent in the SF group ( $29.6 \pm 18.4^\circ$  vs  $13.2 \pm 12.5^\circ$ ) in comparison with the non-SF group ( $30.8 \pm 14.5^\circ$  vs  $20.8 \pm 13.5^\circ$ ). The vessel would be straightened after stenting, but over the time it would attempt to regain its original shape, thus an external force would be applied to the stent, with greater forces resulting from increasing angular change, hence an associated increase in risk of SF.

In contrast with Shaikh et al. (2008), Umeda et al. (2009) believed that stent length is a predictor factor of SF due to the generation of greater radial force in longer stents (Sianos et al. 2004). In their study, the incidence of SF in longer stents ( $34.8 \pm 11.1$  mm) was observed more than in shorter stents ( $23.6 \pm 9.8$  mm) with an odds ratio (OR) of 2.22.

Umeda et al. (2009) found out that ISR occurred in both SF group and non-SF group, but it was more frequent in SF lesions with 15.2% and all of them observed at SF site which is much lower than Aoki et al. (2007) reports (37.5%). Umeda et al. (2009) is also in agreement with previous studies which indicated occurrence of ISR at fracture site as a result of discontinuities in local drug elution, loss of mechanical structure of the stent, and an increase in the mechanical stimulation on the artery wall by the interaction with broken struts (Halkin et al. 2004, Hamilos et al. 2005, Lee et al. 2007).

A clinical report by Ino et al. (2009) investigated predictors and prognosis of SF in SES among 273 patients with 364 lesions. Patients were followed up coronary angiography 6-9 months and divided into 2 groups: without or with SF, where SF was defined as partial

fracture or complete separation. Of 364 lesions, 14 complete SF and 4 partial type were documented (18 SF, 4.9% in total).

Since vessel tortuosity and hinge motion have been suggested as predictors of SF, Ino et al. (2009) measured the maximal angle of target lesion before PCI in order to characterize vessel angulation, as well as the difference angulation between end of diastole and end of systole to quantify the hinge motion during the cardiac cycle (see Figure 3.2). As was expected, the fracture group had greater target lesion angle (vessel angle) and hinge motion with  $49.8^\circ$  vs  $36.0^\circ$  and  $28.3^\circ$  vs  $12.3^\circ$ , respectively. Likewise, stent length ( $39.7 \pm 18.8$  vs  $24.2 \pm 9.6$  mm) and stent overlapping (67% vs 17%) were identified as independent predictors of SF.

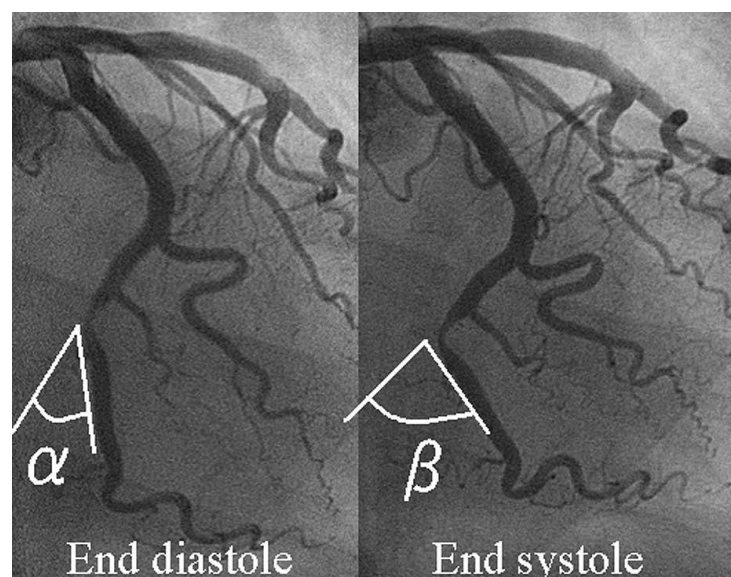


**Figure 3.2: Quantifying the hinge motion of the coronary arteries. The difference between angle  $\alpha$  ( $^\circ$ ) end of diastole (left) and angle  $\beta$  ( $^\circ$ ) end of systole is the degree of hinge motion. Also the maximal angle in target lesion is represented as  $\beta$  ( $^\circ$ ) (Ino et al. 2009).**

Although major adverse cardiac event (MACE), such as death of cardiac organ and late ST, was not considerably different in both groups (0% SF group vs 1.4% without SF group), other clinical complications including ISR and TLR, were more common in the fracture group (33% vs 4% and 28% vs 3.5%, respectively), where all the ISR occurred at the fracture site (Ino et al. 2009), similar to previous studies.

In a pathological analysis by Nakazawa et al. (2009), 144 autopsy cases with 200 DES lesions were examined. High contrast film-based radiography (X-ray) was used and SF was detected in 51 lesions (29%), where the fractures were classified into 5 grades, namely, single strut fracture (I) (n=10), two or more fractures without deformation (II) (n= 14), two or more fractures with deformation (III) (n= 12), multiple fractures with acquired transaction but without no gap (IV) (n= 6), and multiple fractures with acquired transaction but with gap (V) (n= 9) (see Figure 3.3A). Also the degree of calcification in the artery was classified as follows: none, mild, moderate, or severe (see Figure 3.3B), where the incidence of fracture in non-calcified arteries was 7, mild 21, moderate 20, and severe 3.

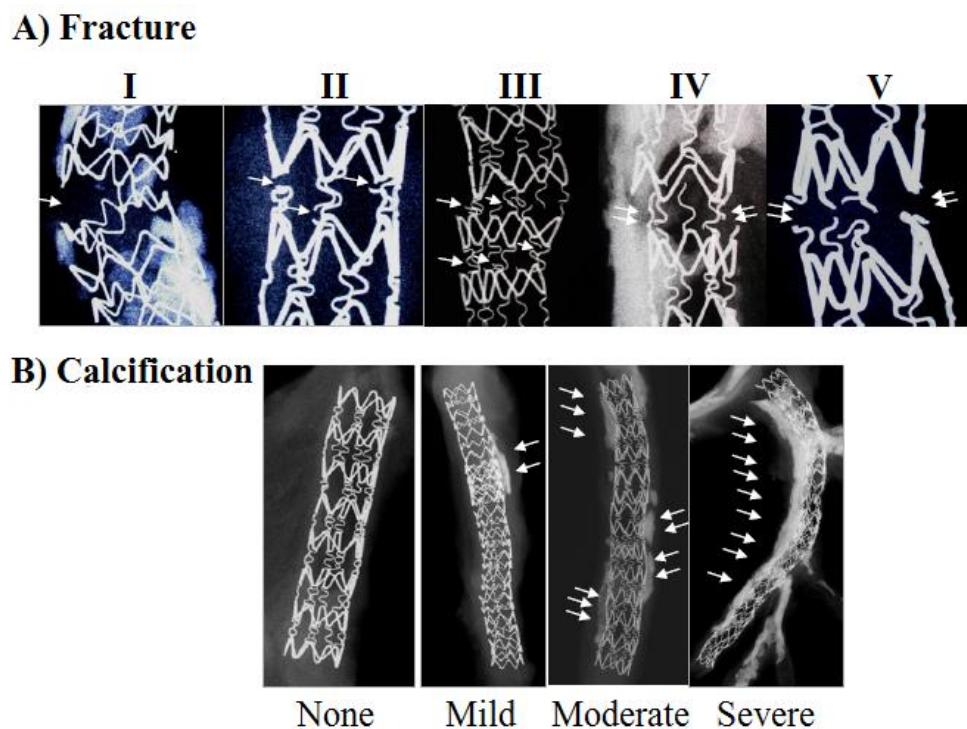


**Figure 3.3: (A) Fracture grade and the white arrows indicate fractured struts. (B) Calcification degree mild= barely seen or focally localized (Almost 25% of stent), moderate= multiple sites, and severe = highly visible diffuse calcification (more than 75% of stent length is associated with calcification). White arrows indicate calcified area (Nakazawa et al. 2009).**

The incident of SF was detected at a much higher level in the autopsy study (29%) when compared to clinical studies (0.8%-8%). It might be due to the detection approach and using X-ray enabling the detection of minor strut fracture, whereas angiography and

IVUS are less sensitive techniques. High contrast film based provides better resolution at  $\approx 80 \mu\text{m}$ , which it is greater than IVUS or angiography, with  $200 \mu\text{m}$  and  $300 \mu\text{m}$  respectively. Consequently, it can be said that SF in patients who have subclinical, low grade of fracture might remain concealed clinically as they would not be visible enough to detect by IVUS or angiography (Nakazawa et al. 2009).

It was observed that fracture occurred more commonly in the Cypher stents when compared to Taxus. The location of fracture in the Cypher stent and Taxus stent were different, where the fracture mostly occurred in N-shaped undulating longitudinal intersinusoidal-ring link segment of the Cypher but interestingly it was located in the straight longitudinal intercrown link in the Taxus stent which is opposite of the FEA (Marrey et al. 2006, Barrera et al. 2012) studies' finding with regard to fatigue and stress distribution within deployed stents (this is discussed in 3.2) (see Figure 3.4). Additionally, the middle segment of stents were observed to have more fractures which agrees with the Lee et al. (2007) report, but in stents longer than 25 mm, it mostly occurred at the proximal portion. In contrast, in overlapping stents, the fracture sites were mostly 5 mm away from the overlap zone. Results also indicated that gender and age were not a risk factor for SF as was deduced in the previous studies.

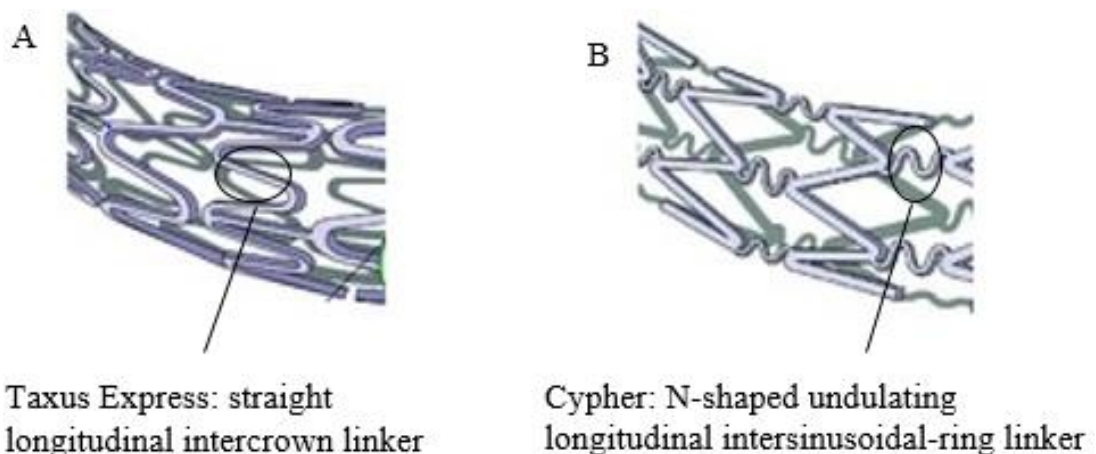


**Figure 3.4: Structure of stents as well as common location of fracture in A) Taxus stent at straight longitudinal segment, and B) Cypher stent at N-shaped linker segment.**

Remarkably, Nakazawa et al. (2009) postulated that calcification of the vessel could not have an impact on the stent and strut fracture as there was no statistical difference between fracture and non-fracture group which related to degree of calcification in their study. However, previous studies such as the report of meta-analysis of SF (Adlakha et al. 2010) stated the degree of calcification to be one of the risk factors of SF, where the artery wall applies extra radial force on stents. The analysis and results show that stents in the RCA are more prone to fracture and it is suggested that it is due to the vessel geometry and its twisting, bending, and stretching motion during cardiac cycle, where additional strain is applied to fundamental points leading to metal structural fatigue (Canan & Lee 2010). Furthermore, bypass grafts, overlapping stents (45% vs 22%), longer stents (30 mm vs 20 mm) OR: 1.07, Cypher stent (63% vs 37%) OR: 3.4, and longer duration of implantation (172 days vs 44 days) OR: 1.002, are independent risk factors of SF (Nakazawa et al. 2009).

In addition to pathological analysis, a histological study was conducted by Nakazawa et al. (2009), where all the cases were considered and it was found that there was no significant difference between the fracture and non-fracture groups with respect to adverse clinical outcomes such as thrombosis and restenosis, in agreement with a clinical report by Ino et al. (2009). However, if only grade V SF was considered, one restenosis and five thromboses were observed in the 9 cases (67%). This equates to 78% of grade V fractures related to MACE (including 5 sudden death), which is much higher than the rate in the non-fracture group with 37% adverse clinical outcomes (Nakazawa et al. 2009).

In another clinical study by Kuramitsu et al. (2012), 1035 patients with 1339 lesions underwent a new generation DES, cobalt chromium everolimus eluting stent (CoCr-EES) implantation, the design of which is based on cobalt chromium alloy and provides thinner strut thickness. Follow up angiography was performed 6 to 9 months after the stenting procedure, and multivariable aspects were considered, such as stent length, placement in

RCA, stent overlapping, chronic total occlusion, hinge motion, tortuosity, calcification, and ostial stent location in the statistical analysis as the risk factors for SF.

Of 1339 lesions, 39 SF were detected (2.9%) in EES. 66.7% of the fractures occurred at the middle part of stent which is in agreement with the previous study by Lee et al. (2007), 15.4% at the proximal portion, and the distal part had the lowest fracture rate with 2.6%. Although, fracture rate at an overlapping site is different where previous studies investigated most of fracture occurred at overlapping region while in this study was reported only 15.4%, but Kuramitsu et al. (2012) also believed that stent length play an important role in SF.

The multivariable logistic regression analysis determined independent prediction chance ratio of SF in 4 top conditions after EES implantation (see Table 3.2), where the hinge motion had highest potential risk of SF. It was defined that lesions with hinge motion, during diastolic\systolic cycle had almost 16-degree difference in angle. Moreover, it was recognized that the point of fracture in lesion with hinge motion was well accorded with the hinge motion point.

	<b>Odds ratio (OR)</b>
<b>Hinge motion</b>	14.57
<b>Ostial stent location</b>	12.38
<b>Tortuosity</b>	5.45
<b>Calcification</b>	4.27

**Table 3.2: Odds ratio of risk factor for stent fracture (Kuramitsu et al. 2012).**

Although the odds ratio (OR) of SF is quite low, it may still be life threatening due to the clinical consequences, as ST, MACE, and TLR were significantly higher in the SF group than non-SF group (5.1% vs 0.4%, 25.6% vs 2.3%, and 25.6% vs 2%, respectively), because at fractured site drug delivery will be lower, and also fractured struts cause more

mechanical irritation to the tissue and then proliferation of smooth muscle cell occurs (Kuramitsu et al. 2012).

Later, Kuramitsu et al. (2015) reviewed 700 patients with 898 lesions treated with PROMUS Element platinum chromium everolimus eluting stent (PtCr-EES) and 16 patients (1.7% of lesions detected) with SFs reported where SF was defined as partial fracture (8 fractures, 44.4%), complete separation (5 fractures, 27.8%) without displacement, and complete separation with displacement (5 fractures, 27.8%).

In this study, 6 variables were considered as the predictive value, ISR at baseline, RCA, stent, overlap, hinge motion, total stent length and tortuosity. Although it was reported calcification, bifurcation, stent diameter, and other factors. may have effect on SF incidence, but once again, RCA, hinge motion, ISR, and total stent length were shown to have significantly higher prevalence (Kuramitsu et al. 2015).

Locations of the fractures within the stents were reported, where the mid-portion had highest rate (50%), overlapping (22.2%), proximal portion (16.7%), and distal portion with lowest rate of fracture (11.1%) (Kuramitsu et al. 2015), in agreement with other studies (Kuramitsu et al. 2015).

The multivariable analysis demonstrated that lesions with hinge motion and having difference angle  $\geq 16^\circ$  between diastole and systole was defined as one of the predictors of SF, where the point of fracture was accorded to the point of hinge motion (Kuramitsu et al. 2012, Kuramitsu et al. 2015). ISR at baseline with OR= 14.20 has higher risk factor, hinge motion OR= 4.31, RAC OR= 3.92, and total stent length OR= 1.32 were the four predictors factors of SF after PtCr-EES implantation (Kuramitsu et al. 2015).

It is interesting that hinge motion was not the biggest risk factor and also tortuosity was not even found as a predictor which is in disagreement with Kuramitsu et al. (2012) report after CoCr-EES implantation. Kuramitsu et al. (2015) believed that the reason for the

difference in results is related to the new design and novel metal alloy of PtCr-EES where it provides more flexibility, however, SF is inevitable. Also Menown et al. (2010) reported that in both PtCr-EES and CoCr-EES, the same drug and polymer is used, but to improve deliverability, radial strength, fracture resistance, and radiopacity in PtCr-EES a novel metal alloy and new stent design was developed which provided thinner struts and increased flexibility.

There are number of limitations during each study such as detecting SF, repeat angiography, short term of using DES, which each of them can be a reason for wide range of SF incidence. In every report different populations were selected as well as the coronary angiography was performed for dissimilar number of cases during follow up in each group of study. Furthermore, studies defined different SF classification, either considering only complete fracture or in some cases also including partial fracture. In addition, it seems that different types of stents do not have equal incidence rates, thus different designs and types clearly have an effect on SF (as would be expected). Furthermore, various diagnostic methods were utilised (e.g. angiography, IVUS, computed tomography), each of which have different sensitivity and accuracy where used to detect fractures. With regard to all these reasons, it is not surprising that autopsy studies have reported much higher rate of coronary SF (29%) (Chinikar & Sadeghipour 2014).

In general, implantation stent in tortuous artery, overlapping stent, stent design, hinge motion and also long stents are more vulnerable, and also RCA appears to be favoured artery location for SF where up to 50% of SF are reported (Wiktor et al. 2016).

## **3.2. Finite Element & Fatigue Life Analysis of Stent**

Atherosclerosis treatment has been significantly improved by angioplasty and stenting procedures. Moreover, development and further improvement of drug eluting stents

increased the success rate of these devices in more tortuous and narrow vessels which was not previously possible (Harewood & McHugh 2007). Stenting procedures in such complex cardiovascular regions are subject to additional forces and stress that can lead to stent fracture (Sianos et al. 2004, Shaikh et al. 2008, Umeda et al. 2009). Other factors such as calcification of the lesions and cardiac wall movement can increase the severity of such phenomena. In general, the mechanical failure of metallic structures such as stents could be due to i) static rupture; when static force is higher than material ultimate stress, and ii) Fatigue rupture due to cyclic loading (Morlacchi et al. 2014). Hence, it is important that the mechanical behaviour of stents be examined to predict potential service life prior to use *in-vivo*.

Computational modelling and finite element (FE) analysis is becoming a reliable and cost effective method to use in such cases instead of *in vitro* testing. It simulates and investigates the mechanical performance of components efficiently, and can quantify parameters which are difficult to ascertain using standard *in vivo* or *in vitro* tests such as stress/strain distribution, fatigue failure and device deformation. Although, there are numerous cardiovascular stent FE modelling studies that concentrate on the stresses in the arteries or the deployment of the devices, little work has been done on the loading endured by the stent during its lifetime *in vivo*.

A strut thickness size dependent (size effective) computer modelling study of cardiovascular stents was conducted by Harewood & McHugh (2007) to determine mechanical properties such as yield strength, hardening modulus, and failure strain. In a tension test it was found that higher microscopic strain is needed to generate shear bands in thick struts, while ultimate tensile stress (UTS) was influenced more by a soft grain (a grain that is favourably oriented for slip) in thin struts. It was stated that the results from the tension modelling are in agreement with experimental results reported by Murphy et al. (2003). Also all the strut failure was placed at or near the grain boundary where the

strain gradient is high. In contrast, bending test revealed an opposite results of the tensile test. It showed that thinner strut provides better flexibility and so would be have better resistance to fracture due to bending (Harewood & McHugh 2007).

A finite element analysis (FEA) study by Chua et al. (2004) demonstrated stress distribution within a stent in three different stages; before stent expansion, at maximum deployment pressure, and after the balloon deflation. A 3-D FE model of the balloon, artery, plaque, and slotted tube stent was created on ANSYS, where the balloon was defined as hyper-elastic and other three geometries were defined as linear isotropic material. The simulation was started by applying 2.65 MPa pressure to inner surface of the balloon, which resulted in the expansion of the slotted stent against the plaque and the artery model. The results illustrated that the maximum von-Mises stresses before the deployment were localized in the corners of the slotted structure while the minimum stress was in the middle of the struts. At the maximum deployment pressure, the location of the peak stress still was at the same place though the struts experienced greater stress due to expansion as well as the compression of the plaque and vessel wall. After the balloon deflated, lower stress was observed at the middle of body and the bridging struts. Moreover, it was found that the stent struts and the plaque experienced higher stress when they were in contact with each other (Chua et al. 2004), and consequently incremental stress within the plaque will raise the risk of plaque rupture (Veress et al. 1998).

Regarding flexibility studies, Wu et al. (2007) also believed that good flexibility in coronary stents is an important key property which will reduce stresses between the stent and vessel wall, as well as to aid the stent delivery in tortuous vessels. Two kind of geometry FEA models of Nirflex stent (Medinol Ltd., Tel Aviv, Israel) were built; a stent unit and a whole stent, which underwent bending load (see Figure 3.5 & Figure 3.6).

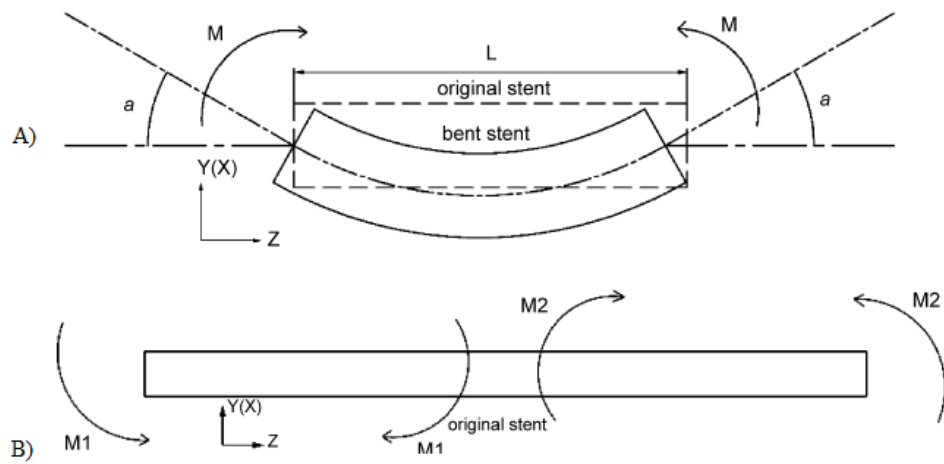


**Figure 3.5: Sketch of A) a bending load  $M$  for the unit stent and B) Multiple bending load  $M1$  and  $M2$  for the whole stent (Wu et al. 2007).**

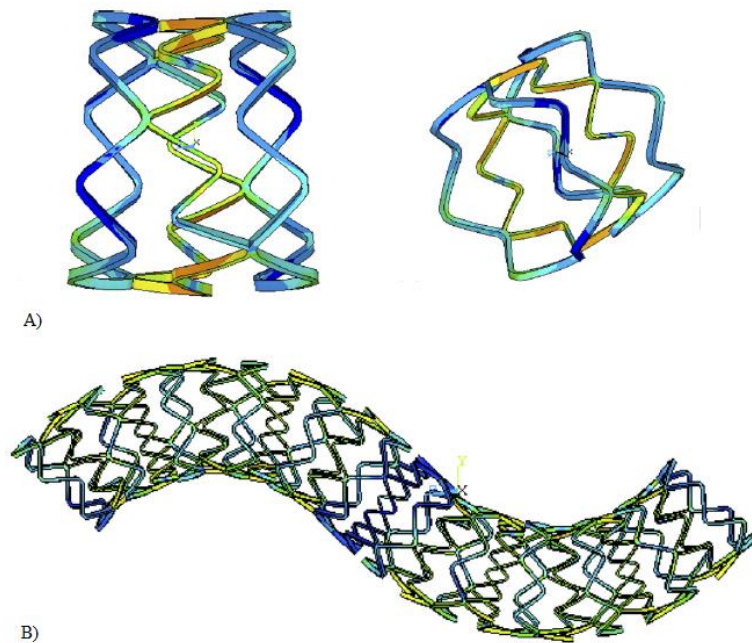


**Figure 3.6: Deformation of stent under bending load A) the unit stent and B) the whole stent (Wu et al. 2007).**

Therefore, Wu et al. (2007) suggested that increasing in plastic deformation, will provide more flexibility is the stent model.

In additional to stent flexibility, most implant devices are assessed on the basis of survival to predict and prevent mechanical failure. The coronary and endovascular stents are designed for 10 years lifetime, which it is almost equal to  $4 \times 10^8$  cycles (at typically 70 bpm) without any fatigue failure occurring. Marrey et al. (2006) performed a study in

order to analyse and predict the fatigue life of coronary stents, specifically L-605 Co-Cr alloy (see Table 3.3). The results showed that the fatigue life of stents were far from the assumption of stent fatigue life prediction. Thus, Marrey et al. (2006) stated that time of failure is unknown and the fatigue lifetime could not be as a satisfactory safety factor. Moreover, they believe that fatigue failure would be better assessed on the basis of testing to failure as is the case in other engineering fields.

Young's modulus, $E$ (GPa)	Tensile strength (MPa)	Fatigue endurance strength (MPa)
243	1449	207

**Table 3.3: Mechanical properties of L-605 Co-Cr alloy (Marrey et al. 2006).**

There are two methodologies to assess on this basis;

1. Stress-strain (S-N): Relationship between applied stress/strain and the total life of a device
2. The damage tolerance (fracture mechanics): Number of cycles and the largest crack would be consider to analysis the lifetime

Marrey et al. (2006) used the stress-strain life analysis to predict the fatigue life of cobalt chromium stent and the damage tolerant method to determine the effect of pre-existing flaws. Regarding the propensity of the flaw to propagate, which would cause stent failure and also cyclic pressure loads (systolic/diastolic); they assessed the severity of micro-cracks and flaws on the expanded stent structure. The model was simulated based on the *in vivo* environment and fatigue loading was considered from fabrication to final step deflation when the stent elastically recoils.

ABAQUS software was used to model the 3 dimensional 8 node brick to analysis the numerical stress during cyclic radial loading. The artery was considered as hyper elastic tube and stent as cobalt chromium (L-650 Co-Cr alloy). The stress analysis showed that by increasing internal pressure loads during systolic-diastolic cycle, the peak stent stress reduced slightly due to increasing contact forces between stent and tube. Furthermore, it

was observed that the stent acted in a linear-elastic manner during the heartbeat cycle (Marrey et al. 2006).

The fatigue limit (endurance strength) of the stent specimen material was calculated for  $4 \times 10^8$  cycles to be 207MPa regardless of any condition and stress, according to stress amplitude versus number of cycle curve (Marrey et al. 2006). However, in the *in vivo* environment as discussed above (diastolic/systolic) there are two internal loads, which have an effect on mean stress and endurance strength. By simulating the conditions the real mean stress and stress amplitude were determined and then used to evaluate the fatigue safety factor (FSF). Table 3.4 represents the stress and fatigue safety factor (FSF) at the worst case fatigue location. Also Figure 3.7 illustrates where fatigue cracks are most likely to initiate.

Max principal stress at systolic pressure	Max principal stress at diastolic pressure	Mean stress	Stress amplitude	Inverse FSF	FSF
683 MPa	787 MPa	735 MPa	52 MPa	0.76	1.32

**Table 3.4: Stress and fatigue safety factor (FSF) at the worst case fatigue location (Marrey et al. 2006).**

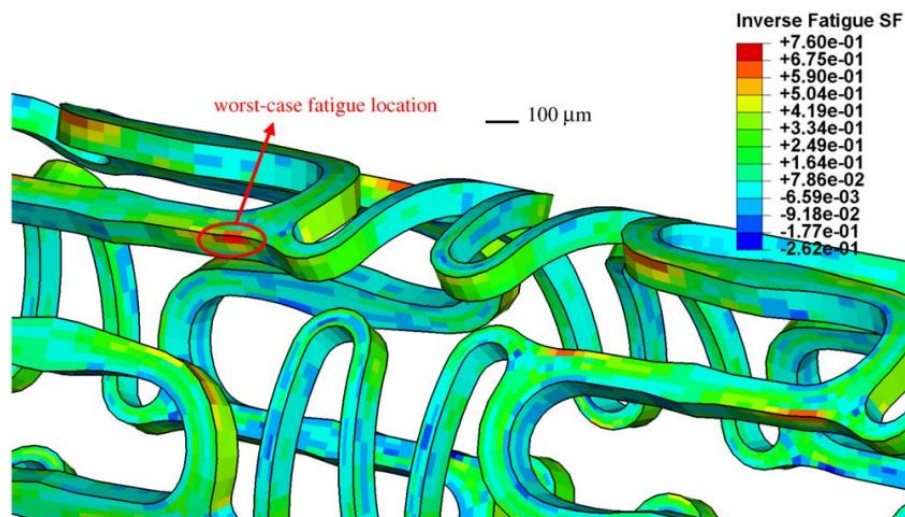


**Figure 3.7: Max inverse FSF location or the zone with lowest FSF on FE stent (Marrey et al. 2006).**

After that, fracture mechanics was used to detect and measure micro-structural anomalies over two expanded and unexpanded stents. It was observed that small cracks could be generated even during production. Two types of flaw, semi-elliptical and corner flaw were determined on the ABAQUS model, which had the worst-case fatigue condition (see Figure 3.8). The analysis indicated that the outer wall surface of the stent had higher tensile stress and during the recoil (spring-back) period it reached its highest point (Marrey et al. 2006).

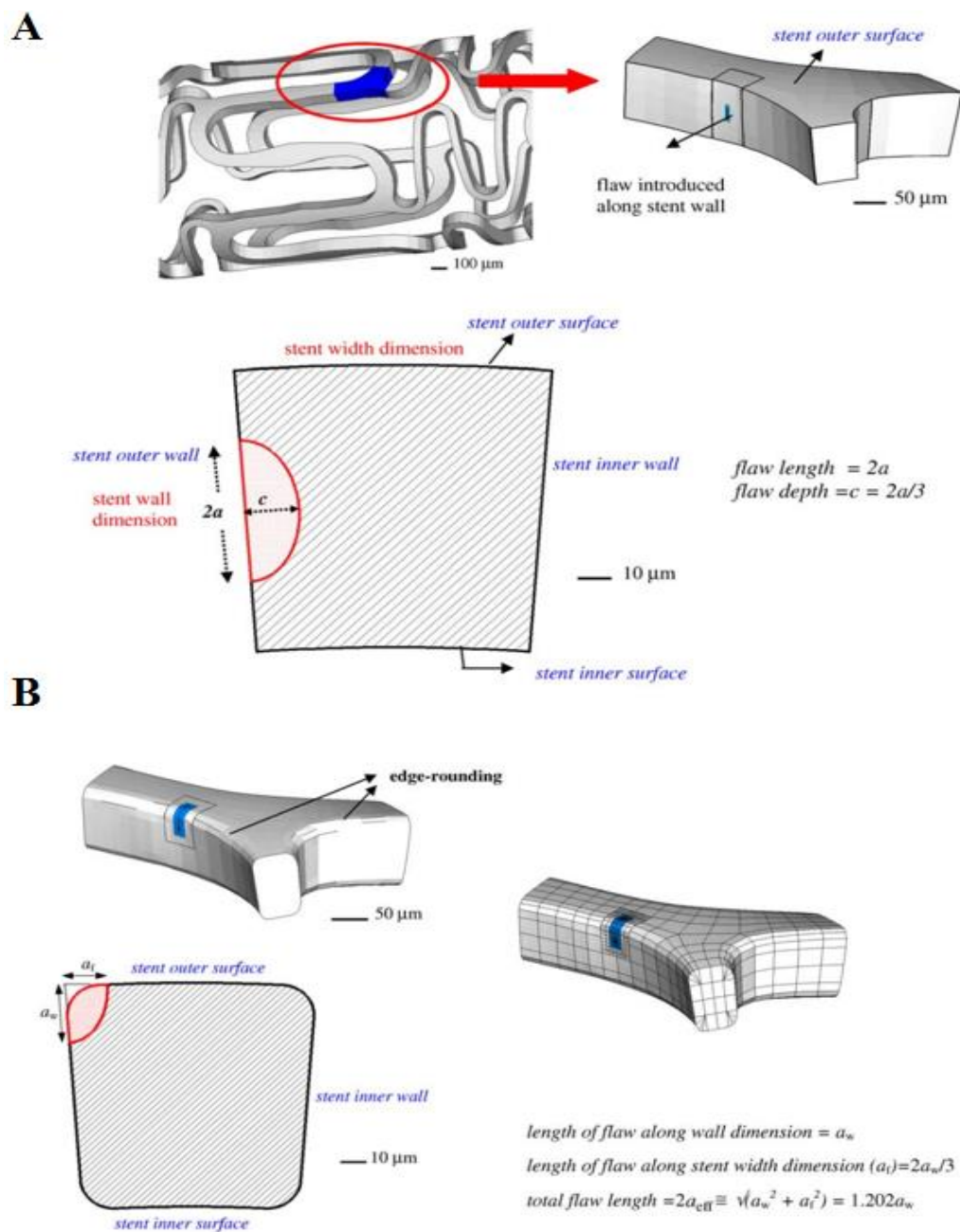


**Figure 3.8: Geometry of (A) semi-elliptical (centre) flaw, and (B) corner flaw at stent wall (Marrey et al. 2006).**

Pre-existing flaw growth can take place under fracture loading conditions while stress intensities are below the fracture toughness of the material. However, when the growth rate is slow, in fact the cracks can be deemed to be inactive, and this stress intensity is known as the fatigue threshold (ASTM International 2001). Although, the existence of micro-cracks and flaws in small components such as a stent struts increases the possibility of abrupt fatigue failure or even complete fracture. The damage tolerant approach clarifies that if the fracture toughness is higher than the peak stress intensity during recoil as well as the fatigue threshold higher than the stress intensity between systolic and diastolic cycle pressure, the fatigue crack instigation and expansion can be avoidable. It was found that instability of local structural conditions under cyclic loading conditions cause stent failure and strut fracture. Nevertheless, the radial pulsatile loading cannot cause premature fatigue failure in flaws greater than 90  $\mu\text{m}$  (Marrey et al. 2006).

Moreover, Barrera et al. (2014) believed systole/diastole is a factor of SF, which might encourage fatigue failure in ballon expanded stents. Simulating cardiac cycle pressure in order to evaluate stent stress distribution, a FE model of a 316L stainless steel stent was created with 7mm, 1.5mm, and 80 $\mu\text{m}$  dimension for length, inner diameter, and strut thickness, respectively. The stent model was deployed in an isotropic hyperelastic cylindrical hollow artery model, where both ends were constrained in order to avoid any rotational or tangential motion. A maximum pressure (systole) of 120mmHg and a minimum pressure (diastole) of 80mmHg were applied as the cardiac cyclic pressure, with 1.2 Hz frequency, applied to the artery in contact with the stent model. The von-Mises stress distribution was observed within the stent to determine the critical area where the first fracture might occur (see Figure 3.9), as the risk of fatigue failure increases in the area where the maximum von-Mises stresses exist (Barrera et al. 2012).

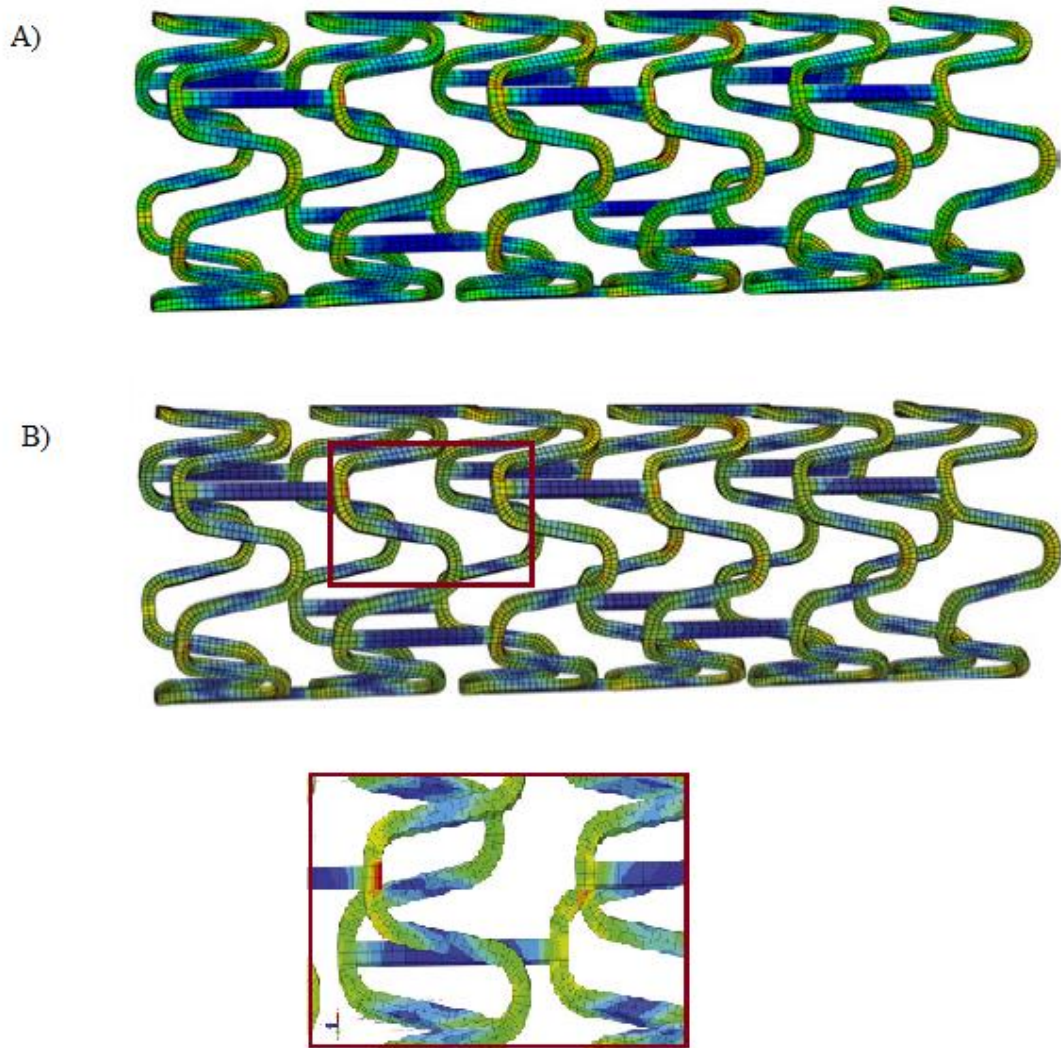


**Figure 3.9: Distribution of von-Mises stress within the stent model due to A) effect of diastolic pressure, and B) effect of systolic pressure (Barrera et al. 2012).**

Yet, the result illustrated that the ring segment of the stent model endures higher stress during the cardiac cycle, which is same location as other studies reported, still the stent is situated in safe region according to the numerical analysis of the study (Barrera et al. 2012).

Along with the fatigue life of stents, Li et al. (2010) conducted a study in order to investigate stress distribution in implanted stents. They started with a computer model of L-605 cobalt chromium alloy stent on ANSYS, and then followed by *in vitro* fatigue experiment to verify the results. As the structure of stent is symmetrical, only half of its length and 1/3 of its circumference were created. Finite element analysis (FEA) presented that during crimping and dilation maximum stress appeared on curvature of the ring while

the middle segment of the bridge links had minimal regions of high stress (see Figure 3.10). However, when the catheter and balloon were removed, the maximum stress reduced significantly whereas the maximum and minimum stress remained at same location. Moreover, during the dilation stage, the stress was closed to the ultimate tensile strength of stent material, which it can lead to the tensile failure in deployment procedure (Li et al. 2010).

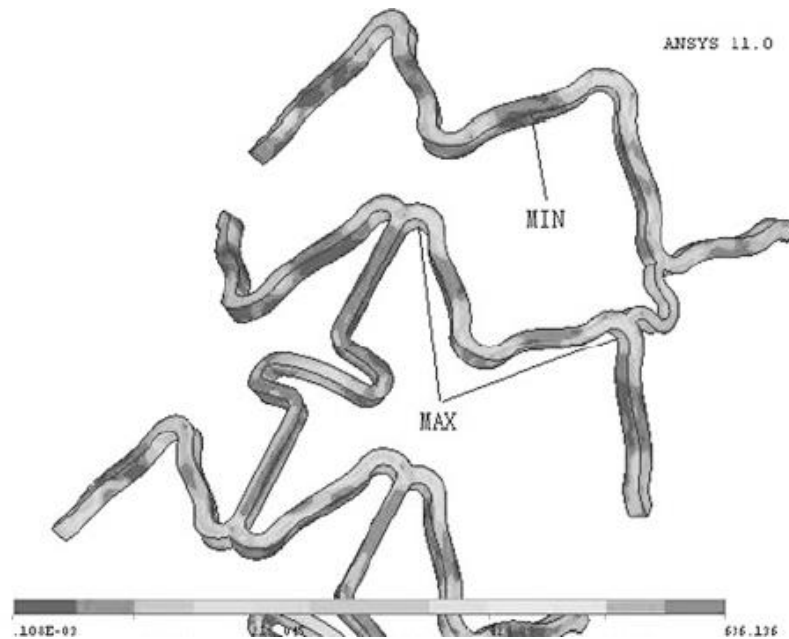


**Figure 3.10: Location of minimum and maximum stress (Li et al. 2010).**

During the fatigue analysis, due to time limitation the worst case scenario was chosen to be tested, based on the FEA results. Also it showed that the curvature of rings were the regions close to the fatigue limit (Li et al. 2010).

In the *in-vitro* fatigue test, 10 stents were deployed in to natural rubber latex tube filled with saline in order to simulate the human artery and blood fluid. The stents were subjected to the systole and diastolic pressure by the assembly of two electrodynamic pumps on either end of the mock artery. Previous to testing, no flaw or crack was observed under scanning electron microscopy (SEM) in all the stents, but after simulation some fatigue bands and corrosion was appeared on the ring curvature location of stent while there were not any mark on the bridging link (see Figure 3.11). Li et al. (2010) concluded

from their computational and experimental simulation, the highest stress and stress distribution occurred at curvature of the ring where it is the highest risk of fatigue failure.

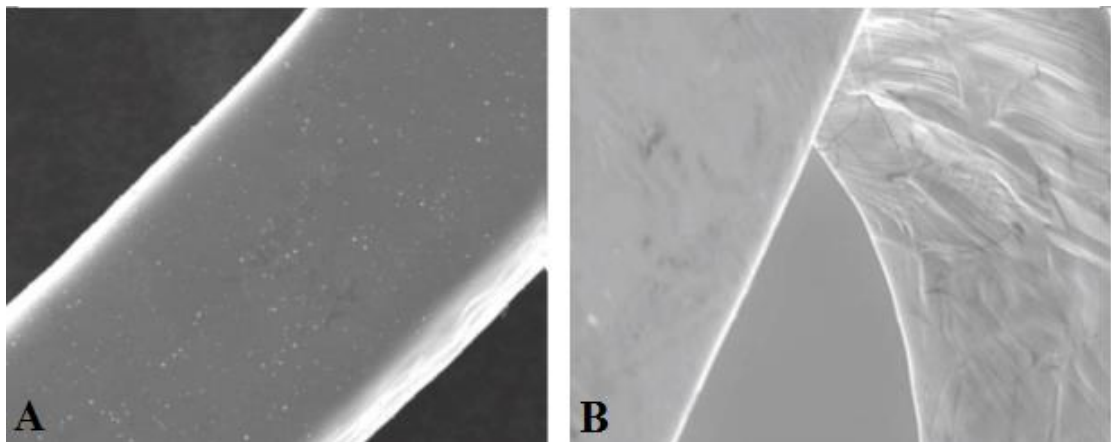


**Figure 3.11: SEM at curvature of ring (A) before simulation (B) after simulation (Li et al. 2010).**

The objective of an FEA study by Early & Kelly (2010) was to investigate the influence of different geometries of blood vessels on the mechanics of stenting. It found that balloon expanded stents (BES) in coronary arteries lead to increases inner diameter of artery (lumen gain) and applied high stress to the inner surface of the artery. Also cardiac cycle caused change in BES diameter by 0.23% causing stent deformation, resulting in stent fatigue failure (Early & Kelly 2010). Interestingly, Early & Kelly (2010) believed that systole and diastolic cycle cannot be the major cause of SF as the strain amplitude created by cardiac cycle is very low. However, it also should be considered as a factor of stent fatigue, because the frequency of the pulsation is very high.

A coronary bifurcation of the left anterior descending (LAD) artery was reconstructed based on a clinical case study utilising tomography angiography (CTA) and conventional coronary angiography (CCA), in order to replicate real artery geometry (see Figure 3.12) (Morlacchi et al. 2013) . As a part of computer simulations of stenting, two stents were deployed back to back with small overlap as is shown in Figure 3.13 (overlapping stent). As was expected, the maximum von Mises stress was observed at the overlapping region which was close to the ultimate stress value and consequently, it increases the risk of SF

and TLR. These results show good agreement with clinical reports where overlapping stents are known as a factor of SF. Furthermore, the location of peak stress was also observed at the same place as Li et al. (2010) and Marrey et al. (2006) reported, at the curvature of the ring (see Figure 3.13) (Morlacchi et al. 2013).

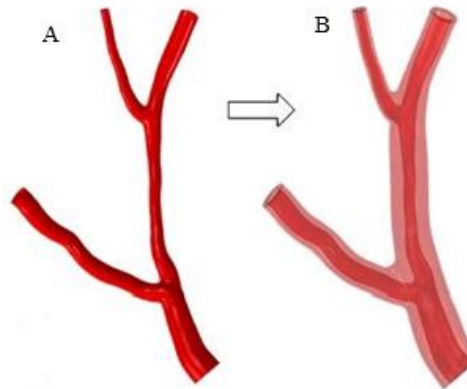


**Figure 3.12: Geometrical reconstruction of LAD: A) Medical image from CTA and CCA, and B) 3D model (Morlacchi et al. 2013).**

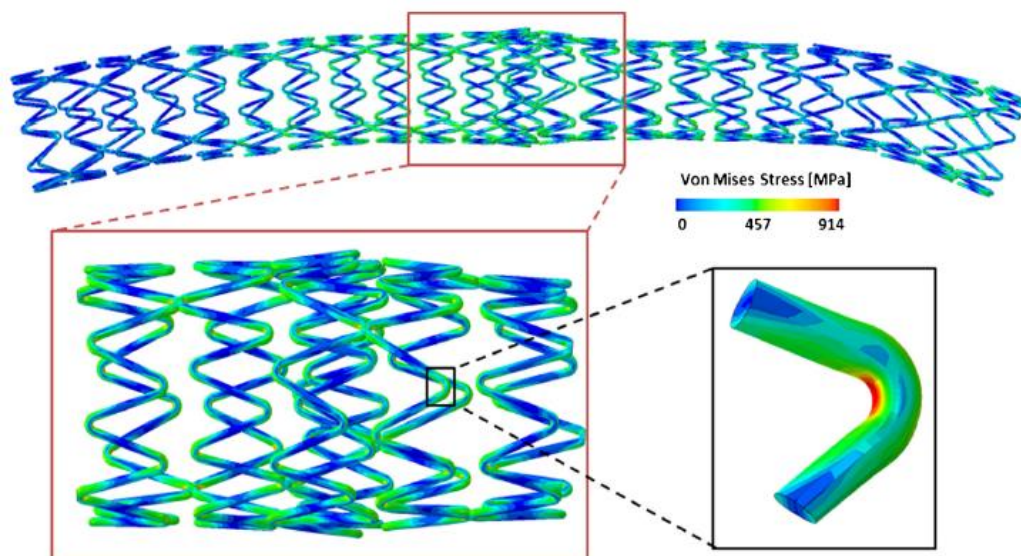


**Figure 3.13: Maximum von Mises stress at the overlapping segment after the stenting procedure (Morlacchi et al. 2013)**

In another study by Wu et al. (2007), the finite element method was used to define the behaviour of stent expansion in curved and straight vessels. The model was created on Pro/Engineer and then transferred into ANSYS to analyse. Each model consisted of 4 parts: stent, artery, plaque and balloon. The artery and plaque both were considered as a hyper-elastic material (following Mooney-Rivlin equation) and the stent as 316L stainless

steel with the standard values for its properties ( $E= 201 \text{ GPa}$ ,  $\nu= 0.3$ , and  $\sigma_y= 280 \text{ MPa}$ ). Design of the stent was unique, 8 rings in the circumferential direction are connected by 4 links in longitudinal direction with a strut thickness of 0.1 mm. The stent had 9 mm length and 0.75 mm radius. A 10 mm rigid body with 1.3 mm diameter was modelled as the balloon. In both models, the artery was created 12 mm in length, 3 mm diameter and 0.5 mm thickness. Also the plaque was modelled as uniform B-splines shape with 8 mm length, which becomes thinner in the middle part. The maximum severity of lesion in the model was assumed to be 56% of the vessel lumen. However, as the models were symmetrical only 1/8 and half of the straight and curved vessel were built, and also the ends of artery and balloon were constrained in both longitudinal and rotation direction (Figure 3.14) (Wei Wu et al. 2007).

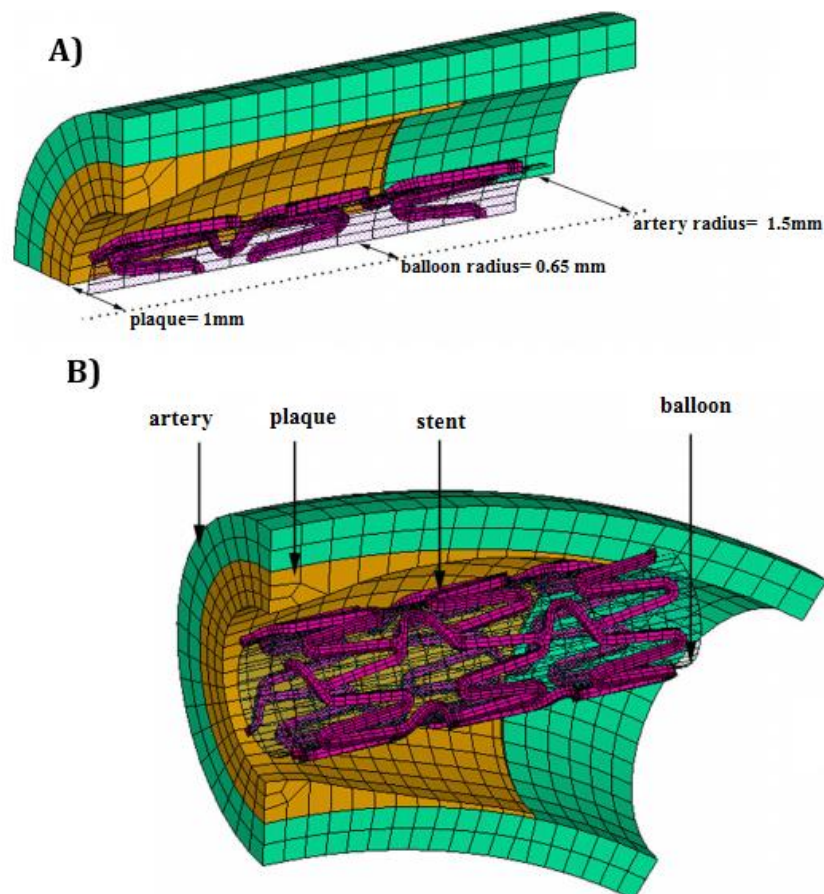


**Figure 3.14:** (A) Straight vessel model, and (B) curved vessel model (Wei Wu et al. 2007).

To simulate the models, the stent model was expanded to 3.3 mm and then a 0.0133 MPa pressure was loaded into inner surface of the artery in terms of blood pressure during balloon expansion. Afterward, the deformation and conformity of both models were collected. During the balloon expansion, the stent had an effect on the vessel and caused some degree of straightening , and then after the balloon deflated, the stent was bent by the curved vessel (Wei Wu et al. 2007).

In a study by Wong et al. (2009), a simulation of an atherosclerotic stented artery under displacement bending load was conducted (using COMSOL Multiphysics version 3.5a). A hollow cylinder was created as the artery with dimensions 3 mm, 0.7 mm, and 80 mm as inner radius, artery thickness and longitudinal length, respectively. The length of the plaque was modelled as the same as the length of artery (80 mm), 2 mm as inner radius with thickness of 1 mm. In both models the artery and the plaque were constructed as nonlinear isotropic hyperplastic materials. Two different stent sets were tested, (I) two 6 mm stent segments with variable spacing (20, 30, 40, and 50 mm), (II) and a 48 mm stent, but the radius 1.8 mm and thickness of 0.2 mm was used for all the stent models.

Applied displacement to the end of artery illustrated that as the displacement loading was increased, the stress within the stents models increased. Also the simulation of two stent segments showed that as the space between the stents increased the maximum stress decreased in the stents. Furthermore, it was observed the maximum stress in the 48 mm stent was significantly higher than the two segments model, therefore it can be said that the segments stent design provided a lower range of stress in comparison with the full length stent (Wong et al. 2009). In addition, as the two boundary conditions were applied, the stress was lower in the one which provided greater amount of movement.

Another elastic-plastic stent model was analysed on ANSYS by Ma (2011). He considered three different ways of deformation of a coronary stent, stent compression,

stent expansion and fatigue life prediction from its production to application as each step affects the mechanical specification differently, which is in agreement with another study by Li et al. (2010)

During the compression processes stress was very low especially at bridging links. The stress was distributed regularly but increasing at the bending location. Nevertheless, there was slightly radial displacement as well as axial elongation where the average recoil size and elongation was 0.0515 mm (4.606%) and 0.187 mm (3.026%). The same phenomenon was noted in expansion processes with 0.0978 mm (2.795%) radial displacement and axial contraction -0.5465 mm (-8.84%). Moreover, the fatigue life analysis with consideration of heart-beat cycles result illustrated the bending location of struts was defined as the fatigue critical location particularly at inner surface with 1.562 fatigue safety factor value (Ma 2011).

Similar to most FE studies examining stress distribution in expanded coronary stents, Eshghi et al. (2011) investigated the mechanical characteristics of implanted stents. An initial pressure (equivalent to 100mmHgs) was applied to the inner surface of the artery as well as plaque model in order to simulate the blood pressure, and then an additional pressure was applied to inner surface of the balloon. As was expected the maximum von-Mises stress was observed at the corners of each cell. Moreover, presence of plaque had an impact on the stress and stent diameter, as the area without plaque had a larger diameter in compare with calcified area at same expansion pressure (see Figure 3.15) (Eshghi et al. 2011).

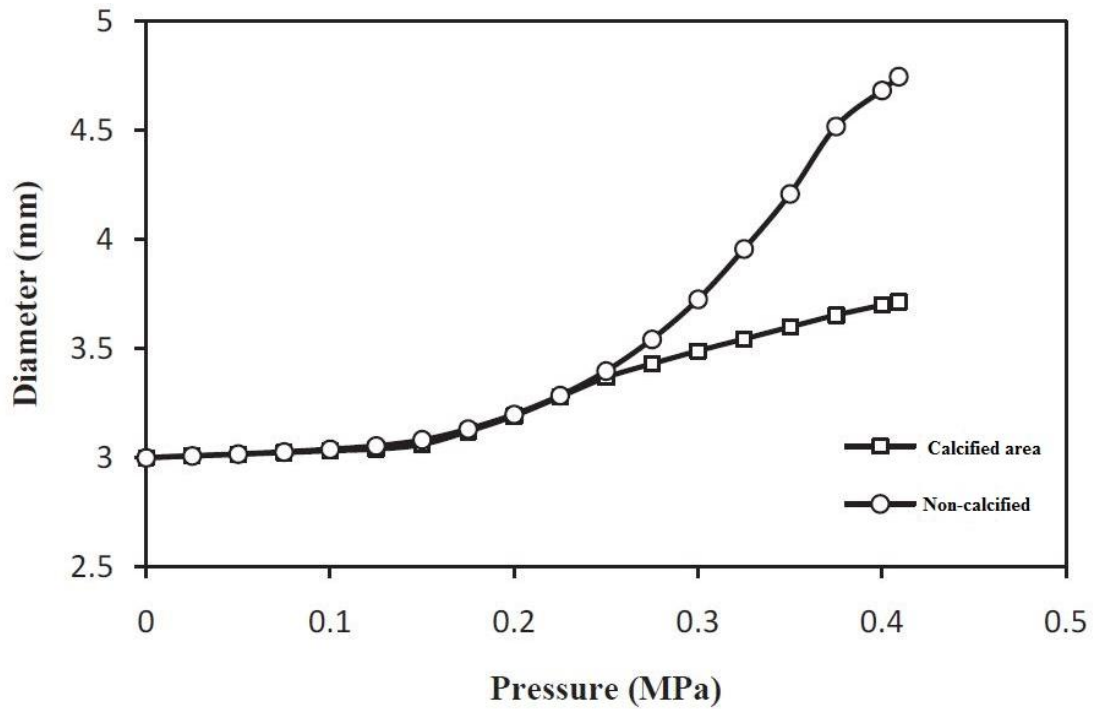


**Figure 3.15: Change in outer diameter of stent during expansion (Eshghi et al. 2011).**

Martin & Boyle (2013) considered another aspect which might influence stress distribution in coronary stent models. They performed an FEA to investigate optimum strategies to model angioplasty balloon configuration. Three different balloon models were analysed in two set of free deployment of stent and within an idealised hyperplastic artery deployment. Although the results illustrated that balloon configuration would have a significant impact on the stress magnitude within both the stent and artery, however, in each of deployment and analysis, the stent underwent a substantial plastic deformation, the stress distribution was similar, and the maximum equivalent stress occurred at the curvature of ring after balloon deflation, especially at mid-segment of the stent model where it was in contact with plaque (see Figure 3.16) (Martin & Boyle 2013).

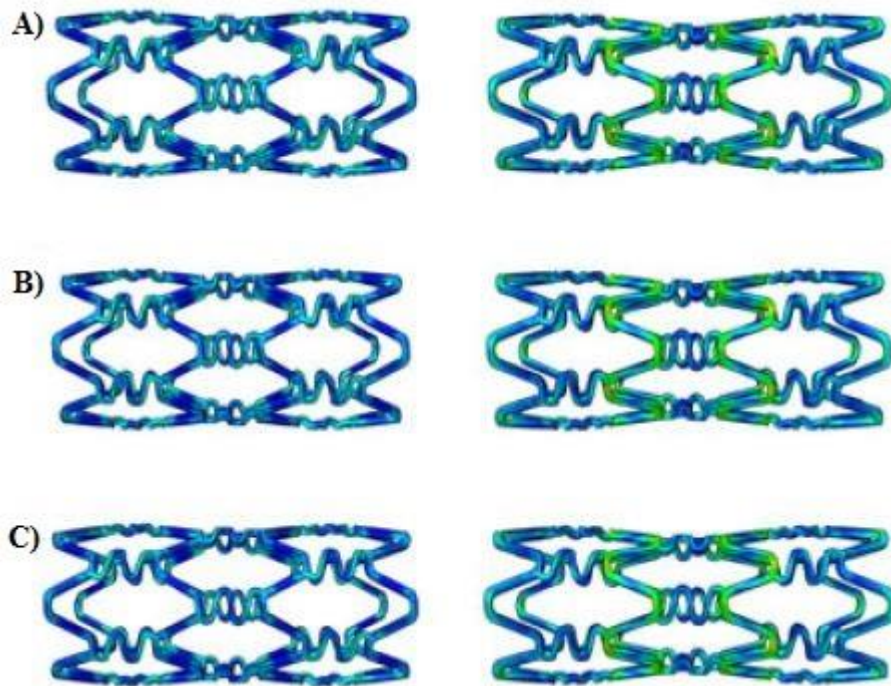


**Figure 3.16: Stress distribution in the stent after balloon deflation A) idealise non-folded angioplasty balloon, B) an idealised folded angioplasty balloon, and C) folded model of a semi-compliant angioplasty balloon. The left side models representing the free deployment stress distribution, and the right models representing the artery deployment stress distribution (Martin & Boyle 2013).**

A simple model of epicardial atherosclerotic coronary artery with calcified plaque was created as a finite element model on Rhinoceros 4.0 Evaluation by Morlacchi et al. (2014). The artery was modelled with a curvature of 20 mm radius and 31 mm length (see Figure 3.17A). Also 7 mm thickness was assumed as the cardiac wall, which surrounded the half circumference of the artery (see Figure 3.17B). Furthermore, two different types of plaque, calcified and non-calcified, were taken into account with stenosis value equal to 60% of the artery lumen which localised in the centre of the artery model (see Figure 3.17C). Afterwards, a commercial Xience Prime stent (open-cell), was expanded in order to evaluate the influence of calcified plaque, blood pressure, and cardiac cycle on the stent stress.

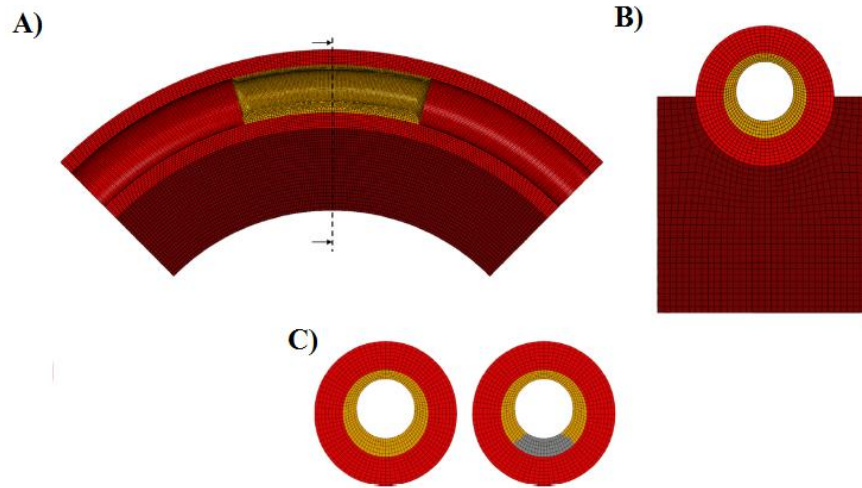


**Figure 3.17: (A) Coronary artery model, (B) Cardiac wall surrounded half of the artery model, and (C) Cross section of vessel lumen without and with (gray area) calcified lesion (Morlacchi et al. 2014).**

In the *in vivo* environment, implanted stents undergo cyclic loading consisting of the internal blood pressure as well as the cardiac wall movement during each heartbeat. By apply loading and displacement, this phenomenon was simulated in the analysis. Figure 3.18 illustrates the different pressure loading conditions during diastole (80 mm Hg) and systole (120 mm Hg) as well as 4 mm displacement being applied to internal node of artery wall to represent the cardiac movement. Additionally, both ends of arterial surfaces were fully constrained in the circumferential and axial directions similar to Wei Wu et al.(2007) study.

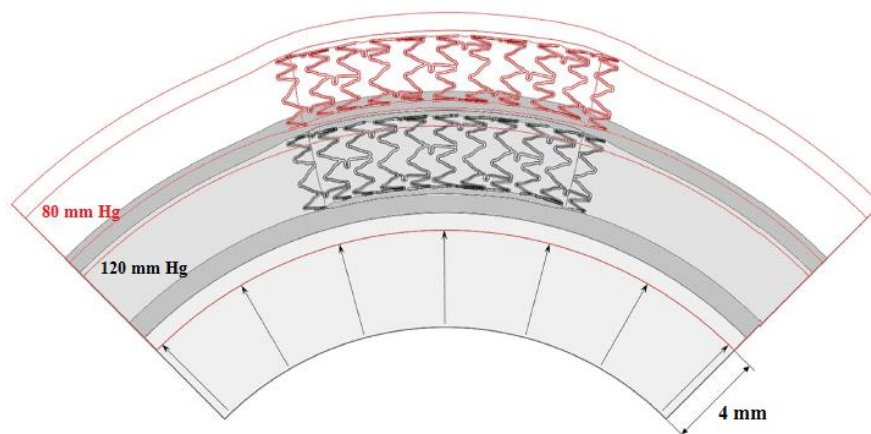


**Figure 3.18: Loading and displacement conditions during the cardiac cycle (Morlacchi et al. 2014).**

Stress/strain analysis of the simulated model shows that the artery lumen with calcified plaque had more resistance to implantation and placement of the stent. Also it was observed that the maximum von Mises strut stress close to the calcified region was 819 MPa whereas at fully cellular plaque decreased to 798 MPa (see Figure 3.19). Thus, from a quantitative point of view it could be said that plaque calcification can be one of the risk factors of the mechanical failure of stents. Also similar to previous reports in literature (e.g. Marrey et al. 2006), curvature of struts have highest value of stress (Morlacchi et al. 2014).

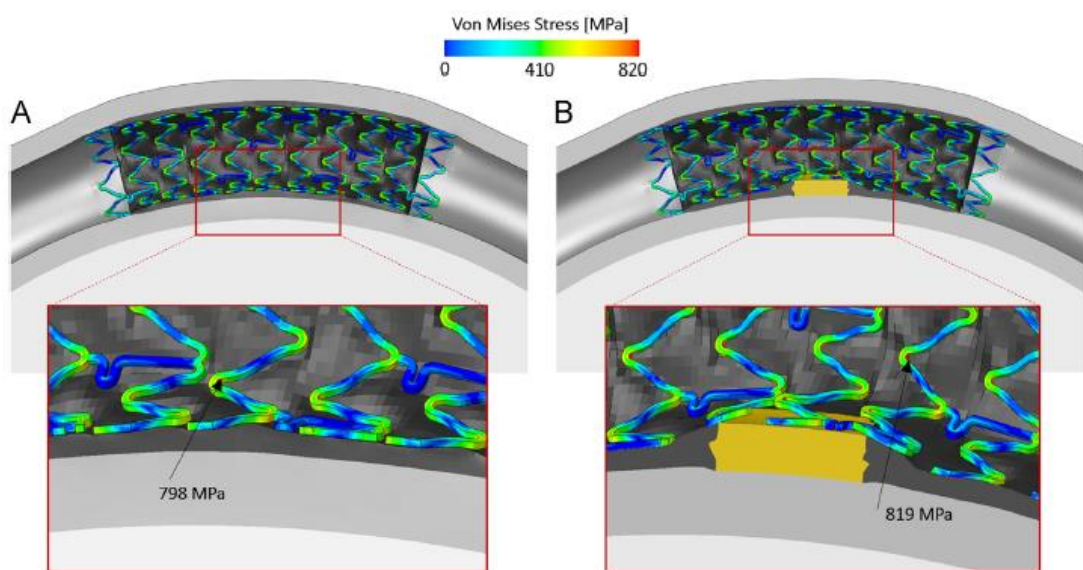


**Figure 3.19: distribution of von-Mises stress after stent deployment A) non-calcified, and B) calcified artery (Morlacchi et al. 2014).**

Furthermore, comparing the blood pressure and cardiac wall movement results on the mechanical failure of stent illustrated that the cardiac wall movement has higher effect on the risk of SF as it could produce alternative stress up to 390 MPa (Morlacchi et al. 2014).

### **3.3. Bench Testing of Stents**

All medical devices need to meet highly specific requirements (see Table 3.5) before they are able to be commercialised. These regulations are more stringent for components which will be implanted in the body (e.g. stents). Therefore all stent manufacturers must consider all possible risks which could lead to device failure. Stents undergo several

mechanical testing forms; testing constituent metal and alloys, compression and flexural, and dynamic simulation of pressure pulsation (Kemp & Ritchey 2011).

Reference	Title
EN ISO 13485:2016	Quality management system
EN ISO 14971:2012	Application of risk management to medical devices.
EN ISO 14155:2011	Clinical investigation of medical devices for human subjects
EN ISO 10993-XX	Biological evaluation of medical devices.

**Table 3.5: Important standard and regulations for medical device manufactures (The British Standards Institution 2018).**

Along with computational analysis, there have been experimental studies to investigate different mechanical characteristics of stents such as flexibility and durability, the relationship between dilation pressure and stent diameter, and stress distribution in environmental conditions close to *in-vivo*.

These mechanical experiments provide more accurate data to help designers and stent developers to evaluate the stents lifetime under variety of loading conditions. It can also provide valuable validation data for FEA, though *in-vitro* experiment will not simulate the *in-vivo* conditions completely. Further, results of the majority of studies are specific to a particular type of stent model, however they can still be informative, aiding the clinician to choose the optimum device.

Balloon expandable stents require a high degree of longitudinal flexibility to be able to pass through tortuous vessels without any difficulty and excessive distortion, as well as expand and shape well with respect to the vessel wall. Ormiston et al. (2000) compared thirteen stent designs before and after deployment to determine longitudinal flexibility changes including: V-Flex (Global Therapeutics), Bard XT (Bard, Galway, Ireland), Jostent (Jomed, Germany), Multi-Link and Multi-Link Duet (Guidant, Santa Clara, CA), nine cell NIR (Boston Scientific), Crossflex (Cordis, Miami, FL), Wiktor-i (Medtronic,

Minneapolis, MN) BeStent (Medtronic), BiodivYsio (Biocompatibles, Surrey, England), Crown (Cordis), AVE GFX (Arterial Vascular Engineering, Santa Rosa, CA), and seven cell NIR-Primo (Boston Scientific, Galway, Ireland). They conducted a three point bend test for measuring the stiffness of each stent, where the results illustrated that the stents became stiffer after expansion.

Szabadits et al. (2008) tested the flexibility of five different designs of coronary stent including Express (Boston Scientific, USA), Orbus R (OrbusNeich, USA), Multi-Link Zeta (Abbott Vascular, Belgium) for open cell structure, and Tecnic Carbostent (Sorin Biomedica Cardio, Italy) and TentaurFlex (Minvasive Ltd., Hungary) for closed cell structure, though all of the specimens were made of 316L stainless steel. The bending test was performed on each stent by using ZWICK 005 bending machine (Zwick Roell Group, USA). One end of each sample was gripped and secured to avoid any movement while the other end was displaced (10mm per min in Y-direction) to a maximum deflection of 5mm. As expected, the comparison of results show that the open cell designs had lower stiffness and higher flexibility in comparison to the closed cell stent samples. The Tentaur specimen was more rigid and required higher force to bend in comparison to others samples which resulted in damage at 3.7mm deflection (type of damage unspecified), whereas the Orbus R had the fewest bridge (connectors) between its cells and was the most flexible one. The study concluded that less bridge connectors between the cells in the stents might be an advantage and provide more flexibility, however it can increase the risk of kinking and reduce the longitudinal integrity (Szabadits et al. 2008).

Moreover, Kinoshita. et al (2009) mechanically tested two different stent designs Cypher (Cordis Corporation, USA) and Taxus Express (Boston Scientific, USA) in a silicon T-tube (n=13 for each group), subjecting them to 20° deflection at a rate of 53 times per minute. The 20° deflection angle was selected as it was the average difference of LAD/LCX (left anterior descending artery/left circumflex) bifurcation between at systole

and diastole from the examination of 100 randomly chosen angiograms. Fracture occurred for all stents, with one of the designs lasting only a mean of  $31.3 \pm 7.6$  minutes

Mori & Saito (2005) believed that in order to examine stent flexibility two factors need be considered; i) radial deformation must be confined, and ii) uniform bending moment must be applied during bending test. Thus, they conducted four-point bending experiments, where two ends of a stent were attached to two bars and then applied load on the bar without any radial deformation on stent circumference. The stents sample structure was different in connectors, W, WD, N, and S shaped were tested (see Figure 3.20).

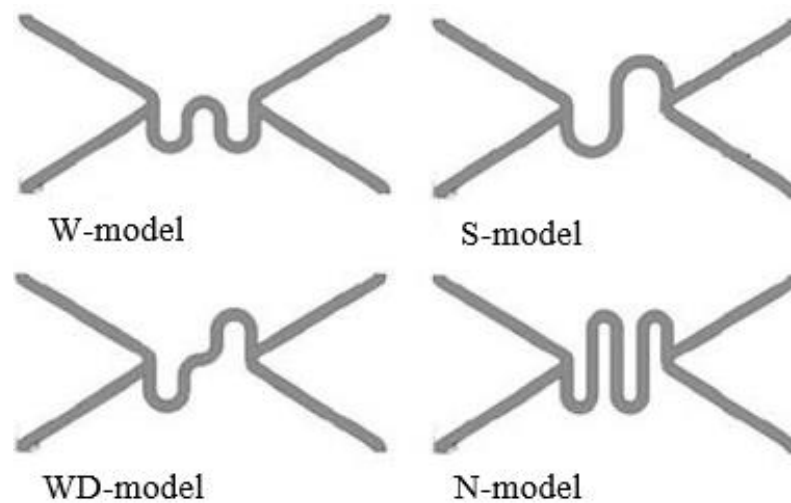


**Figure 3.20: Stent experiment model (Mori & Saito 2005).**

The result showed that N-shape stent struts had more flexibility while the W-shape was the most rigid one (see Figure 3.21). Also the length of strut seems to have an important role regarding to the bending stiffness as the N-shape one was the longer (3.637mm) and well deformed, whereas W-shape was the shortest (2.522mm) and kinked at the compressive side of deformation (Mori & Saito 2005).

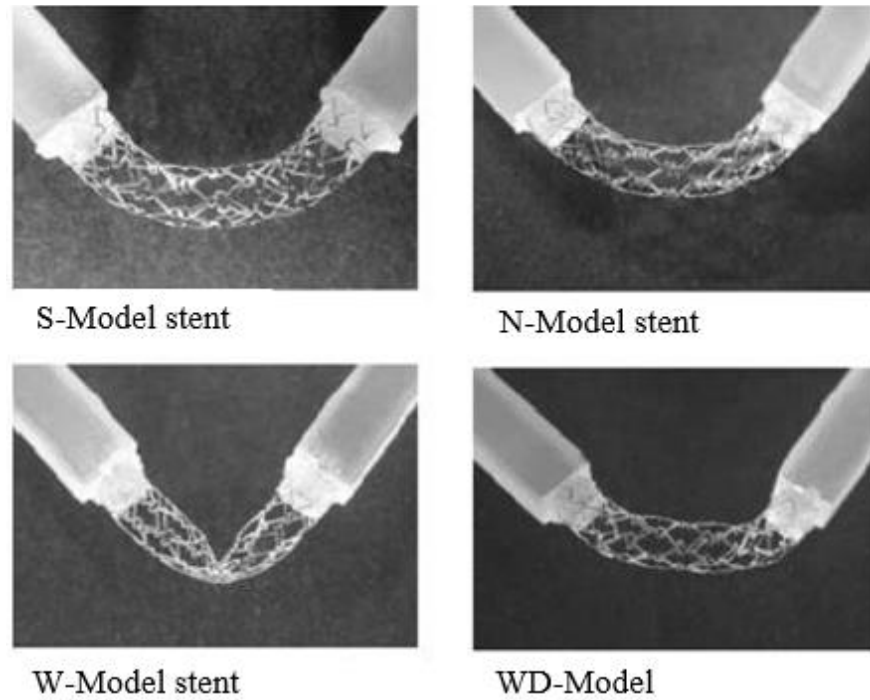


**Figure 3.21: stent configuration after the bending test (Mori & Saito 2005).**

Later, Szabadits et al. (2009) investigated the effect of length on the stent flexibility, examining two stent designs, Pro-Kinetic (Biotronik AG, Switzerland) (13 and 22mm length), and Multi-Link (Abbott Vascular, Belgium) (15 and 23mm length). The stents were passed through a tortuous silicon coronary artery model (see Figure 3.22). It was observed that longer stents had more difficulties negotiating the curvature where it was necessary to bend. Furthermore, the Pro-Kinetic stent which it is made of L-605 cobalt-chromium required less force to pass through the artery model in comparison with the Multi-Link 316L stainless steel at the similar length.

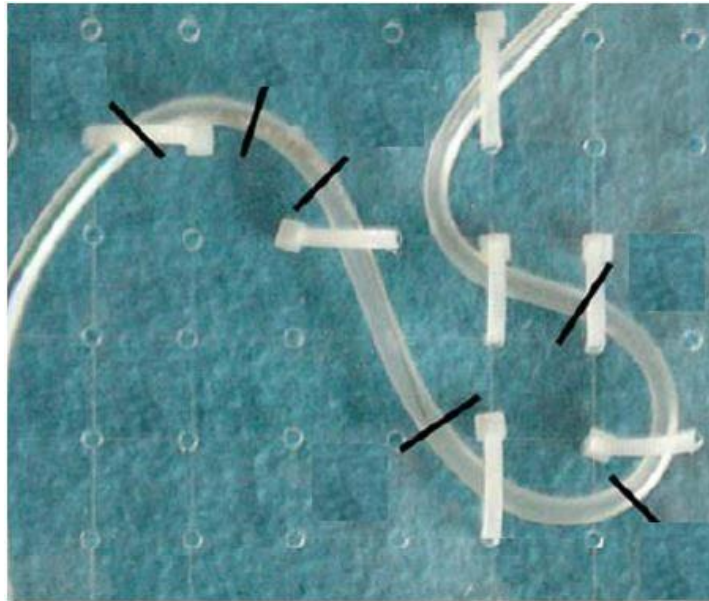


**Figure 3.22: Coronary artery route model to measure the track-ability force. (Szabadits et al. 2009).**

Another flaw of coronary stents can be longitudinal deformation. It is as a result of poor longitudinal strength within the stent structure due to the thinner struts in the new generation drug eluting stents (DES). Although it is not a typical phenomenon, it is likely if struts are malapposed (separation of stent strut from artery surface), then it could lead to adverse clinical complications. Ormiston et al. (2014) developed a bench testing procedure to assess the longitudinal strength of 6 different designs of coronary stents; Multi-Link Vision (Abbott Vascular, Belgium), Multi-Link 8 (Abbott), BioMatrix Flex (Biosensors Europe SA, Switzerland), Integrity (Medtronic, CA), Omega/Element (Boston Scientific, USA), and Promus Premier (Boston Scientific, USA). They simulated a common clinical scenario where a localised force is applied to one segment of the circumference of a malapposed proximal stent. Five 3mm diameter samples of each design were examined, where the distal portion of each stent was secured, and only 5mm of the proximal portion was subjected to a compression force. The test apparatus involves a polytetrafluoroethylene (PTFE) tube with 2.75mm internal diameter inside a silicon tube with 3.5mm inner diameter. The distal portion of each stent was deployed into PTFE tube, and only 5mm of the proximal length lay malapposed within silicon tube.

Afterwards, a rod with concave foot which was attached to an Instron universal testing machine (Instron, UK) applied 0.5N compressive force to one point at the proximal hoop of each sample (see Figure 3.23).

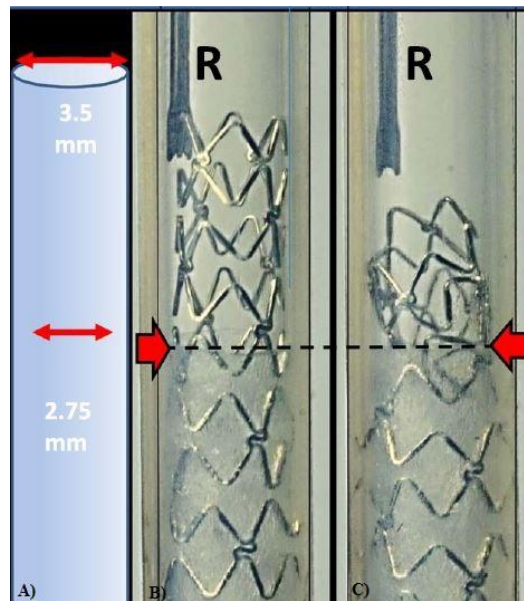


**Figure 3.23: The test apparatus set up to determine the longitudinal strength of a stent. A) A polytetrafluoroethylene (PTFE) tube with 2.75mm inner diameter placed inside a silicone tube with 3.5mm inner diameter. B) The stent is deployed and the distal portion secured the distal portion within the PTFE tube with 5mm of the proximal portion exposed in the silicone tube. Subsequently, a rod (R) connected to an Instron testing machine compress the sample. C) The rod (R) is removed after compressing the stent. (Ormiston et al. 2014).**

The proximal hoop portion where the force was applied maximally compressed and caused side overlapping and obstruction of the stent lumen. Thereby the opposite side of the stent was lifted off the tube and caused further malposition and lumen obstruction. The compression distance demonstrated that the Biomatrix Flex design required the highest load to compress while the Omega design required the least pressure and the rest of designs were similar to each other. Therefore, the longitudinal deformation is dependent on stent design, and increased distortion within a stent would result in a more significant obstruction in the lumen (see Figure 3.24).

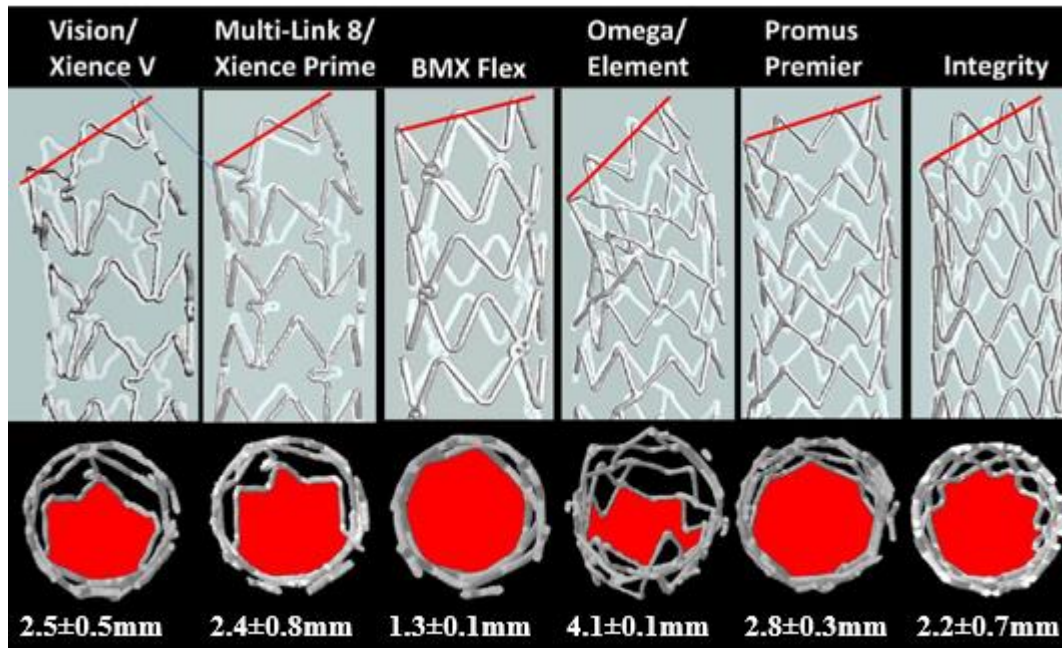


**Figure 3.24: Proximal deformation after 0.5N compression force on six different coronary stent design. Microcomputed tomography images were taken to illustrate the inflow hoop angle (red line). The bottom is the proximal view of stent lumen (red area), beneath it the mean and standard deviation (SD) compressed distance of each design (Ormiston et al. 2014)**

A further study by Ormiston et al. (2015) examined the durability and time to fracture of coronary stents. Fifteen 3mm diameter samples of six different designs were tested; Multi-Link Vision (Abbott Vascular, Belgium), Multi-Link 8 (Abbott), BioMatrix Flex (Biosensors Europe SA, Switzerland), Integrity (Medtronic, CA), Omega/Element (Boston Scientific, USA), and Promus Premier (Boston Scientific, USA) (similar to the longitudinal strength testing conducted by Ormiston et al. 2014). Accelerated bend fatigue testing apparatus was used to compare the durability of the stent designs. Each stent was deployed and mounted on a vertical mandrel where one end was fixed and the other end was subjected to  $\pm 3.5$ mm movement along the horizontal axis at 6Hz frequency (six cycles per second) which resulted in a bending angle of  $13^\circ$  (see Figure 3.25).

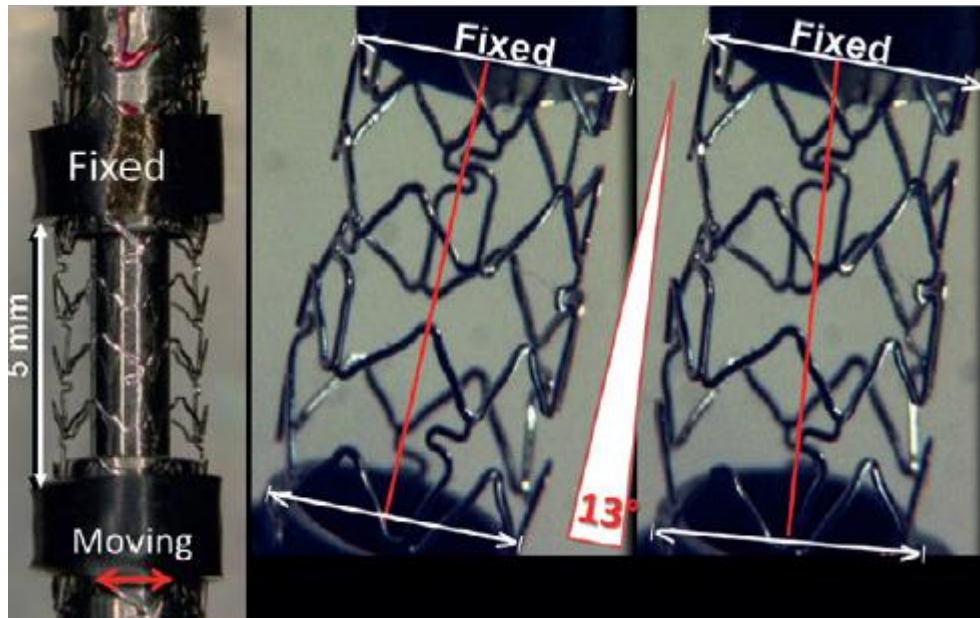


**Figure 3.25: The testing instrument Bose ELF 3220 (Bose Corporation, Eden Prairie, MN, USA) to evaluate the durability of a coronary stent. (Ormiston et al. 2015).**

The samples were repeatedly translocated for up to ten million cycles. Periodically, microscopic inspection was performed to detect any strut fracture, and once a fracture was observed in a specimen, it was removed from the apparatus. Unlike the longitudinal experiment where the BioMatrix stent had higher strength, in the bend testing strut fracture occurred more rapidly than the other designs, at  $38,904 \pm 13,160$  cycles, while fractures in the Vision and the Multi-Link 8 designs were observed after a significantly higher number of cycles at  $288,411 \pm 193,391$  and  $314,475 \pm 239,869$ , respectively. The Omega (Element), Integrity, and Promus Premier had no fracture up to 10 million cycles, but there were 27 fractures in the BioMatrix samples, 19 fractures in the Vision and 16 fractures in the Multi-Link 8. Almost all of the fractures were observed in the curvature of connectors which agrees with computer modelling studies (Li et al. 2010, Barrera et al. 2014, mentioned in section 3.2 ), and interestingly, these bends in connectors are designed to increase the flexibility but evidently these can be areas of stress concentration and compromise the fatigue performance. (Ormiston et al. 2015)

The material properties of stents obviously has a substantial impact on the fracture resistance, particularly as the new stent alloys (e.g. Co-Cr and Pt-Cr) are less susceptible

to fatigue and fracture, however Müller-Hülsbeck et al. (2010) believed that the stent design has the most critical role in this concept. Consequently, Ormiston et al. (2015) suggested that stents with fewer connectors are more flexible and have a higher resistance to fracture, but conversely, fewer connectors would result in less longitudinal strength. However, in the Ormiston et al. (2015) study, the BioMatrix stent was the most vulnerable sample to fracture which has only two connectors (the least required), and in the longitudinal strength evaluation experiment (Ormiston et al. 2014) the BioMatrix had greatest resistance.

Over-expansion is mentioned as another drawback which might increase fracture risk in a stent (Aoki et al. 2007 mentioned in Section 3.1). Unfortunately, sometimes clinically it is unavoidable due to different diameters of the vessel and the stent especially in bifurcation and long stenting, where sometimes the proximal segment of the stent needs to be over-dilated. An *in vitro* study was performed by Ng et al. (2016) to investigate the effect of over-expansion on the stent structure for six different coronary stent designs including Synergy (Boston Scientific, USA), Xience Xpedition (Abbott Vascular, USA), Ultimaster (Terumo Corporation, Japan), Orsiro (BIOTRONIK AG, Germany), Resolute Onyx (Medtronic, USA), and Biomatrix Alpha (Biosensors Interventional Technologies, Singapore). All samples were deployed at nominal pressure (NP) and then post dilation was performed on the proximal portion of each sample. Although, all specimens were able to expand over (by an average 56%) their nominal diameter uniformly, it was found to result in strut distortion and large cell enlargement, which implies that the failure risks such as recoil and restenosis (Berrocal et al. 2008) would be increased (see Figure 3.26).

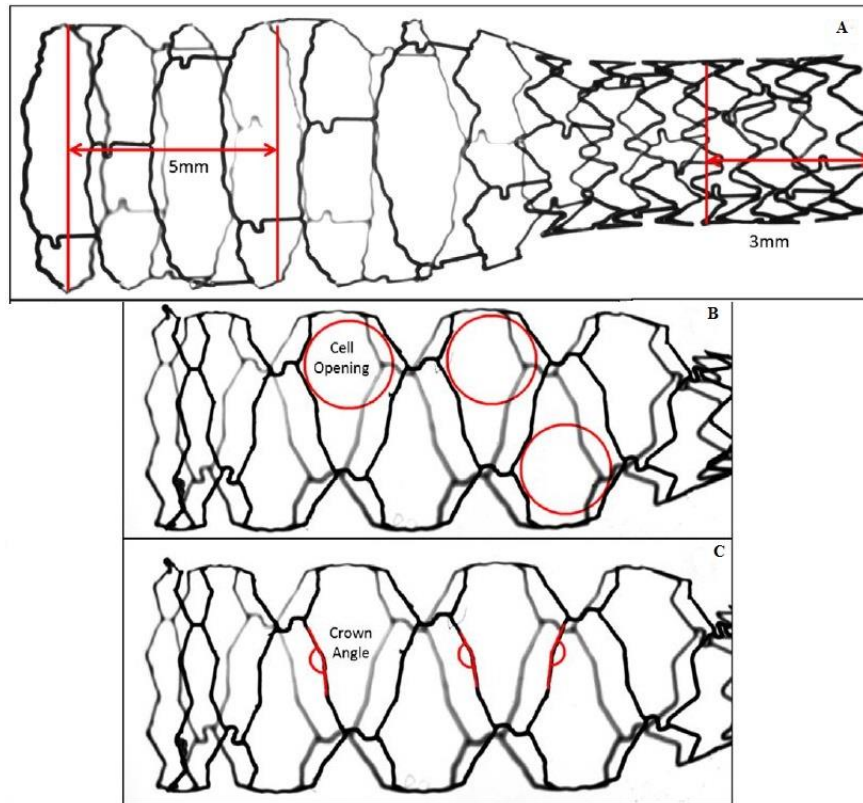


**Figure 3.26: Over expansion of a stent. A) Side view of distal segment of stent at nominal pressure, and oversized at the proximal segment. B) Large cell enlargement, and C) struts straightened at crown connector by an average of  $77 \pm 8^\circ$  at NP placement to  $146 \pm 15^\circ$  after over expansion (Ng et al. 2016).**

According to the previous studies (Ormiston et al. 2000; Szabadits et al. 2008; Ormiston et al. 2015) alterations in stent design, connectors, and strut thickness, as well as other factors, impact on the mechanical behaviour of stents. Therefore, although straightening of struts increases radial strength of stent, it also increases stiffness of the stent, which can reduce the stability, and lead to mechanical fatigue and strut fracture (Ng et al. 2016).

Coronary stents have been continually improved over recent years, and advanced technology allows manufacturers to design and produce stents in a smaller size with higher endurance making it more feasible to access narrow and tortuous vessels. Murphy et al. (2003) conducted a mechanical testing study to investigate the relationship between stent strut size and its effect on stress/strain in 316L stainless steel. Series of experiments were performed by laser cutting the specimens from 1.75mm diameter tube, a constant

thickness of  $85\mu\text{m}$ , and varies width 60, 80, 100, 150, 300, and  $500\mu\text{m}$  in order to examine the dependence of 316L stainless steel stress/strain on stent strut size (see Figure 3.27).

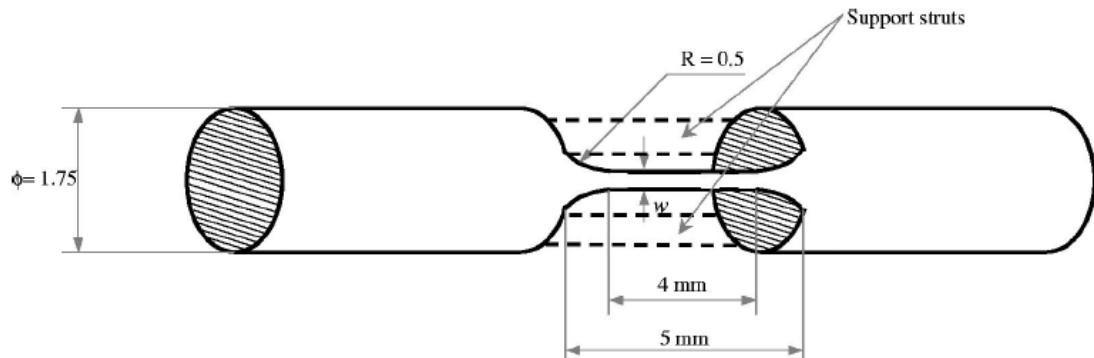


**Figure 3.27: Specimen dimensions where  $w$  is the strut size. All samples have 4mm gauge length and three struts which two of them were to support the specimen and avoid any damage prior to the test. Once the example was placed in the testing rig, the supporting struts were snipped. (Murphy et al. 2003).**

The test rig was designed to grip the specimen tube vertically by clamping with V shape notch from both sides (see Figure 3.28). The tensile testing results illustrate that stress/strain in 316L stainless steel is not constant for varies the size and it depends on the size of the sample at such a micro scale, therefore to describe stress/strain behaviour in 316L stainless steel, the size of component must be included. Murphy et al. (2003) determined the risk of failure in a smaller size is higher than thicker struts under the tensile test. Moreover, it could be said that some segment of stent might experience local failure especially during dilation where the stent undergoes plastic deformation.

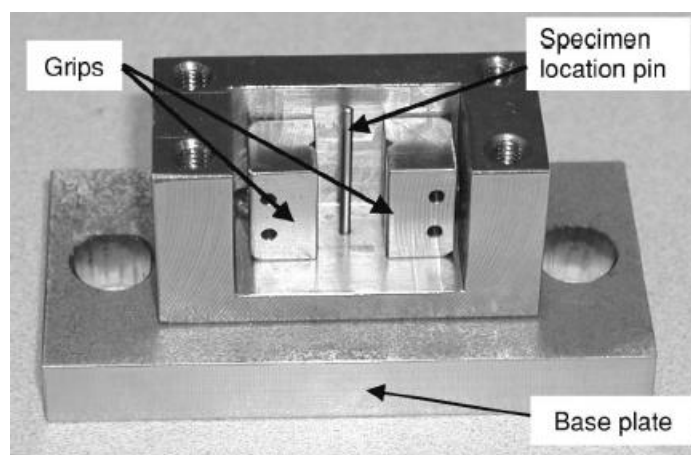


**Figure 3.28: The lower part of test rig without a specimen. The sample tube is located over the pin bar, and then upper grip part is lowered on top of the sample. (Murphy et al. 2003).**

In general, the desirable features of coronary stent include several factors such as adequate strength to keep the coronary artery open and control plaque prolapse, while providing an acceptable level of flexibility and conformability (ability of the expanded stent to bend to artery geometry). However, the clinician should be responsible to choose the right type of stent to use regarding to level of artery disease (e.g. soft, calcified lesion).

### **3.4. Summary**

Despite all the improvement in the new generation of DES, SF is still known to occur. Several factors have been reported which are associated with an increase in SF incidence including, RCA, total stent length, artery tortuosity, overlapping stents, stent design, hinge motion, and calcification all of which can cause a substantial mechanical force and then increasing risk of metal fatigue. However, despite SF being a rare phenomenon (0.84% to 18.6%) (Yang et al. 2017), still it could lead to serious clinical complications such as: ISR, thrombosis, TLR, and myocardial infarction, thereby intensifying MACE and the risk of morbidity and mortality.

In the literature, to investigate the factors related to SF, a number of studies and experiments have been performed through computer modelling and mechanical testing. As stents are subjected to a repetitive cardiac cycle, computer analyses have illustrated that it is a risk of metal fatigue. Besides, implementation longer stent in an angulated, calcified and complex lesion, is facing higher amount of stress particularly at curvature of strut connectors.

Mechanical bench testing was performed in order to test various aspect of coronary stent such as strut thickness, over expansion, bending test, material and design, longitudinal strength, overlapping, flexibility and delivery through tortoise artery. Moreover, these experiments validated the finding of clinical and FE studies. It confirms that stent design

has a fundamental role in flexibility. Also thinner strut seems to have lower resistance to fatigue failure and fracture due to bending, whereas thicker struts provides less flexibility. Nonetheless, using advance technology and novel alloys helps to design and produce the most reliable coronary stents with thinner struts.

However, none of the studies have evaluated in detail the hinge-type loading, and also the effect of vessel angulation on the stresses in a coronary stent. Clearly, it is important to determine the risk of SF in such a critical conditions as they are reported as susceptible factors in clinical studies. Thus, investigation exploring the effect of vessel geometry on stent stress which could lead to stent fatigue is clearly necessary. This will be informative for clinicians, indicating what degree of angulation in coronary arteries can create greater hinge-type loading under cardiac cycle movement. Moreover, it illustrates that these circumstances need to be considered more seriously when engineers are designing coronary stents.

This current study will address these issues, hence increasing the understanding of the mechanism of stent fracture in tortuous vessels by a combination of computer modelling (see Chapter 4) and mechanical testing (see Chapter 5).

# **4. Idealised Modelling of a Stent in an Angulated Coronary Artery**

## **4.1. Introduction**

Clinical studies have demonstrated that while implantation of coronary artery stents can be an effective process to treat arteriosclerotic disease, in some cases it causes further complications such as ISR, ST, TLR, and other outcomes which may not be easy to predict (Kastrati et al. 2005, Schömig et al. 2007, Simard et al. 2014).

Finite element analysis (FEA) is a numerical technique used to solve problems mostly in engineering and physics for instance structural analysis, solid mechanics, dynamic, biomaterial, electrical analysis, and other engineering products and systems. It is a comprehensive method to design and test a product by simulating the loading conditions in a virtual environment to predict stress distribution. However, the accuracy of the results from any FEA modelling undertaken is highly dependent on the user input, where small changes to loading/constraints or material properties can have a huge impact on the predicted values. It is necessary to create a geometry, define a realistic loading condition and adequate material properties for a simulation. It has been proven that FEA is a powerful technique to evaluating a device performance without requiring multiple experiments, yielding information quickly, in a cost effective, and reliable manner. For example, fatigue stent bench testing can contribute significantly to the understanding of stent behaviour, but it is limited to specific designs, and requires expensive equipment such as micro-CT scan. Nevertheless, FEA should be used in conjunction with some bench testing in order to validate the accuracy of the simulation study.

A review of FE modelling and computational analysis of stenting in coronary arteries was conducted in section 3.1. These studies considered several stent structures at different stages of deployment, as well as various boundary/loading conditions to gain a better

understanding of the mechanical behaviour of stents and the stress/ strain distribution (both in the stent and in the surrounding vessel), which can lead to the development of more effective device designs. In general the results highlighted the potential application of FEA in furthering understanding of the stenting process in coronary arteries. However, these simulation studies did not consider all the factors, which might influence the outcome, in particular the hinge-type movement that stents are subjected to in angulated vessels was not considered, and this is a significant factor in the likelihood of stent fracture (Wu et al. 2007, Morlacchi et al. 2014).

Hence, the main objective of this chapter is to investigate the correlation between the degree of artery angulation and the stress distribution within a stent during the cardiac cycle due to hinge-movement. To date, the hinge type loading has not been represented, while in this, the stress distribution of a generic deployed stent in an angulated vessel is reviewed. To ensure that the study related the stent stress to vessel angulation as opposed to stent design, it was made design-independent by idealising the usually complex stent structure, to a simple thin-walled tube, with a structural modulus that took account of the stent fenestration. The artery and stent were then subjected to a displacement representative of that which would be experienced during the cardiac cycle.

To ensure model accuracy, a preliminary convergence study on a straight section of vessel/stent construct was performed as 3-point bending test to define the sufficient number of elements to have accurate results by monitoring two parameters, deflection and stress and comparing to the theoretical values

## **4.2. Methodology**

A series of 9 idealised finite element models of stent/artery constructs at different angulation were created to investigate the relationship between artery angulation and stent stress. The vessel was represented in the model as an idealised tube with the stent

represented by shell elements on the inner surface of the tube. Two set of boundary conditions were applied in the simulation; first, a segment of artery was constrained where there was no displacement in all degree of freedom (DOF). Likewise, series of displacement load (maximum of 20°) was applied to the artery in order to represent the characteristic hinge movement in angulated arteries during the cardiac cycle. The constraint and loading area were different in each model, to ascertain the most suitable loading conditions for the simulation. Furthermore, various artery angulations were modelled from 30° to 90° and each time the angle was transformed in 10° increments.

#### **4.2.1. Effective Modulus for Idealised Stent**

Since the stent model was idealised and created as a cylinder, the intricate cell patterns were not represented, so the effective modulus was considered instead of the Young's modulus ( $E$ ) of the stent material. In order to determine the effective Young's modulus, an expanded Cypher™ stent (28mm length, 3mm diameter) was  $\mu$ CT scanned using X-Tek HMX160 microCT system (X-Tek, Tring, UK) at the University of Hull. The scan data was exported as a stack of .tiff (tagged Image File Format) image and imported into AVIZO 3D Visualization and Analysis Software (FEI Inc., USA) to generate a 3D image of the stent (see Figure 4.1).

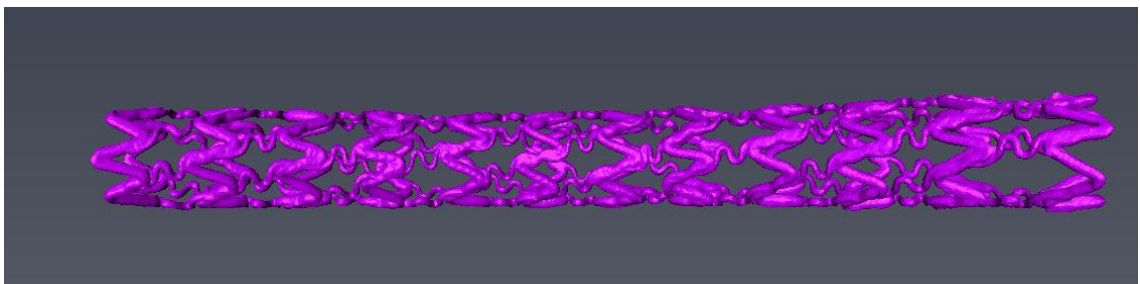


**Figure 4.1: 3D digitised Cypher stent in AVIZO**

The digitised model was converted into a polygon surface model and then meshed with 10-noded volumetric tetrahedrals within AVIZO. To achieve an optimum quality of mesh, the tetrahedral element parameters were adjusted to give a reasonable aspect ratio while

the tetrahedral quality improvements suggested by the software were implemented. Subsequently, the meshed model was imported into ANSYS (ANSYS Inc., Canonsburg, PA, USA) where 4-noded solid elements (SOLID 92) were used with material properties relates to stainless steel,  $E= 196\text{MPa}$ , and  $\nu= 0.3$  (Mortier et al. 2009) chosen to represent the 3D stent model (see Figure 4.2).

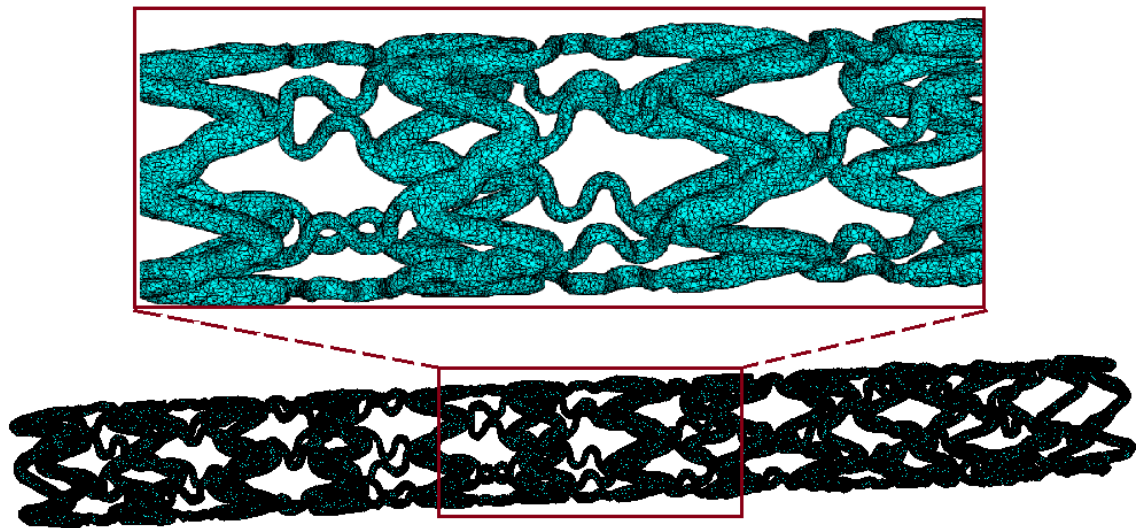


**Figure 4.2: The FE model of the Cypher (Cordis Corporation, USA) stent, 3mm ID and 28mm length.**

A bending test was modelled on both the idealised and the actual stent model, where the von-Mises and maximum deflection were compared, in order to determine an appropriate effective modulus to use for the idealised stent model (see

Table 4.1 ). The idealised stent was created as a thin wall cylinder using 8-node SHELL 281; 3mm ID, 0.2mm wall thickness (strut thickness of Cypher was measured  $\sim 150\text{-}200\ \mu\text{m}$ ), 28mm length same as Cypher stent. All the nodes at one end of the FE model of the Cypher stent as well as the idealised stent model were constrained in all degrees of freedom (DOF), and an equal force was applied to one node in y-direction at the other end of the both models. This trial was continued with numbers of Young's modulus ( $E$ ) for the idealised model until the maximum deflection and von-Mises stress in the both models were matched.

Properties of the Cypher stent		Properties of FE stent model	
Young's modulus ( $E$ )	196GPa	Effective modulus	250MPa
Strut thickness	0.15/0.2 mm	Strut thickness	0.2 mm
Poisson's ratio ( $\nu$ )	0.3	Poisson's ration ( $\nu$ )	0.3

**Table 4.1: Stent properties base on the Cypher stent (Mortier et al. 2009), and the effective modulus of idealised stent model**

### 4.2.2. Validation & Convergence Study

To ensure validity and convergence, the FEA simulation was first carried out by examining stress distribution and deflection within straight models of artery and stent using ANSYS (ANSYS Inc., Canonsburg, PA, USA) program (the full study is available in Appendix I). This was achieved through a 3-point bending test on artery and stent models individually to ensure that each of the models were behaving in the expected way (see Figure 4.3). Moreover, to assess the accuracy of the bending test and enhance its credibility, the results was compared to theoretical value (see Appendix I).

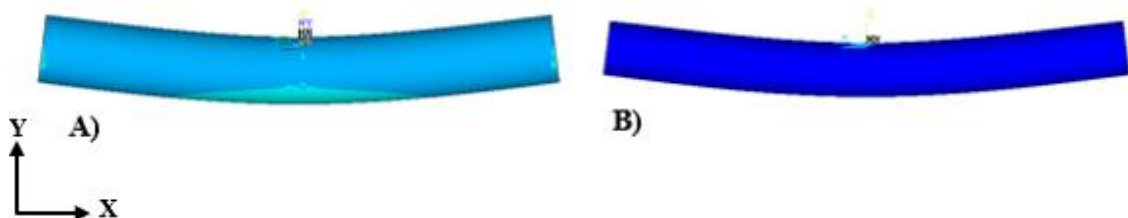


**Figure 4.3: Deformation of A) artery and B) stent models when both ends of the models were constrained in all DOF, and a force was applied in y-direction (negative) to a node in the middle of each model.**

Moreover, a convergence study was conducted to define the optimum number of elements for the both artery and stent model to predict an accurate mechanical response. A total of 12 meshes were analysed (see Appendix I), in the range ~3,700 to ~105,000 elements for the artery (see Figure 4.4 A), and between ~400 and ~19,000 elements for the stent model (see Figure 4.4 B).

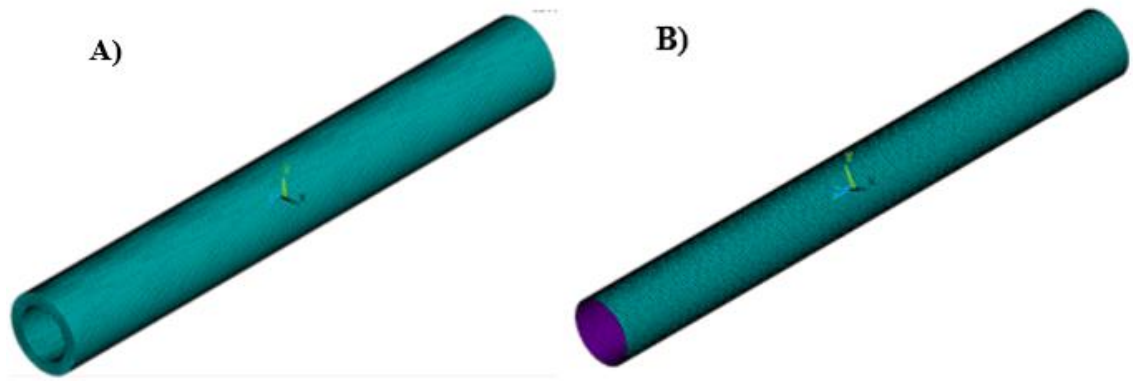


**Figure 4.4: Mesh model of A) artery, B) stent**

Two parameters the maximum stress and displacement were compared when identical loading was applied during the bending test. The results dictated that the artery model should have at least 62,500 number of elements, while for the stent model due to its volume and elements type the convergence was achieved with much less elements number ~5,500 (see Appendix I).

### **4.2.3. Stenting in Angulated Artery**

A series of FE models were constructed using ANSYS, to represent stents deployed in vessels of varying angulations. The model was simplified by idealising both the artery and the stent to be hollow cylinders. A cylinder represented the artery with a bend in the middle along its half way length. Moreover, to create the stent model inside the artery, it was assumed that the stent was deployed into the vessel and has direct contact with inside the lumen of artery (ignoring any plaque or calcification).

The parameters length, inner radius, and wall thickness, were set as 33mm, 1.5mm, and 0.7mm respectively (Holzapfel et al. 2005), with adjustable angulation at the middle of the artery model (see Figure 4.5). Models were created with a bending angle range between 30° and 90°, in 10° stages. 10-node SOLID 187 elements were selected for the artery and initially defined it as a linear elastic tube, however, later the artery also was run as a hyper elastic non-linear material.

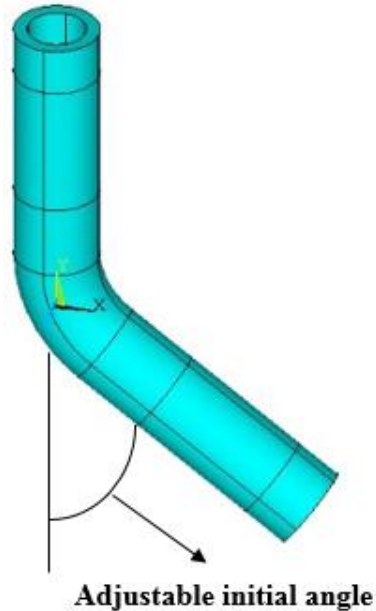


**Figure 4.5: Artery model at initial angle (30°) at its mid-length. The angle can be adjusted up to 90°, and undergo a displacement loading to represent cardiac loading.**

Many studies have been conducted to determine the mechanical behaviour and properties of arteries, and most of them concluded it acts as a non-linear hyper-elastic material like most other biological tissues (Holzapfel et al. 2005). Nevertheless, in this study both linear and non-linear material were considered in order to identify any significant difference in their outcome with respect to the stent stresses. The artery was simulated as linear isotropic based on the work of Chua et al. (2004), and non-linear hyper-elastic model following Mooney Rivlin theory (Lally et al. 2003) (see Table 4.2).

<b>Coronary artery</b>	<b><math>E</math> (Pa)</b>	<b>Poisson's ratio (<math>\nu</math>)</b>	<b>C10 (Pa)</b>	<b>C01 (Pa)</b>	<b>C20 (Pa)</b>	<b>C11 (Pa)</b>	<b>C02 (Pa)</b>
Linear	1.75e06	0.499	-	-	-	-	-
Non-linear	-	0.45	18900	2750	590420	857180	0

**Table 4.2: Material property for the artery model, linear and non-linear model**

The stent was modelled based on the Cypher™ (Cordis Corporation) stent, 28mm longitudinal length, 3mm inner diameter, and 0.2mm wall thickness. The stent was situated such that the artery was 2.5mm longer than the stent each end, with direct contact between inner surface of artery and the outer surface of stent (perfect connection was

assumed). The stent was created by the inner areas of the artery being cladded with element type 8-node SHELL 281, and attributed the effective modulus of 250MPa, and  $\nu= 0.3$ .

However, the stent validation model illustrated that around 5450 elements were required for the model, but in the actual model the stent could not be meshed independently because it was cladded to the inner surface of the artery model, thus the mesh was dependent on and controlled by the artery mesh size. The artery model was meshed with 77,643 elements with 6,118 elements inner surface elements that were clad with shell elements, hence exceeding the required element number, ensuring accuracy of results. The Figure 4.6 shows the completed model at initial angle ( $30^\circ$ ), with A) the idealised mesh stent in isolation, and B) the full construct of the model, with the idealised stent within the artery model with a total of 83,761 elements.

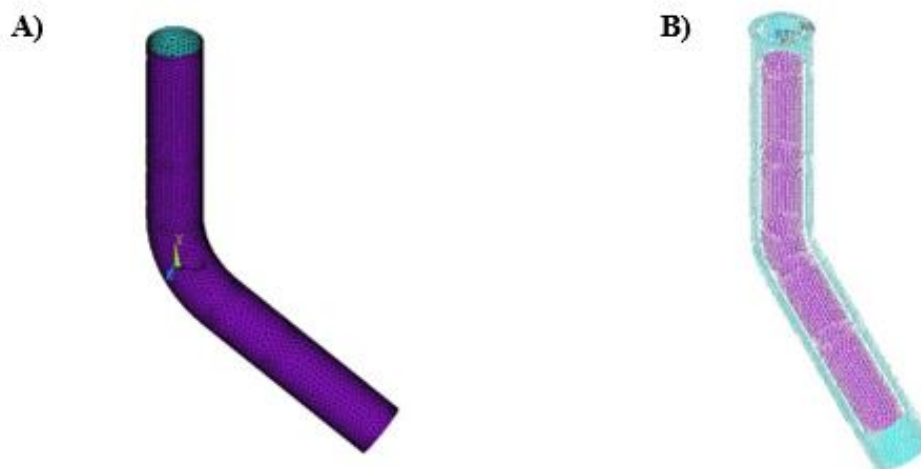


**Figure 4.6: A completed idealised FE model at initial angle of  $30^\circ$ . A) Idealised meshed stent comprising shell elements, and B) full model of idealised stent (purple area) within the artery model (blue area).**

The optimum boundary conditions were ascertained by conducting sensitivity studies as described in Section 4.2.4 and Section 4.2.5. The hinge-type motion undergone during the cardiac cycle was represented in a number of ways by varying the loading and constraints. Two set of loading conditions were considered in the simulation as the

boundary conditions. In some models, nodes at one end of the artery model were fixed and a displacement was applied to the nodes at other end. Furthermore in some other models displacement was applied to nodes at both ends of the artery model and middle segment was constraints. The displacements applied initially totalled between 5° and 20°, increasing in 5° increments, and the application of constraints was varied for all models in the linear and non-linear artery models. It is important to note that although the total displacement was same throughout each simulation, in some models total displacement was applied to one end of the artery and in some models the total displacement was equally shared when applied to both ends of the artery, where they were subjected to an identical displacement. Moreover, in order to determine and compare the effect of artery angulation on the stent stress, different bending angles were modelled from 30° to 90° and each time the angle was transformed in 10°.

#### **4.2.4. Stent in Linear Artery**

Initially, the artery was defined as with linear isotropic material properties, and 9 models (Model I to IX) were explored, with varying loading and constraint conditions. The initial angle varied between 30° and 90° (in 10° stages), with an applied total displacement of either 5°, 10°, 15°, or 20° to represent the cardiac cycle. The areas constrained varied with each model as described below.

- **Model I**

The first loading condition is shown in Figure 4.7. All exterior nodes of the artery in the lower part of the model (13mm) were constrained in all directions (yellow part of Figure 4.7), and the displacement ranged from 5° to 20° applied in the x-direction to the exterior nodes covering half the circumference of the artery for 9.5 mm from the top (as shown in light blue in Figure 4.7).

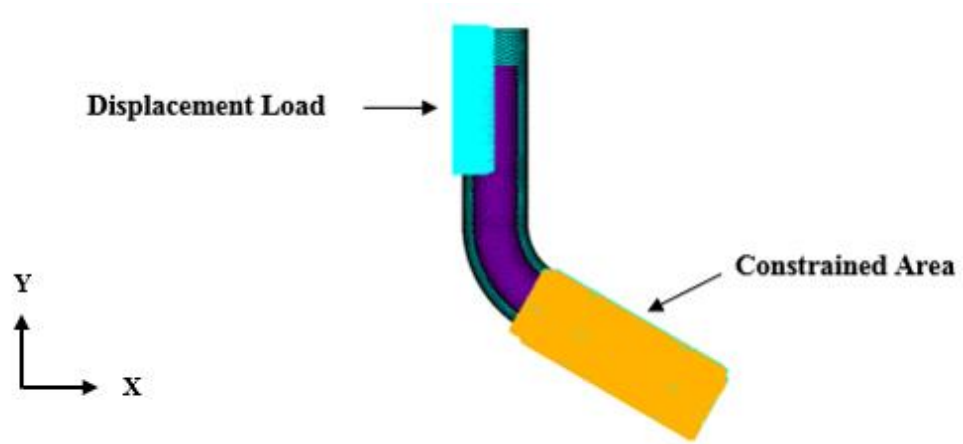


**Figure 4.7: Model I; artery modelled with linear isotropic material properties. Displacement load between  $5^\circ$  and  $20^\circ$  was applied in the x-direction to nodes at the top end of the artery for 9.5mm (blue part), and the lower end of the artery was constrained in all DOF for 13mm (yellow part).**

○ **Model II**

The second model had similar boundary conditions to the first, but the constrained area and the displacement was limited to the segment of the artery which housed the stent (see Figure 4.8). The displacement and constraint was 10.5mm from top and bottom of the stent model, respectively.

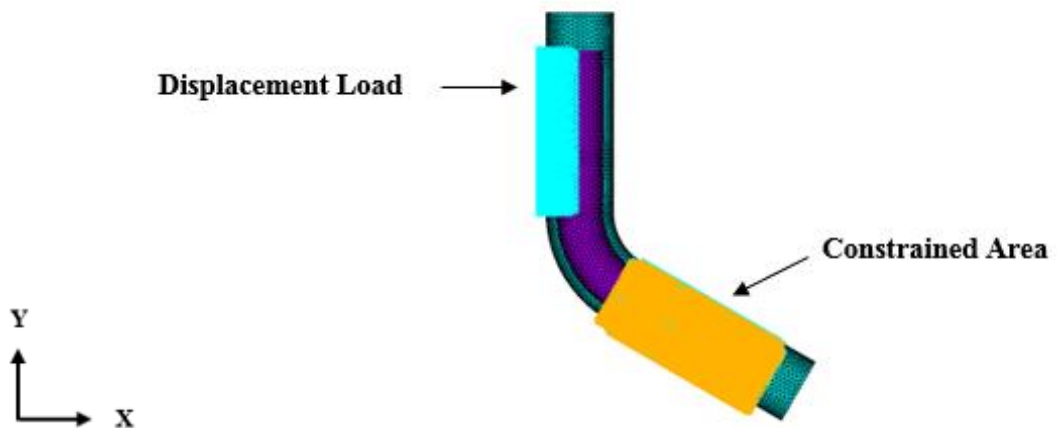


**Figure 4.8: Model II; artery modelled with linear isotropic material properties. Displacement load and constrained area were limited to the segment of artery which housed the stent. Displacement between  $5^\circ$  and  $20^\circ$  was applied in the x-direction to the artery nodes for 10.5mm (blue part), and the lower end of the artery was constrained in all DOF for 10.5mm (yellow part).**

- **Model III**

In the third FE model, the displacement load was same as the first one applied to the half circumference of the outer surface of artery at the top along to the bending area for 9.5mm, and the constrained area was same as model II, was applied to the lower part of the artery which housed the stent (see Figure 4.9).

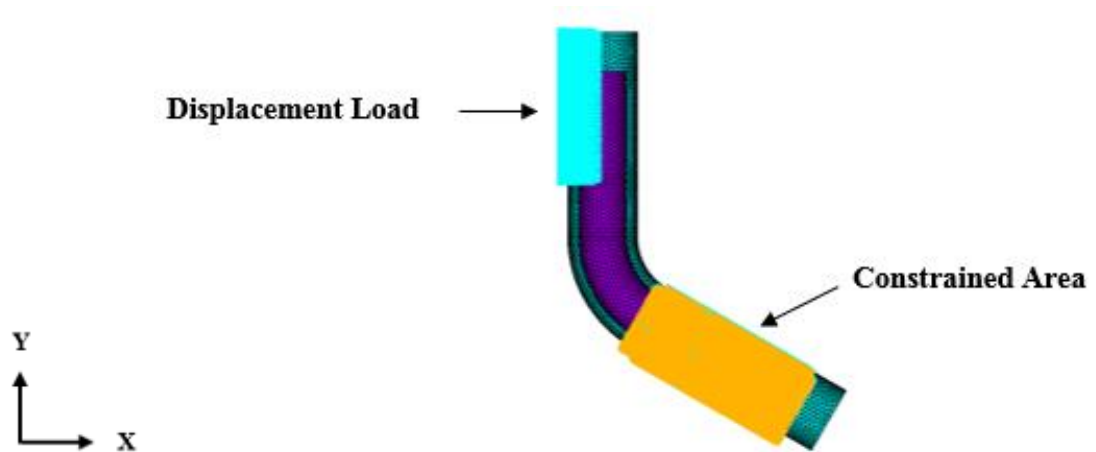


**Figure 4.9: Model III; artery modelled with linear isotropic material properties. Displacement load between 5° and 20° was applied in the x-direction to nodes at the top end of the artery for 9.5mm (blue part), and the lower end of the artery which housed the stent was constrained in all DOF for 10.5mm (yellow part).**

- **Model IV**

In the fourth model the displacement was applied to the top part of the artery which corresponded to a length of 2.5mm of artery without stent, and 7mm with the stent enclosed within the artery. The constrained area was reduced to only 7mm of the lower section artery which enclosed the stent (see Figure 4.10).

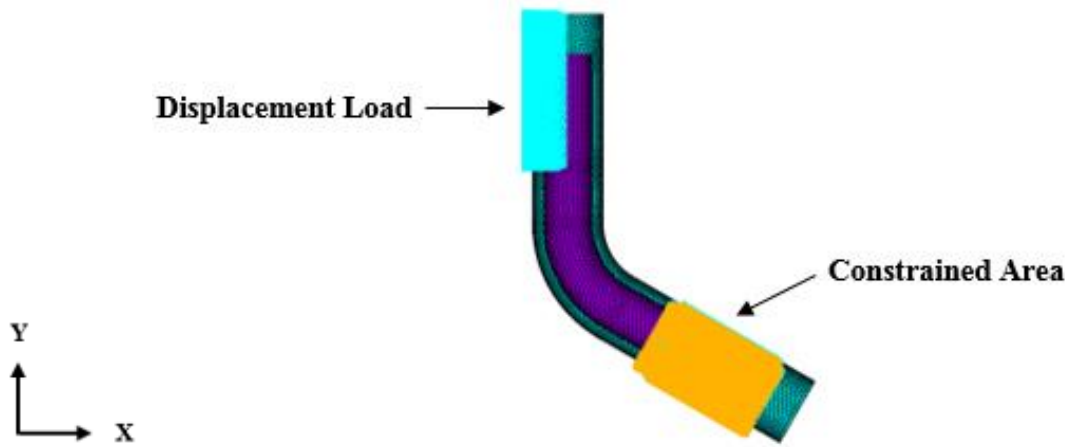


**Figure 4.10: Model IV; artery modelled with linear isotropic material properties. Displacement load between  $5^\circ$  and  $20^\circ$  was applied in the x-direction to nodes at the top end of the artery for 9.5mm (blue part), and the lower end of the artery which housed the stent was constrained in all DOF for 7mm (yellow part).**

- **Model V**

The displacement applied in the next five simulation models (V to IX) was identically applied to the same segments, but different parts were selected for the constraints. These boundary conditions were in replication of the motion of the test rig and *in vitro* experiment, which will be elaborated on in Section 5.

Two equal displacement loads were applied, one to the distal and one to the proximal portion. The exterior nodes covering half the circumference of the artery for 9.5 mm from the top and bottom of the artery were subjected to identical  $2.5^\circ$ ,  $5^\circ$ ,  $7.5^\circ$ , and  $10^\circ$  displacement in order to give the total displacement range between  $5^\circ$  and  $20^\circ$  (as shown in blue in Figure 4.11). The displacement in top part of the artery was only in the x-direction, while in the lower part of the artery displacement was replicated in both y and x direction. The constrained part was located in the middle section area (bending point) where all exterior nodes of the artery were constrained in all DOF (yellow part of Figure 4.11),

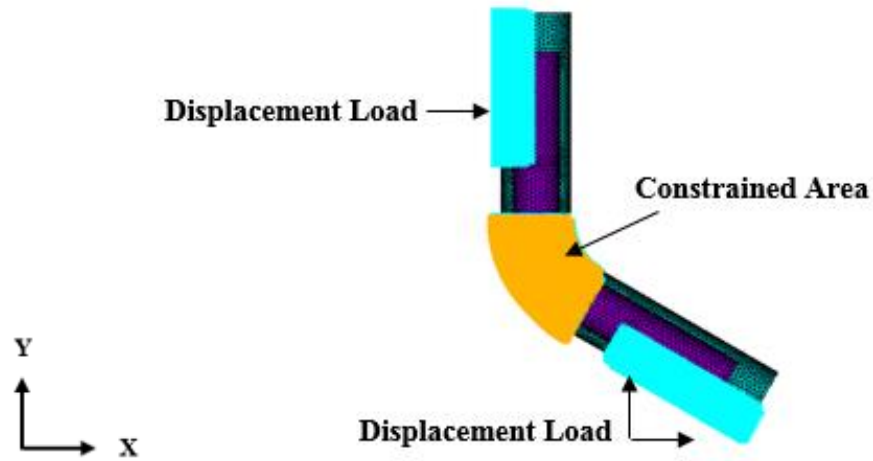


Figure 4.11: Model V; artery modelled with linear isotropic material properties. Two identical displacement load were applied to both ends of the artery on all nodes on the half outer surface of the artery for 9.5mm (blue part), where in the top section it is in the x-direction and in the bottom section it is in both y and x direction. All exterior nodes in the middle segment of the artery were constrained in all DOF (yellow part).

○ Model VI

The displacement load was similar to the type (V), but constrained area was decreased to only one node was constrained in all DOF in the outer surface of artery at the back of bending region (see Figure 4.12), which allowed the artery more degrees of freedom.

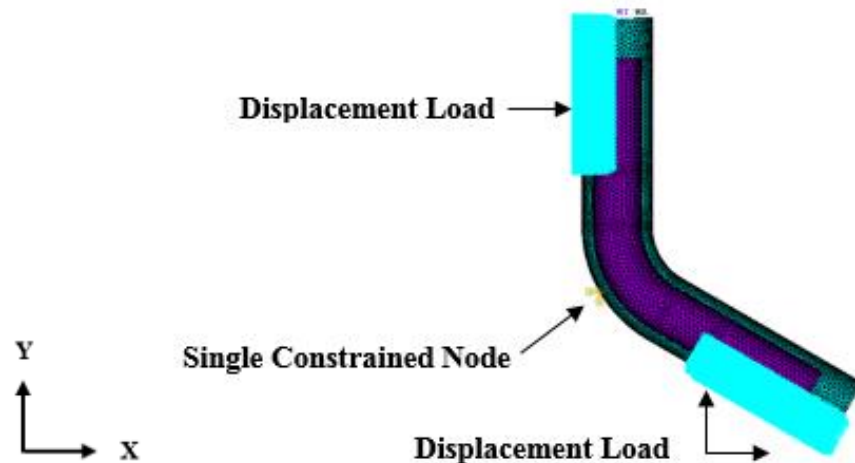
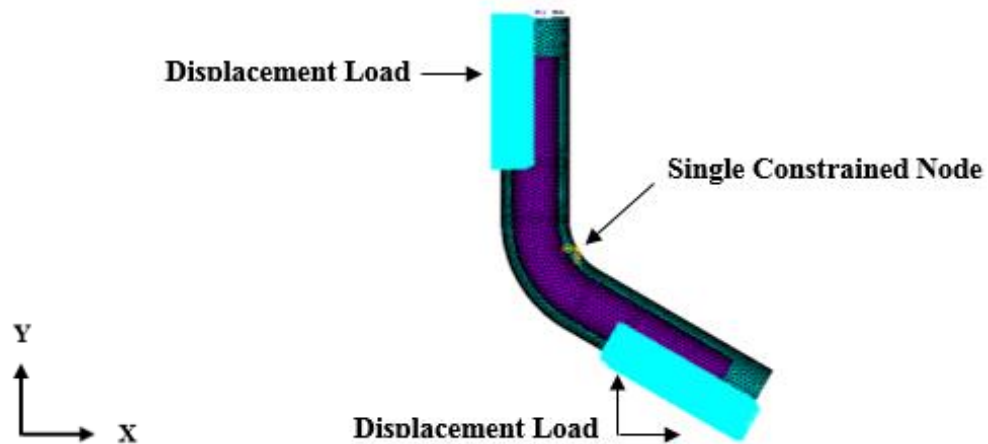


Figure 4.12: Model VI; artery modelled with linear isotropic material properties. Two identical displacement load were applied to both ends of the artery on all nodes on the half outer surface of the artery for 9.5mm (blue part), where in the top section it is in the x-direction and in the bottom section it is in both y and x direction. One exterior node in the outer surface of artery at the back of bending region was constrained in all DOF.

- Model VII

One node on the surface of artery at the inner angle of bending region was constrained in all DOF (see Figure 4.13).



**Figure 4.13: Model VII; artery modelled with linear isotropic material properties. Two identical displacement load were applied to both ends of the artery on all nodes on the half outer surface of the artery for 9.5mm (blue part), where in the top section it is in the x-direction and in the bottom section it is in both y and x direction. One node in the inner surface of artery at the bending region was constrained in all DOF.**

- Model VIII

In the eighth model, the constraint conditions of model VI and VII combined were applied, where the two nodes at back and front of bending angle of the model were selected to be constrained in all DOF (see Figure 4.14).

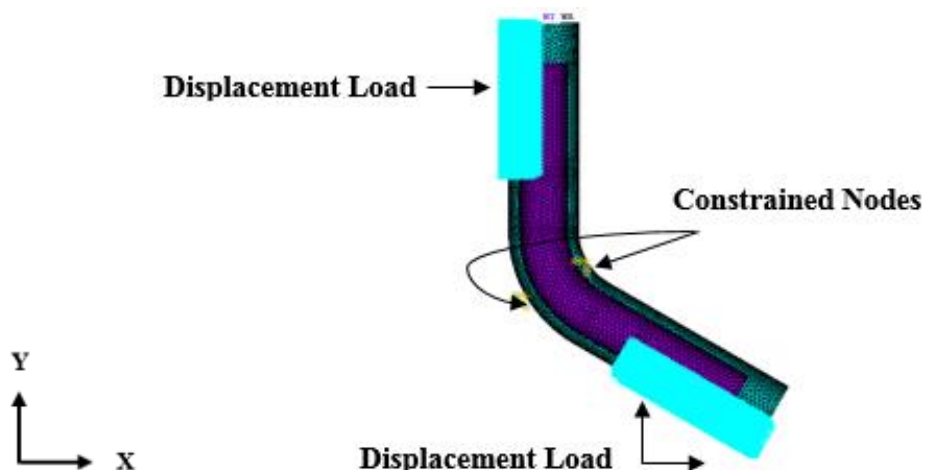


**Figure 4.14: Model VIII; artery modelled with linear isotropic material properties. Two identical displacement load were applied to both ends of the artery on all nodes on the half outer surface of the artery for 9.5mm (blue part), where in the top section it is in the x-direction and in the bottom section it is in both y and x direction. Two nodes in the inner and outer surface of artery at the bending region were constrained in all DOF.**

- **Model IX**

In the last FE model, three nodes were constrained in all DOF, one on the back and one on each side of the artery model (see Figure 4.15)

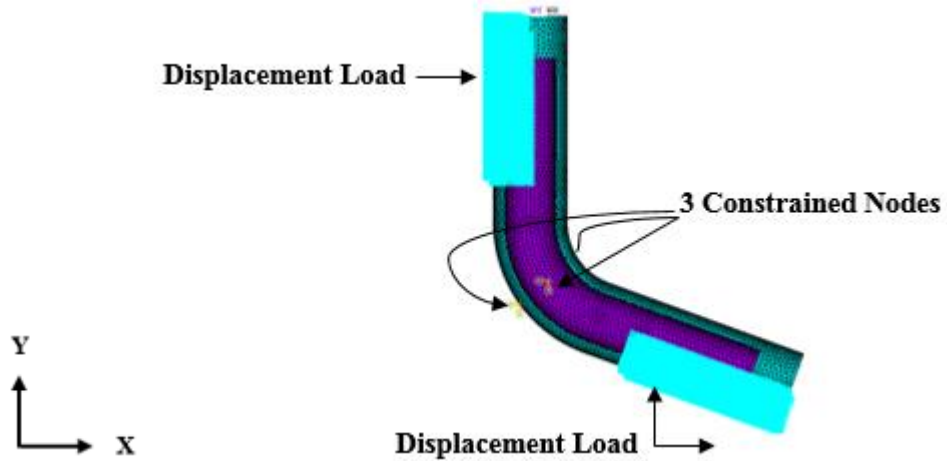


**Figure 4.15: Model IX; artery modelled with linear isotropic material properties. Two identical displacement load were applied to both ends of the artery on all nodes on the half outer surface of the artery for 9.5mm (blue part), where in the top section it is in the x-direction and in the bottom section it is in both y and x direction. Three nodes in the inner and both sides of artery surface at the bending region were constrained in all DOF.**

## **4.2.5. Stent in Non-Linear Artery**

Based on the linear models result and *in-vitro* experiment, the non-linear simulation was run for the model VI to IX (see Figure 4.16). Therefore, the boundary conditions and geometry of the models remained the same, but the material properties of the artery was changed to represent hyper-elastic material behaviour, as described in Section 4.2.3.

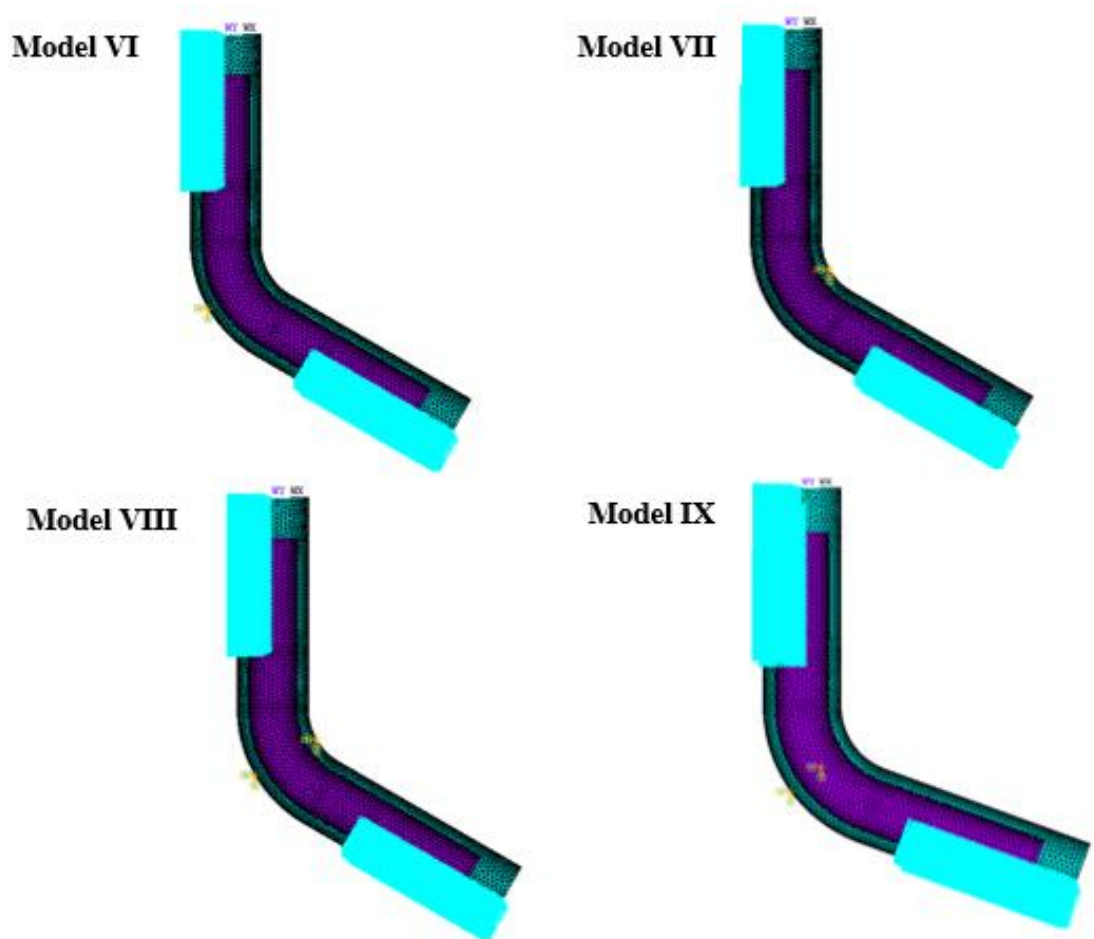


**Figure 4.16: Models VI to IX simulated angulate artery with non-linear material property for the artery.**

### **4.3. Results**

Stent tensile, compressive, and von-Mises stress distribution were obtained for each model with different boundary conditions. Two parameters, stresses at the same point (in high stress region) and maximum deflection were considered for all reconstructed models. These results were recorded for the stent model only, not the artery, when the idealised models with various initial vessel angulation between 30° and 90° were subjected to 5° to 20° displacement load (the results for displacement loads of 5°, 10°, and 15° is available in Appendix II). The aim of this study was to simulate (idealised) stenting in an angulated artery under cardiac cycle movement in order to determine the effect of vessel angulation on stress within the deployed stent. Moreover, the study was performed as linear isotropic

and non-linear hyper elastic material properties for the artery model to investigate if it has a significant effect on the results.

### **4.3.1. Stent Results in Linear Artery**

Firstly, stress distribution within the idealised stent model was observed for all models with 70° bending angle at the middle length after applying total 20° displacement load. Isolating the stent from the artery, Figure 4.17 represents 1<sup>st</sup> and 3<sup>rd</sup> principal (tensile & compressive) stresses, and von-Mises stress and stent deflection are illustrated in Figure 4.18. These figures indicate the region of the stent which would experience high stresses during the cardiac cycle in an angulated vessel.

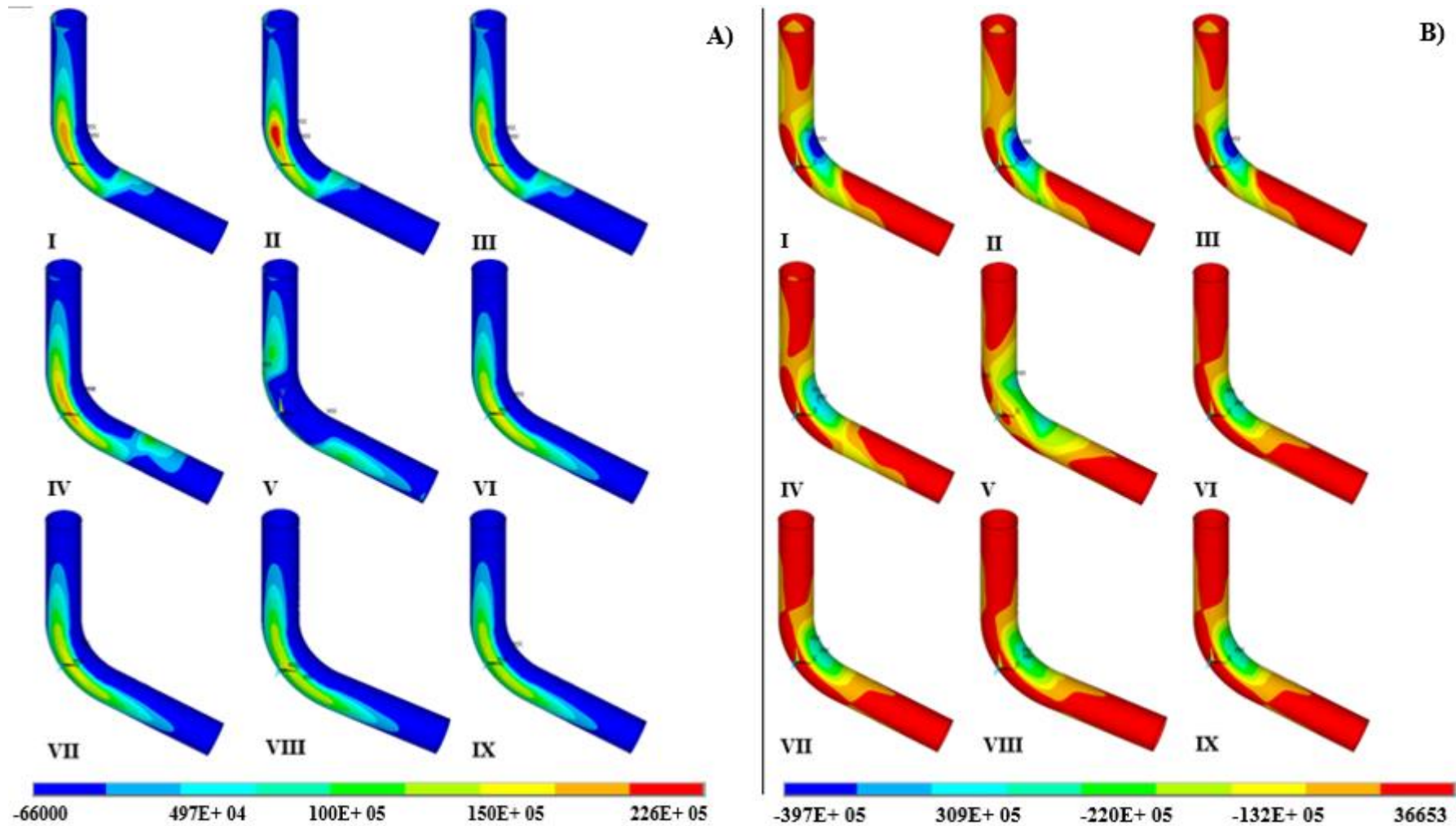


Figure 4.17: Stress distribution within idealised stent model at an initial angulation of  $70^\circ$ . A total of  $20^\circ$  displacement load was exerted to the linear models artery I to IX. A) 1<sup>st</sup> principal (tensile) stress, B) 3<sup>rd</sup> principal (compressive) stress.

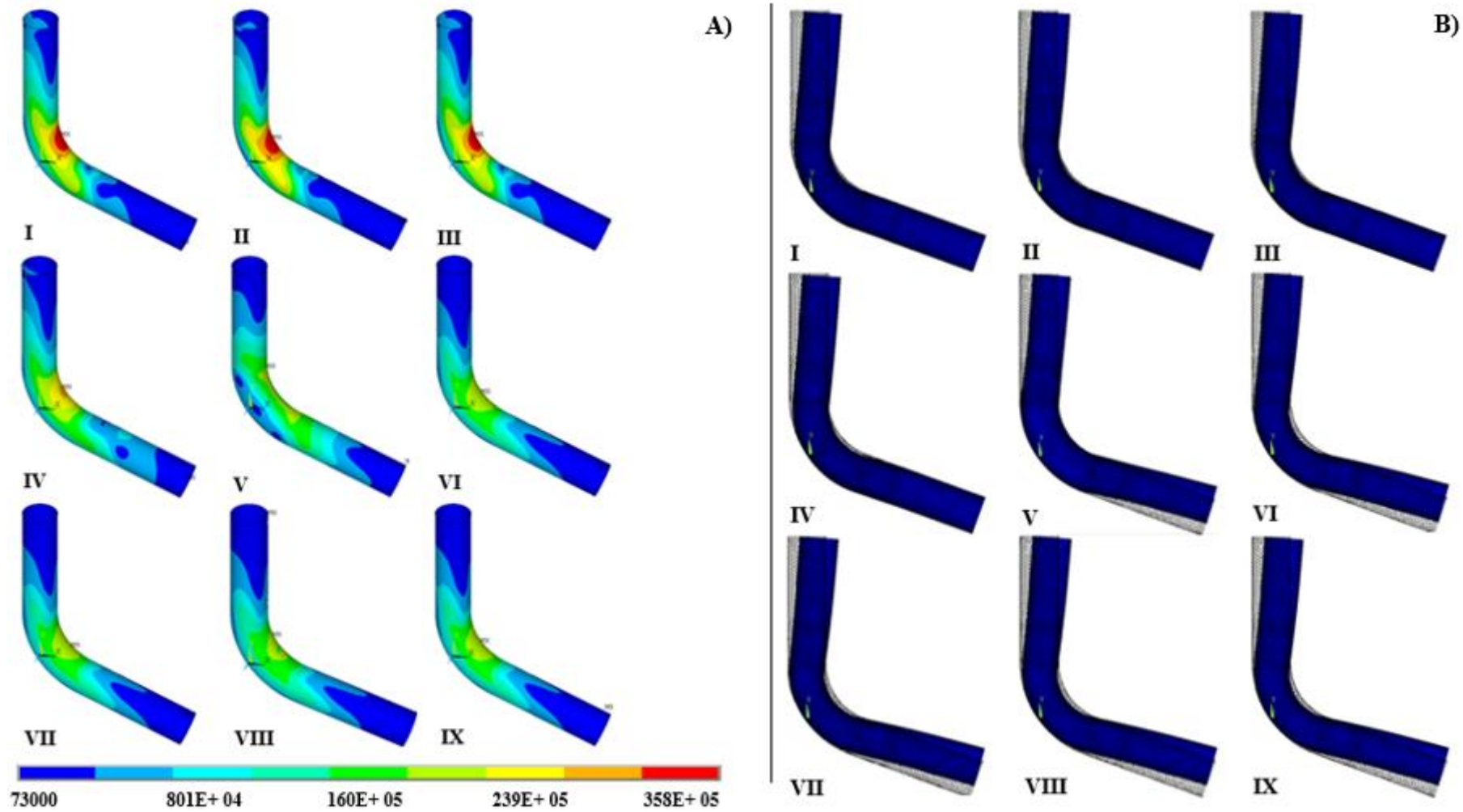
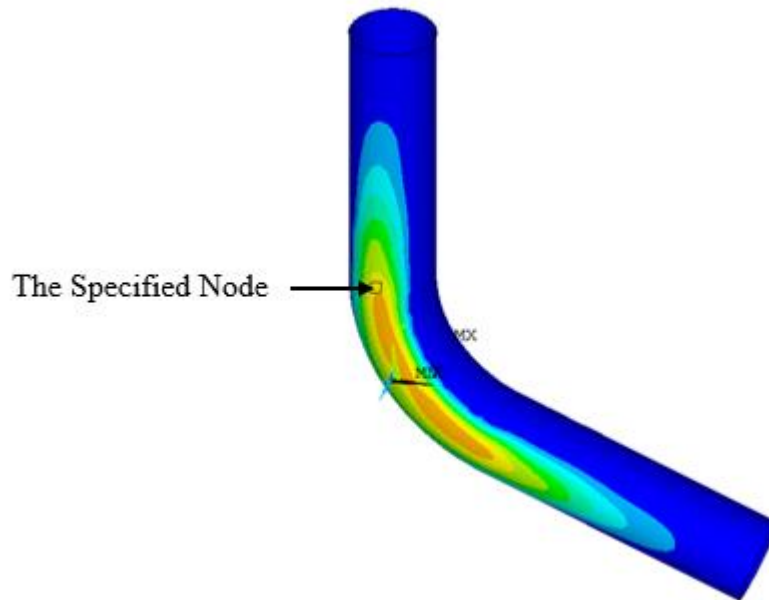


Figure 4.18: Stress distribution and displacement within idealised stent model at an initial angulation of 70°. A total of 20° displacement load was applied to the linear models artery I to IX. A) Von-Mises stress distribution, and B) displacement of the stent model.

To further quantify and compare the stress in each of the stent model, specific location was selected (see Figure 4.19) around the bending point (high stress region area) and the 1<sup>st</sup>, 3<sup>rd</sup>, and von-Mises stress examined. It was ensured that this location was not subject to loading and constraint artefacts.



**Figure 4.19: The tensile stress distribution within the stent model in the linear artery with 70° initial angle in the IX design under 20° displacement load. The same node was chosen throughout the models to compare the stresses.**

Figure 4.20 to 4.23 represent changes in maximum displacement and stresses within the stent model with respect to different bending angle after applying 20° displacement load. Also deflection and changes in the stresses were recorded for others displacement loads 5°, 10°, and 15° (see Appendix II).

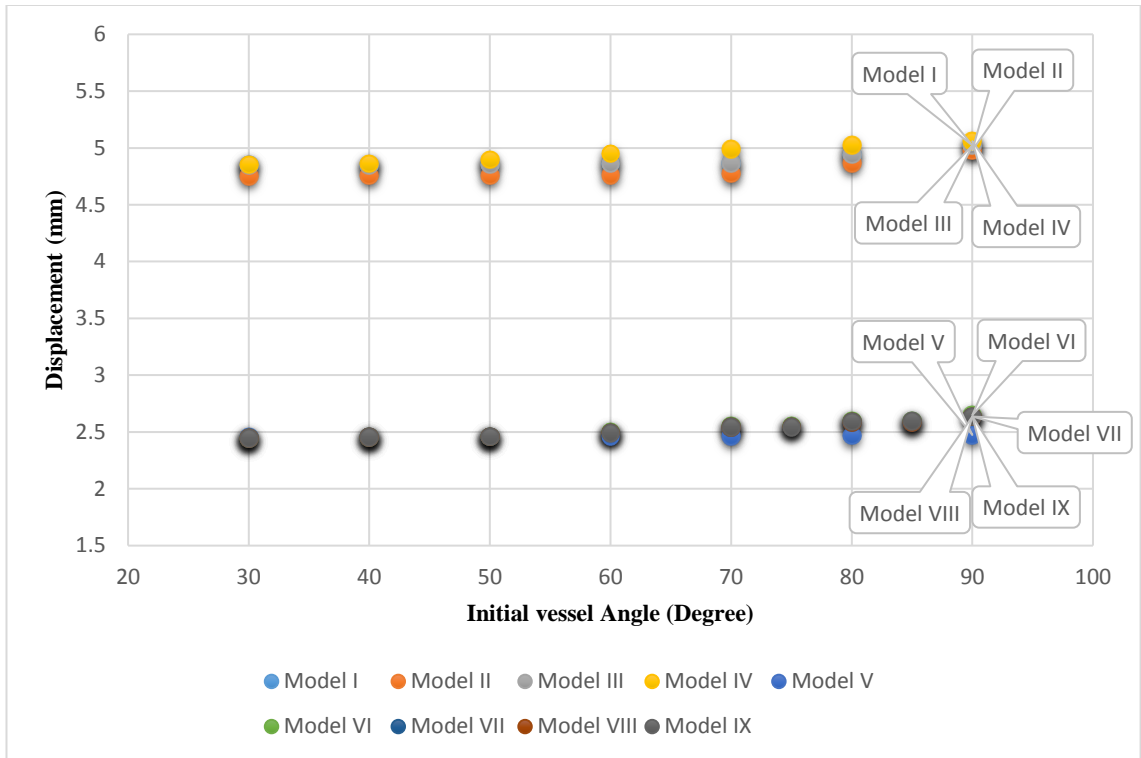


**Figure 4.20: Variation of displacement in the stent with respect to initial vessel angulation, when a total 20° displacement load applied. The vessel has linear material properties.**

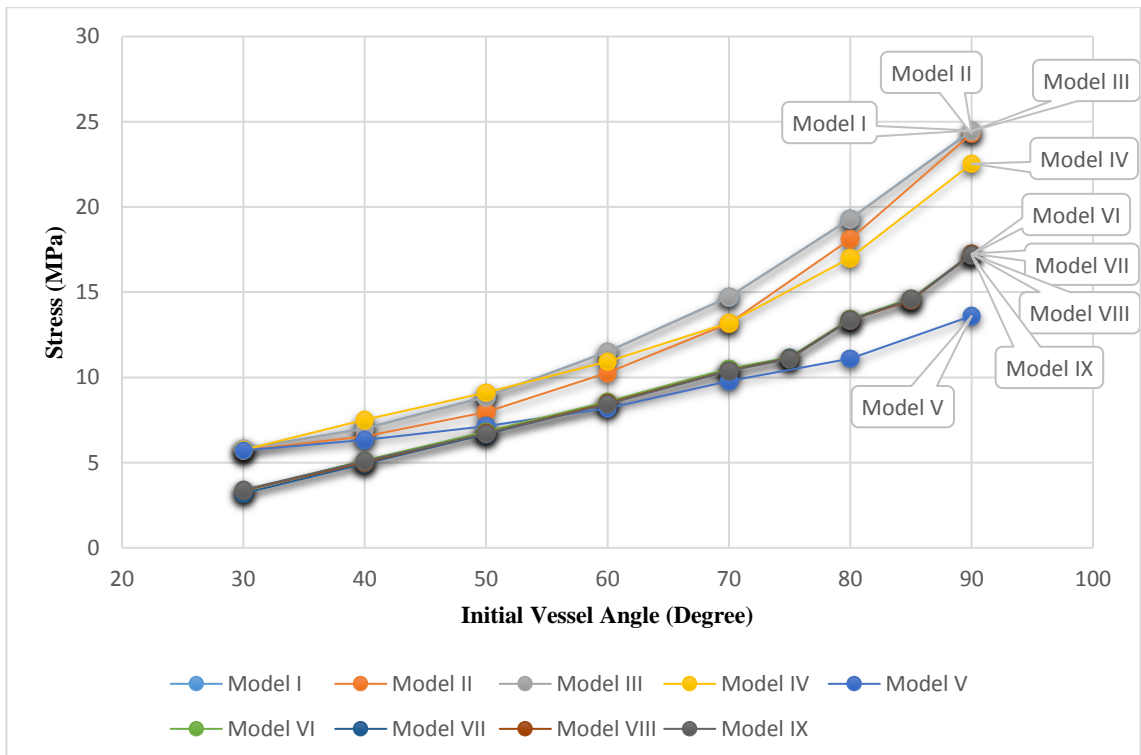


**Figure 4.21: Variation of tensile stress at the specified node in the stent with respect to initial vessel angulation, when a total 20° displacement load applied. The vessel has linear material properties.**

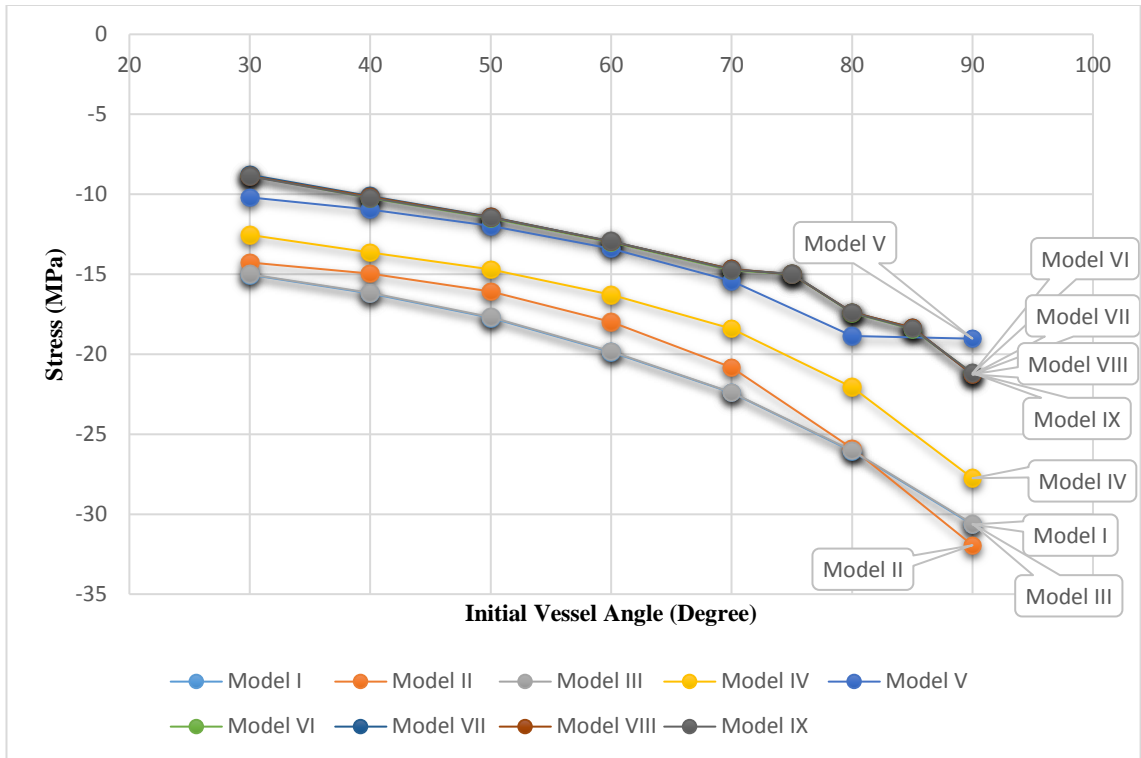


**Figure 4.22: Variation of compressive stress at the specified node in the stent with respect to initial vessel angulation, when a total 20° displacement load applied. The vessel has linear material properties.**

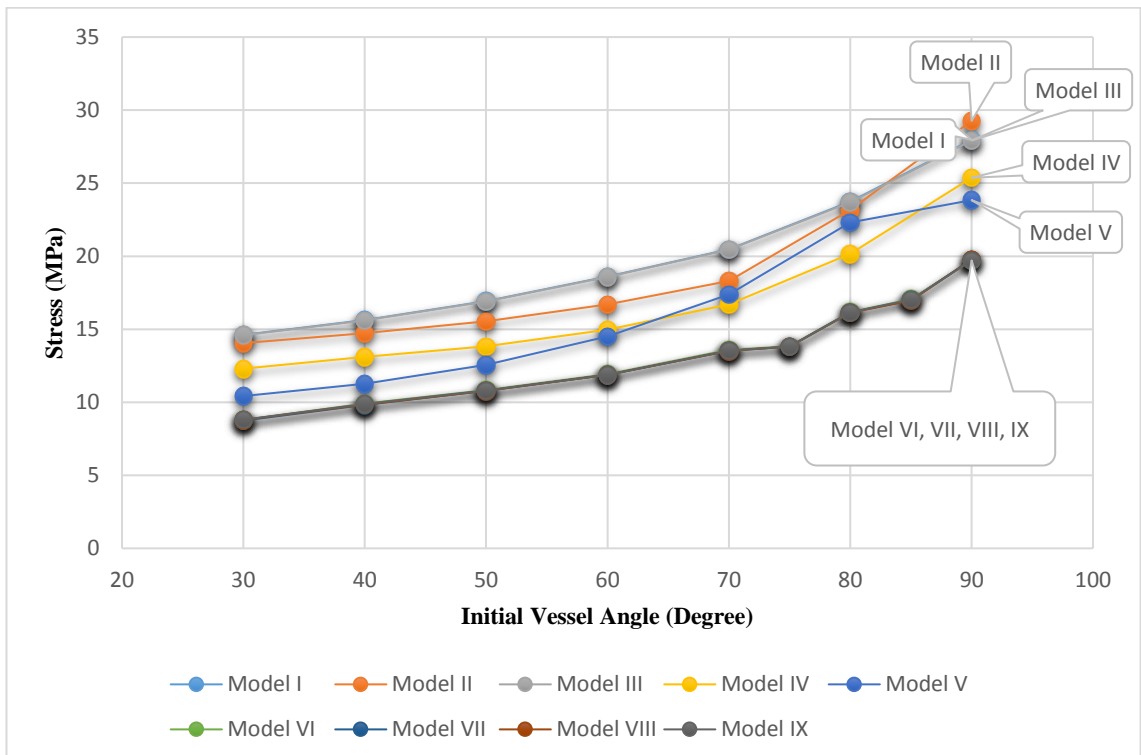


**Figure 4.23: Variation of von-Mises stress at the specified node in the stent with respect to initial vessel angulation, when a total 20° displacement load applied. The vessel has linear material properties.**

Additionally, the global maximum and von-Mises stress were observed as it is shown in Figure 4.24 to 4.26, respectively.

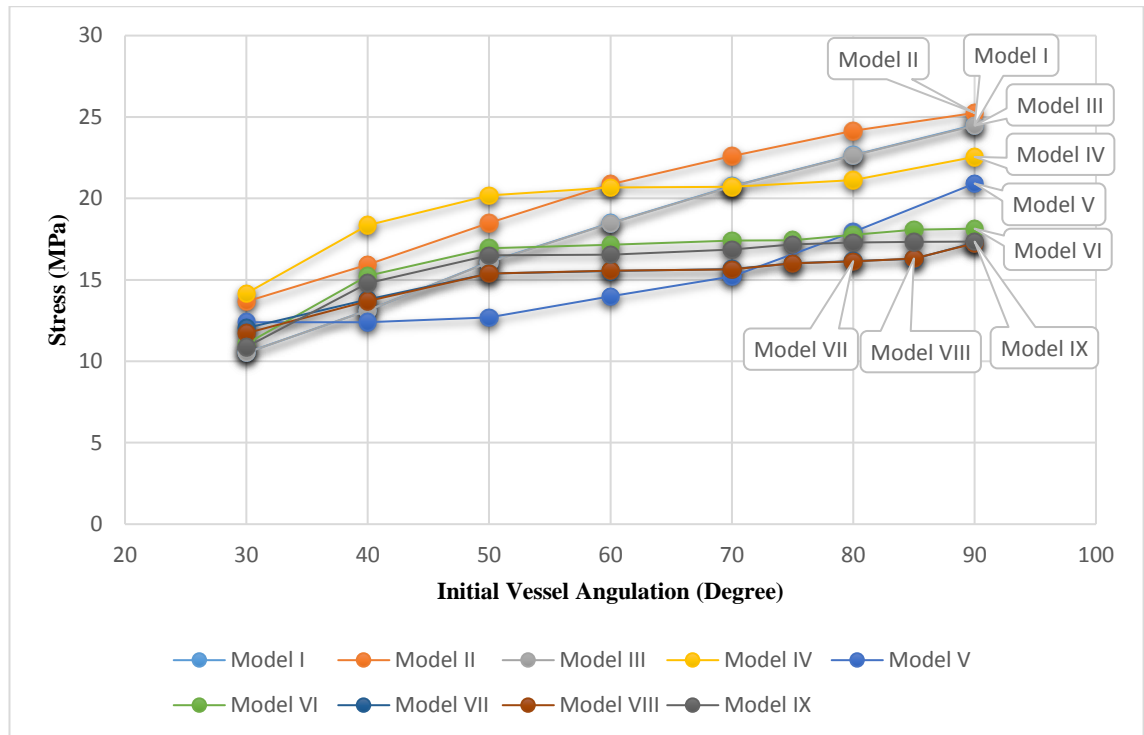


**Figure 4.24: Variation of maximum tensile stress in the stent with respect to initial vessel angulation, when a total 20° displacement load applied. The vessel has linear material properties.**

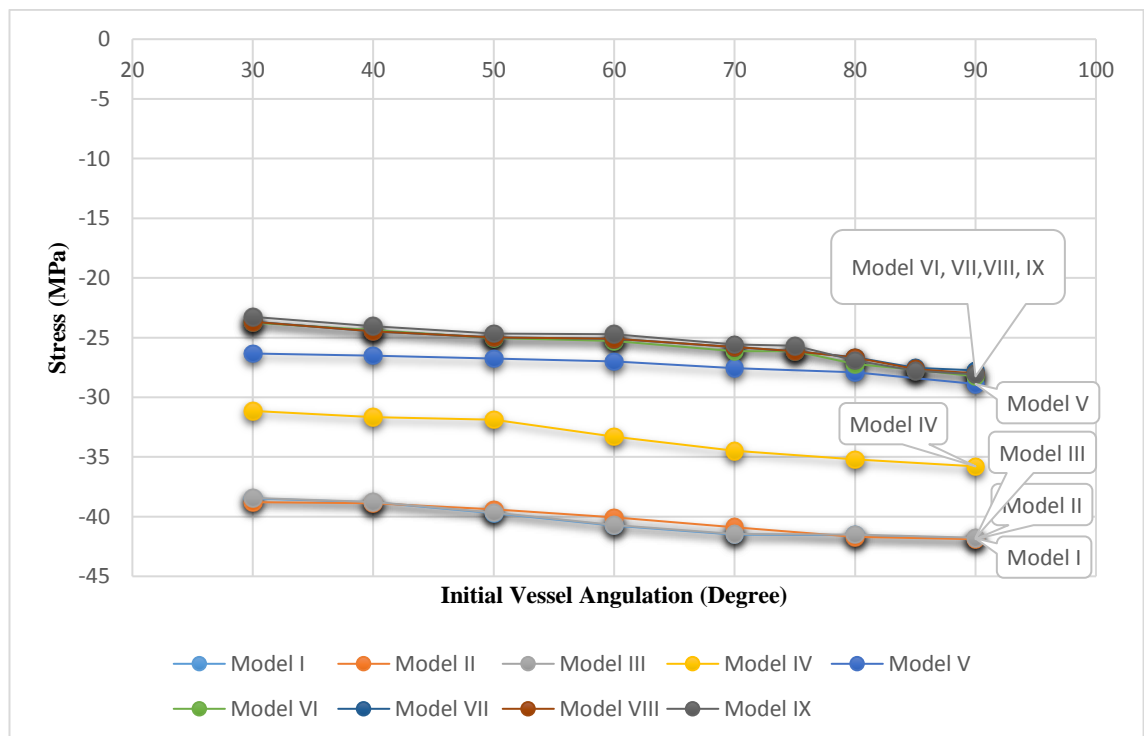


**Figure 4.25: Variation of maximum compressive stress in the stent with respect to initial vessel angulation, when a total 20° displacement load applied. The vessel has linear material properties.**

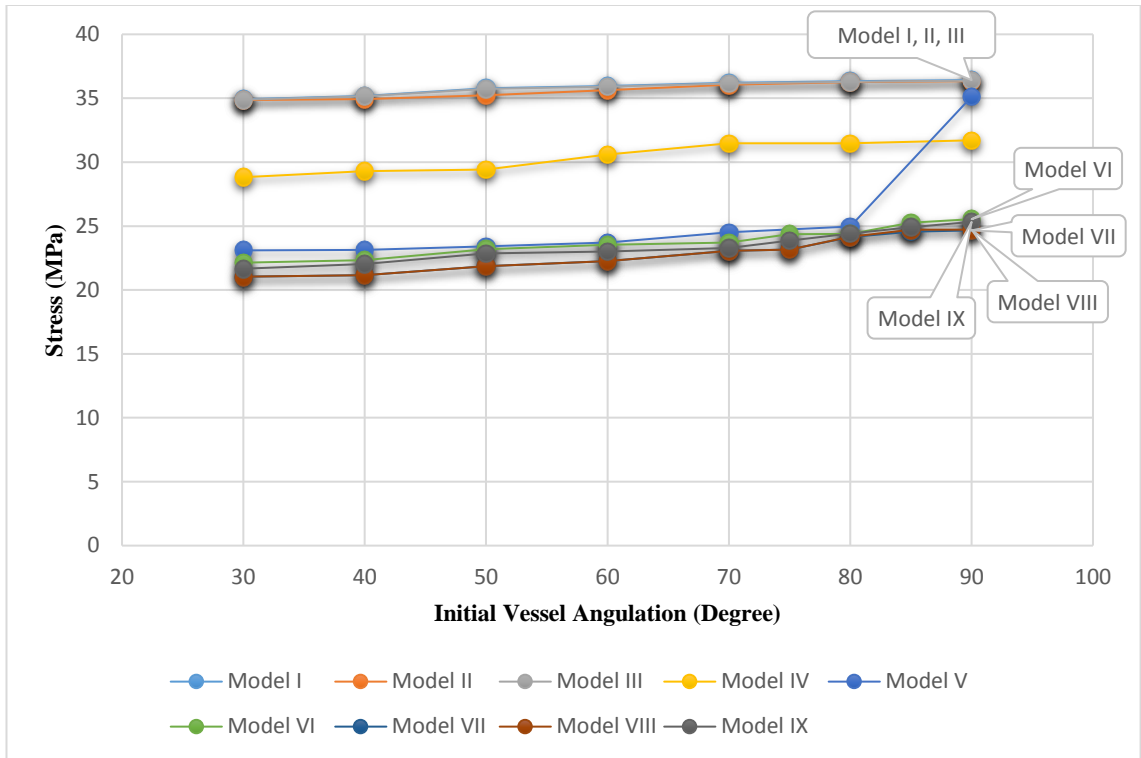


**Figure 4.26: Variation of maximum von-Mises stress in the stent with respect to initial vessel angulation, when a total 20° displacement load applied. The vessel has linear material properties.**

### 4.3.2. Stent Results in Non-Linear Artery

The stent modelling was then repeated with the artery being represented as a non-linear hyper-elastic material. However, regarding to the results from the linear models it was decided that run the simulation only for limited models VI to IX, where these were seen to have more realistic results as well as similar conditions to our in-vitro experiment. Figure 4.27 to 4.30 show the stress distribution within the stent model with respect to the vessel angulation, when 10° displacement load was applied to each end (20° load in total) as per load case in the models VI to IX.

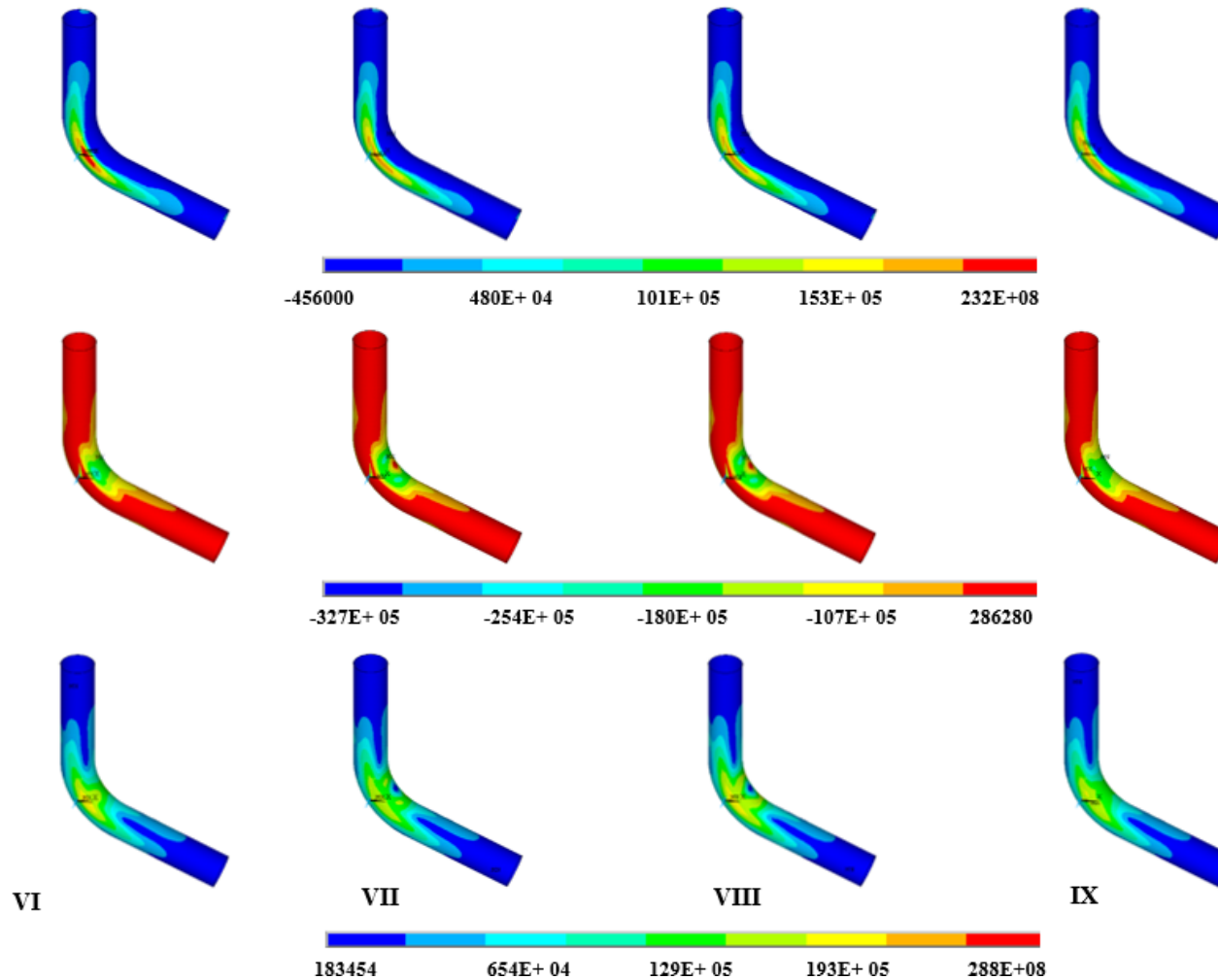
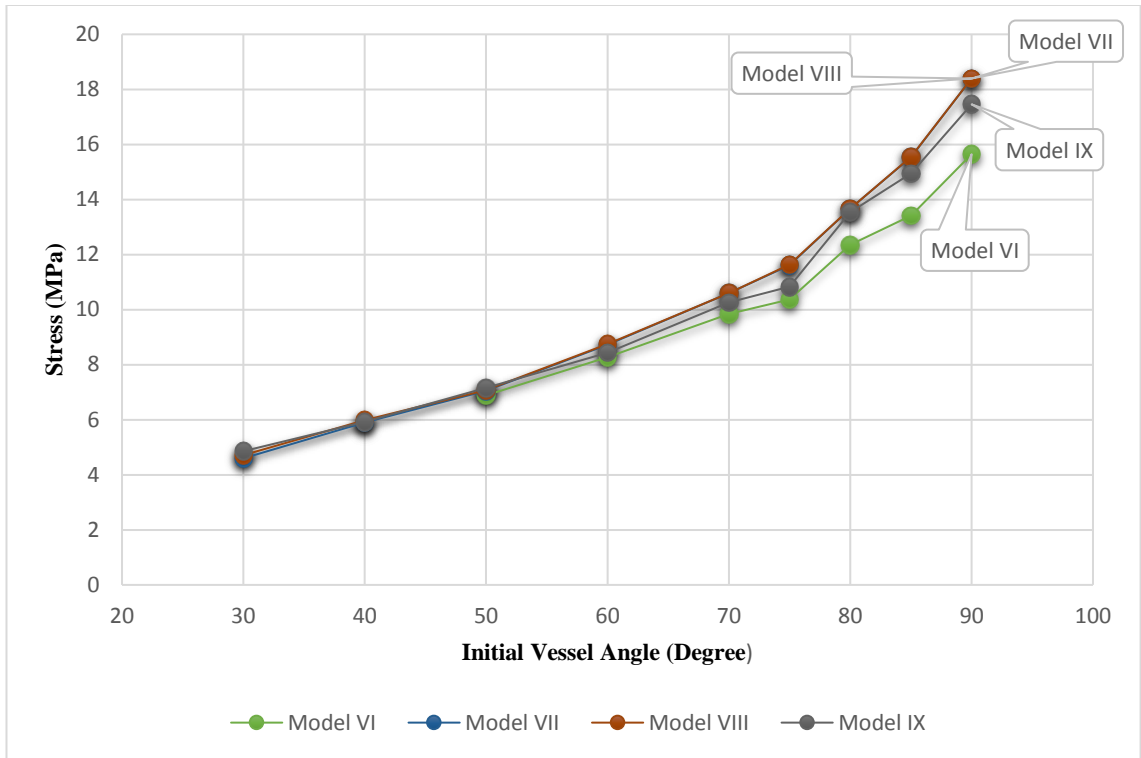
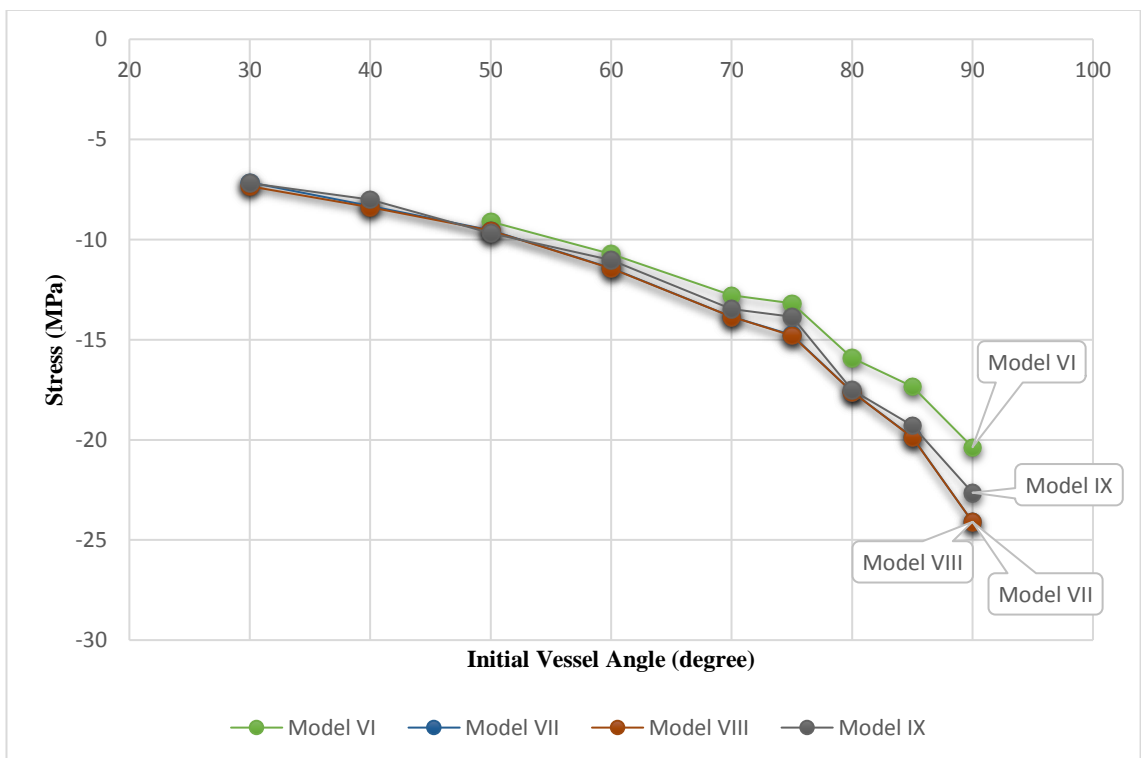


Figure 4.27: Stress distribution within idealised stent model at an initial angulation of 70°. A total of 20° displacement load was applied to the non-linear models artery VI to IX. 1<sup>st</sup> principal stress (top row), 3<sup>rd</sup> principal stress (middle row), and von-Mises stress (bottom row).



**Figure 4.28:** Variation of tensile stress at the specified node in the stent with respect to initial vessel angulation, when a total 20° displacement load applied. The vessel has non-linear material properties.



**Figure 4.29:** Variation of compressive stress at the specified node in the stent with respect to initial vessel angulation, when a total 20° displacement load applied. The vessel has non-linear material properties.

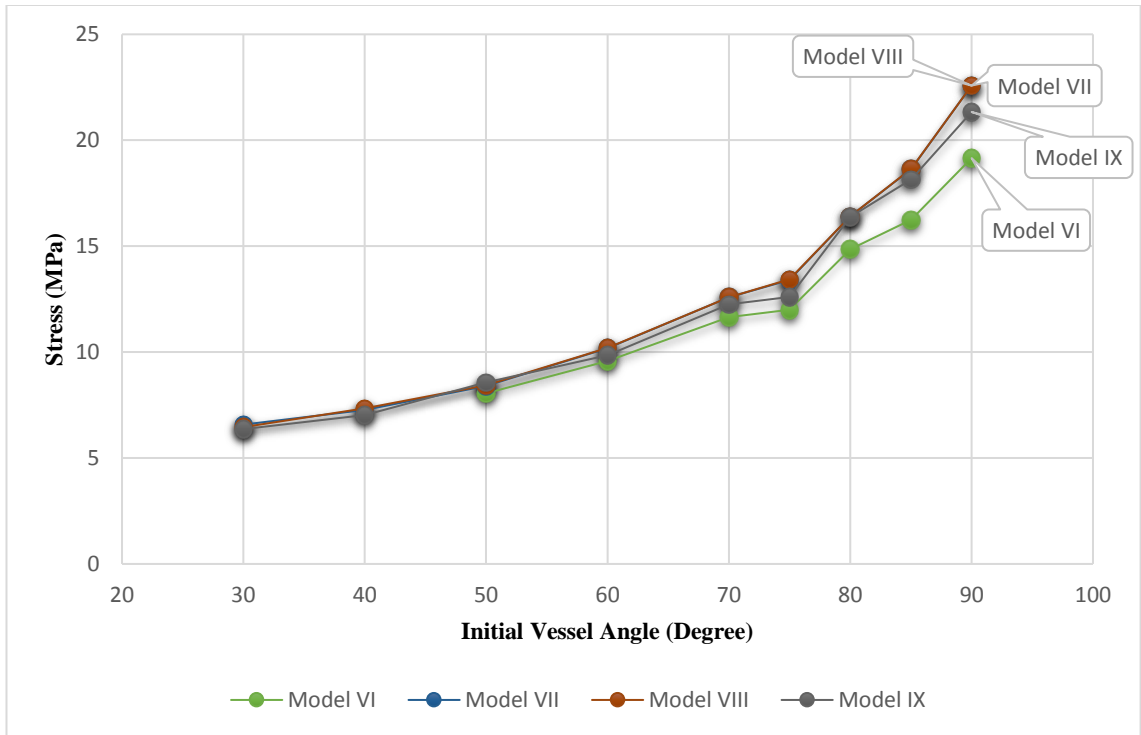


**Figure 4.30: Variation of von-Mises stress at the specified node in the stent with to initial vessel angulation, when a total 20° displacement load applied. The vessel has non-linear material properties.**

Correspondingly, the maximum displacement in these models were analysed and reordered as in Figure 4.31.

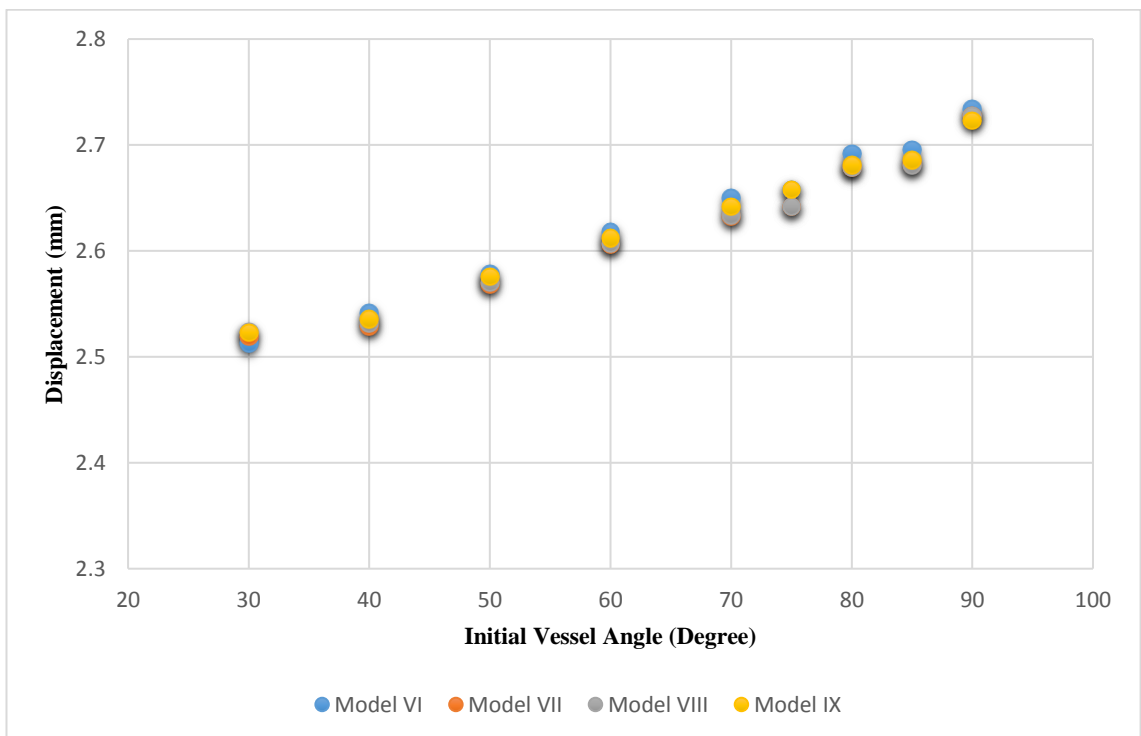


**Figure 4.31: Variation of displacement in the stent with respect to initial vessel angulation, when a total 20° displacement load applied. The vessel has non-linear material properties.**

Moreover, the global maximum and von-Mises stress for these reconstructed non-linear model were observed as it is shown in Figure 4.32 to 4.34.

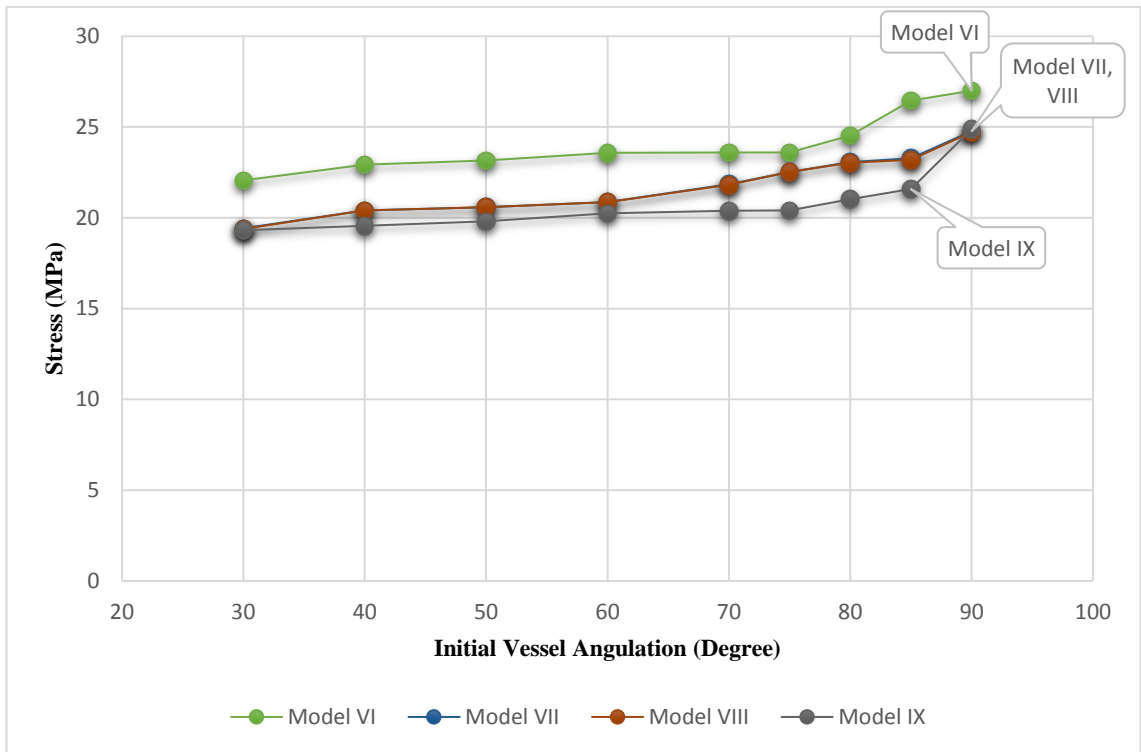


**Figure 4.32: Variation of maximum tensile stress in the stent with respect to initial vessel angulation, when a total 20° displacement load applied. The vessel has non-linear material properties.**

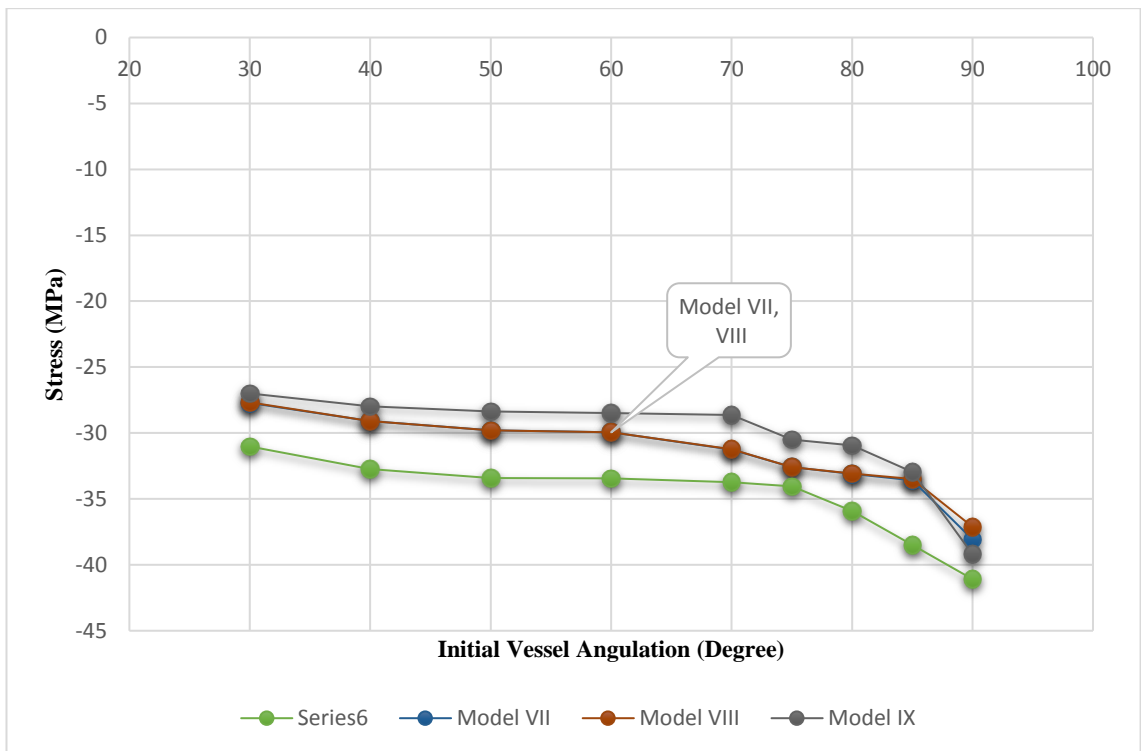


**Figure 4.33 Variation of maximum compressive stress in the stent with respect to initial vessel angulation, when a total 20° displacement load applied. The vessel has non-linear material properties.**

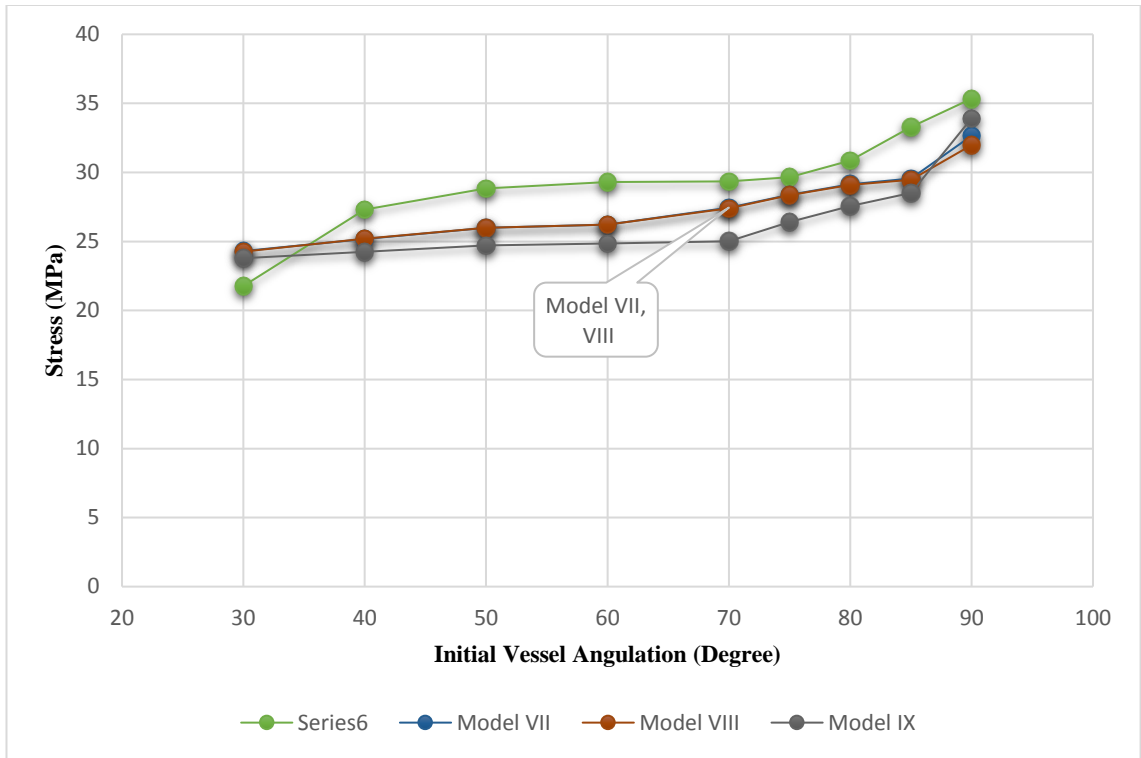


**Figure 4.34: Variation of maximum von-Mises stress  $\sigma$  in the stent with to initial vessel angulation, when a total  $20^\circ$  displacement load applied. The vessel has non-linear material properties.**

Further details and outcomes was observed through the simulation for all reconstructed models such as, distribution of the stresses in each individual model at different vessel angulation. Figure 4.35 is an example of changes in stress distribution in the model IX through various artery angulation from  $30^\circ$  to  $90^\circ$  angle, which is representative for all the linear and non-linear simulations.

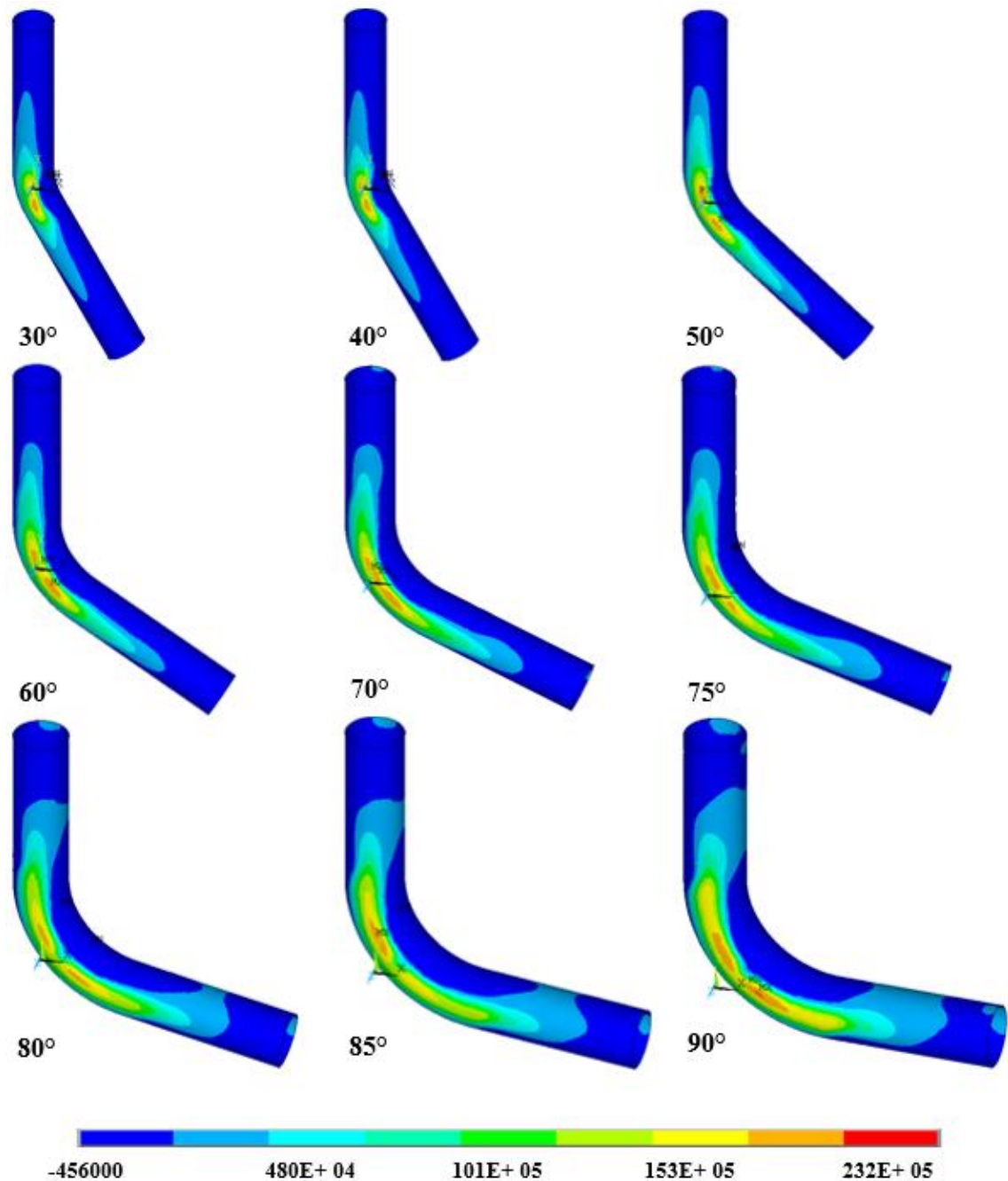


**Figure 4.35: Variations of the tensile stress distribution within the stent model in the non-linear artery with initial angle from 30° to 90° in the IX design under 20° applied displacement.**

## 4.4. Discussion

A series of design independent FE models of idealised stents were created to represent a stent deployed in an angulated vessel, with an initial angle range between 30° and 90°. Applied displacement was also varied from 5 degree to 20 degree, as patients with stent fracture have been found to have a greater angle between end diastole and end systole

( $28.3^{\circ} \pm 11.5$ ), than the patients that did not present with stent fracture ( $12.3^{\circ} \pm 9$ ) (Ino et al. 2009).

A sensitivity study of the loading and constraints for the idealised FE model enabled the selection of the optimum loading conditions to replicate the *in vivo* situation, whilst minimising artefacts. It provides an increased understanding of the relationship between angle of tortuosity and stent stress, and understanding of the relationship between angle of displacement during the cardiac cycle and stent stress, which are known as predictable SF factors. Stent design was disregarded in the work by idealising the stent to a simple cylinder.

#### **4.4.1. Stent in Linear Artery Model**

The idealised modelling was constructed with 9 different boundary conditions with artery as linear elastic isotropic (see Figure 4.7 to 4.15) to evaluate stress and its behaviour with respect to vessel angulation. The 1<sup>st</sup> principal stress with  $\sim 13$  to  $15$ MPa (see Figure 4.21), the 3<sup>rd</sup> principal stress with  $\sim -18$  to  $-22$ MPa (see Figure 4.22), and the von Mises stress with  $\sim 17$  to  $20$ MPa (see Figure 4.23) in the first four models were observed (at initial  $70^{\circ}$  artery angle) to have higher stresses at the chosen point (in high stress region area, where it was not subject to loading and constraint artefacts) under  $20^{\circ}$  displacement load, due to the increased constraint which was applied to a larger area than in designs VI to IX  $\sim 10$ MPa,  $\sim -15$ MPa, and  $\sim 14$ MPa, respectively (see Figure 4.21 to 4.23). These values were greater at the global locations at initial  $70^{\circ}$  artery angle, and still models I to IV had highest value for the maximum 1<sup>st</sup> principal stress with  $\sim 20$  to  $22$  MPa, the maximum 3<sup>rd</sup> principal stress with  $\sim -35$  to  $-41$  MPa, and the maximum von Mises stress with  $\sim 32$  to  $36$  MPa in compare to models VI to IX with  $\sim 17$ MPa,  $\sim -26$ MPa, and  $\sim 24$  MPa, respectively (see Figure 4.24 to 4.26). Also it can be seen that the variation of stresses at global maximum for all models were more moderated than the changes at the specified node,

however, still the pattern of changes are similar (see Figure 4.22 to 4.26). Although, the maximum displacement in the models I to IV, where the total load was applied only to one end of the artery was from ~4.9mm at initial 30° artery angle and reached up to ~5mm at initial 90° artery angle which it is almost twice as the designs V to IX with ~2.4mm to ~2.6mm between 30° and 90° initial artery angle (see Figure 4.20), but in the constructed models V to IX, as the displacement was applied from the two ends of the artery, there is movement from both sides which means the total displacement in these models also is similar to the rest of the designs. Additionally, the displacement results show that a particular displacement can correspond to different initial angulations, where increasing in initial angle resulted in larger deflection, following greater amount of stresses.

However, the distribution of the applied displacement had effect on these results, as in the models I to IV the total loading 20°, was applied on the one end of the artery, while in the models VI to IX it was 10° on each end of the artery model, but the model V results illustrated that constraint area also can have an effect on the amount of magnitude of stress. The displacement load in model V was identical to the VI to IX design where both ends of the artery model were subjected to an equal 10° displacement loading and resulted in similar maximum deflection, while the bending region of artery model was constrained in the model V which it was much larger than design VI to XI where only a few nodes were constrained, and it leads to 5MPa greater von-Mises stress in the model V with ~17MPa at initial 70° artery angle (see Figure 4.23).

Moreover, the stent results from the model I and III are identical through all boundary conditions simulated. Although they were subjected to same displacement, but the constraint area in the model I was 2.5mm larger than the model III, where in the model III the artery segment which only housed the stent was constrained. Hence it can be said that as long as the stent was not directly in the constraint area, the stent outcomes (e.g. stress) would not have been affected. The model II and IV results are a proof of this

conclusion, where the same distribution load was applied to the area of the artery which only enclosed the stent part in the model II, and it resulted to have an increment in all parameters. Similarly, in the model IV, the constrained area was reduced in part of the artery which involve the stent model, and as it was expected the stresses were reduced within the stent in compare to the models I, II, and III due to greater amount of freedom (Wong et al. 2009) (see Figure 4.21 to 4.23).

Even though, the coronary arteries are surrounded by the cardiac wall, they still have some degree of movement during the cardiac cycle. In other words, to attempt to replicate the *in vivo* environment in the simulation, the constrained area of the artery should be minimized, as in reality the artery might have five different type of movement during the heart beat such as translocation, rotation, twisting, accordian-like motion, and movement towards the centre of the ventricular chamber (Reichek 1999). Likewise, the displacement load should be applied to the both ends of artery model as the cardiac cycle force would be exerted all over the artery surface, and the difference in angle at end of systole/diastole would be as a result of artery movement from both sides (Ino et al. 2009). Therefore models VI to IX were constructed, in order to have larger amount of freedom, as well as exert displacement load to both ends of the artery model. Additionally, these constructed designs more closely replicate the loading undergone to the *in vitro* experimental study (see Chapter 5), hence providing more relevant results to validate the total outcome of the study.

The displacement and stress magnitude within the model VI to XI did not vary significantly through the various angulation. It started at ~3MPa, ~ -9MPa, and ~9MPa for tensile, compressive, and von-Mises stress, respectively, at 30° and reached up to ~17MPa, ~ -21MPa, and ~20MPa at 90° under total 20° displacement loading (see Figure 4.21 to 4.23). The outcome results were almost similar in these models, where the identical displacement load and similar constrained part, might be the reasons of this

resemblance. However, these models seem to replicate better situation of the *in vivo* conditions, as larger area of the artery undergoes the displacement loads while it has more degrees of freedom.

The deflection results demonstrate that the maximum displacement increased with respect to the increment in initial artery angle. This was more evident for the stress magnitude in the stent where it had direct ratio with the angulation for all the constructed models throughout all the simulations, where the degree of artery angle increased, the stress in the stent increased. The connection between the deflection and the stress can be described here, as the stent undergoes a load and following by displacement, because metals resist deflection and deformation, hence resulting in stress. Therefore, as expected, it can be said that larger deflection would result in greater stress.

Figure 4.21 to 4.23 show the variation of stresses in the stent with respect to initial vessel angulation, when a total 20° displacement load applied. It can be seen that these variation are more moderate from 30° to 70° than 70° to 90°, and once the angle exceeded 70° the stress experienced increased more rapidly. Therefore, to investigate the changes in stress more closely, the artery angle was transformed in 5° (instead of 10°) after the initial angle was exceeded 70° for the models V to IX. The stresses increase with initial angulation was observed to be more pronounced for all load cases once the angulation exceeded 70°. Hence it was concluded that these more pronounced angles were critical and hence more prone to fracture, which is in agreement with clinical results where vessel angles of 75° and over were identified as a substantial independent predictor of SF (Sianos et al. 2004).

Tensile stress distributions within the stent models, show the sides of the bending area of the stent has the highest stress value, indicated by the red area in Figure 4.17A. Moreover, the von Mises stress (see Figure 4.18A) is another proof of high stress in the bending segment as well as 3<sup>rd</sup> principal stress illustrating the most compressive part in the stent

model in blue in Figure 4.17B. All these results of the stress distributions regardless of their boundary conditions, show areas of high stress occurring in the region which is associated with hinge-type movement. According to the literatures stents are more likely to fracture in this area (Ino et al. 2009, Wu et al. 2007, Morlacchi et al. 2014).

#### **4.4.2. Stent in Non-Linear Artery Model**

Coronary arteries have been determined to behave as a hyper-elastic material (Loree et al. 1994), with most of the literature modelling it in this way (Barrera et al. 2012, Martin & Boyle 2013, Bukala et al. 2014). However, as the focus of the studies in the literature was not on the underlying stent stresses, it was necessary to ascertain whether the properties of the artery had an effect on the predicted stent stresses. Hence the same FE analysis as described in Section 4.2 was repeated with the artery defined as a non-linear material to evaluate the results and quantify any difference on the outcomes of the deployed stent. The modelling was conducted only for the four reconstructed designs VI to IX (see Figure 4.16), as these were deemed to be the most appropriate boundary conditions from the linear results. In these four models the conditions were more similar to the *in-vitro* experimental study in Chapter 5.

The stress distribution within the stent model in the non-linear artery (see Figure 4.27) indicate somewhat similar results to the linear artery (see Figure 4.17 & Figure 4.18A), where the highest tensile stress occurred on the both sides of the stent around the curvature site and highest point for the compressive and von Mises stress were observed on the inner surface of the stent at the bending point (on the inner bend). Nevertheless, stent in non-linear artery experienced greater stresses. This is clearly due to material difference between linear and non-linear, because the hyper elastic property allows the force to have more impact on the design, and thus it leads to larger displacement deformation. The stiffness of the non-linear material would be altered under applied force and affects the

model's deformation, whereas in the linear material as long as the stress remains in the limit range (Yield strength) of linear elastic, the stiffness is constant. Hence the non-linear artery deforms easily under applied force and it resulted in the stent model as the applied load had more impact on the stent model, while in the linear model, the stiffness of the artery stayed constant and played like a protector and prevent any deformation within the stent model.

Along with the stress distribution, as it was expected the trend of increasing stresses in the stent observed similar to linear models, but some changes in the magnitude. The pattern of increasing in stresses within the stent model at the maximum global locations were similar in both linear and non-linear artery, though, in terms of magnitude the stent experienced higher stresses in the non-linear artery and the difference between the linear and non-linear artery was more clear. Once again, this changes and higher stresses within stent model only can be described as a result of artery property, since all structural and the boundary conditions were same through the modelling, but artery property.

The stress range in the non-linear artery model at the specified node is greater, albeit 1<sup>st</sup> principal stress is almost the same as that of the linear model (up to 18MPa in the design VIII, see Figure 4.36), but for the compressive and von Mises stress it increases to - 24MPa and 23MPa at 90°, respectively (see Figure 4.37 & Figure 4.38). However, 3<sup>rd</sup> and von-Mises stresses at the initial angle between 30° to 70° are slightly higher in the linear artery models, and once the initial angle exceeded 70°, stress increment are greater in the non-linear artery models. Furthermore, increment of the stent's stresses with respect to initial vessel angulation in both the linear and non-linear artery were similar between 30° and 70°, however once the initial angulation overstepped 70° in the non-linear artery, variation of stresses in the stent became more fluctuated unlike the linear artery models. While there is still rapid increases within stent stresses, when the initial artery angle exceed 70°.

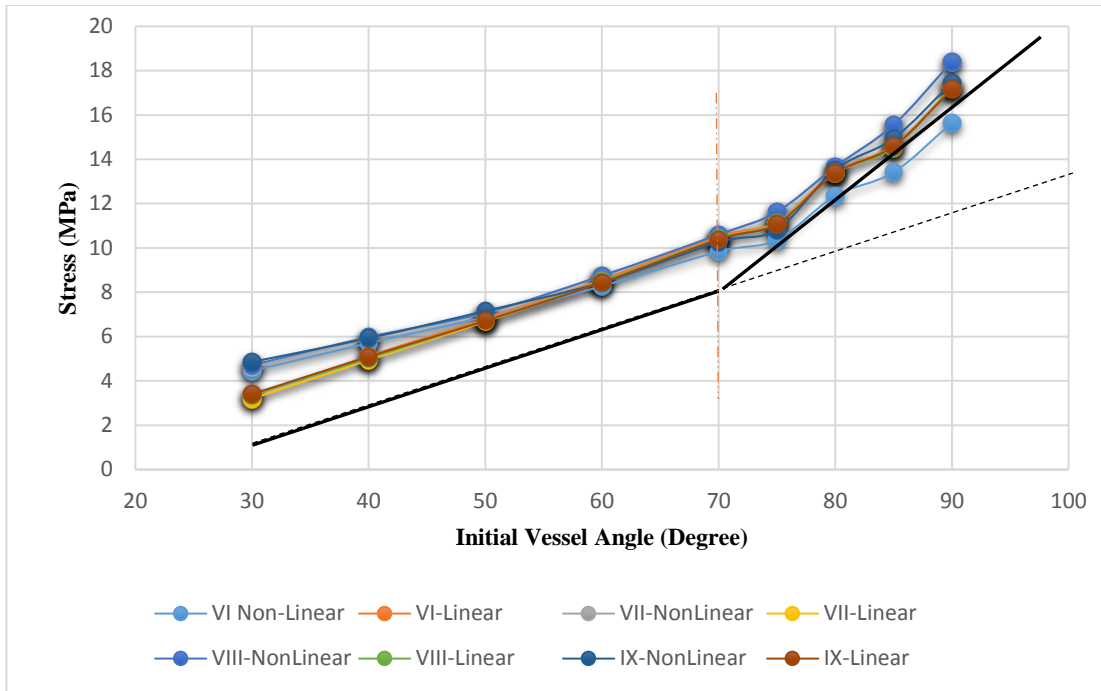


**Figure 4.36: Variation of tensile stress in the stent with respect to initial vessel angulation, when a total 20° displacement load applied. A comparison of the non-linear and linear artery material properties.**

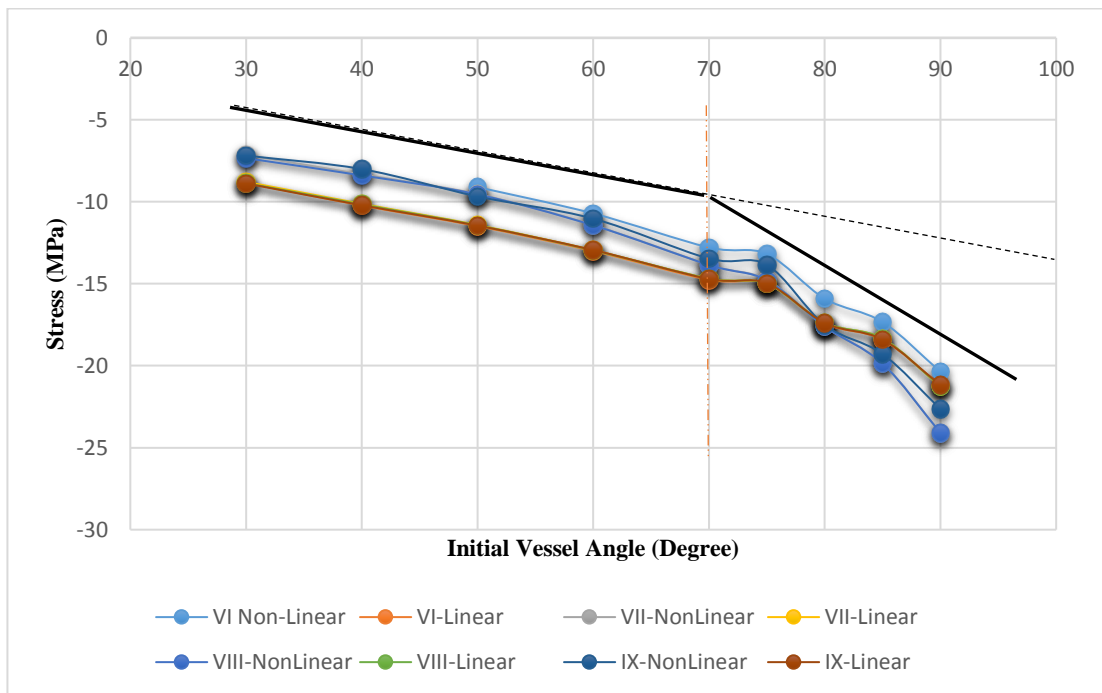


**Figure 4.37: Variation of compressive stress in the stent with respect to initial vessel angulation, when a total 20° displacement load applied. A comparison of the non-linear and linear artery material properties.**

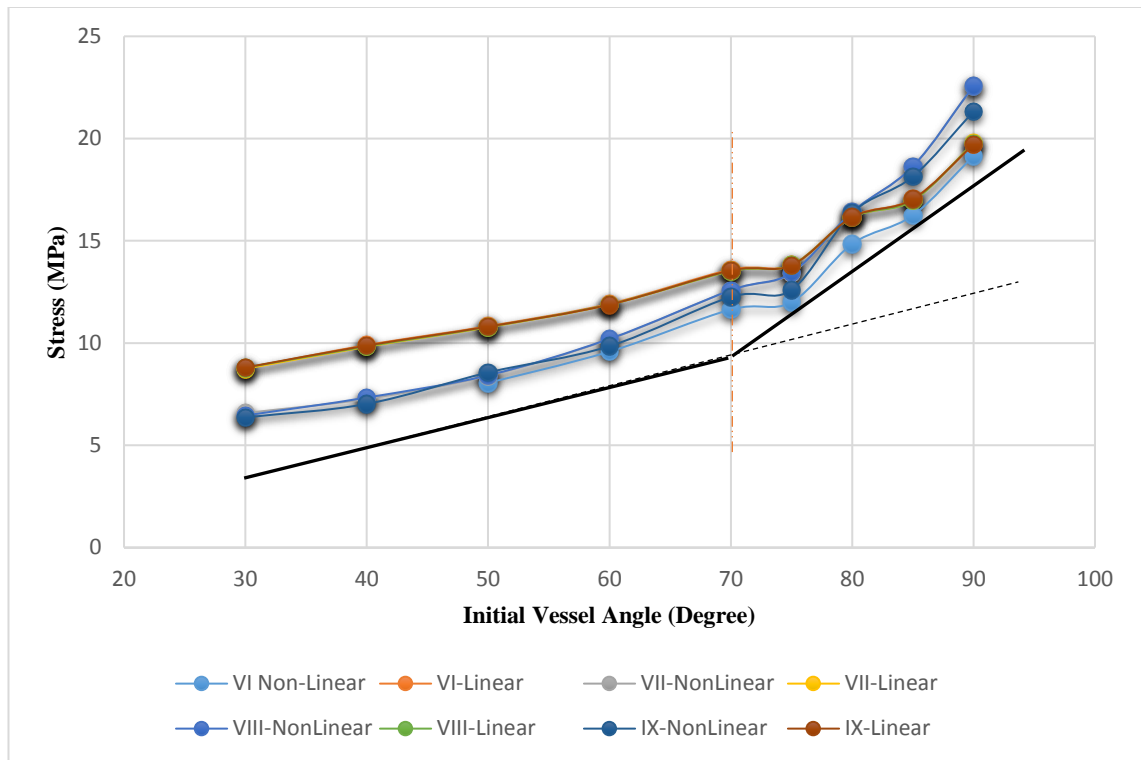


**Figure 4.38: Variation of von-Mises stress in the stent with respect to initial vessel angulation, when a total 20° displacement load applied. A comparison of the non-linear and linear artery material properties.**

The stress distribution within the stent model at various angle also represents the reason for this increase, where the initial artery angle goes up, a larger area of the stent undergoes higher stresses (see Figure 4.35).

In general, this FE analysis study and its results demonstrate the behaviour of coronary stents which are deployed in torturous vessels and undergo a typical hinge motion. Although, it illustrated the difference and importance of artery material, but also it proved that the stress will be increased with respect to vessel angulation, thus the risk of SF will be increased. In other words, when the artery angle increases, the cardiac cycle movement would affect the artery displacement and amplify the bending angle more, where increases in bending leads to enlarge the stress magnitude as well as spread out over a larger area at the bending region, and once it goes over 70° the stress is intensified, thus more likely the SF takes place around these region. Furthermore, it was defined that the artery

properties also have effect on the stent's results, where non-linear properties demonstrated more accurate results.

Although, these models do not consider all *in vivo* conditions (e.g. blood flow, different type of artery movement during cardiac cycle), and may not predict stent behaviour in humans precisely, but it can still offer insight for clinicians as to the mechanical environments stents operate in, for instance, how the risk of stent fracture would increase in angulated vessels. Hence it aids clinical decision making when considering intervention for tortuous anatomies.

# 5. *In vitro* Experimental Fatigue Test

## 5.1. Introduction

Fatigue failure is one possible failure mechanism that cardiovascular stents can undergo (Marrey et al. 2006), particularly in angulated vessels, leading to stent fracture (SF) which is followed by clinical complications (Lee et al. 2007, Chakravarty et al. 2010, Kuramitsu et al. 2012). Whilst the material properties of the stent are undoubtedly a consideration in fatigue (Perry et al. 2002), many other factors also need to be considered such as location and vessel geometry, lesion type, and heart contraction. Moreover, stent design has been determined to have critical role in this concept (Müller-Hülsbeck et al. 2010), hence it can be said that a successful stent is a combination of several desirable characteristics. The development of alloys in the new stent generation has provided higher fracture resistance as they are less susceptible to fatigue. The first stent generation was made from stainless steel which has a lower yield strength and ultimate tensile stress (UTS) than nickel-cobalt, platinum-chromium or cobalt-chromium in the new stent generation (see Table 5.1) (O'Brien et al. 2010, Huibregtse & Juan F. Granada 2011).

	<b>Yield strength (MPa)</b>	<b>Ultimate tensile stress (MPa)</b>
<b>Stainless steel</b>	275	595
<b>Nickel-cobalt</b>	414	930
<b>Platinum-chromium</b>	480	834
<b>Cobalt-chromium</b>	500	1000

**Table 5.1: Material properties of different alloys used for coronary stent (O'Brien et al. 2010, Huibregtse & Juan F. Granada 2011).**

To assess endovascular device fatigue performance, various approaches including stress-strain and energy models have been conducted, though to predict stent fatigue most recent studies are based on material, design and scale size which have a considerable effect on the likelihood of fatigue failure and the stents durability (Barrera et al. 2012).

According to previous reports (Marrey et al. 2006, Pelton et al. 2008) to evaluate the durability of balloon expanded stents, they have been tested based on survival time. Whilst, the 1995 Food and Drug Administration (FDA) guidance suggested to achieve a design for cardiovascular stent, it needs to be tested for  $4 \times 10^8$  cycles (approximately equivalent to 10 years implant time) without any fracture in simulating physiological conditions (the basis of test to success) (FDA 2008),

This part of the project involved the mechanical testing of cardiovascular balloon expandable stents in angulated mock artery. Furthermore, as the cardiac cycle causes the arteries to undergo a significant amount of repetitive hinge-type motion, with the degree of movement depending on the intensity of blood flow and location of the vessels, thus the samples were subjected to a repetitive movement, representative of the *in vivo* loading the stent would undergo.

By end of this phase of the project, the fracture time and location are reported on for four stent types within angulated vessels as well as observations on the progression of fracture from single strut (type 1) to total fracture. Additionally,  $\mu$ CT scan data of each stent at each stage of fracture from initial deployed to failure were obtained for future studies.

## **5.2. Methodology**

Although 15 each of four different stent designs were available, however due to limited capacity of the test rig, 9 samples of each designs were investigated in the study:

- ◆ Multi-Link Vision<sup>®</sup> (Abbott Vascular)
- ◆ PRO-Kinetic Energy (Biotronik)
- ◆ BioMatrix NeoFlex<sup>™</sup> (Biosensors International)
- ◆ Promus PREMIER (Boston Scientific)

These particular stents; Multi-Link Vision, BioMatrix NeoFlex™, and Promus PREMIER were selected as in the Ormiston et al. (2015) study, where BioMatrix fractured most readily and Promus PREMIER were found to be unlikely to fracture. Also PRO-Kinetic Energy is interesting as they have very thin struts and helical meanders structure. The repetitive bench test undertaken in the current study was conducted under more physiological realistic loading conditions, deploying the stents into silastic tubing at an initial angle and then subjecting them to repetitive displacement in order to represent the cardiac cycle. The stents were examined at regular intervals for signs of fracture using a micro-CT scanner, and when a strut fracture was identified a full micro-CT scan was obtained to create finite element models for future studies. Moreover, pilot studies have been performed with Cypher™ (Cordis Corporation, USA) and Multi-Link 8 (Abbott Vascular) stents to optimise the test protocol and to ensure that the optimum mock artery was used, with Cypher™ (Cordis Corporation, USA) and Multi-Link 8 (Abbott Vascular) stents.

This is an observational study, to increase understanding of the way that stent fracture occurs in these type of conditions. We hypothesise that as the test rig we have designed replicates a more realistic physiological loading than other studies, and provides better representation of the loading stents undergo *in vivo* and hence will inform clinical practice.

### **5.2.1. Experimental Procedure**

A test rig has been designed and built at University of Hull (contributed by Alice Clough, Frances O’Keeffe and Mohammad Hossein Izadian; funded by a Nuffield Foundation – Royal Academy of Engineering Undergraduate Research Bursary) to enable the deployment of stents at a predetermined angle into silastic tubing which represents the artery. The initial angle of the artery can be set between 90° and 150°, by placing the tubing in the loading arm as shown in Figure 5.2B, which is initially locked at the chosen

angle by means of a grub screw. The stent is deployed via a prepared pathway on top of the arm to allow access to insert the guidewire into the tube, ensuring that it is deployed at the desired angle (see Figure 5.1).

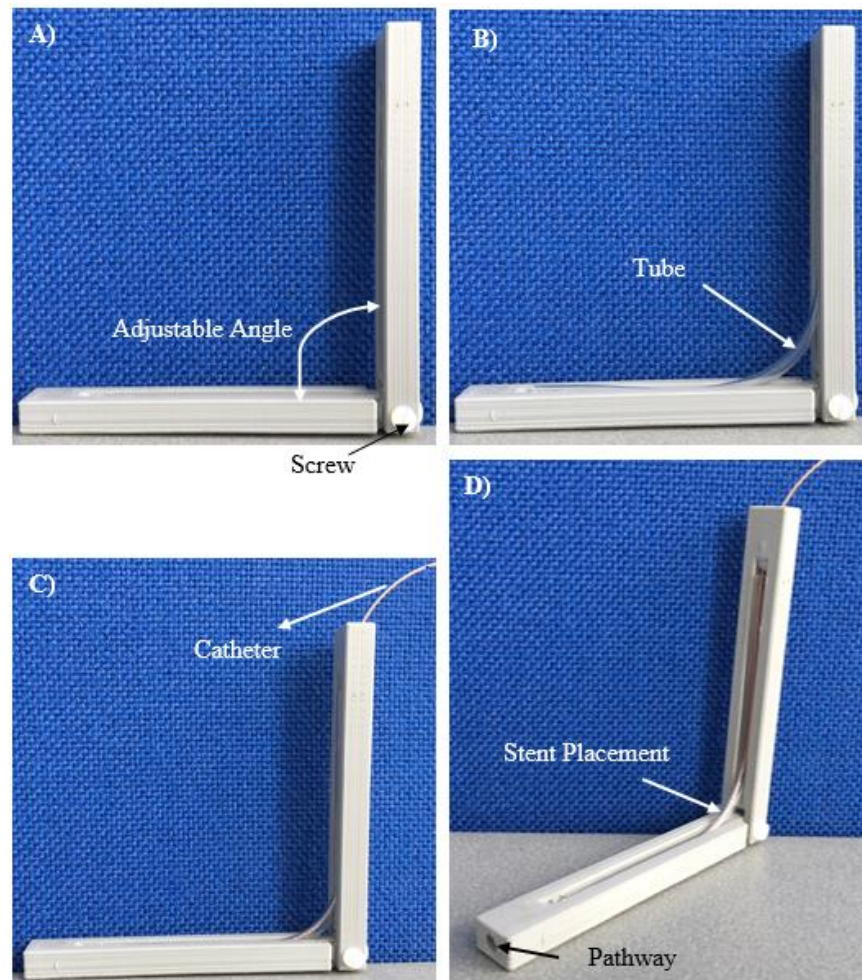


**Figure 5.1: Procedure of stent placement in angulated mock artery. A) Loading arm is set at initial angle of 90°, B) the mock artery is placed into the loading arm at the pre-determined initial angle, C & D) Catheter inserts via prepared pathway to deploy stent at the initial angle.**

Once the stent is deployed into initial angulated mock artery as shown in Figure 5.2, the load arm is then placed into the test rig shown in Figure 5.3, unlocking the loading arm once securely in place to enable hinge motion during testing. The test rig subjects the stent to a repetitive hinge-motion type loading, with an angulation movement of 20° (hence a stent deployed at 90 ° would be repetitively reduced to 70 ° during testing). In addition, 28 samples can be tested simultaneously under same conditions. The heart beat was assumed to be 70 bpm, 100,800 cycles for a day, and the motor for the test rig is

capable of ~165 cycles per minutes, hence 610 minutes of testing represents the number of heart beats in one day. However, to have an accurate number of cycles, a sensor was attached to the motor to record the precise number of cycles.

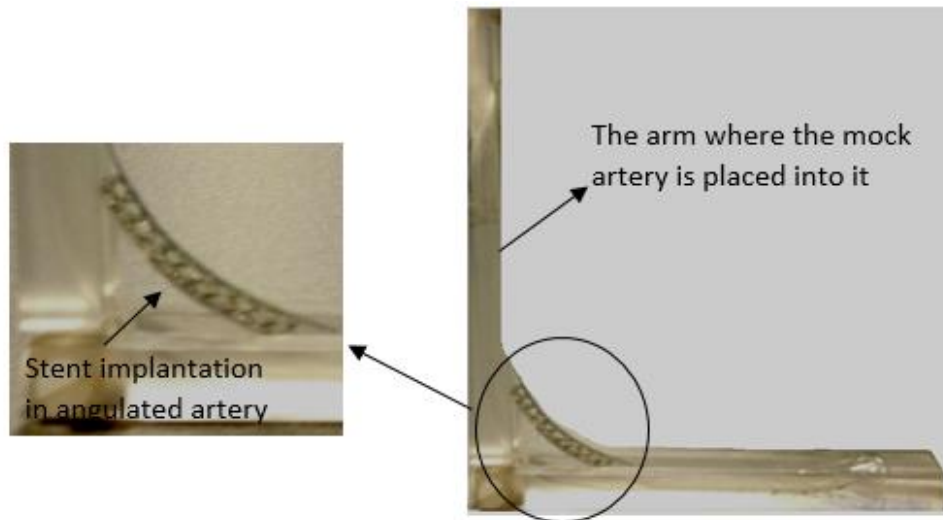


**Figure 5.2: Stent deployment in silastic tubing at predetermined angle in loading arm (90°)**

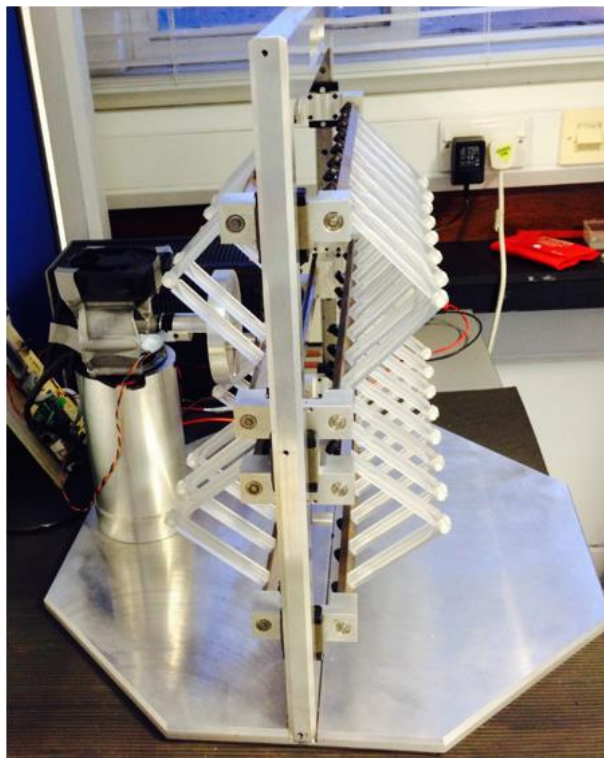


**Figure 5.3: Stent testing rig – capable of testing 28 angulated samples simultaneously, subjecting each stent to an identical repetitive hinge motion loading of 20°.**

## 5.2.2. Testing Protocol 1

To develop the test protocol, select the silastic tubing to use and to estimate the frequency with which stents should be examined, a small pilot study was conducted. Two Cypher (Cordis Corporation, USA) stents (length= 28mm, inner diameter (ID)= 3mm) were deployed at 12atm (nominal pressure) at an angle of 90° in two types of tubing, BDC labs tube (supplied by BDC Laboratories, Wheat Ridge CO, specification: straight silicone mock vessels, ID = 3.0 +/- 0.2 mm at 100 mm Hg, wall thickness= 0.45 mm, length= 15 cm, radial compliance = 5-7% per 100 mm Hg at 120/80 mm Hg and 1.2 HZ) and a silicone mock artery sample provides by Bose corporation , (Bose Corporation, Electro Force Systems Group, USA, specification: ID= 3 mm, wall thickness= 0.75 mm, length= 15 cm) in fixed loading arms as shown in Figure 5.4. The stent was then  $\mu$ CT scanned to ascertain the original structure and ensure structural integrity, as well as to enable future FEA modelling (the loading arm was purposely designed to contain no metal to enable  $\mu$ CT scanning). The arms were loaded into the test rig and unlocked and subjected to repetitive 20° hinge motion loading, typically running for between 115,000 and 140,000 cycles per day. At intervals, the test rig was stopped, a loading arm was fixed at the initial angle of 90°, and then removed from the test rig for examination in a  $\mu$ CT scanner (X-Tek HMX160 micro-CT system X-Tek, Tring, UK at the University of Hull), to identify any potential fractures. This procedure was used to identify any fractures by carefully examining visually the stent sample in the scanner, however, in case of observing a new fracture a full  $\mu$ CT scan was conducted to enable the creation of 3D finite element models for future study. Whether fractured or not, the stents would then be returned to the test rig for further testing (this procedure was continued until complete strut disconnection (stage 4 fracture) was identified).

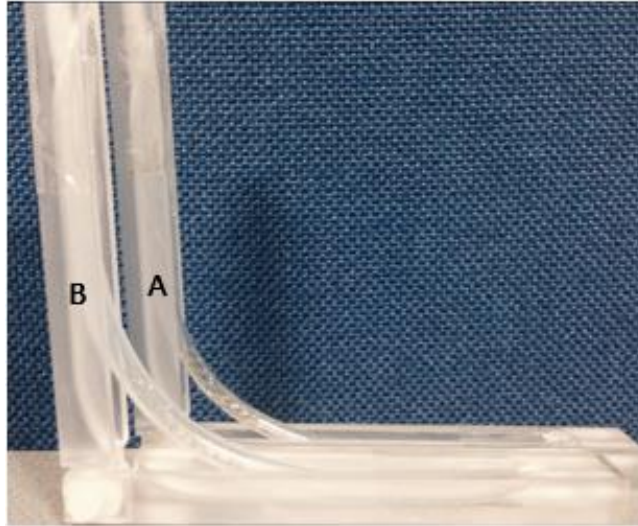


**Figure 5.4: Two identical (ID= 3mm, 28mm length) Cypher (Cordis Corporation, USA) stents deployed in two types of silastic tubing; A) BDC labs tube (thin tube), and B) Bose corporation tube (thick tube) at initial 90°.**

### **5.2.3. Testing Protocol 2**

As Cypher stents are well known to fracture, thus to evaluate and optimise the test rig, a more reliable stent was tested under similar conditions to the first pilot study. A Multi-Link 8 (Abbott Vascular) stent with 3 mm ID and 28mm length was deployed at nominal pressure (NP) 12atm at an angle of 90° in the BDS labs tube (thin tube). According to a private conversation Boston Scientific suggested that Multi-Link fatigue lives almost 100 times greater than Cypher. Hence, due to time limit the test rig subjects the stent to a repetitive hinge-motion type loading, with an angulation movement of 25° between 95° and 70° to accelerate the fracture time (Ino et al. 2009).

### **5.2.4. Stent Durability Experiment**

The test rig was upgraded in the Mechanical Workshop at University of Hull (see Figure 5.5A) (funded by the Hull and East Riding Cardiac Trust) for the full study in order to test larger number of stent in angulated mock artery up to 38 units simultaneously, subjecting each stent to an identical repetitive hinge motion loading as well as the speed of testing can be adjustable to higher frequency between 400 and 1500rpm.

The initial angle of the artery was set to be  $90^\circ$ , with the stent deployed at this initial angle. This was then subjected to a  $20^\circ$  continuous repetitive hinge-type movement, at a rate of 1100rpm, which is almost 6.5 times faster than the previous test rig. To clarify the loading, a vessel initially angulated at  $90^\circ$  would have that angle further exacerbated to  $70^\circ$  during testing ( $10^\circ$  from each side of loading arm) (see Figure 5.5B).

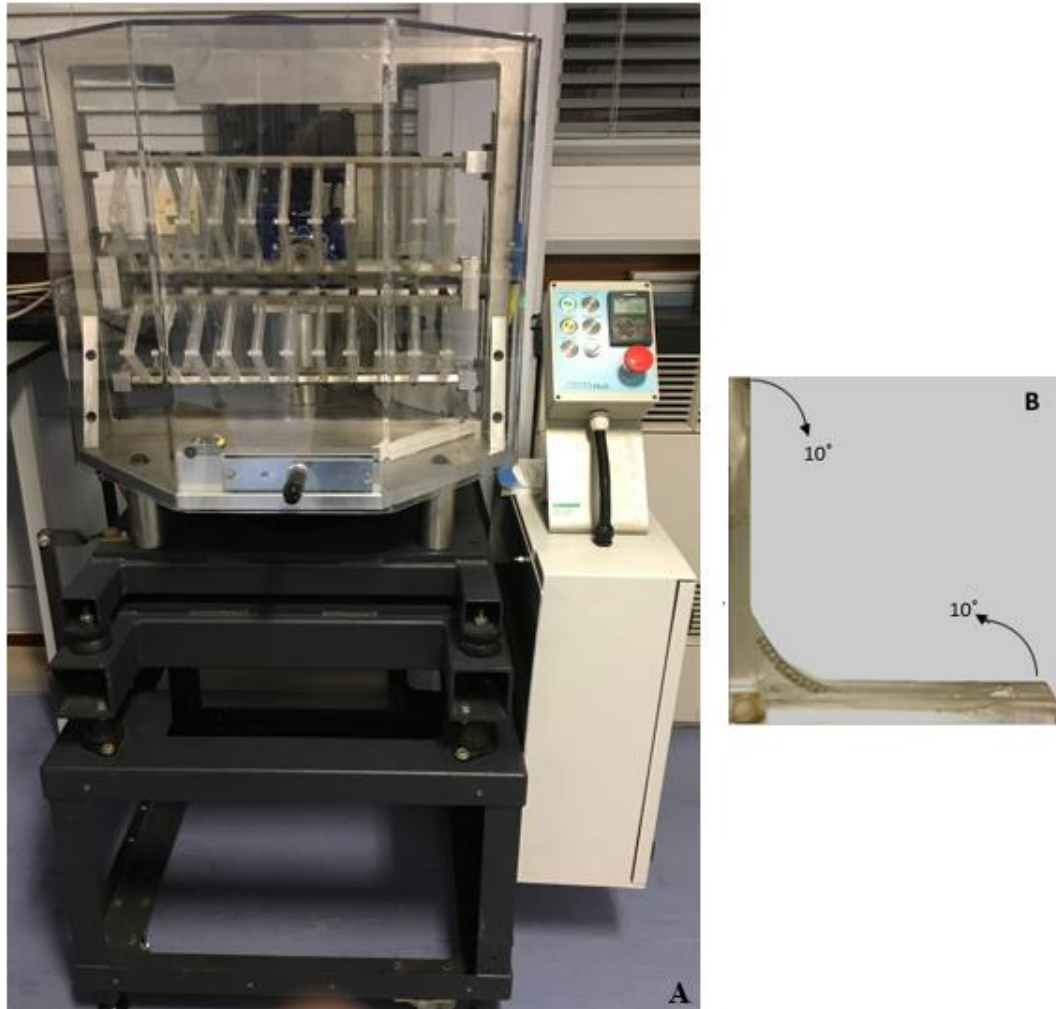


**Figure 5.5: A) Upgraded test rig, optimised the capacity and speed of test. B) Inset of stent deployed in testing arm at initial  $90^\circ$  showing direction of hinge-movement totalling  $20^\circ$ .**

The full study went ahead with 9 each of the following stents: Multi-Link Vision® (Abbott Vascular), PRO-Kinetic Energy (Biotronik), BioMatrix NeoFlex™ (Biosensors International) and Promus PREMIER (Boston Scientific), all of 3mm ID, length 28mm,

except Prokinetic which were 30mm (as 28mm is not available) were tested. An example of deployed stents of each design is shown in Figure 5.6.

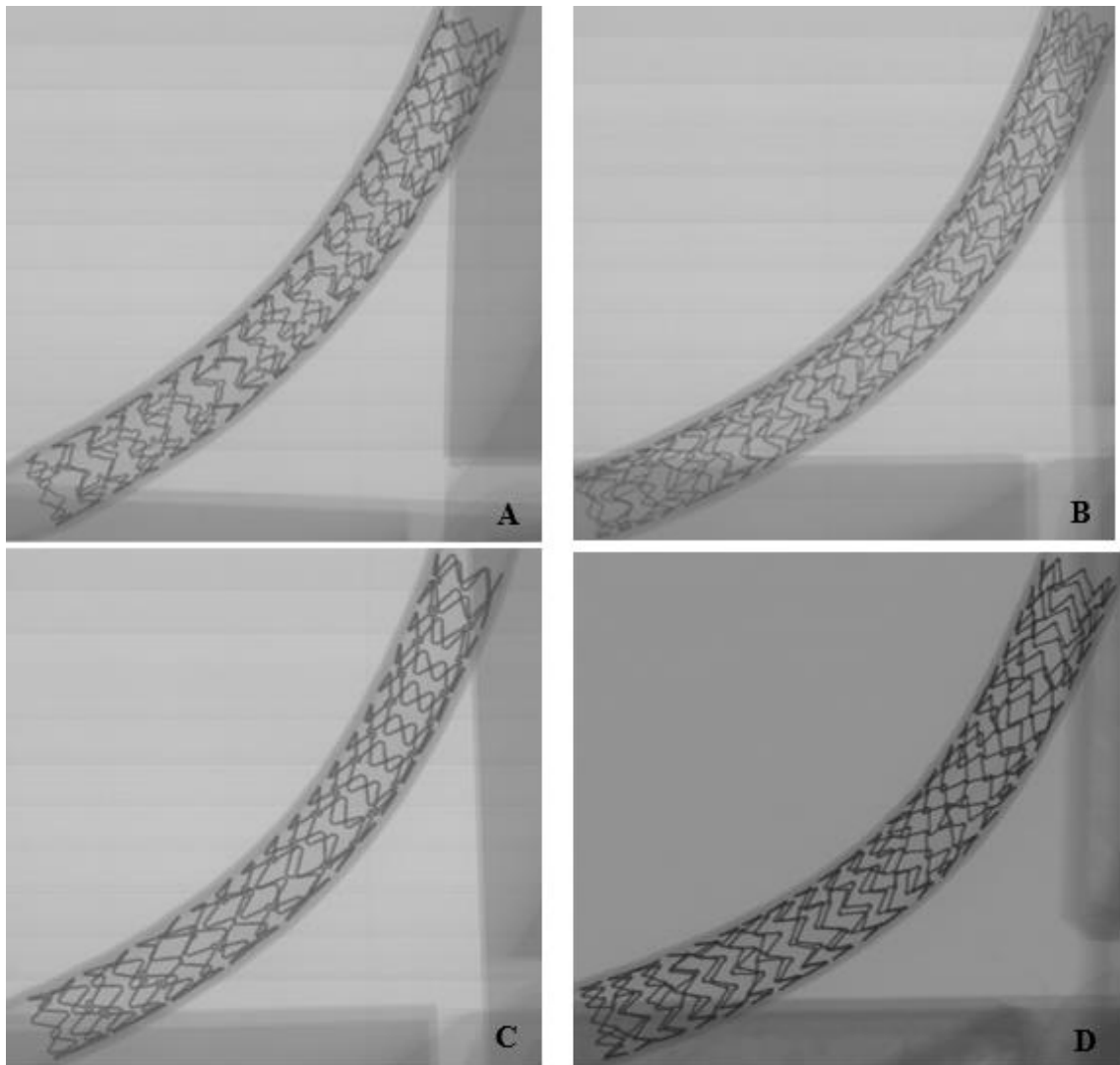


**Figure 5.6: Sample of micro-CT images of stents: A) Multi-Link Vision, B) PRO-Kinetic Energy, C) BioMatrix, and D) Promus PREMIER when deployed at initial 90° into the mock artery tube.**

All stent samples were deployed according to the manufacturers guidelines at nominal pressure (NP) (see Table 5.2) into the BDC labs tube (supplied by BDC Laboratories, Wheat Ridge CO, specification: straight silicone mock vessels, ID = 3.0 +/- 0.2 mm at 100 mm Hg, wall thickness= 0.45 mm, length= 15 cm, radial compliance = 5-7% per 100 mm Hg at 120/80 mm Hg and 1.2 HZ). A procedure to maximise test time and minimise disruption to the rig was adopted based on the pilot studies, with all stents examined in the  $\mu$ CT at least every 7 million cycles to identify any fractures.

Stent type	NP*	Material	Coating	Strut thickness	Stent design
<b>Multi-Link Vision</b>	12atm	Cobalt Chromium, L605	–	81 $\mu\text{m}$	Open cell, sinusoidal hoops
<b>PRO-Kinetic Energy</b>	9atm	Cobalt Chromium, L605	PROBIO® Amorphous Silicon Carbide	60 $\mu\text{m}$	Open cell, double helix
<b>BioMatrix NeoFlex</b>	6atm	316 L Stainless Steel	Poly-lactic Acid & BA9	120 $\mu\text{m}$	Open cell sinusoidal hoops
<b>Promus PREMIER</b>	9~10atm	Platinum Chromium	Everolimus	81 $\mu\text{m}$	Open cell, sinusoidal hoops

**Table 5.2: Specification of the four stent designs tested. (NP= Nominal pressure for 3mm ID)**

### 5.3. Results

All the stent samples were tested simultaneously the under same conditions throughout the *in vitro* experiment. Each stent specimen was examined by micro-CT scan machine at specific intervals to identify any strut fractures.

#### 5.3.1. Testing Protocol 1 Result

The inspection scan to look for fractures was limited to availability of the  $\mu\text{CT}$  scanner. Also the motor of the test rig over heated and needed to cool down to able to continue. Additionally, according to Lee et al. (2007) study, the time of stent fracture was reported in the range of 7 to 620 days. Therefore, a  $\mu\text{CT}$  scan examination was performed on all 3 stents at 552,257 cycles (equivalent to approx. 5.5 days of heart beat), identifying 3 fractures in the thick tube sample (see Figure 5.7) and 1 in the thinner tube (see Figure 5.8).



**Figure 5.7: Fractures observed in Cypher stent deployed in silastic tubing of wall thickness 0.75 mm, after 552,257 cycles.**



**Figure 5.8: Single fracture observed in Cypher stent deployed in silastic tubing of wall thickness 0.45 mm, after 552,257 cycles.**

The sampling frequency was subsequently increased with the stents being examined in the  $\mu$ CT scanner on a daily basis. Despite initially showing less fractures for the same number of cycles, as the testing continued the stent deployed in the thinner tube was seen to fracture more readily. The test was continued up to approximately 4.2 million cycles, where the stent in the thinner tube appeared a complete disconnection with total 16 fractures at different region as shown in Figure 5.9, while it was only 6 fractures for the stent in the thick tube (see Figure 5.10).



**Figure 5.9: 16 fractures observed in Cypher stent deployed in silastic tubing of wall thickness 0.45 mm, after approx. 4.2 million cycles.**

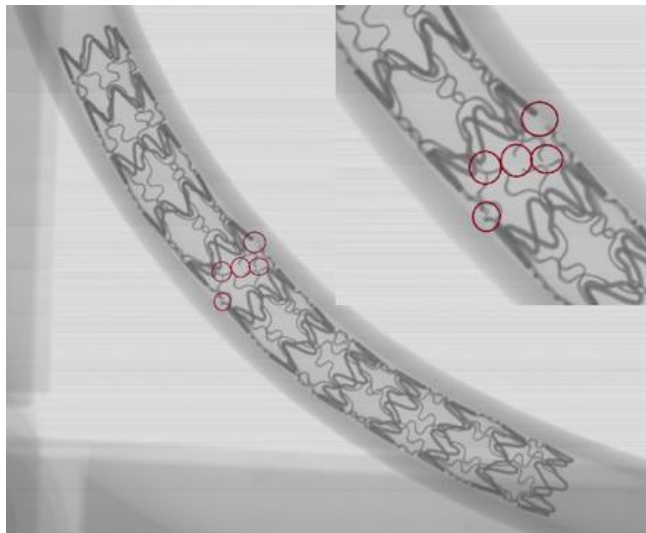


**Figure 5.10: 6 fractures observed in Cypher stent deployed in silastic tubing of wall thickness 0.75 mm, after approx. 4.2 million cycles**

A graphical representation of the time scale and fracture frequency of Cypher stents deployed in both thin and thick silicon mock artery during the pilot test is shown in Figure 5.11. It clearly shows that fractures in the thin tube took place over time/cycles until total separation occurred. Up to approximately 1.4 million cycles, strut fractures occurred gradually, and once 2.5 million cycles were reached a steep increase in the number of stent fractures observed in the thin tube was evident. Conversely, the stent housed in the thick tube was more stable particularly between 1.4 and 3.4 million cycles

where there was no new fractures detected, and by the end of the experiment only 6 fractures were identified.

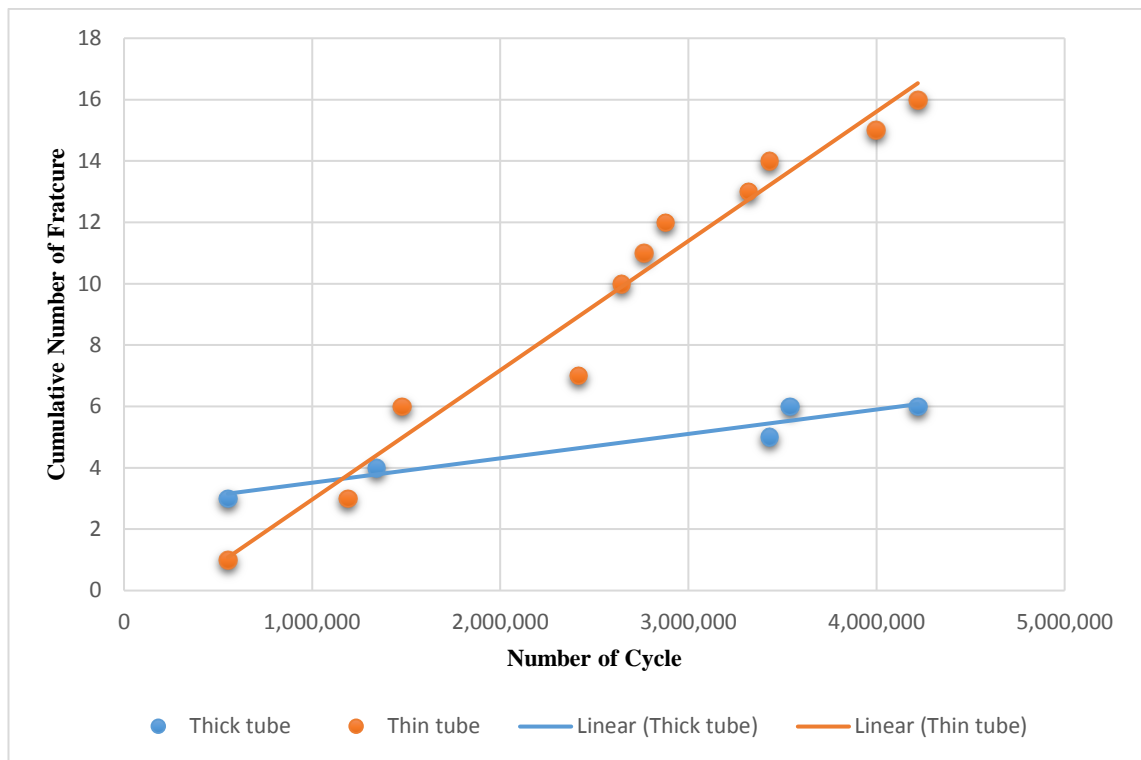


**Figure 5.11: Fracture frequency of deployed stent in silicon mock artery with two different wall thicknesses. Blue line indicates the progress of fracture in thicker tube versus orange line for the thinner tube.**

### 5.3.2. Testing Protocol 2 Result

Further pilot work was ongoing with a Multi-Link 8 (Abbott Vascular) stent after testing Cypher stents with 5° rise in changing angle. Notwithstanding, the Multi-Link 8 was subjected to greater displacement, it survived longer than the Cyphers and the first fracture occurred at 21.5 million cycles (approx. 215 days) . Almost after 2 more million cycles the total number of fracture reached to 4, and by end of this phase of study at 225 million cycles (approx. 2,232 days of heart beat) 5 fractures were identified. Figure 5.12 shows the site of fractures where all of them occurred in the curvature of the connectors. Also 4 fractures were placed at the region where underwent hinge-type movement and experienced higher stress.

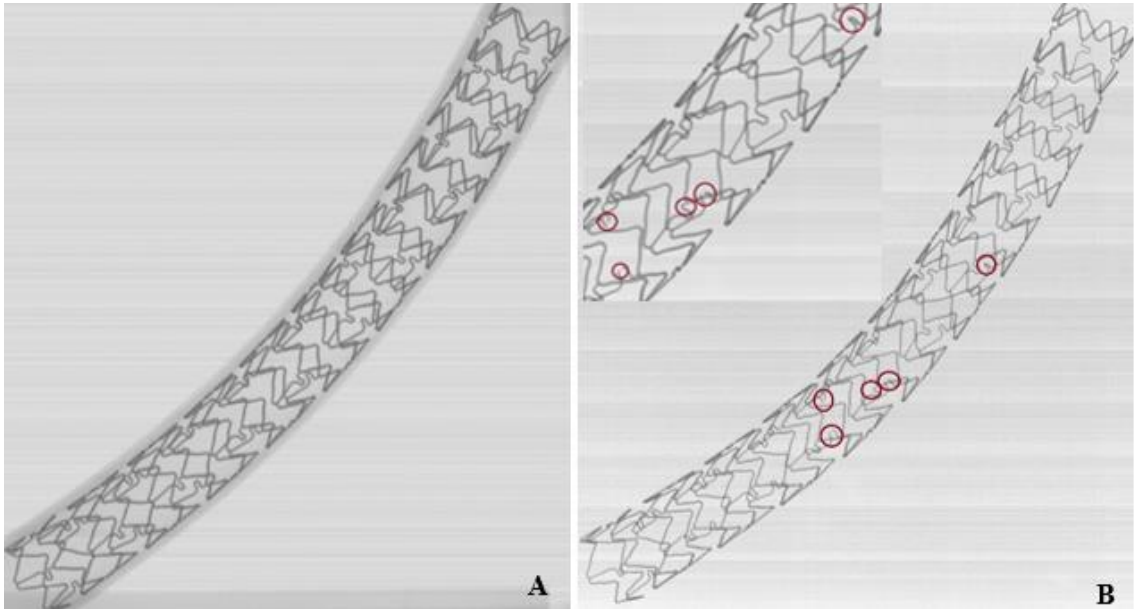


**Figure 5.12: Micro-CT images of deployed Multi Link 8 stent at 90° initial angle in thin tube (BDS labs tube). A) Deployed stent before starting the test, B) Red circles define the strut fracture after 225 million cycles where the stent was subjected to 25° (between 95° and 70°) repetitive hinge-type movement.**

### 5.3.3. Stent Durability Result

The repetitive bend test was continued up to 300 million cycles. Fractures have been identified in 7 stents ( $34.67 \pm 28.78$  million cycles), and are limited to only the BioMatrix NeoFlex™ (Biosensors International), and no sign of strut fracture was identified in the Multi-Link Vision, the Pro-Kinetic and the Promus PEIMER samples.

An example of micro CT images of three stent designs; Multi-Link Vision, Pro-Kinetic and Promus PEIMER are shown in the Figure 5.13 to 5.15, respectively, after deployment in to the mock artery at initial angle of 90°, and at the end of the experiment at 300 million cycles. Also, it can be seen that by end of the test, these stents did not have any significant longitudinal and radial deformation.

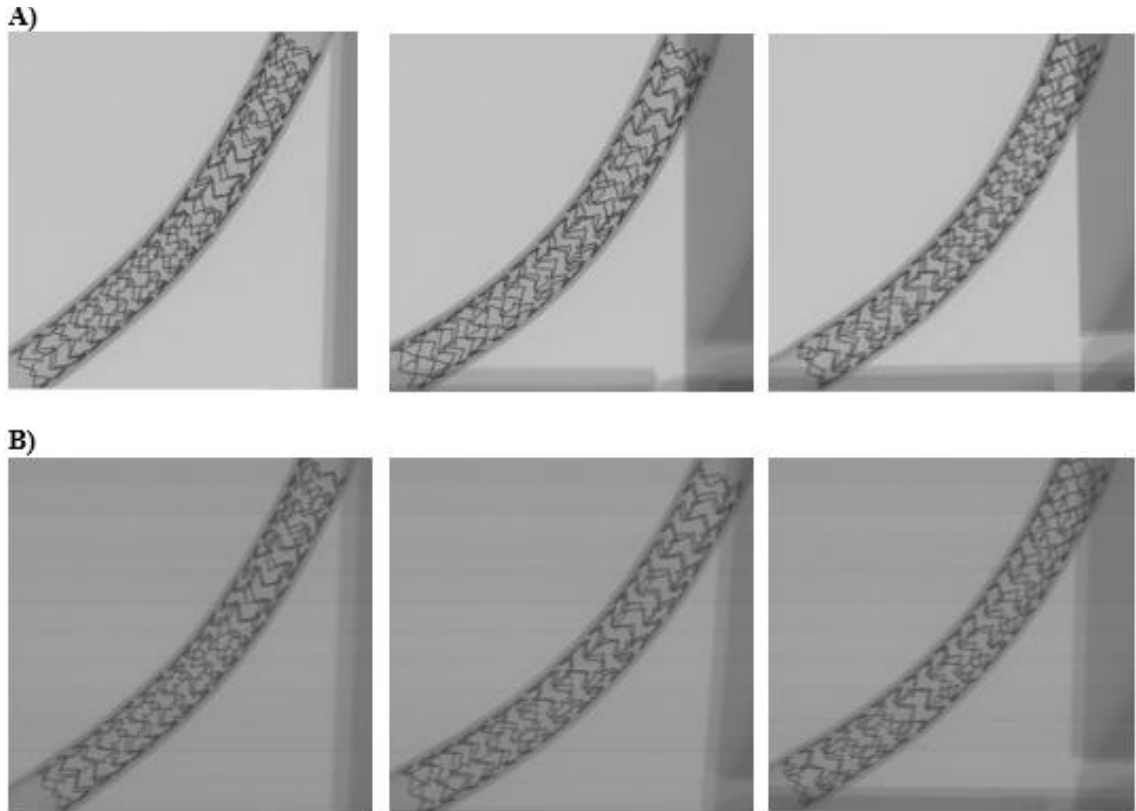


**Figure 5.13: Micro-CT images of three samples of Multi-Link Vision stent design: A) Deployed stent in to the mock artery at initial angle of 90° before starting the test, B) After 300 million cycles no fracture was identified**

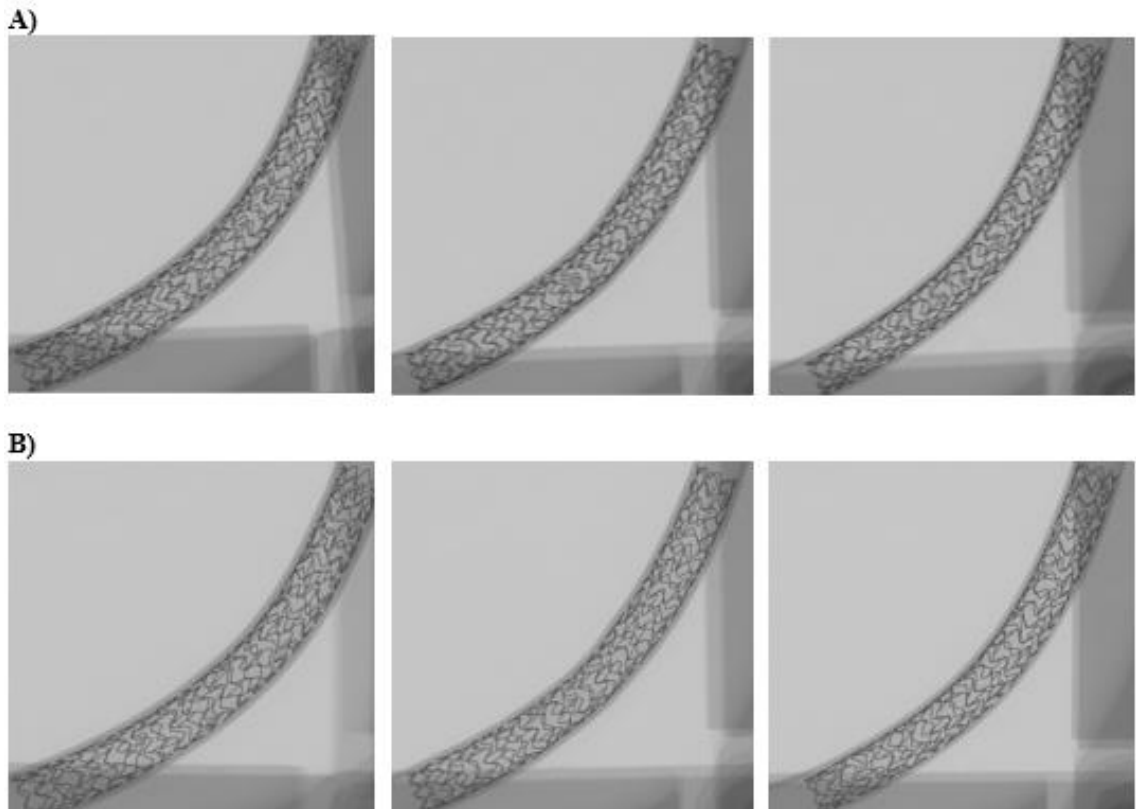


**Figure 5.14: Micro-CT images of three samples of PRO-Kinetic Energy stent design: A) Deployed stent in to the mock artery at initial angle of 90° before starting the test, B) After 300 million cycles no fracture was identified.**

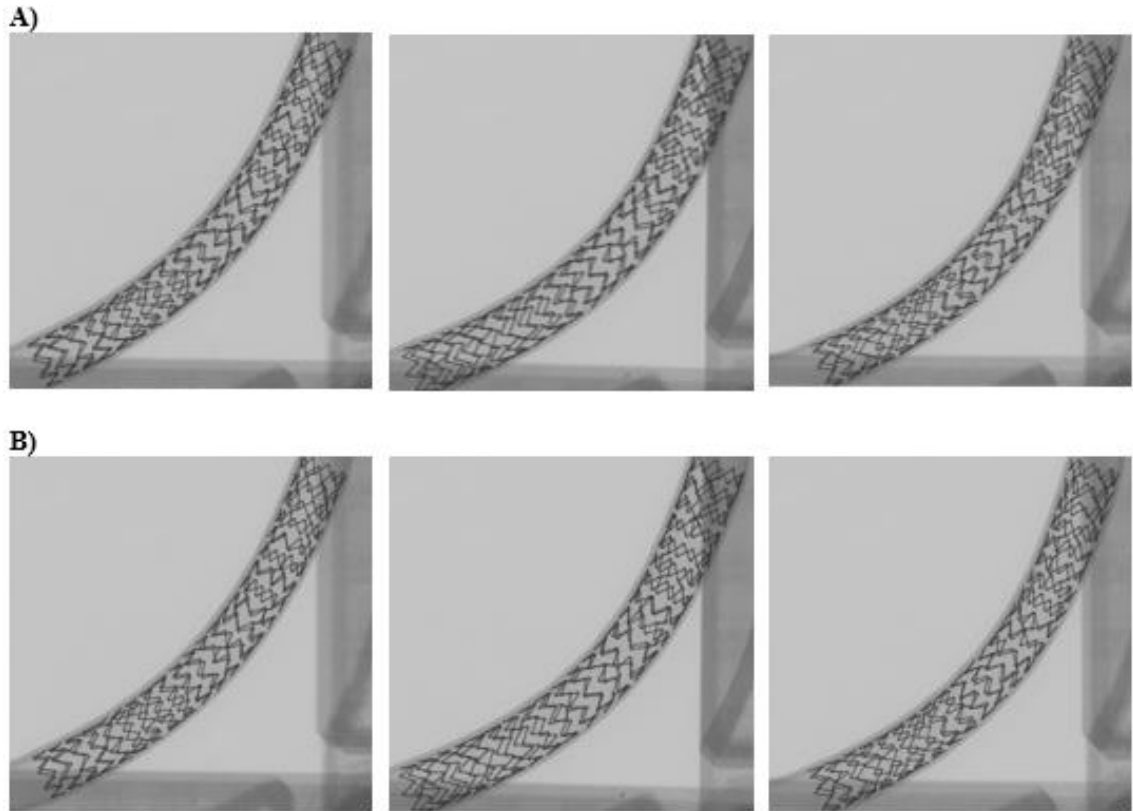


**Figure 5.15: Micro-CT images of three samples of Promus PREMIER stent design: A) Deployed stent in to the mock artery at initial angle of 90° before starting the test, B) After 300 million cycles no fracture was identified.**

In the BioMatrix design, fractures were first seen to occur at 13.4 million cycles (which relates to approximately 133 days *in vivo*), where fractures were observed in 2 stents, (one strut fracture, and 2 strut fractures). By 77 million cycles (763 days), 7 of the Biomatrix stents had fractured, exhibiting between one and four strut fractures, while in other two BioMatrix specimens no sign of fracture was identified by end of the experiment at 300 million cycles. Strut fracture progress in the BioMatrix samples from initial stage (deployed stent at initial degree of 90°) to the end of the test at 300 million cycles are shown in Figure 5.16 to 5.18.

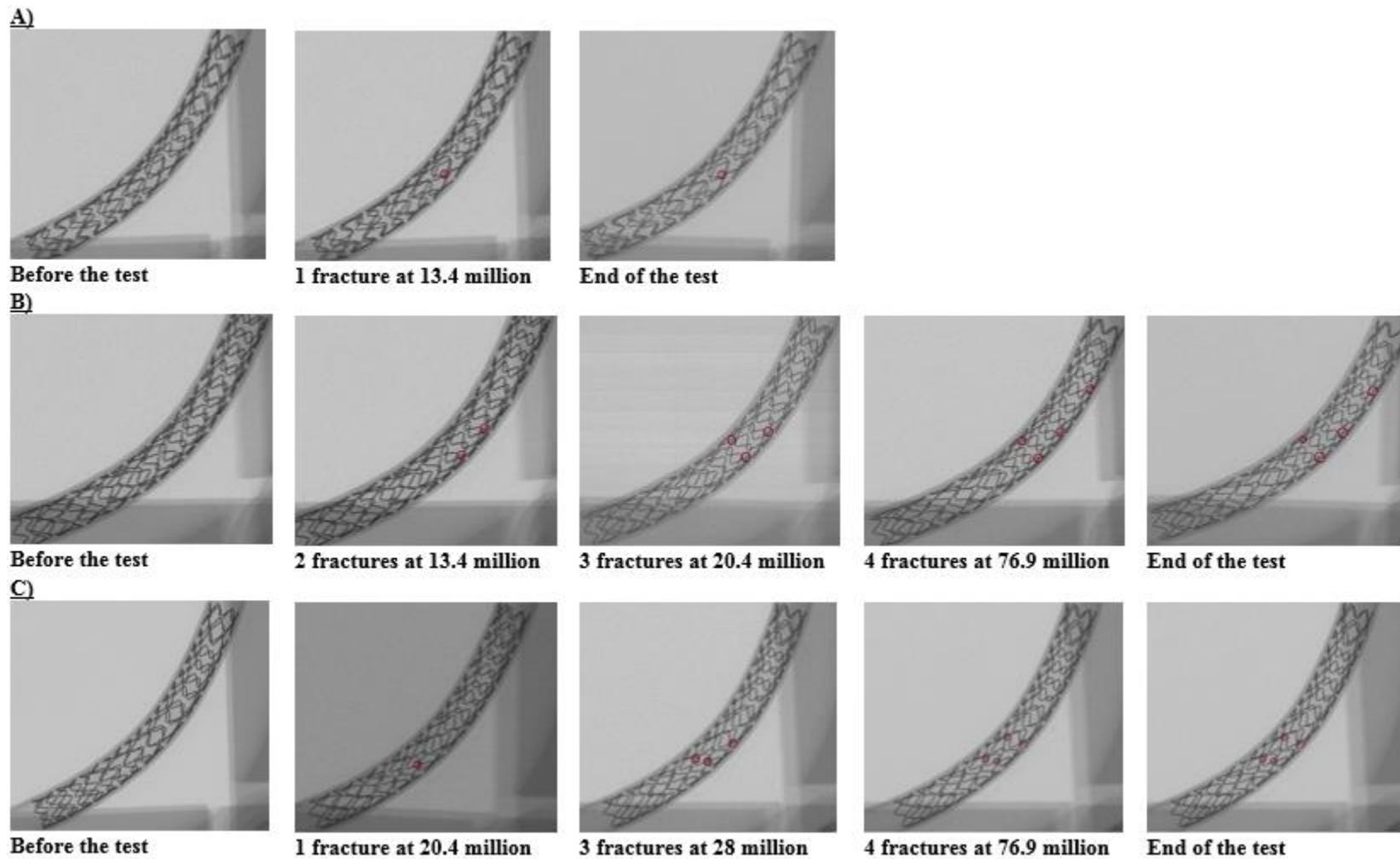
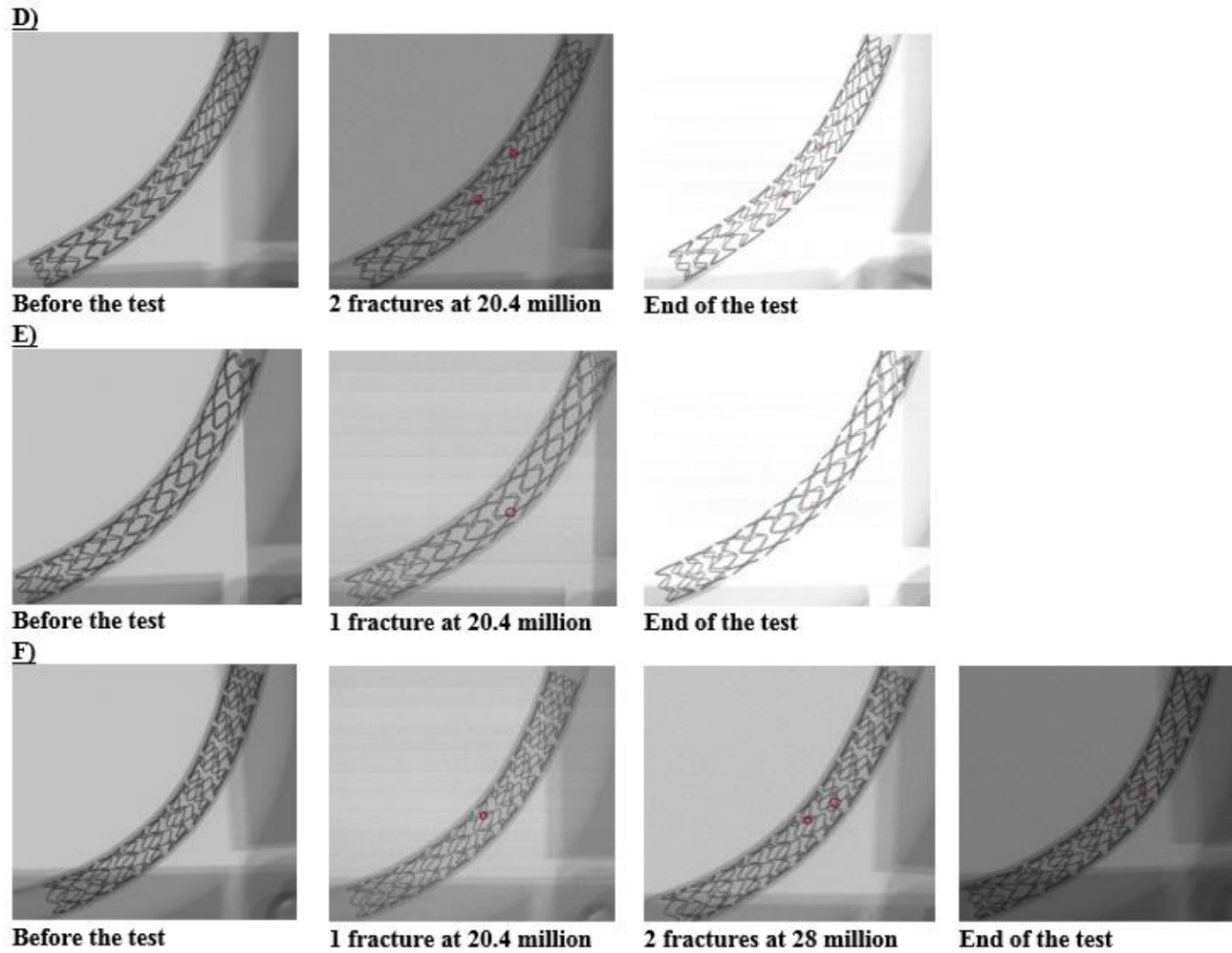


Figure 5.16: Micro-CT images of sample A to C of BioMatrix stent design. The progress of strut fracture from beginning to end of the experiment at 300 million cycles.



**Figure 5.17: Micro-CT images of sample D to F of BioMatrix stent design. The progress of strut fracture from beginning to end of the experiment at 300 million cycles.**

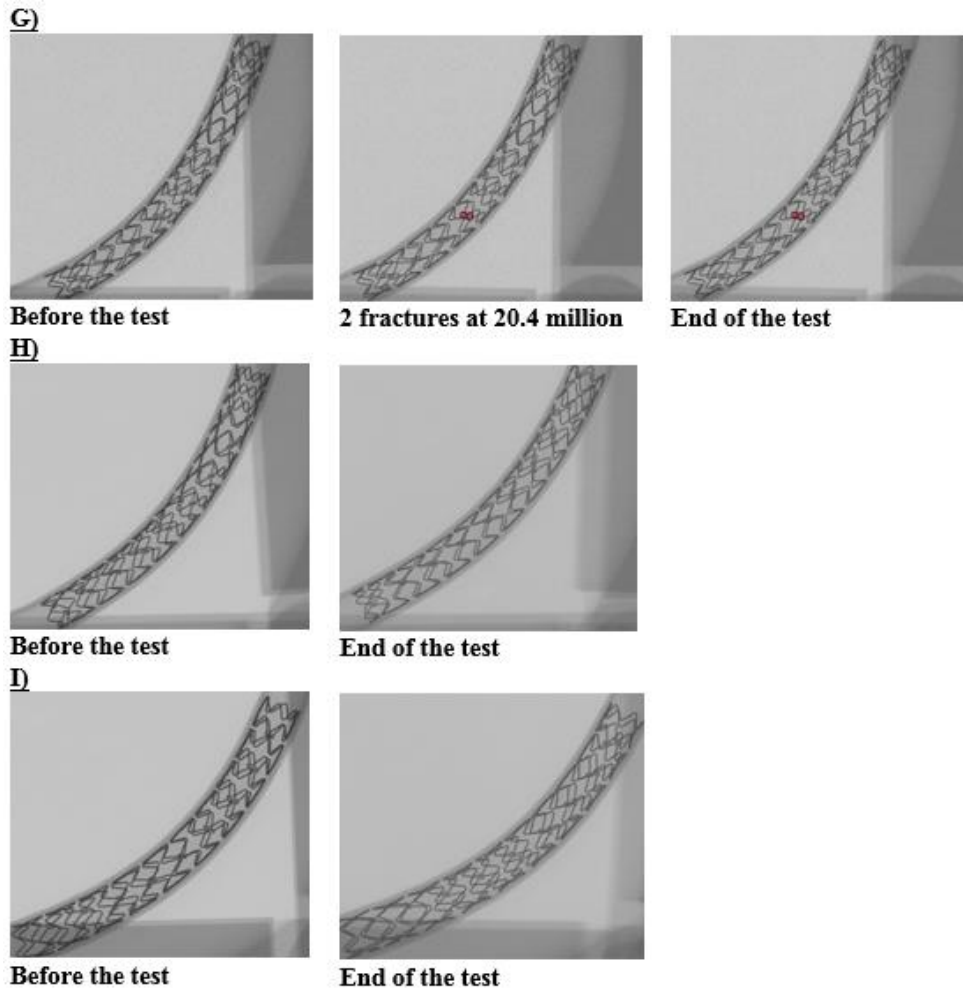


Figure 5.18: Micro-CT images of sample G to I of BioMatrix stent design. The progress of strut fracture from beginning to end of the experiment at 300 million cycle

Location and total number of strut fracture within all stent samples after 300 million cycles repetitive bend test are shown in Table 5.3.

Stent Type	Number of Sample	Total Fracture	Site of Fracture
Multi-Link Vision	9	0	-
Pro-Kinetic	9	0	-
Promus PREMIER	9	0	-
BioMatrix Neoflex	9	17	In the “S” shaped connectors, between hoops
	Sample A	1	In the “S” shaped connectors, and in the middle segment (hinge point).
	Sample B	4	All in the “S” shaped connectors. 3 fractures in the middle and 1 at the proximal segment.
	Sample C	4	All in the “S” shaped connectors, and in the middle segment.
	Sample D	2	All in the “S” shaped connectors, and in the middle segment.
	Sample E	1	In the “S” shaped connectors, and in the middle segment.
	Sample F	2	All in the “S” shaped connectors, and in the middle segment.
	Sample G	2	All in the “S” shaped connectors, and in the middle segment.
	Sample H	0	-
	Sample I	0	-

**Table 5.3: Site and total number of strut fracture within the four stent designs, 9 of each after 300 million cycles bend test**

Furthermore, Figure 5.19 shows  $\mu$ -CT images of these fractures in the BioMatrix samples with total A) one B) four, C) four, D) two, E) one, F) two, and G) two struts fracture, where all fractures were seen to occur at the ring linker parts of the stent and in the areas which would undergo the most severe tensile loading (Aoki et al. 2007) , (i.e. side portion).

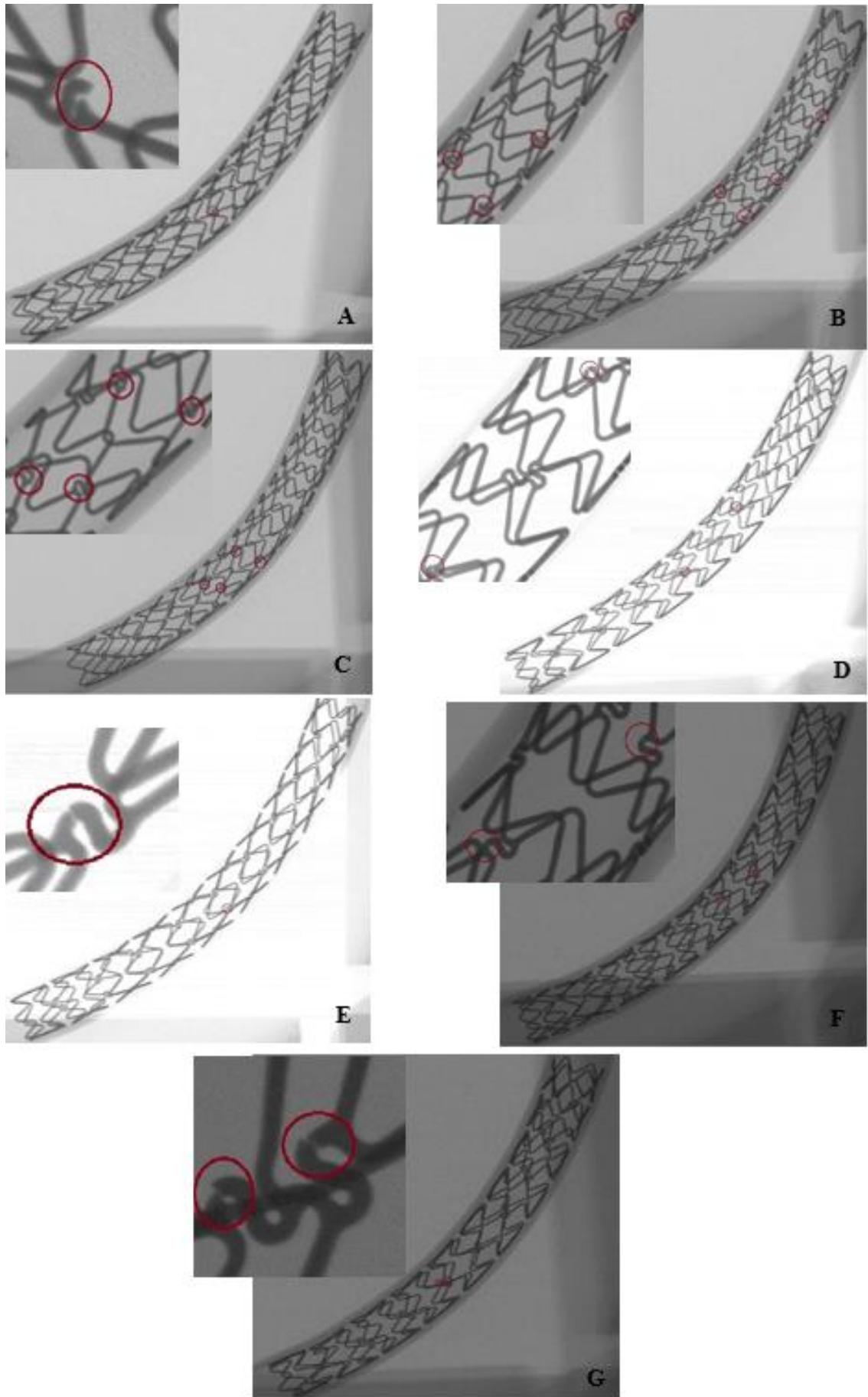


**Figure 5.19: Representative  $\mu$ -CT images of the strut fracture in 7 samples of BioMatrix stent design. With total A) one B) four, C) four, D) two, E) one, F) two, and G) two struts fractures.**

Although, strut fractures were observed within 7 BioMatrix stents, however, the time and frequency within each stent were different as is shown in Figure 5.20. It clearly shows that stent fracture is more likely to occur in the earlier 50 million cycles after implantation, while the risk of fracture decreases over the time/cycles.

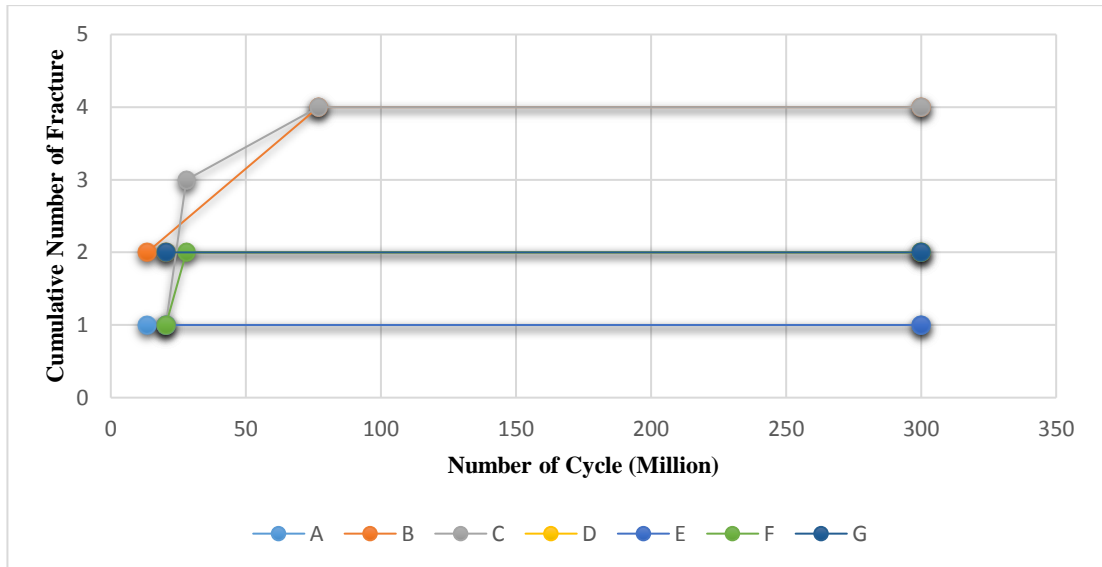


**Figure 5.20: Number of stent strut fractures observed for BioMatrix stents, vs. number of cycles of 20° hinge loading, on a vessel of initial angulation of 90°.**

Figure 5.21 illustrates the risk of strut fracture within BioMatrix stent samples (n=9) with respect to the number of bend cycles. It shows around 20 million cycles struts are more likely to fracture, while over 70 million cycles the risk has been minimized.

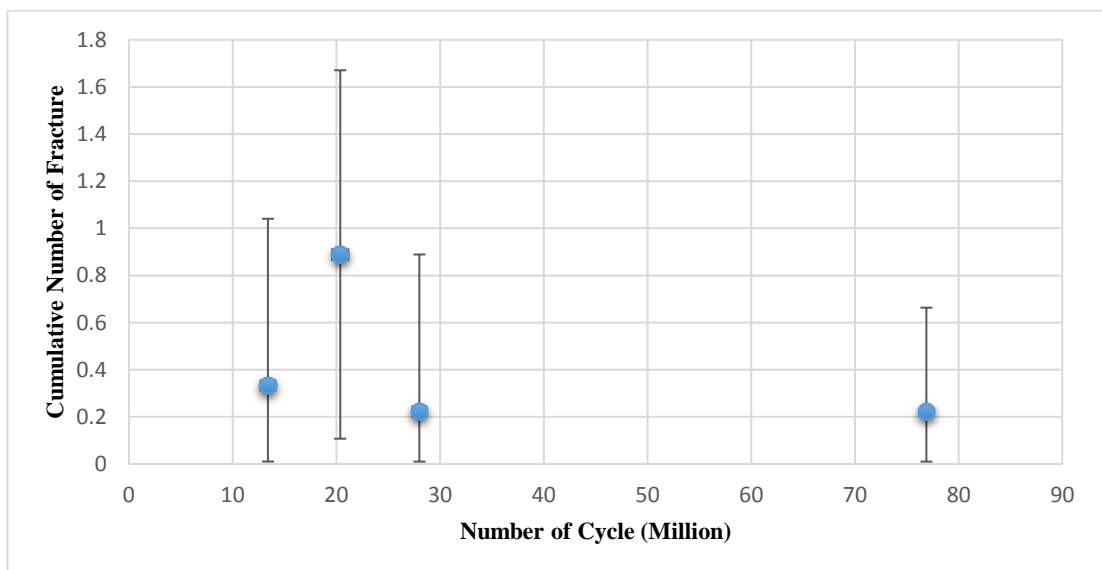


**Figure 5.21: Mean and standard deviation (SD) of number of strut fracture to number of cycles for the BioMatrix stent design.**

## 5.4. Discussion

The experiment compared four different coronary balloon expandable stents (BMS as well as DES), which underwent accelerated 20° repetitive hinge-type movement in order to investigate their susceptibility to strut fracture. The results (see Table 5.3) illustrated that the BioMatrix Flex had less resistance to fatigue and strut fracture under repetitive hinge loading in an angulated artery. The fractures were observed between 13.5 and 75 million cycles ( $34.67 \pm 28.78$ ) (equivalent approx. to 133 and 744 days of normal heart beat). The Multi-Link Vision, PRO-Kinetic Energy and Promus PREMIER survive without any strut fracture by end of the experiment at 300 million cycles.

The rate of stent fracture (SF) incidence were reported between 0.8% and 8% in available clinical studies (Wiktor et al. 2016) (see Section 3.1), where most of them occurred in the first stent generation specially Cypher design. Advance technology, improving the stent structure, and using new alloys such as Co-Cr and Pt-Cr allowed to manufacture more flexible and durable coronary stents, known as second generation DES. Although, the second stent generation has improved the PCI procedure and significantly reduces the risk of restenosis, still SF is known as a challenging phenomenon. It is important to diagnose and minimize the risk of stent fracture, as it can lead to an increased risk of several undesirable clinical complications such as in-stent restenosis (ISR), stent thrombosis (ST), aneurysm formation, acute myocardial infarction (MI) or sudden death (Lee et al. 2007, Kuramitsu et al. 2012, Chakravarty et al. 2010).

Little *in vitro* experimental work has been conducted on the examination of SF at bifurcations or when deployed in highly angulated vessels. In Kinoshita. et al (2009) study two different stent designs were tested in a silicon t-tube, subjecting them to 20° deflection. All fracture were observed with the Cypher design lasting only a mean of  $31.3 \pm 7.6$  minutes. Clearly this is not representative of *in vivo* stent life, and the Cypher

stents are known to fracture and not used anymore. Also few experimental details are given (e.g. silicon tube properties) and therefore it is difficult to assess the reason for this early failure. Later, Ormiston et al. (2015) conducted an experiment to simulate the cyclic bending of overlapping stent. Although, fractures were observed in the BioMatrix Flex, Vision, and Multi-Link 8, yet the number of testing cycle was much less than the suggested time life of coronary stent 400 million cycles by FDA. Also the test was performed without and intimal coverage for the stents, which can increase the risk of fracture. Other studies such as Mori & Saito (2005) and Szabadits et al. (2008) conducted different bending point experiment to evaluate different type of stent structure and stiffness, which they were not close to the *in vivo* conditions. In addition, Murphy et al. (2003) tested different thickness of stainless steel to investigate the effect of the strut size on strain/stress. Ormiston et al. (2014) examined longitudinal strength of different stent designs under a compression load, and Ng et al. (2016) examined effect of overexpansion on the SF risk. Although, the results of these studies illustrate useful information, but none of them study mechanism of SF in an angulated artery under repetitive hinge-type movement.

Pilot testing has shown that the test rig is capable of causing stent fracture under physiological representative conditions in a timely manner. The fractures observed occurred in areas of the stent that vessels subjected to hinge motion. The optimum sampling frequency has been identified, and the use of high specification tubing, representative of arteries, has been justified as it has been shown that fractures occur more rapidly in the thinner tubing, as an *in vitro* bending experiment suggested that intimal coverage (e.g. thicker tube) protects the stent and then reduce the risk of strut fracture (Ormiston et al. 2015). It was noted that Cypher stents are known to fracture, hence further pilot work was continued with a Multi-Link 8 stent. Once again the results illustrated that how the stent structure plays a significant role to resist and prevent the

strut fracture. Cypher stents are known as a closed cell design and provide rigid platform which increases risk of stent failure consequently, under such a hinge-loading condition. The fractures were observed only after testing ~550,000 cycles in the Cypher samples, and total separation occurred at 4.2 million cycles (approx. 42 days). The Multi-link 8 survived almost 39 times longer than the Cypher stents, and the first fracture was identified at 21.5 million cycles, while the moving angle was 5° greater than Cypher, which was expected to apply higher stress at the bending area of the stent. Moreover, as one of the SF factors relate to stent material property, Multi-Link 8 stent benefits from new alloy Co-Cr which yield strength and ultimate tensile stress (UTS) is almost twice as the stainless steel in Cypher (see Table 5.1), thus its resistance to fatigue and fracture is higher.

Following the pilot work, the full study was performed to test 9 stents each of 4 designs; BioMatrix Flex, Multi-Link Vision, PRO-Kinetic Energy and Promus PREMIER. Although, all the designs are open cell, still each of them provides a unique structure. Micro-CT images (see Figure 5.6) clarified that Multi-Link Vision, BioMatrix and Promus PREMIER have similar sinusoidal structure, however in Multi-Link cells are connected by three U shaped bridges, BioMatrix cells are connected by two S shaped bridges, and in Promus PREMIER cells are connected by two straight bridges. Whereas PRO-Kinetic Energy consist helical meanders structure and longitudinal connectors.

In the current study, fractures have been identified in 7 stents, and are limited to only the BioMatrix, which it was reported as the most susceptible stent design to fracture in a mechanical experiment by Ormiston et al. (2015). Fractures were first seen to occur at 13.5 million cycles (relates to 133days), where fractures were observed in 2 stents, (one strut fracture, and 3 strut fractures), and then by 77 million cycles (763 days), 7 of the Biomatrix stents had fractured, exhibiting between one and four strut fractures (see Figure 5.16 to 5.18). Whereas Multi-Link, PRO-Kinetic, and Promus PREMIER did not

fracture up to 300 million cycles, and clinically it has been observed that the mean time to stent fracture is 450 days  $\pm$  330days, with little likelihood of new fractures being observed after this time (Lee et al. 2009). Moreover, Figure 5.21 shows most critical time of fracture is around 20 million cycles (approx. 200 days) and over 77 million cycles, the risk of fracture has been minimised.

Interestingly, BioMatrix has the thickest struts (120 $\mu$ m), so it has better resistance to fatigue and fracture, but will be stiffer overall. Nonetheless, improvement in new alloys Co-Cr and Pt-Cr allows to construct stent with thinner struts in Multi-Link, PRO-Kinetic, and Promus PREMIER (varied 60 to 81  $\mu$ m) without any effect on the fatigue resistance. Thus, it can be said that one of the fracture factors in BioMatrix is endurance limit, which in Co-Cr and Pt-Cr alloy is greater than stainless steel material.

All fractures were seen to occur at the ring linker (S-shaped connector) parts of the stent (see Figure 5.19) and in the areas which would undergo the most severe tensile loading (Aoki et al. 2007, Nakazawa et al. 2009, Ormiston et al. 2015) (i.e. middle segment, side portion). Although, existence of curvature in connectors helps to increase flexibility of stent, but it also can be an area where stress accumulate and increase risk of the SF. Hence, stent design is another criteria in stent fracture. Double helix structure in PRO-Kinetic improves flexibility as well as smooth deliverability (Biotronic 2016), and in Promus PREMIER straight connectors reduce the risk of stent fatigue.

The number of connectors between hoops in the BioMatrix, Multi-Link Vision, Promus PREMIER are 2, 3 and 2 (4 between proximal hoops), respectively. Although, it has been reported that fewer number of connector between hoops in a stent design provides better flexibility and resistant to a fracture (Ormiston et al. 2011), but the results of this study illustrates that all fracture were taken place in the design which have less number of connectors between the hoops. Furthermore, as in the Biomatrix design , hoops are

connected by 2 connectors, and in the sample B, C, and G there are 2 strut fractures where both of them were occurred between same hoops, thus it caused total transected in these samples (see Figure 5.19).

The polymeric coating of DES might not have any significant influence on fatigue failure progress as PRO-Kinetic and Promus PREMIER did not fracture in our study. Also in the pilot test, fracture occurred in BMS Multi-Link 8 design, though the movement was 5° greater. However, the incidence of SF in DES have been reported higher than BMS clinically (Nakazawa et al. 2009), and it can be explained by using DES in more complex lesion (e.g. RCA, calcified lesion) which are associated with higher rate of fracture.

These results yielded useful information on the incidence and progression of fracture in the different stent designs, particularly for those deployed in challenging loading conditions. Once again, the results clarified that numbers of factors such as, material and design play an important role in a stent failure process.

## 6. Discussion

The work covered in this thesis is discussed further in this chapter, highlighting the most significant findings and outcomes with regards to the aims of the project which were outlined in Chapter 1. Although the results have been already discussed in the previous chapters individually, a general overview of the main aspects is taken and demonstrates how the work contributes to the understanding of the mechanisms of stent fracture.

Coronary heart disease (CHD) is a life threatening phenomenon and it is a result of an occlusion in the coronary arteries. Percutaneous coronary intervention (PCI) is the most common treatment which has been developed over the time (particularly stenting). Stent fracture (SF) is a potential complication which is associated with several factors such as total stent length, artery tortuosity, overlapping stents, stent design, hinge motion, and calcification. Clinical observation has shown that though SF is a rare phenomenon, it still could cause serious clinical complications and intensify the risk of morbidity and mortality (Garg & Serruys 2010).

Numerous studies have been conducted using computer modelling in order to simulate different stent designs and stenting procedures to evaluate the influence of correlated factors of SF. Harewood & McHugh (2007) determined that thicker struts have higher resistance to metal fatigue while thinner struts provide better flexibility and have better resistance to fracture due to bending. Also Wei Wu et al. (2007) suggested that increasing plastic deformation leads to better flexibility. With regards to stress distribution, several computer models such as Marrey et al. (2006), Li et al. (2010), Ma (2011), Eshghi et al. (2011), and Barrera et al. (2012) identified that curved sections of the cell struts experience higher stress than the straight link bridges under repetitive cardiac cycles. In addition, the presence of plaque which is in direct contact with the stent, intensifies the stress at these locations, and consequently increases the risk of SF (Chua et al. 2004, Eshghi et al. 2011, Martin & Boyle 2013, Morlacchi et al. 2014). Other SF factors such

as overlapping stents, stenting in a curved vessel, and longer stent length have been proved to increase the risk of SF (Morlacchi et al. 2013, Wu et al. 2007, and Wong et al. 2009).

Likewise, several mechanical experiments have been performed to investigate different mechanical characteristics of stents. Examining strut thickness illustrated that thinner struts have a higher risk of fracture than thicker struts, also some segments might have local failure during dilation (Murphy et al. 2003). New alloys such as Co-Cr and Pt-Cr in the new generation of drug eluting stent (DES) have enhanced durability and fatigue failure and provide better platforms with thinner struts which are less susceptible to fracture. Nevertheless, many studies believe that stent design plays a more critical role. For instance, Ormiston et al. (2014) reported that stent design has a high impact on the stent longitudinal deformation. Also Szabadits et al. (2008) and Ormiston et al. (2015) concluded that less connectors between stent cells, increases the flexibility which leads to have higher resistance to fracture, however, it also increases the risk of kinking and longitudinal deformation. In Ormiston et al's (2015) durability experiment, it was observed that almost all of the strut fractures were placed at the curvature of connectors, where higher stress is predicted in the computer modelling studies. Ormiston et al. (2000) reported that stents became stiffer after expansion, and Ng et al. (2016) stated that over-expansion causes strut distortion and increase the risk of the failure.

Yet, none of these studies using computer modelling or mechanical testing, have explored the impact of vessel angulation on the behaviour of implanted coronary stents. Specifically, how the stresses within a coronary stent would be altered with increased artery angulation under cardiac motion? There were no previous investigations into the most critical vessel angulation quantify why coronary stents in arteries with an angulation of 70° and over are more prone to fracture. Additionally, the literature does not report any determining how the artery properties assigned to FE models can affect on the final results?

Furthermore, no study has performed an *in vitro* experiment to validate that is the time life of different commercial coronary stent designs, implant in such a conditions (i.e. curved vessel and then subjected to a repetitive movement) similar to their predicted life time? Investigate how stent design can have influence on stent flexibility as well as how advance material does improve and provide better the resistance? Additionally, does the mechanical testing meet the computer simulation results?

In this project an idealised stent model was created in an angulated artery model, and subjected to a uniform displacement loading. It provides an overview and understanding of the stent behaviour, when implanted in a tortuous artery under cardiac cycle movement, regardless of the stent design. Moreover, to ascertain whether the properties of the artery had an effect on the predicted stent stresses and deflection, the artery model was created as linear and non-linear hyper-elastic material. Through the simulation, different boundary conditions were taken into account in order to identify an optimum model which replicates the *in vivo* conditions, however, these models did not consider the *in vivo* environment completely. With regard to the different type of artery movement during cardiac cycles (Reichek 1999) and changing in angle at end of systole/diastole (Ino et al. 2009), the ideal models need to be constructed with minimum constrained area, and subjected to uniform load at the both ends of artery model.

Although, the stress distribution (not magnitude) within the stent model in the both linear and non-linear artery indicate almost similar results, where the highest stresses occurred at the bending point, but the stress range (magnitude) in the non-linear artery model is greater. Undoubtedly, the properties of the artery model can affect the stent results, as stiffness of non-linear material would be changed under applied load which leads to larger deformation and consequently greater amount of stress. In other words, it is essential to use appropriate material properties in order to have more accurate out comes.

As the focus of this study is to investigate the effect of vessel angulation on the stent, all the FE models were created with an initial angle range between 30° and 90°. Under the same displacement load, the displacement results illustrated that increasing in initial angle resulted in larger deflection. Clearly, deflection has a direct ratio with stress in metals (linear material), hence as the stent undergoes a load and following by displacement, because metals resist deflection and deformation, consequently resulting in stress. Furthermore, variation in stress within the stent model with respect to the initial artery angulation, proved that increasing in vessel angulation leads to increasing stent stress, where these variation are more moderate from 30° to 70°, and once the angle exceeded 70° the stress experienced rises more rapidly. It can be concluded that artery tortuosity has a critical impact on the stent fatigue failure and larger angle are more prone to increase the risk of SF, which is in agreement with clinical results where vessel angles of 75° and over were identified as a substantial independent predictor of SF (Sianos et al. 2004).

In additional, different range of uniform load; 5°, 10°, 15°, and 20° were applied to all the models. Of course, the trend of increasing in stress with the respect to vessel angulation are similar as has been discussed. However, they resulted in different stress magnitude due to low to high applied uniform displacement, and increasing in displacement caused increasing in deflection and stress as it is also reported by Wong et al. (2009).

Along with computer simulation, the second part of this work conducted a mechanical experiment to test 9 balloon expandable coronary stents each of 4 designs; BioMatrix Flex, Multi-Link Vision, PRO-Kinetic Energy and Promus PREMIER, all open cell with different structure as well as material composite. The results showed that the BioMatrix Flex design is the most vulnerable sample to fracture under accelerated 20° repetitive hinge-type movement in an angulated artery, which is in agreement with Ormiston et al. (2015) mechanical durability experiment. Total 17 strut fractures occurred within 7 samples of the BioMatrix Flex design between 13.5 and 75 million cycles ( $34.67 \pm 28.78$ ),

whereas no fracture was detected in the Multi-Link Vision, PRO-Kinetic Energy and Promus PREMIER after 300 million cycles. Although, it was tried to deploy all the stents sample under same condition and procedure, however, during the experiment stents might move along the tube and underwent larger/smaller hinge movement angle which it is also might be happened in *in vivo* circumstance.

Most of fractures occurred around 20 million cycles (approx. 200 days) and after 75 million cycles (approx. 750 days) it has been seen that it is unlikely to have a new strut fracture, as Lee et al. (2009) also reported in a clinical study the time of SF  $450 \pm 330$  days. Additionally, as the cells in BioMatrix design are connected by 2 S-shaped connector, fracture in two struts at same cells caused total transection in these samples.

Fewer number of connectors between stent cells and existence of curvature on these connectors both are to provide better flexibility. However, lack of connectors can be resulted in reduction longitudinal stent strength, as well as these curvatures have a high potential to be an area where stress accumulate and increase risk of the SF (Aoki et al. 2007, Nakazawa et al. 2009, Ormiston et al. 2015). With regards to this factors and the assumption from the FE modelling, as it was expected most of the fracture were observed to take a place at the curvature of the connectors (S-shaped connector) of the stent and in the areas which would undergo the most severe tensile loading (see Figure 6.1).

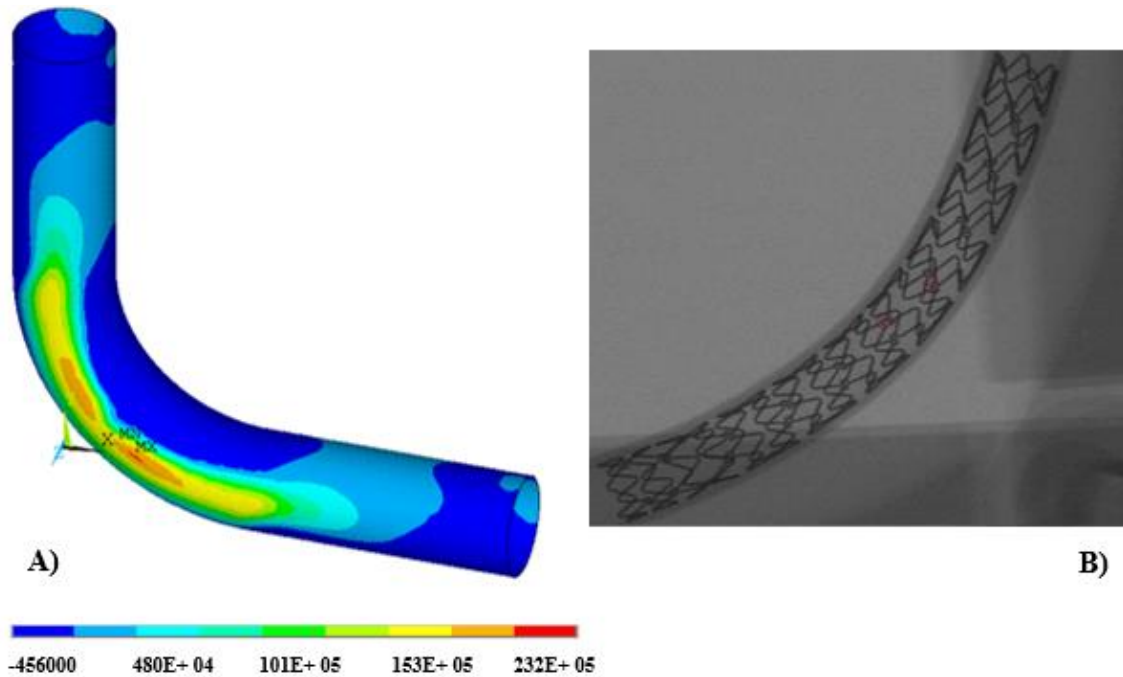


**Figure 6.1: A) Distribution of tensile stress within the stent model at initial angle  $90^\circ$ , when it was housed by non-linear artery model IX subjected to  $20^\circ$  displacement. B) Site of strut fracture in a BioMatrix sample, when it was deployed at initial  $90^\circ$  and then subjected to  $20^\circ$  repetitive hinge-type movement. Stent fracture occurs at sites of increased stress on the stent due to hinge movement.**

According to the Murphy et al. (2003) study, the thicker struts have better resistance to the fatigue failure, however, all fracture occurred within the BioMatrix design which had the thickest strut ( $120\mu\text{m}$ ) in compare with other tested stent designs (varied 60 to  $81\mu\text{m}$ ). Therefore, it can be said that new alloys Co-Cr and Pt-Cr in coronary stents allowed to manufacture more flexible thinner strut and greater endurance limit. Moreover, stent design have an important role in a coronary stent to resist and prevent strut fracture, where helical meanders structure and longitudinal connector in PRO-Kinetic improves flexibility and in Promus PREMIER straight connectors reduce the risk of SF. Subsequently, it can be said that polymeric coating of DES may not have any substantial impact on the SF progress as PRO-Kinetic and Promus PREMIER survive without any fatigue failure in our *in vitro* experiment.

In general, the idealised FE modelling of stent in an angulated artery models illustrated that area which is associated with hinge-type movement (bending point), experienced greater stresses which might lead to increased risk of metal fatigue and eventually strut

fracture. With regards to the literatures, it can be predicted that stent struts are more likely to fracture at the curvature of connectors in the hinge point, which it is in agreement with clinical observations. Moreover, with regards to all these finding the angle  $70^\circ$  and above is a critical condition in terms of stent fracture due to increase the stresses significantly, and it requires to take more consideration to treat this lesion including using suitable stent (e.g. appropriate design and composite) and technique.

As regards to the mechanical testing different designs may have different flexibility and resistance to the fatigue failure, and also advance material such as Co-Cr and Pt-Cr in new generation of DES improve the endurance fatigue limit in coronary stent in compare to stainless steel coronary stent. However, the outcomes illustrated that the fatigue life a balloon expandable coronary stent might not be same as the assumption of their fatigue life prediction for 10 years. It has been determined that strut fracture may occurred shortly after deployment in some stent design under a particular conditions. For example in this work time of strut fracture in the BioMatrix design which was deployed into an angulated mock artery, and subjected to a hinge-type movement was approximately  $344 \pm 285$  days. It yielded information about progress and incidence of SF, particularly for those designs which deployed in angulated artery and subjected to repetitive hinge-type movement. It exhibited that the time of fracture is unknown and it is highly dependent on several factors such as stent composition, stent design.

All these information and finding are improving and providing better insight for clinicians about mechanism of stent fracture. How the risk of SF would increase in such a challenging conditions, and how the risk can be minimized by choosing the optimum treatment procedure and stent. Also it takes into account that the stent manufacturing companies and stent designer need to take more attention to this matter and stent failure in order to fix the defect or at least improve the functionality of stent in such hazardous condition.

## 7. Conclusion & Future Work

This thesis aimed to investigate the mechanism of stent fracture in angulated vessels. It examined the relationship between initial vessel angulation, degree of hinge movement and stent fracture, through a combined computer modelling (finite element analysis (FEA)) and experimental approach.

In recent years, stent fracture has been recognised as an important factor that contributes to stent failure and an adverse outcome following percutaneous coronary intervention. Stent fracture has been associated with restenosis, aneurysm formation, or more worryingly with the occurrence of an acute coronary syndrome including acute myocardial infarction or sudden death. The true incidence of SF is not known as it is not always clinically apparent, and diagnosis may be difficult if only a single strut is fractured.

FE analysis has been applied to studying various aspects of cardiovascular stents. Often the focus of the studies is upon the stress in the vessel wall, examining the stent deformation upon balloon deployment, overlapping, and presence of plaque in straight stents and therefore did not address vessel tortuosity and the cardiac cycle loading both at same time. To fully understand the mechanism of stent fracture it is essential that the stresses induced in the stent due to the hinge movement of the vessel during the cardiac cycle are examined in detail.

This work established a relationship between vessel angulation and stresses within the stent. FE results were based on stent design independent (i.e. related to the angle of bend and type of loading as opposed to specific stent structures), hence, an idealised FE model was utilised, which a thin wall shell element model represented the stent model deployed in an angulated vessel range between 30° and 90°, subjected to a 20° displacement to represent the movement during the cardiac cycle. The results from the models indicated

that a sharp increase in stresses occurs once the angulation of the vessel is increased above 70°. This agrees with clinical observation by Sianos et al. (2004).

Second part of this thesis involved *in vitro* experimental fatigue testing of stents deployed in angulated vessels. Stents deployed in a silicon tube at a predetermined angle to represent deployment in a tortuous vessel. All strut fractures occurred at sites of increased stress on the stent due to hinge movement, particularly at the curvature of connectors, which is in agreement to the FE modelling results and clinical incidences. It was founded that stent design and stent material play a critical role in this phenomenon. Although, the thicker strut increases the resistance to fracture, but it makes the stent more rigid and stiff. The new Co-Cr and Pt-Cr alloys in the newer stent provides more flexible and resistible platform than the stainless steel stent design. Although the experiment and test rig might not predict the *in vivo* conditions accurately, it illustrates the mechanism and progress of stent fracture in an angulated artery under simulated cardiac cycle. However, the bench testing can be developed to test more stent designs in larger number of samples, as well as consider more predictor SF factors such as plaque.

The proposed model has the potential to be developed, with the development of more sophisticated modelling techniques and FE models of actual stent designs. The actual stent model can be produced from the scan data of the actual stents, both in the initially deployed geometry and also at each stage of fracture, with suitable material properties as in this project elastic plastic behaviour of the stent was not modelled, and that linear elastic was assumed. By examining the resulting stress distributions throughout the stent, the effect of deployment in the angulated vessel, and also fracture on stress distribution can be examined and used to predict where the next fracture may occur, hence gaining further understanding of the mechanism of stent fracture. Moreover, CFD modelling can be conducted to carry out three-dimensional steady state and transient simulations for stents when first deployed and at the various stages of fracture. This will allow the spatial

and temporal variations of blood flow velocity and wall shear stress to be investigated, taking into account the complex three-dimensional geometry and blood pulsation. The characterisation of wall shear stress and of blood flow patterns in both undamaged and fractured stented arteries will promote the further understanding of the underlying role of hemodynamics in the development of in-stent restenosis.

## 8. References

- Adlakha, S. et al., 2010. Stent fracture in the coronary and peripheral arteries. *Journal of Interventional Cardiology*, 23(4), pp.411–419.
- Alexopoulos, D., 2011. Editorial Coronary Stent Fracture: How Frequent It Is? Does It Matter?. *Hellenic J Cardiol*, 52, pp.1–5.
- American Heart Association, 2015. Coronary Artery Disease - Coronary Heart Disease. Available: [http://www.heart.org/HEARTORG/Conditions/More/MyHeartandStrokeNews/Coronary-Artery-Disease---Coronary-Heart-Disease\\_UCM\\_436416\\_Article.jsp#.V6G\\_W4MrJpg](http://www.heart.org/HEARTORG/Conditions/More/MyHeartandStrokeNews/Coronary-Artery-Disease---Coronary-Heart-Disease_UCM_436416_Article.jsp#.V6G_W4MrJpg) [Accessed March 11, 2016].
- Aoki, J. et al., 2007. Incidence and clinical impact of coronary stent fracture after sirolimus-eluting stent implantation. *Catheterization and Cardiovascular Interventions*, 69(3), pp.380–386.
- Asakura, T. & Karino, T., 1990. Flow Patterns and Spatial Distribution of Atherosclerotic Lesions in Human Coronary Arteries. *Circulation Research*, 66, pp.1045–1066.
- ASTM International, 2001. Standard Test Method for Measurement of Fatigue Crack Growth Rates. *ASTM International*, 3, pp.1–43.
- Barrera, O. et al., 2012. On high-cycle fatigue of 316L stents. *Computer Methods in Biomechanics and Biomedical Engineering*, 17(3), pp.239–250.
- Berrocal, D.H. et al., 2008. Effects of overexpansion on stents' recoil, symmetry/asymmetry, and neointimal hyperplasia in aortas of hypercholesterolemic rabbits. *Cardiovascular Pathology*, 17(5), pp.289–296.
- Bertrand, O.F., Sipehia, R. & Mongrain, R., 1998. Biocompatibility Aspects of New Stent Technology. *Journal of the American College of Cardiology*, 32(3), pp.562–571.
- Biotronic, 2016. PRO-Kinetic Energy Cobalt Chromium Coronary Stent System Technical Specification. Available at: <https://www.biotronik.com/en-ch/products/vi/coronary/pro-kinetic-energy> [Accessed October 12, 2017].
- British Heart Foundation, 2014a. Atherosclerosis. Available at: <https://www.bhf.org.uk/heart-health/conditions/atherosclerosis> [Accessed April 22, 2017].

- British Heart Foundation, 2014b. *Your heart rate*,
- Bukala, J., Malachowski, J. & Kwiatkowski, P., 2014. Finite element analysis of the percutaneous coronary intervention in a coronary bifurcation. *Acta of Bioengineering and Biomechanics*, 16(4), pp.23–31.
- Burt, H.M. & Hunter, W.L., 2006. Drug-eluting stents: A multidisciplinary success story. *Advanced Drug Delivery Reviews*, 58(3), pp.350–357.
- Canan, T. & Lee, M.S., 2010. Drug-eluting stent fracture: Incidence, contributing factors, and clinical implications. *Catheterization and Cardiovascular Interventions*, 75(2), pp.237–245.
- Cannon, L.A. et al., 2011. A prospective evaluation of the safety and efficacy of TAXUS Element paclitaxel-eluting coronary stent implantation for the treatment of de novo coronary artery lesions in small vessels: The PERSEUS Small Vessel trial. *EuroIntervention*, 6(8), pp.920–927.
- Carter, A.J., 2008. Stent strut fracture: Seeing is believing. *Catheterization and Cardiovascular Interventions*, 71(5), pp.619–620.
- Chaichana, T., Sun, Z. & Jewkes, J., 2011. Computation of hemodynamics in the left coronary artery with variable angulations. *Journal of Biomechanics*, 44(10), pp.1869–1878.
- Chakravarty, T. et al., 2010. Meta-analysis of incidence, clinical characteristics and implications of stent fracture. *American Journal of Cardiology*, 106(8), pp.1075–1080.
- Chinikar, M. & Sadeghipour, P., 2014. Coronary stent fracture: a recently appreciated phenomenon with clinical relevance. *Current Cardiology Reviews*, 10(4), pp.349–54.
- Chua, S.N.D., Macdonald, B.J. & Hashmi, M.S.J., 2004. Finite element simulation of slotted tube ( stent ) with the presence of plaque and artery by balloon expansion. *Journal of Materials Processing Tech* , 156, pp.1772–1779.
- Chung, W.S. et al., 2008. The incidence and clinical impact of stent strut fractures developed after drug-eluting stent implantation. *International Journal of Cardiology*, 125(3), pp.325–331.

- Combined, F., 2007. I ) Risk factors for CHD. *H.E.A.R.T UK The Cholesterol Charity*, pp.6–7.
- Dangas, G.D. et al., 2010. In-stent restenosis in the drug-eluting stent era. *Journal of the American College of Cardiology*, 56(23), pp.1897–1907.
- Dawkins, K.D. et al., 2005. Percutaneous coronary intervention: recommendations for good practice and training. *Heart (British Cardiac Society)*, 91 Suppl 6, p.vi1-i27.
- Deckelbaum, L., 1992. Heart attacks and coronary artery disease. *Yale University School of Medicine Heart Book*, pp.133–148.
- Early, M. & Kelly, D.J., 2010. The role of vessel geometry and material properties on the mechanics of stenting in the coronary and peripheral arteries. *Proceedings of the Institution of Mechanical Engineers. Part H, Journal of Engineering in Medicine*, 224(3), pp.465–476.
- Egred, M., Andron, M. & Perry, R.A., 2008. The dark side of the drug-eluting stent : stent thrombosis with cessation of dual antiplatelet therapy. *The British Journal of Cardiology*, 15(6), pp.326–328.
- Elaine N, M., 2010. *Essentials of Human Anatomy and Physiology* 10th ed., England. Pearson.
- Eshghi, N. et al., 2011. Finite element analysis of mechanical behaviors of coronary stent. *Procedia Engineering*, 10, pp.3056–3061.
- Farooq, V., Gogas, B.D. & Serruys, P.W., 2011. Restenosis: Delineating the numerous causes of drug-eluting stent restenosis. *Circulation: Cardiovascular Interventions*, 4(2), pp.195–205.
- FDA, 2008. Coronary Drug-Eluting Stents—Nonclinical and Clinical Studies. *Guidance*, (March).
- Galvin, E. et al., 2017. In Vitro Corrosion and Biological Assessment of Bioabsorbable WE43 Mg Alloy Specimens. *Journal of Manufacturing and Materials Processing*, 1(1), p.8.
- Garg, S. et al., 2010. Coronary Stents: Current Status. *Journal of the American College of Cardiology*, 56(10), pp. 1-42

- Gonzalo, N. & Macaya, C., 2012. Absorbable stent: Focus on clinical applications and benefits. *Vascular Health and Risk Management*, 8(1), pp.125–132.
- Gray's Anatomy, 2005. Coronary arteries. *ElsevierLtd*. Available at: [www.graysanatomyonline.com](http://www.graysanatomyonline.com) [Accessed May 22, 2015].
- Halkin, a, Carlier, S. & Leon, M.B., 2004. Late incomplete lesion coverage following Cypher stent deployment for diffuse right coronary artery stenosis. *Heart British Cardiac Society*, 90(8), p.e45.
- Hamilos, M.I. et al., 2005. Stent fracture and restenosis of a paclitaxel-eluting stent. *Hellenic Journal of Cardiology*, 46(6), pp.439–42.
- Hannan, E.L. et al., 2000. A comparison of short- and long-term outcomes for balloon angioplasty and coronary stent placement. *Journal of the American College of Cardiology*, 36(2), pp.395–403.
- Harewood, F.. & McHugh, P., 2007. Modeling of Size Dependent Failure in Cardiovascular Stent Struts under Tension and Bending. *Annals of Biomedical Engineering*, 35(9), pp.1539–1553.
- Healthwise, 2007. Heart valves and chambers. Available at: <https://myhealth.alberta.ca/Health/Pages/conditions.aspx?hwid=ue1003> [Accessed January 27, 2015].
- Heartsite, 2013. Coronary Stents. Available at: <http://www.heartsite.com/html/stent.html> [Accessed February 11, 2014].
- Holzapfel, G. a et al., 2005. Determination of layer-specific mechanical properties of human coronary arteries with nonatherosclerotic intimal thickening and related constitutive modeling. *Heart and Circulatory Physiology*, 289(5), pp.2048–2058.
- Huibregtse, B. & Juan F. Granada, 2011. New DES platforms. Does the metal alloy matter? *Cardiac Interventions Today*, (August), pp.35–39.
- Ino, Y. et al., 2009. Predictors and prognosis of stent fracture after sirolimus-eluting stent implantation. *Circulation journal: Official Journal of the Japanese Circulation Society*, 73(11), pp.2036–2041.
- Jr, J.T.D. et al., 1992. Lumen Diameter of Normal Human Coronary Arteries Influence of Age , Sex , Anatomic Variation , and Left. *Circulation*, 86, pp.232–247.

- Jules Y. T. Lam, 2012. Atherosclerosis. *MERCK MANUAL*. Available at: <http://www.merckmanuals.com/professional/cardiovascular-disorders/arteriosclerosis/atherosclerosis#v933668> [Accessed August 2, 2015].
- Julian, D.G., 2004. *Cardiology* 8th ed., United States. Saunders.
- Kastrati, A. et al., 2001. Intracoronary Stenting and Angiographic Results. *World Wide Web Internet And Web Information Systems*, pp.2816–2821.
- Kastrati, A. et al., 2005. Sirolimus-eluting stents vs paclitaxel-eluting stents in patients with coronary artery disease: meta-analysis of randomized trials. *JAMA : the Journal of the American Medical Association*, 294(7), pp.819–825.
- Katona, B. et al., 2013. Chemical etching of nitinol stents. *Acta of Bioengineering and Biomechanics*, 15(4), pp.3–8.
- Katz, M.J. & Ness, S.M., 2015. Coronary Artery Disease ( CAD ). *Iris, Wild Education, Medical*.
- Kim, M.S. et al., 2010. Coronary stent fracture: Clinical use of image enhancement. *JACC: Cardiovascular Imaging*, 3(4), pp.446–447.
- Kinoshita Y. et al, 2009. Cypher or Taxus, Which stent fractures in bifurcation lesion? Percutaneous coronary intervention and coronary bifurcation lesion. *EuroIntervention*, p.Supplement 5 Suppl.E: E115.
- Kuramitsu, S. et al., 2012. Incidence and clinical impact of stent fracture after everolimus-eluting stent implantation. *Circulation: Cardiovascular Interventions*, 5(5), pp.663–671.
- Kuramitsu, S. et al., 2015. Incidence and Clinical Impact of Stent Fracture after PROMUS Element Platinum Chromium Everolimus-Eluting Stent Implantation. *Cardiovascular Interventions*, 8(9), pp.1180–1188.
- Lakatta, E.G., 2011. Cardiovascular System. *Circulation* , pp.547–570.
- Lally, C. et al., 2003. Analysis of Prolapse in Cardiovascular Stents : A Constitutive Equation for Vascular Tissue and Finite-Element. *Journal Biomechanics Engineering*, 125(5), 692-699

- Lee, M.S. et al., 2007. Stent fracture associated with drug-eluting stents: clinical characteristics and implications. *Catheterization and Cardiovascular Interventions : Official Journal of the Society for Cardiac Angiography & Interventions*, 69(3), pp.387–94.
- Lee, S.E. et al., 2009. Clinical outcomes and optimal treatment for stent fracture after drug-eluting stent implantation. *Journal of Cardiology*, 53(3), pp.422–428.
- Lee, T.H., 2008. *Slow rehabilitation of drug-coated stents* 18th ed., Harvard Haert Letter.
- Leong, D.P. et al., 2008. Very Late Stent Fracture Associated With a Sirolimus-eluting Stent. *Heart Lung and Circulation*, 17(5), pp.426–428.
- Li, J. et al., 2010. Fatigue life analysis and experimental verification of coronary stent. *Heart and Vessels*, 25(4), pp.333–7.
- Lilly, L.S., 2014. *Pathophysiology of Heart Disease* 5th ed., United States. Wolters Kluwer.
- Liu, G. et al., 2015. Hemodynamic characterization of transient blood flow in right coronary arteries with varying curvature and side-branch bifurcation angles. *Computers in Biology and Medicine*, 64, pp.117–126.
- Loree, H.M. et al., 1994. Static circumferential tangential modulus of human atherosclerotic tissue. *Journal of Biomechanics*, 27(2), pp.195–204.
- Lousinha, A. et al., 2011. Stent fracture: case report and literature review. *Seminars in Perinatology*, 30(2), p.213.
- Ma, W., 2011. Fatigue Analysis of a Coronary Artery Stent, *PERA Technology, on Behalf of MicroPoint Medical (Shanghai) Co Ltd*,
- Marrey, R. V et al., 2006. Fatigue and life prediction for cobalt-chromium stents: A fracture mechanics analysis. *Biomaterials*, 27(9), pp.1988–2000.
- Martin, D. & Boyle, F., 2013. Finite element analysis of balloon-expandable coronary stent deployment: Influence of angioplasty balloon configuration. *International Journal for Numerical Methods in Biomedical Engineering*, 29(11), pp.1161–1175.
- Medina, M.-C., de Lezo, J.S. & Pan, M., 2006. [A new classification of coronary

- bifurcation lesions]. *Rev Esp Cardiol*, 59(2), pp.183–4.
- Medtronic, 2002. Advantages of Cobalt Alloy for Coronary Stents. Available at: <http://wwwp.medtronic.com/newsroom/content/1110132739468.pdf> [Accessed November 1, 2015].
- MelbourneHeartcare, 2015. Atherosclerosis. Available at: <http://www.melbourneheartcare.com.au/for-patients/conditions/atherosclerosis/> [Accessed March 27, 2016].
- Menown, I.B.A. et al., 2010. The platinum chromium element stent platform: From alloy, to design, to clinical practice. *Advances in Therapy*, 27(3), pp.129–141.
- Min, P.K., Yoon, Y.W. & Moon Kwon, H., 2006. Delayed strut fracture of sirolimus-eluting stent: A significant problem or an occasional observation? *International Journal of Cardiology*, 106(3), pp.404–406.
- Mori, K. & Saito, T., 2005. Effects of stent structure on stent flexibility measurements. *Annals of Biomedical Engineering*, 33(6), pp.733–742.
- Morice, M.M., 2002. Number 23 With a Standard Stent for Coronary Revascularization. *The New England Journal of Medicine*, 346(23), pp.1773–1780.
- Morlacchi, S. et al., 2014. Influence of plaque calcifications on coronary stent fracture: a numerical fatigue life analysis including cardiac wall movement. *Journal of Biomechanics*, 47(4), pp.899–907.
- Morlacchi, S. et al., 2013. Patient-specific simulations of stenting procedures in coronary bifurcations: Two clinical cases. *Medical Engineering and Physics*, 35(9), pp.1272–1281.
- Mortier, P. et al., 2009. Finite element analysis of side branch access during bifurcation stenting. *Medical Engineering & Physics*, 31(4), pp.434–40.
- Mukherjee, D. & Moliterno, D.J., 2009. Second-Generation Drug-Eluting Stents and the Continuous Need for Rapidly Available Real-World Data. *Cardiovascular Interventions*, 2(12), pp.1236–1239.
- Müller-Hülsbeck, S. et al., 2010. Comparison of Second-Generation Stents for Application in the Superficial Femoral Artery: An In Vitro Evaluation Focusing on Stent Design. *Journal of Endovascular Therapy*, 17(6), pp.767–776.

- Murphy, B.P. et al., 2003. The Stress – Strain Behavior of Coronary Stent Struts is Size Dependent. *Annals of Biomedical Engineering*, 31, pp.686–691.
- Nair, R.N. & Quadros, K., 2011. Coronary Stent Fracture: A Review of the Literature. *Cardiac Cath Lab Director*, 1(1), pp.32–38.
- Nakazawa, G. et al., 2009. Incidence and predictors of drug-eluting stent fracture in human coronary artery a pathologic analysis. *Journal of the American College of Cardiology*, 54(21), pp.1924–31.
- National Heart Lung and Blood Institute, 2009. At a Glance: Atherosclerosis.
- National Heart Lung and Blood Institute, 2013. What Is a Stent? Available at: <http://www.nhlbi.nih.gov/health/health-topics/topics/stents/> [Accessed February 13, 2014].
- Ng, J. et al., 2016. Over-expansion capacity and stent design model: An update with contemporary DES platforms. *International Journal of Cardiology*, 221, pp.171–179.
- NHS, 2014. Treating heart disease. Available at: <http://www.nhs.uk/Conditions/Coronary-heart-disease/Pages/Treatment.aspx> [Accessed December 13, 2014].
- O'Brien, B.J. et al., 2010. A platinum-chromium steel for cardiovascular stents. *Biomaterials*, 31(14), pp.3755–3761.
- Oliva, G., Espallargues, M. & Pons, J.M. V, 2004. ORIGINAL ARTICLES Antiproliferative Drug-Eluting Stents: Systematic Review of the Benefits and Estimate of Economic Impact. *Rev Esp Cardiol*, 57(7), pp.617–628.
- Ormiston, J.A. et al., 2015. Coronary stent durability and fracture: An independent bench comparison of six contemporary designs using a repetitive bend test. *EuroIntervention*, 10(12), pp.1449–1455.
- Ormiston, J.A. et al., 2000. Stent longitudinal flexibility: A comparison of 13 stent designs before and after balloon expansion. *Catheterization and Cardiovascular Interventions*, 50(1), pp.120–124.

- Ormiston, J.A. et al., 2014. Stent longitudinal strength assessed using point compression insights from a second-generation, clinically related bench test. *Circulation: Cardiovascular Interventions*, 7(1), pp.62–69.
- Ormiston, J.A., Webber, B. & Webster, M.W.I., 2011. Stent longitudinal integrity: Bench insights into a clinical problem. *JACC: Cardiovascular Interventions*, 4(12), pp.1310–1317.
- Pache, J. et al., 2003. Intracoronary stenting and angiographic results: Strut thickness effect on restenosis outcome (ISAR-STereo-2) trial. *Journal of the American College of Cardiology*, 41(8), pp.1283–1288.
- Park, A., 2013. A Cardiac Conundrum. *Harvard Magazine*. Available at: <http://harvardmagazine.com/2013/03/a-cardiac-conundrum> [Accessed February 22, 2017].
- Park, K.W. et al., 2011. Clinical characteristics of coronary drug-eluting stent fracture: Insights from a two-center DES registry. *Journal of Korean Medical Science*, 26(1), pp.53–58.
- Pelton, A.R. et al., 2008. Fatigue and durability of Nitinol stents. *Journal of the Mechanical Behavior of Biomedical Materials*, 1(2), pp.153–164.
- Perry, M., Oktay, S. & Muskivitch, J., 2002. Finite element analysis and fatigue of stents. *Minimally Invasive Therapy & Allied Technologies*, 11, pp.165–171.
- Phatak, O., 2013. What is a Heart Stent Operation. Available at: <http://www.buzzle.com/articles/what-is-a-heart-stent-operation.html> [Accessed February 11, 2014].
- Reichek, N., 1999. MRI myocardial tagging. *Journal of Magnetic Resonance Imaging*, 10(5), pp.609–616.
- Rogers, C. et al., 1999. Design as Contributors to Vascular Injury. *October*, pp.378–383.
- Ryan, T.J. et al., 1993. Guidelines for percutaneous transluminal coronary angioplasty. , 22(7), pp.2033–54.
- Sangiorgi, G. et al., 2007. Engineering aspects of stents design and their translation into

- clinical practice. *Annali dell'Istituto Superiore di Sanita*, 43(1), pp.89–100.
- Schömig, A. et al., 2007. A Meta-Analysis of 16 Randomized Trials of Sirolimus-Eluting Stents Versus Paclitaxel-Eluting Stents in Patients With Coronary Artery Disease. *Journal of the American College of Cardiology*, 50(14), pp.1373–1380.
- Shaikh, F. et al., 2008. Stent fracture, an incidental finding or a significant marker of clinical in-stent restenosis? *Catheterization and Cardiovascular Interventions*, 71(5), pp.614–618.
- Sianos, G. et al., 2004. Stent Fracture and Restenosis in the Drug-Eluting Stent Era. *Catheterization and Cardiovascular Interventions*, 61(1), pp.111–116.
- Simard, T. et al., 2014. The Evolution of Coronary Stents: A Brief Review. *Canadian Journal of Cardiology*, 30(1), pp.35–45.
- Smuclovsky, C., 2011. Coronary Artery CTA: A Case-Based Atlas. *Radiology*, 258(3), pp.694–694.
- Sousa, J.E. et al., 2001. Clinical Investigation and Reports Sustained Suppression of Neointimal Proliferation by Sirolimus-Eluting Stents One-Year Angiographic and Intravascular Ultrasound Follow-Up. *Circulation*, 104, pp.2007–2012.
- Szabadíts, P., Bagi, I. & Dobránszky, J., 2008. Comparison the flexibility of balloon-expandable coronary stents. *Proceedings of the Third Hungarian Conference on Biomechanics.*, pp.315–9.
- Szabadíts, P., Puskas, Z. & Dobránszky, J., 2009. Flexibility and trackability of laser cut coronary stent systems. *Acta of Bioengineering and Biomechanics*, 11(3), pp.11–18.
- Texas heart institute, 2016. The coronary arteries.
- TheBritishStandardsInstitution, 2018. Medical Devices. Available at: <http://www.abhi.org.uk/what-we-do/medical-device-regulation/medical-device-standards/> [Accessed March 6, 2018].
- Ther, M.I. et al., 2002. A Survey of Stent D . signs. *Cell*.
- Tran, H. et al., 2004. Oral antiplatelet therapy in cerebrovascular disease, coronary artery disease, and peripheral arterial disease ., *Jama*, 292(15), pp.1867–1874.

- Umeda, H. et al., 2009. Frequency, predictors and outcome of stent fracture after sirolimus-eluting stent implantation. *International Journal of Cardiology*, 133(3), pp.321–326.
- Veress, A. et al., 1998. Age-related development of atherosclerotic plaque stress: a population-based finite-element analysis. *Journal of Coronary Artery Disease*, (9), pp.13–19.
- Waller, B.F. et al., 1992. Anatomy, histology, and pathology of coronary arteries: A review relevant to new interventional and imaging techniques—Part I. *Clinical Cardiology*, 15(6), pp.451–457.
- Wiktor, D.M., Waldo, S.W. & Armstrong, E.J., 2016. Coronary Stent Failure: Fracture, Compression, Recoil, and Prolapse. *Interventional Cardiology Clinics*, 5(3), pp.405–414.
- Wong, H.C., Cho, K.N. & Tang, W.C., 2009. Bending of a Stented Atherosclerotic Artery. *Proceedings of the COMSOL Conference*, pp.1–6.
- Wu, W. et al., 2007. An FEA method to study flexibility of expanded coronary stents. *Journal of Materials Processing Technology*, 184(1–3), pp.447–450.
- Wu, W. et al., 2007. Stent expansion in curved vessel and their interactions: a finite element analysis. *Journal of Biomechanics*, 40(11), pp.2580–5.
- Zhen, Z., Xi, T.F. & Zheng, Y.F., 2013. A review on in vitro corrosion performance test of biodegradable metallic materials. *Transactions of Nonferrous Metals Society of China (English Edition)*, 23(8), pp.2283–2293.

# Appendix I

Convergence tests were performed for two simple models of 1. An artery using solid elements; and 2. A stent using shell elements, both in ANSYS, in order to define the necessary number of elements to have an accurate mechanical response represented by the modelling.

The artery model was created as a 3D solid cylinder. First, an annulus with 3mm inner diameter and 0.7mm wall thickness (Holzapfel et al. 2005) was created, and then it was extruded four times along its normal by 8.25mm each time. After four times extrusion, all four volumes were glued together to have one single cylinder with 33mm in length (see Figure A).

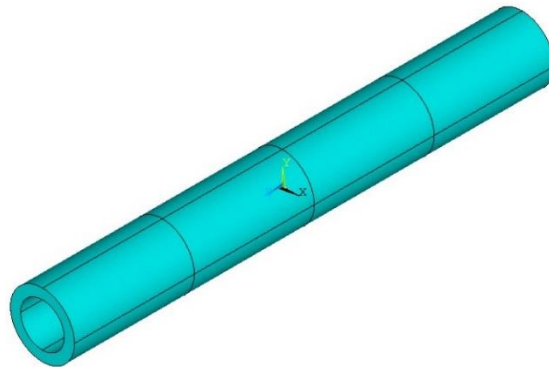


**Figure A: 3D solid model of the artery**

The element type 20-node SOLID 186 was chosen for the artery model as well as the material properties. (Linear isotropic material with Young's modulus ( $E$ ) = 1.75 MPa and Poisson's ratio ( $\nu$ ) = 0.499 (Chua et al. 2004)). Next the model was meshed by defining the number of element divisions on each line and then boundary conditions were applied to the beam to represent 3-point bending test.

The 5 nodes at the two ends of the beam were constrained where there is no displacement in the y-direction. Also nodes in the middle cross section area of the beam was constrain in the x and z-direction to prevent any movement in these directions and then applied

0.1N load acting downward (y-direction) to a top-middle node of the beam (see Figure B).

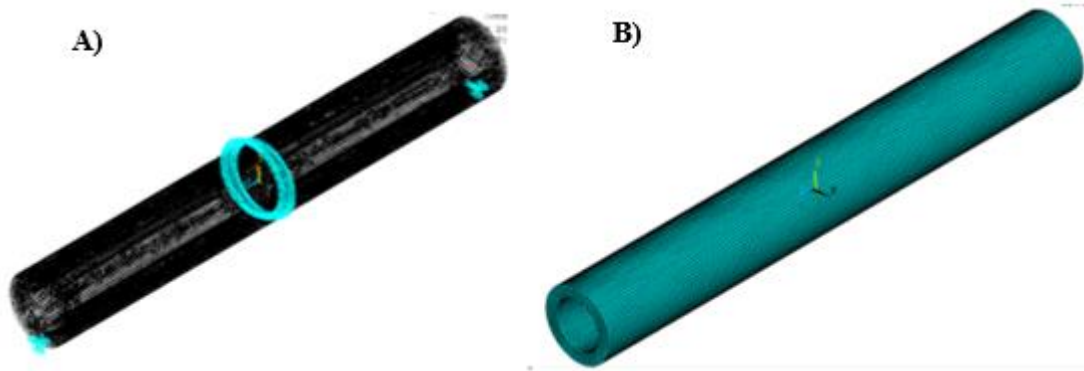


**Figure B: Artery validation model. A) Highlighted area indicates constraint nodes. B) Meshed solid artery model**

Convergence was evaluated with respect to the Von-Mises stress and maximum deflection were considered through the convergence study. A total of 12 meshes were evaluated ~5,200 elements (0.7 mm elements size) up to ~115,000 elements (0.1 mm element size) for the artery model. The Figure C illustrates the Von-Mises stress variation at middle section of the artery. It can be seen that as the mesh was refined and the number of elements increased for both the convergence and theoretical value. It was unstable at the beginning till the number of elements was increased approximately to 62,000 and they became almost constant at 124KPa. In other hand, the deflection fluctuated as well from 2.34 mm to 2.91 mm, and became stable at ~76,000 elements (see Figure D).

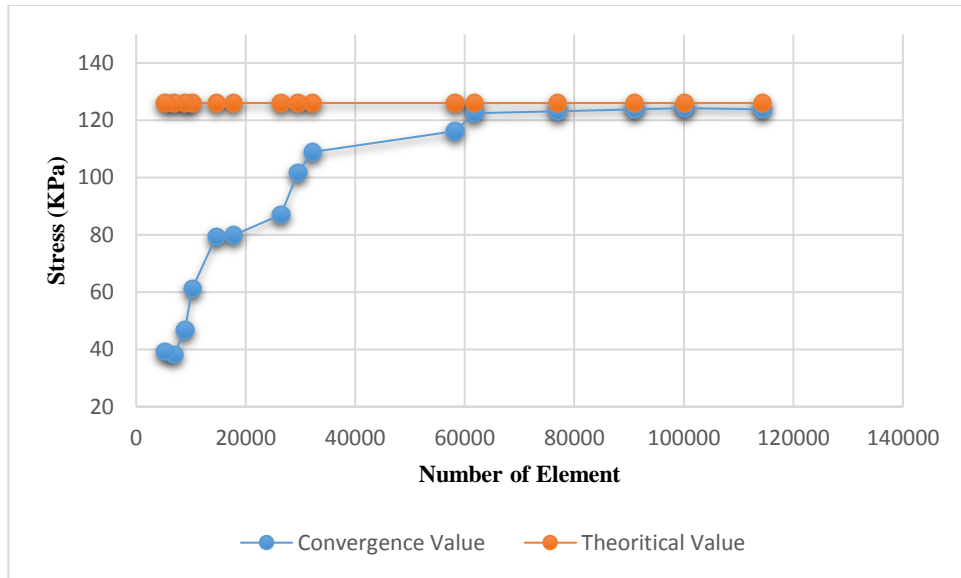


**Figure C: Variation of stress in the artery validation model with respect to number of elements through convergence study and theoretical calculation.**

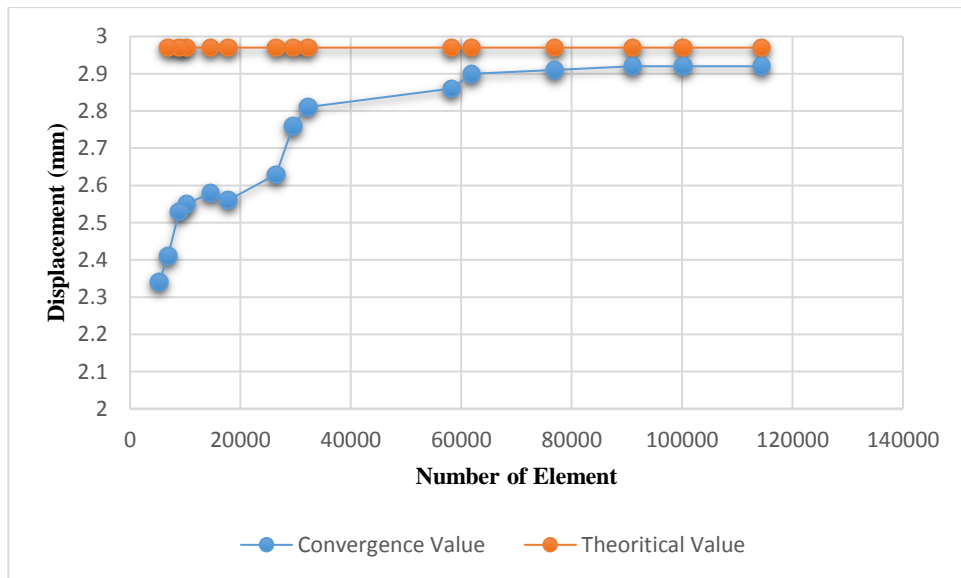


**Figure D: Variation of displacement in the artery validation model with respect to number of elements through convergence study and theoretical calculation.**

The second model was built in order to validate the stent model. A circle surface with 1.5mm radius was created, then deleted the area but left the lines of the circle. Five key points was created, one at the origin, 2 key points in the negative and 2 key points in the positive z-direction with distance of 7mm from each other. These key points were joined by line and the circle extruded along these lines to model 28mm cylindrical area. For the stent model the 8-node SHELL 281 was chosen, Effective modulus =250 MPa (See

Section 4.2.1),  $\nu = 0.3$  and a real constant for the thickness was defined as 0.2mm. Similar to the artery model, number of divisions on the lines was defined and then meshed the model, though to have sufficient number of element different division number was tried on each line of the stent model. Next applied boundary conditions, constrained nodes at the way around (edges) on both ends in y-direction and constrained the middle part in x and z-direction where there is no displacement. Also 0.1N load applied to the top node in the middle part of the model which acting downward in negative y-direction (see Figure E).

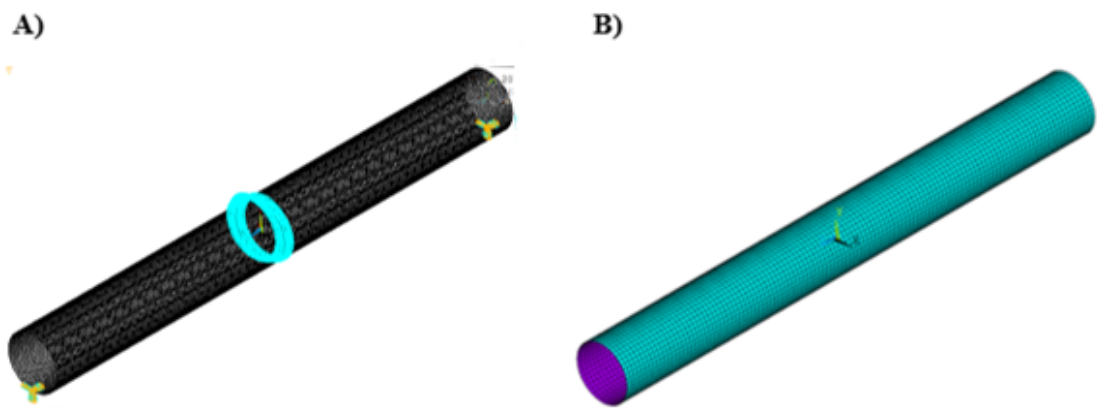


**Figure E: Stent validation model, A) Highlighted area indicates constraint nodes. B) Meshed shell stent model**

The variation of stresses and deflection in the stent model were smaller than the artery as well as it converged with much less elements number due to its volume and elements type. The test was began with ~400 elements and continued up to ~22,500 elements, though, both elements of interest, stresses and deflection were stabled with 6,720 elements number at 513KPa and 0.084 mm, respectively. Figures F & G show the stress and deflection magnitude through convergence and theoretical calculation.

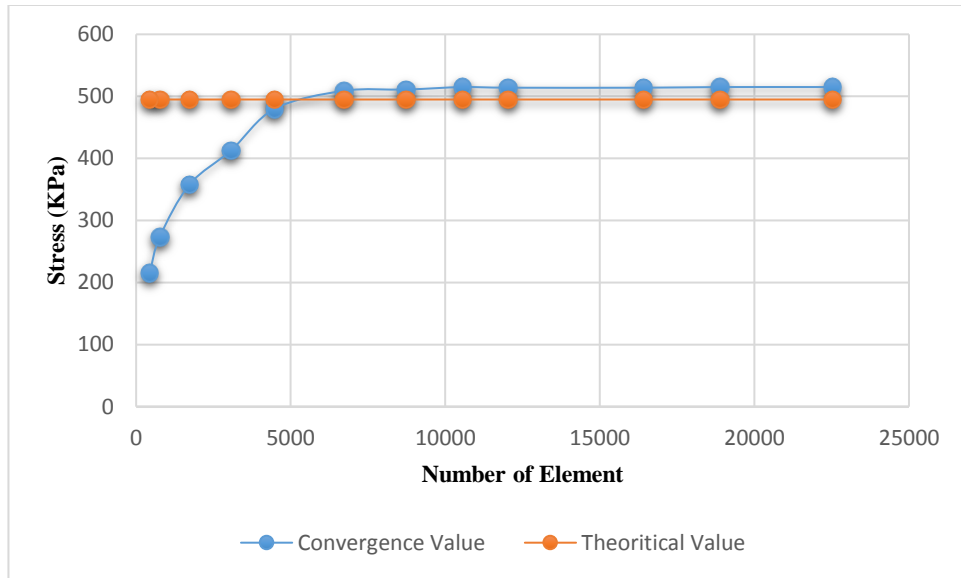


**Figure F: Variation of stress in the stent validation model with respect to number of elements through convergence study and theoretical calculation.**

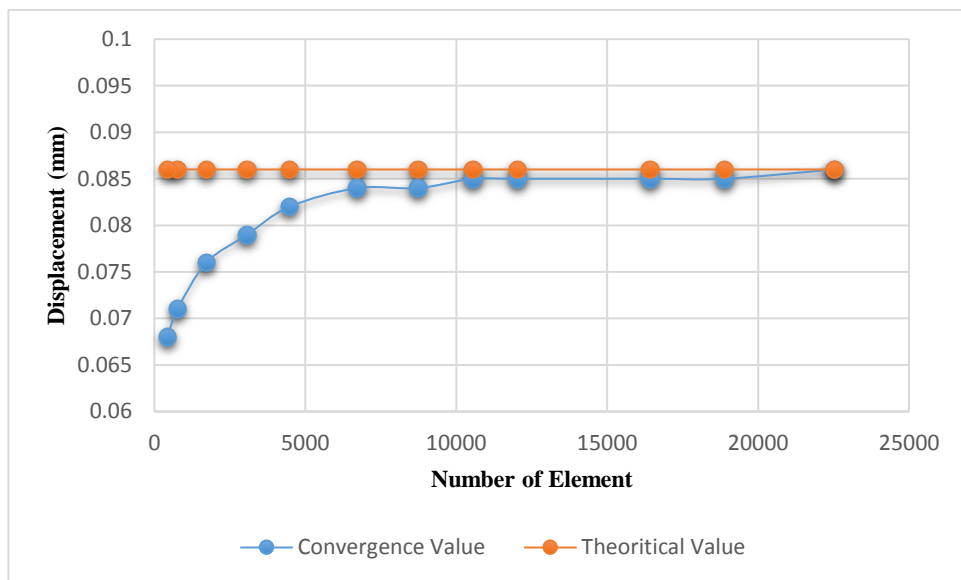


**Figure G: Variation of displacement in the stent validation with respect to number of elements through convergence study and theoretical calculation.**

Regarding to the convergence study and validation results from ANSYS for the artery and stent mode, the mathematical method was conducted to evaluate the stress and maximum deflection.

## ○ Artery Theoretical Results

In addition to the convergence study, mathematical calculation was performed for the both artery and stent model in order to validate the results from the bending simulation.

Table A represents the artery parameters.

Length (L)	Outer Diameter (D)	Inner Diameter (d)	Young's Modulus (E)	Applied Force (F)
33 mm	4.4 mm	3 mm	1.75 MPa	0.1 N

**Table A: Artery model specification**

$$\text{Bending Moment (BM)} = \frac{FL}{4} = \mathbf{0.825 \text{ Nmm}}$$

$$\text{Second Moment of Area (I)} = \frac{\pi(D^4 - d^4)}{64} = \mathbf{14.42 \text{ mm}^4}$$

$$\text{Stress } (\sigma) = \frac{BMy}{I} = \mathbf{0.126 \text{ Nmm}^2} \text{ (where } y \text{ is vertical distance away from the neutral axis)}$$

$$\text{Maximum Deflection} = \frac{FL^3}{48EI} = \mathbf{2.97 \text{ mm}}$$

## ○ Stent Theoretical Results

Table B represents the stent parameters.

Length (L)	Diameter (D)	Thickness (t)	Young's Modulus (E)	Force (F)
28 mm	3 mm	0.2 mm	250 MPa	0.1 N

**Table B: Stent model specification**

$$\text{Bending Moment (BM)} = \frac{FL}{4} = \mathbf{0.7 \text{ Nmm}}$$

$$\text{Second Moment of Area for thin tube (I)} = \pi r^3 t = \mathbf{2.12 \text{ mm}^4}$$

$$\text{Stress } (\sigma) = \frac{BMy}{I} = \mathbf{0.495 \text{ Nmm}^2} \text{ (where } y \text{ is vertical distance away from the neutral axis)}$$

$$\text{Maximum Deflection} = \frac{FL^3}{48EI} = \mathbf{0.086 \text{ mm}}$$

Although these results are not identical to the ANSYS simulation, but they are close enough to meet each other. In fact, these amount of difference is acceptable due to different method of calculation Computer Analysis and Mathematical Determination. Table C shows the results from both computer analysis and theoretical calculation of stress and deflection for the artery and the stent model.

	Convergence Value		Theoretical Value		Match Percentage	
	Stress (KPa)	Deflection (mm)	Stress (KPa)	Deflection (mm)	Stress	Deflection
<b>Artery</b>	124	2.91	126	2.97	98.4%	98.0%
<b>Stent</b>	509	0.084	495	0.086	97.2%	97.7%

**Table C: Stress and deflection in both artery and stent model, via computer simulation and theoretical calculation.**

## Appendix II

As the cardiac cycle may cause different degrees of movement in an artery, therefore following figures illustrate the more results of creation of stress within the stent models, when the artery was subjected to various displacement loading.

Figure H to J are representing the tensile stress within the stent model in the linear artery under 5°, 10°, and 15° displacement load, respectively. Of course, the trend of increasing in stress with the respect to vessel angulation are similar as it was discussed in section 4.4.1 and 4.4.2. However, they have different stress magnitude due to low to high applied displacement load.

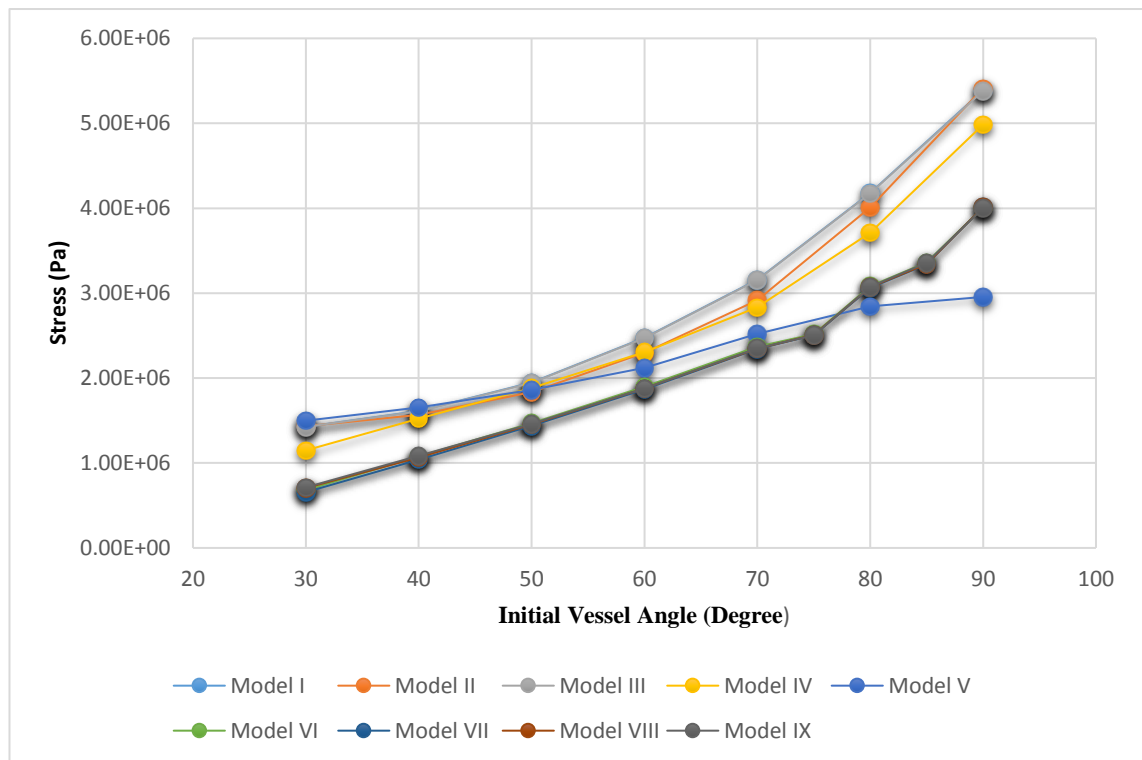


**Figure H: Variation of tensile stress in the stent with respect to initial vessel angulation, when a total 5° displacement load applied. The vessel has linear material properties.**

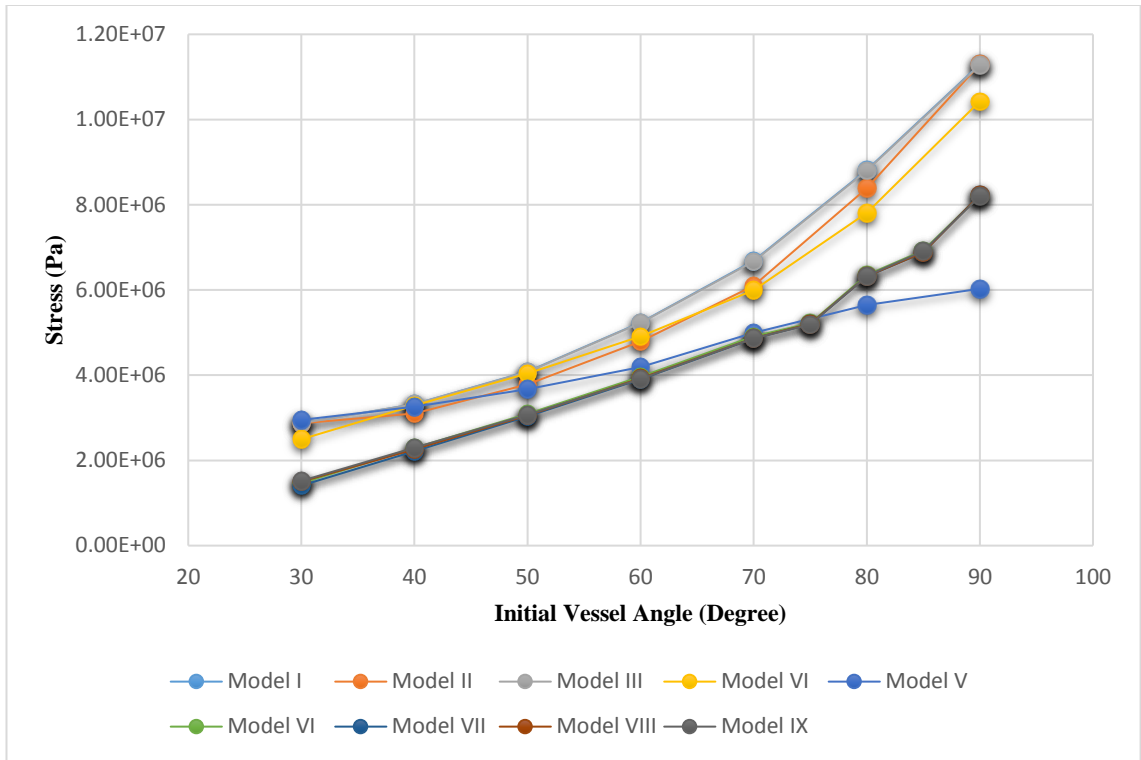


**Figure I: Variation of tensile stress in the stent with respect to initial vessel angulation, when a total 10° displacement load applied. The vessel has linear material properties.**

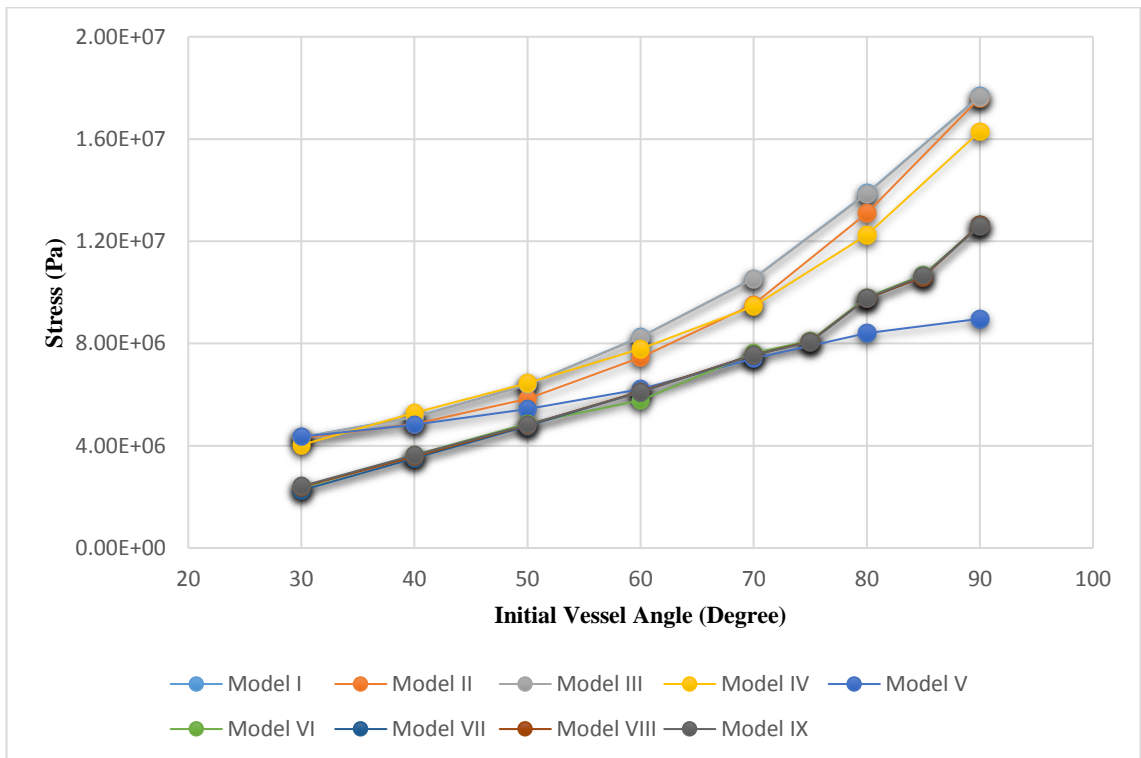


**Figure J: Variation of tensile stress in the stent with respect to initial vessel angulation, when a total 15° displacement load applied. The vessel has linear material properties.**

Likewise, the increment trend analysis of changes in compressive (see Figure K to M) and von-Mises (see Figure N to P) stent stress under 5°, 10°, and 15° were similar to the 20°, but in lower scale.

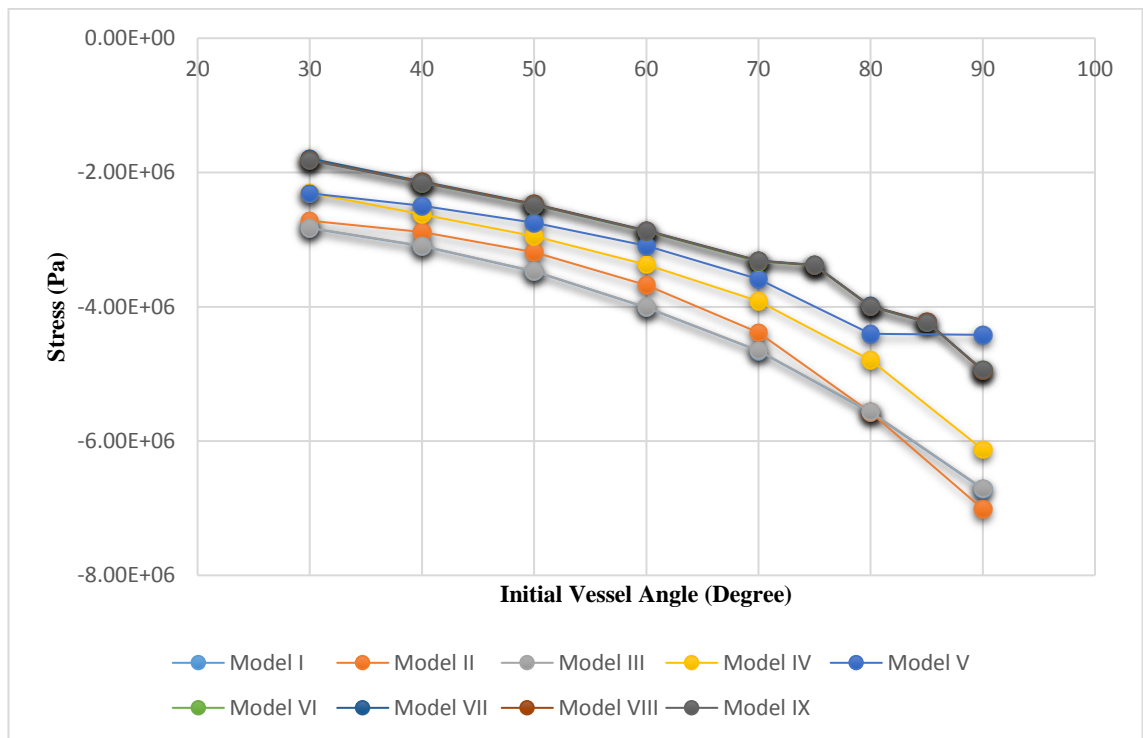


**Figure K: Variation of compressive stress in the stent with respect to initial vessel angulation, when a total 5° displacement load applied. The vessel has linear material properties.**

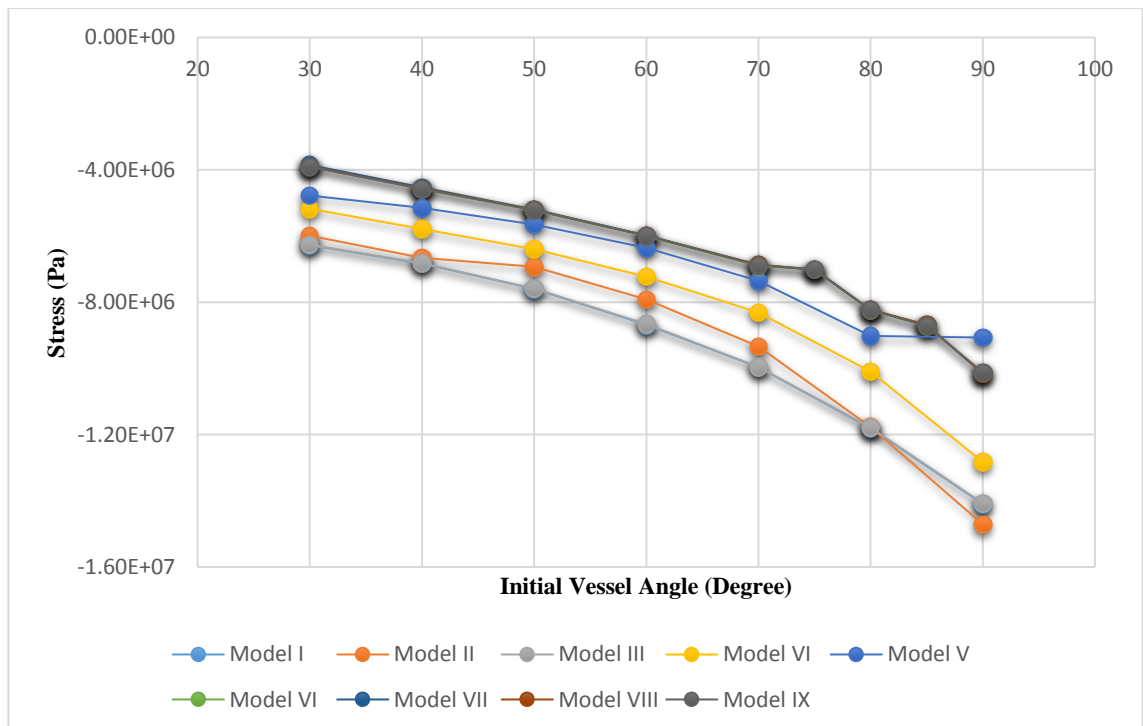


**Figure L: Variation of compressive stress in the stent with respect to initial vessel angulation, when a total 10° displacement load applied. The vessel has linear material properties.**

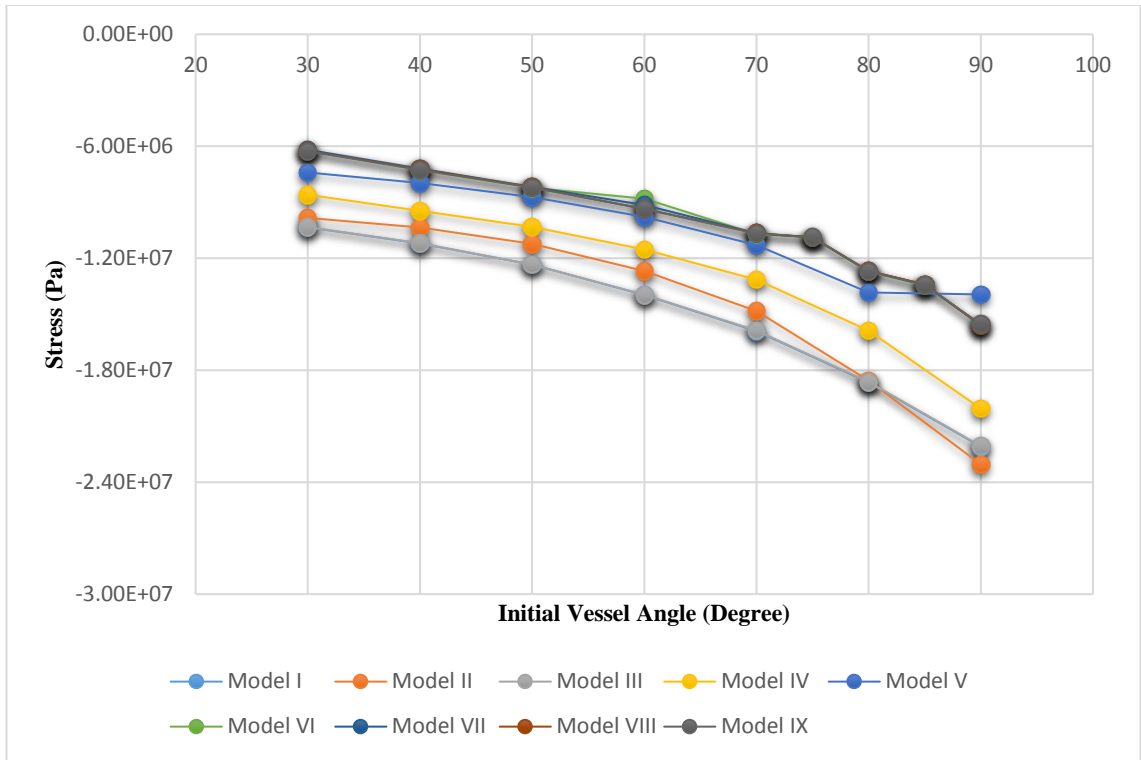


**Figure M: Variation of compressive stress in the stent with respect to initial vessel angulation, when a total 15° displacement load applied. The vessel has linear material properties.**

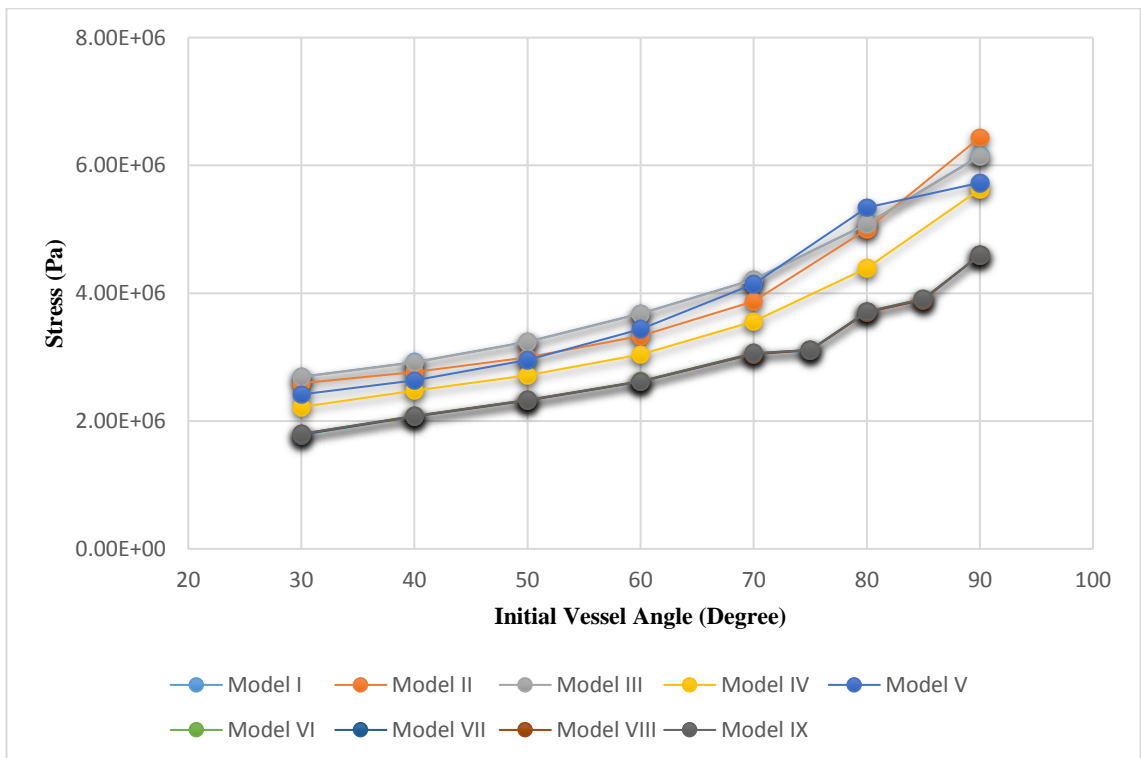


**Figure N: Variation of von-Mises stress in the stent with respect to initial vessel angulation, when a total 5° displacement load applied. The vessel has linear material properties.**

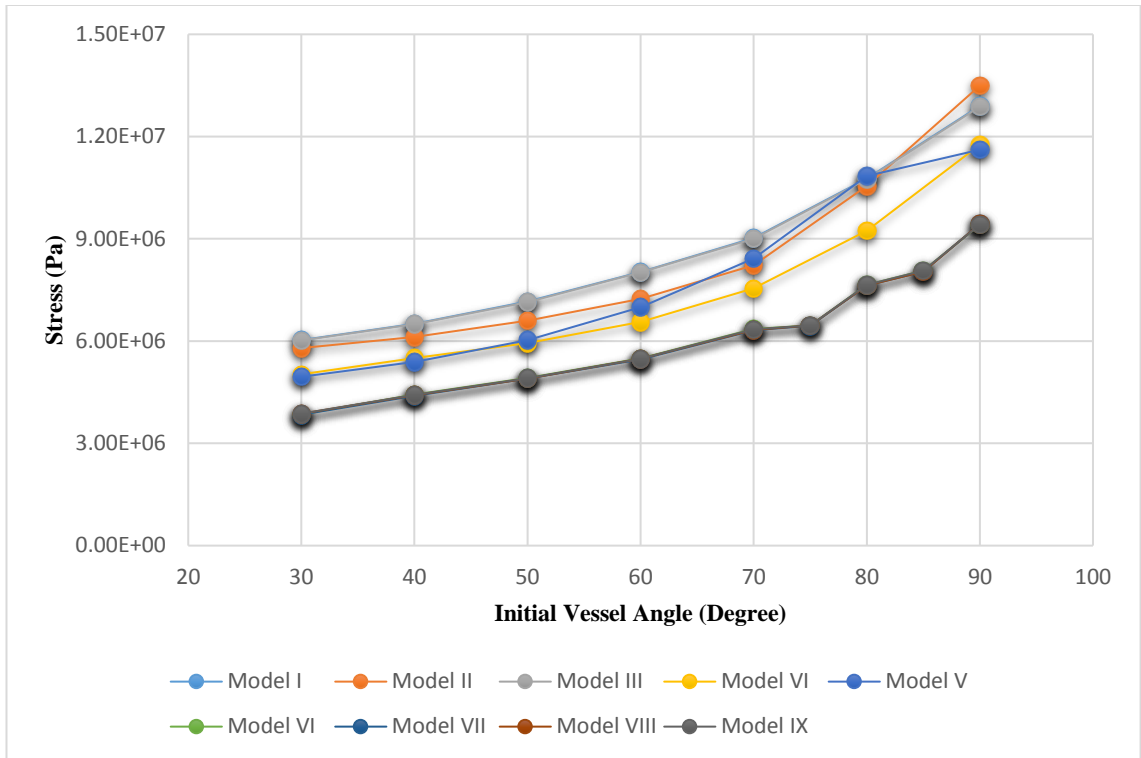


**Figure O: Variation of von-Mises stress in the stent with respect to initial vessel angulation, when a total 10° displacement load applied. The vessel has linear material properties.**

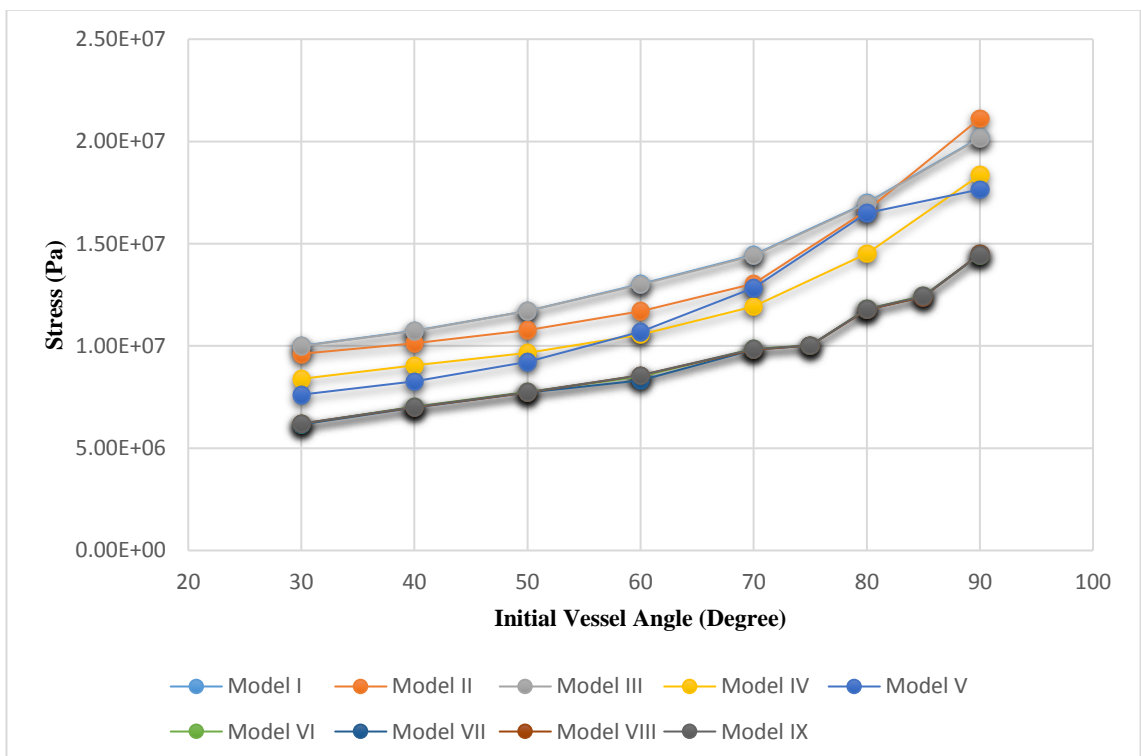


**Figure P: Variation of von-Mises stress in the stent with respect to initial vessel angulation, when a total 15° displacement load applied. The vessel has linear material properties.**

Furthermore, similar analysis have been performed for the specific models (VI to IX), when the artery was defined as a nonlinear hyper elastic material. Figure Q to S are showing the tensile stress within the stent when the nonlinear artery was subjected to 5°, 10°, and 15° displacement load.

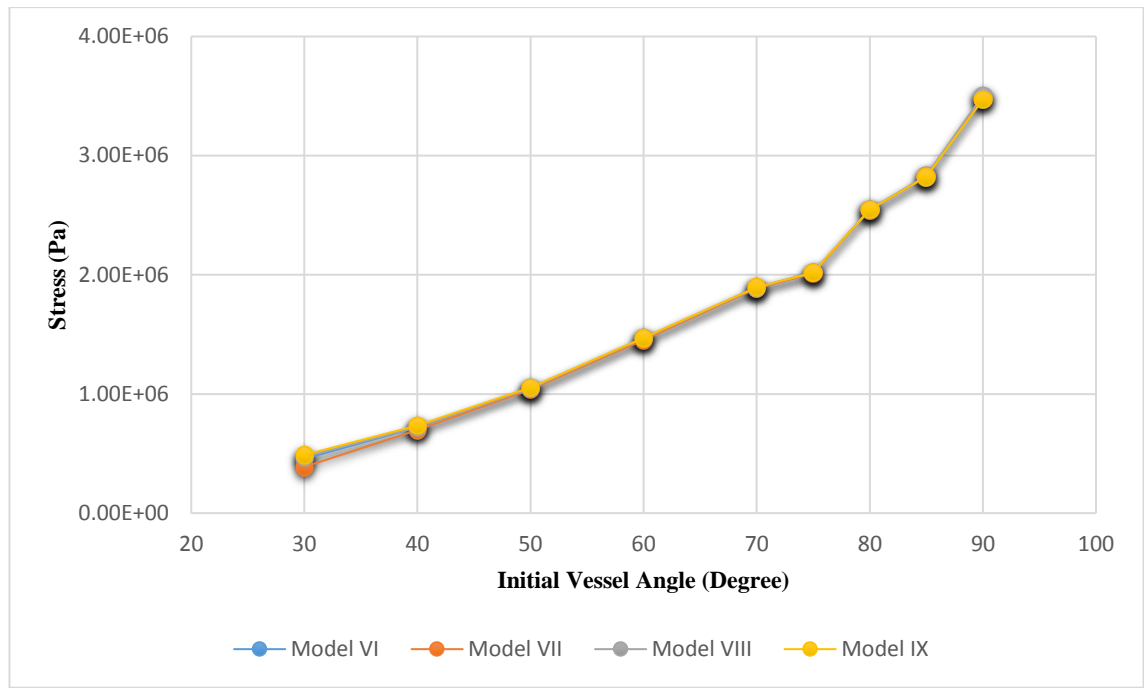


**Figure Q: Variation of tensile stress in the stent with respect to initial vessel angulation, when a total 5° displacement load applied. The vessel has non-linear material properties.**

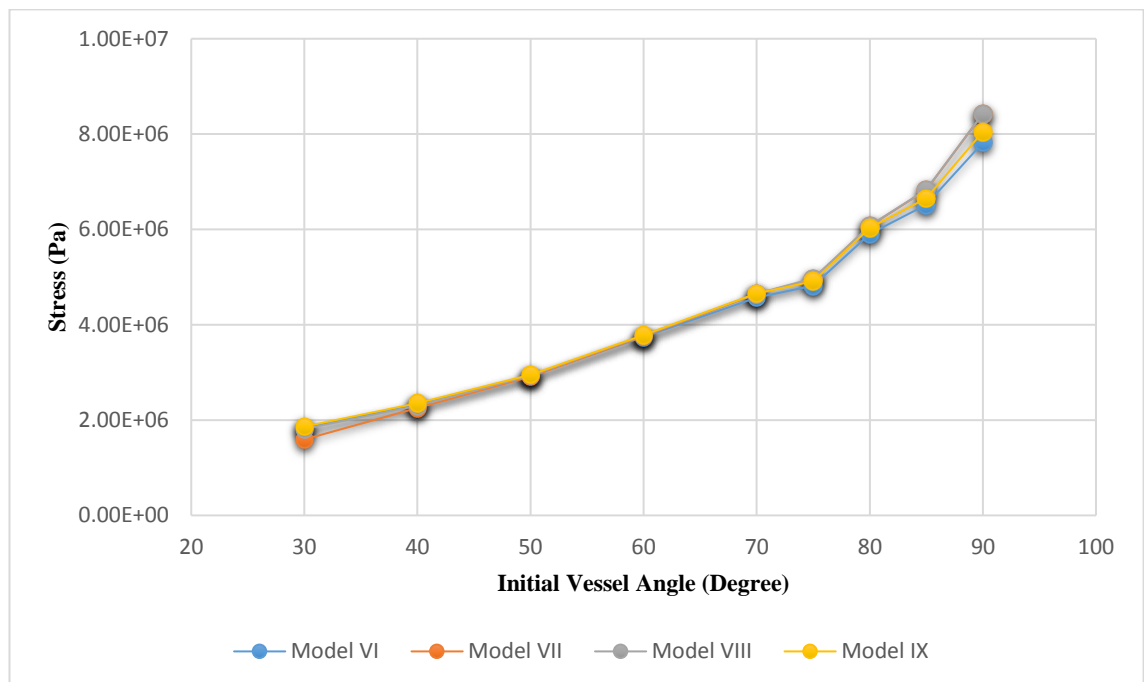


**Figure R: Variation of tensile stress in the stent with respect to initial vessel angulation, when a total 10° displacement load applied. The vessel has non-linear material properties.**

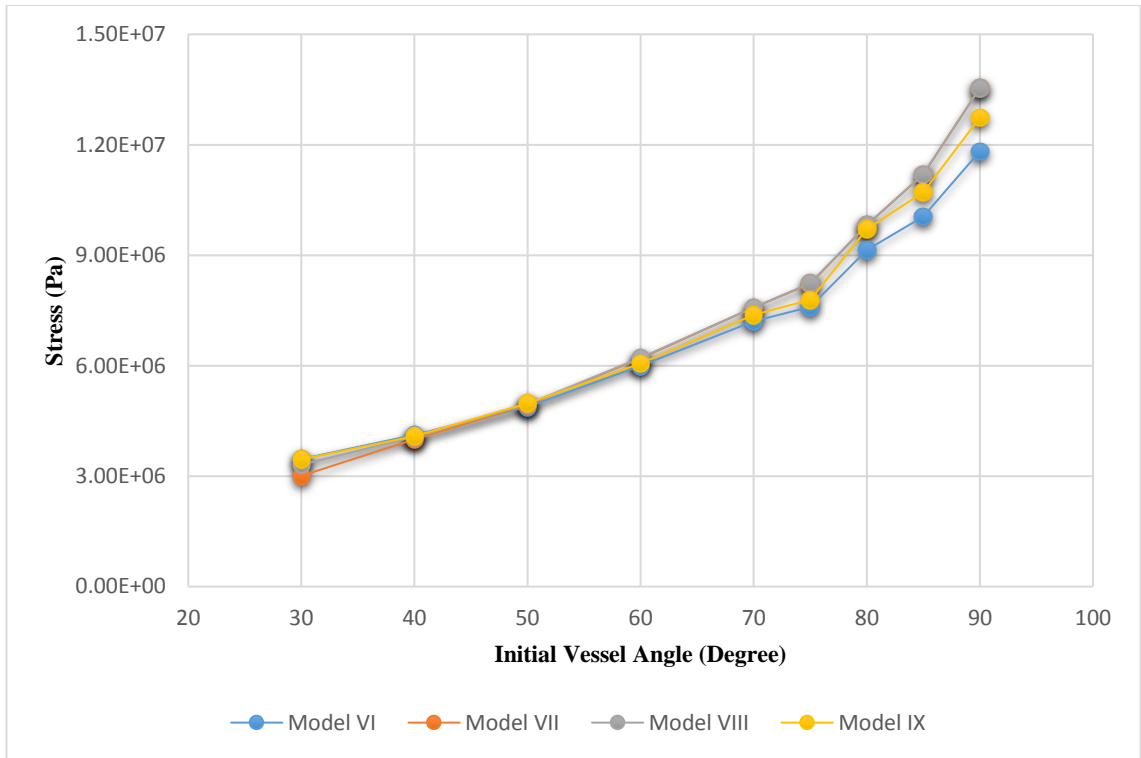


**Figure S: Variation of tensile stress in the stent with respect to initial vessel angulation, when a total 15° displacement load applied. The vessel has non-linear material properties.**

Figure T to V are the results of compressive stress when stent was deployed into the nonlinear artery under various load.

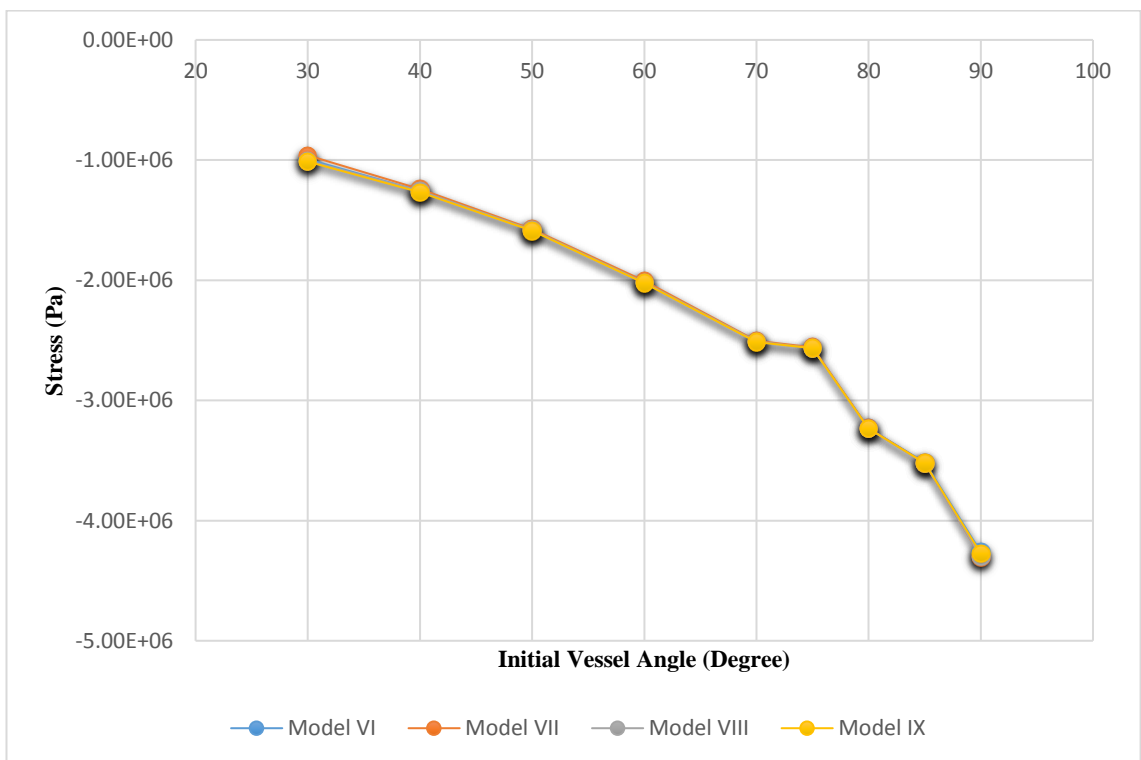


**Figure T: Variation of compressive stress in the stent with respect initial vessel angulation, when a total 5° displacement load applied. The vessel has non-linear material properties.**

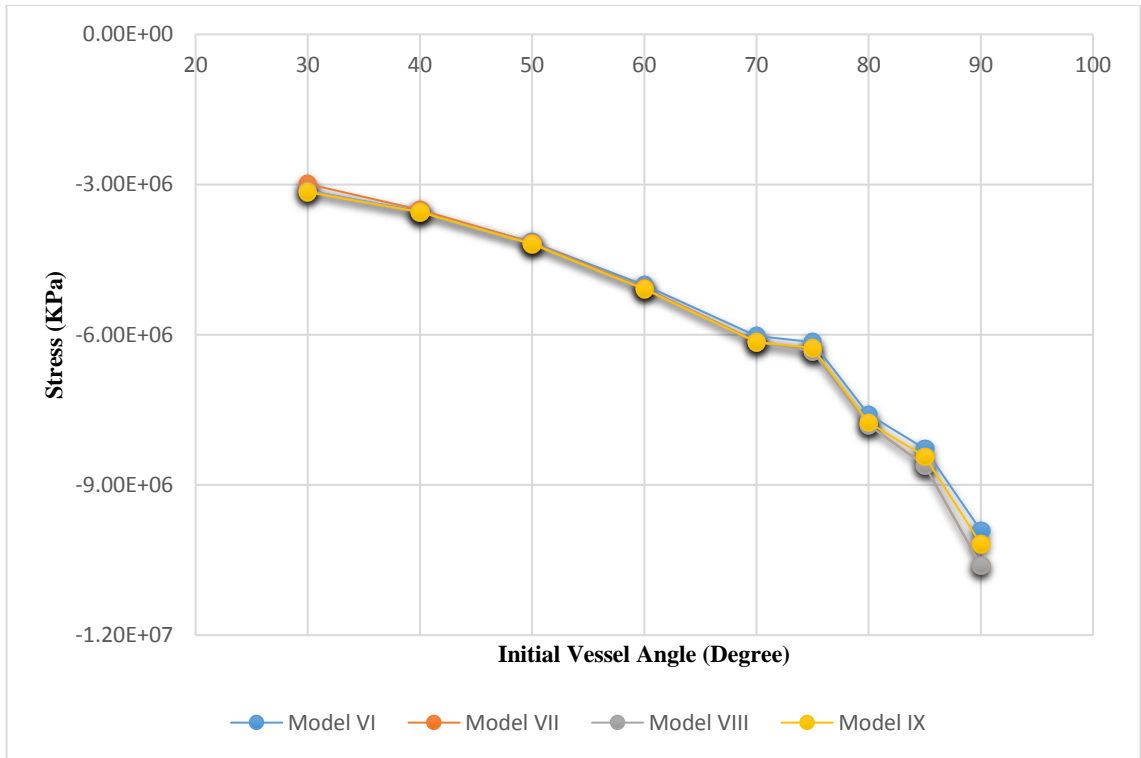


**Figure U: Variation of compressive stress in the stent with respect to initial vessel angulation, when a total 10° displacement load applied. The vessel has non-linear material properties.**

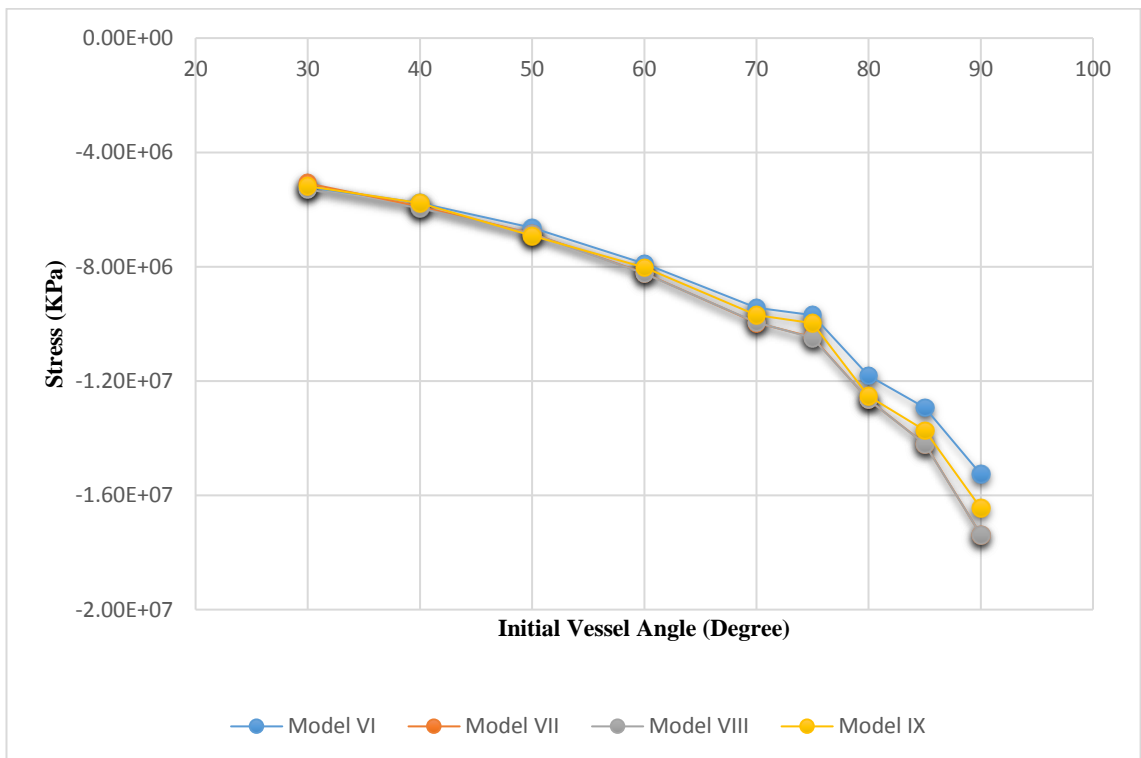


**Figure V: Variation of compressive stress in the stent with respect to initial vessel angulation, when a total 15° displacement load applied. The vessel has non-linear material properties.**

The last series of result were recorder according to changes in stent von-Mises stress, when the nonlinear artery model underwent loading 5°, 10°, and 15° (see Figure W to Y)

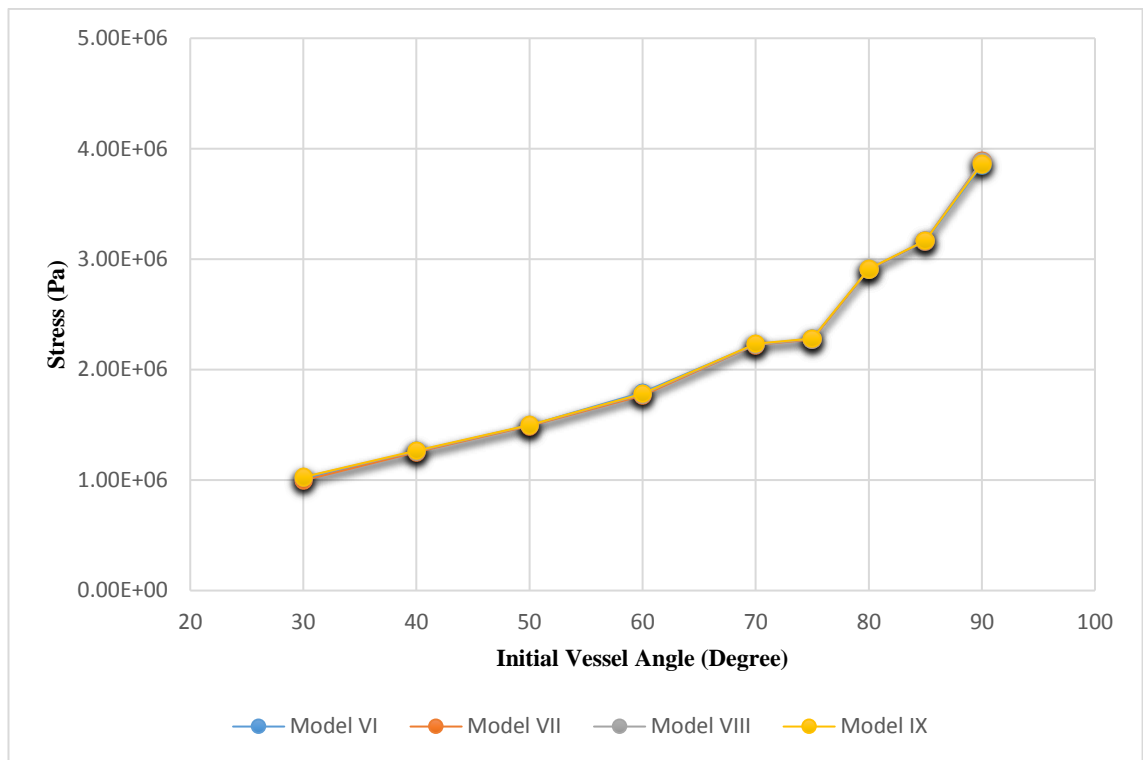


**Figure W: Variation of von-Mises stress in the stent with respect to initial vessel angulation, when a total 5° displacement load applied. The vessel has non-linear material properties.**

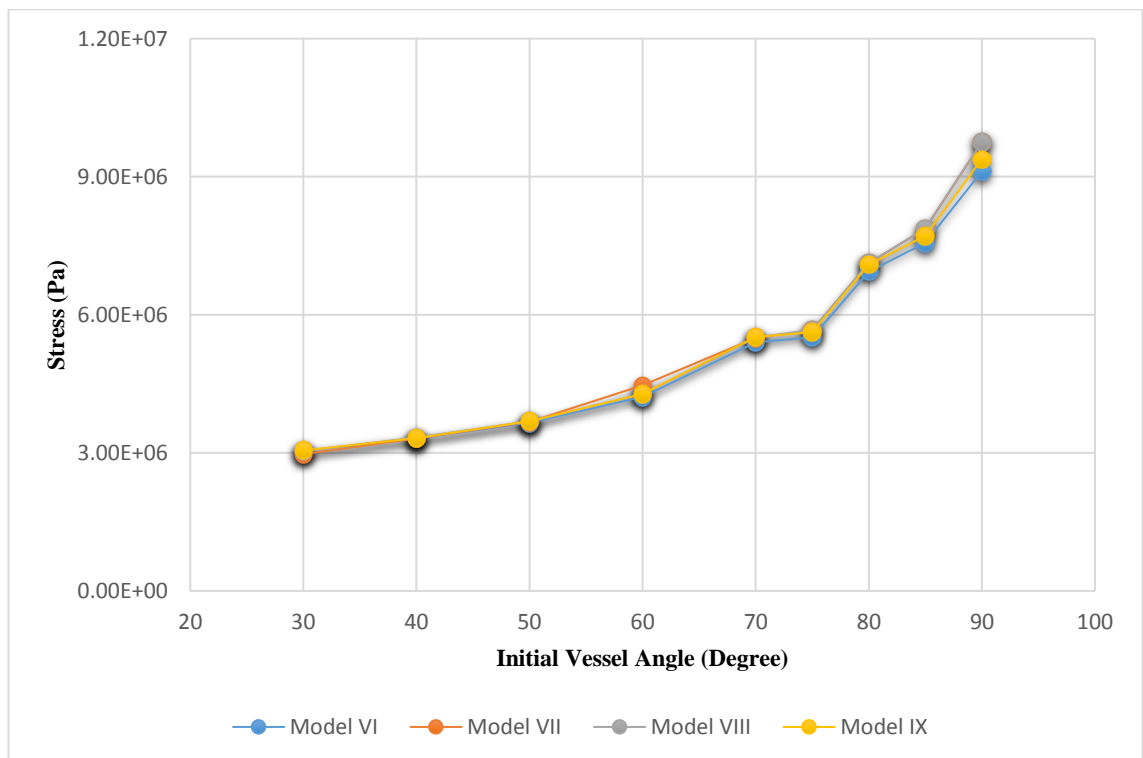


**Figure X: Variation of von-Mises stress in the stent with respect to initial vessel angulation, when a total 10° displacement load applied. The vessel has non-linear material properties.**

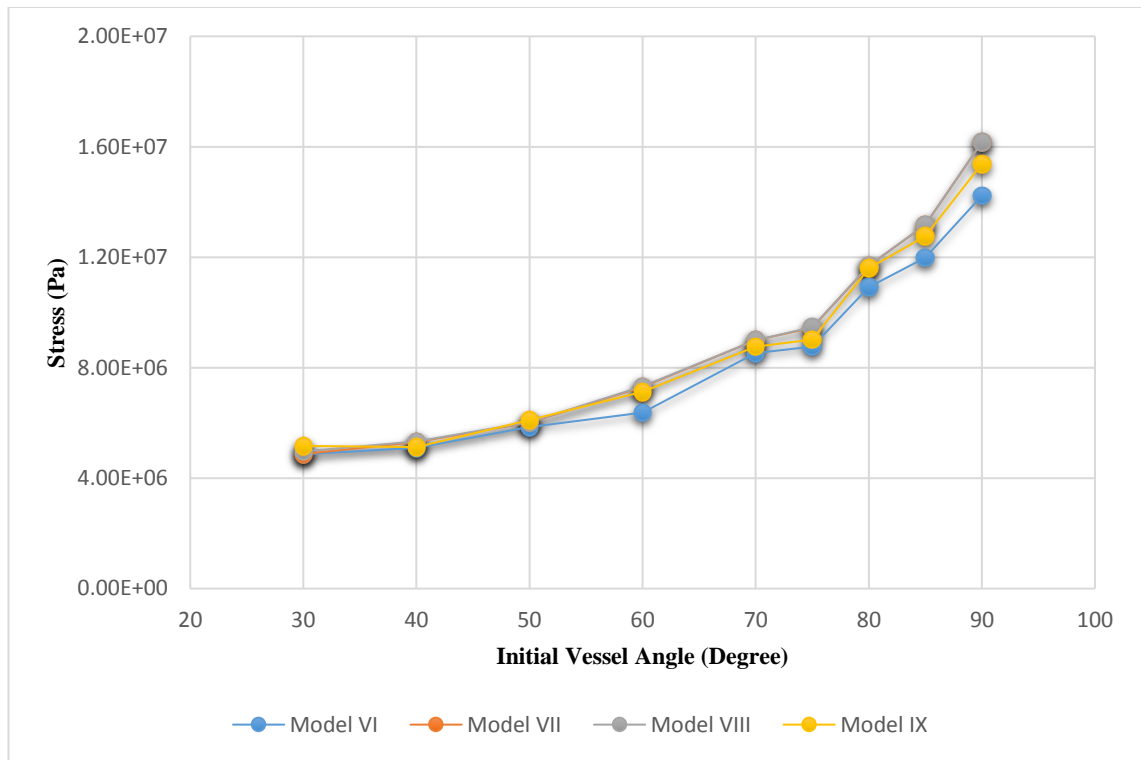


**Figure Y: Variation of von-Mises stress in the stent with respect to initial vessel angulation, when a total 15° displacement load applied. The vessel has non-linear material properties.**

Once again, all the models simulation result were showing, that the stress was increasing within deployed stent with respect to the artery angles, and it was intensified once the angle exceed 70°. Moreover, various applied loading have been shown that the trend of stress increment in smoother in lower displacement load, while as the exerted displacement load increased the stress increased more fluctuated especially in nonlinear models after 70° angle.